SEARCH FOR MAGNETIC MONOPOLES IN 8 TEV CENTRE-OF-MASS ENERGY PROTON-PROTON COLLISIONS WITH THE ATLAS DETECTOR AT THE LHC

GABRIEL DAVID PALACINO CAVIEDES

A DISSERTATION SUBMITTED TO THE FACULTY OF GRADUATE STUDIES
IN PARTIAL FULFILLMENT OF THE REQUIREMENTS
FOR THE DEGREE OF

DOCTOR OF PHILOSOPHY

GRADUATE PROGRAM IN PHYSICS AND ASTRONOMY
YORK UNIVERSITY
TORONTO, ONTARIO

DECEMBER 2015

Abstract

Symmetry is fundamental to our understanding of the laws of nature. The simplicity that is found in the symmetries that explain the most fundamental interactions is remarkably beautiful. Physicists have worked hard and continue to work even harder to deepen the understanding of nature with the hope of revealing higher symmetries, among them the symmetry between electricity and magnetism, but one piece is still missing from this puzzle: the elusive magnetic monopole.

This dissertation presents a search for magnetic monopoles produced at the Large Hadron Collider in 8 TeV centre-of-mass energy proton–proton collisions using the ATLAS detector. The highly ionizing nature of monopoles was exploited to look for regions of high ionization density in the Transition Radiation Tracker and energy deposits in the Liquid-Argon electromagnetic calorimeter with very low lateral dispersion. The search used 7 fb^{-1} of data collected by a dedicated trigger for highly ionizing particles, which made the ATLAS detector sensitive to monopoles with charge greater than the Dirac charge, in particular, twice the Dirac charge, for the first time. The results of the search were interpreted for models of pair production of spin-0 and spin-$1/2$ monopoles through the Drell-Yan process. A model-independent interpretation of the search is also presented. In the absence of an observation of events that were consistent with the expected monopole signal, upper limits on production cross section were set for all the scenarios considered. A model-independent limit of 0.5 fb was set for monopoles in fiducial regions of high selection efficiency. Lower mass limits were obtained for pair-produced spin-0 and spin-$1/2$ monopoles. This search excluded pair-produced spin-$1/2$ monopoles with the Dirac charge with mass below 1340 GeV, the most stringent mass limit to date.

Estos años de trabajo se los dedico a mi mami y a mi abuelita Trini quienes me guiaron e inspiraron durante los primeros pasos de este viaje...

Acknowledgements

It has been a while since I arrived in Canada to pursue my graduate studies. This has been a process in which my interest in understanding the world has grown dramatically. Many people have helped me achieve my goals and I will surely forget to mention some of them, to whom I will always be grateful.

I would like to acknowledge my supervisor Wendy Taylor. I am immensely grateful to you for your guidance and support throughout my time at York, which have made me an aspiring scientist. I am particularly thankful for the opportunity you gave me to travel the world and learn of other places and cultures. I would also like to thank you for the time you spent reviewing and editing this dissertation. My writing skills have certainly improved in the process.

I would like to thank the York ATLAS team, those who left and those that remain. Despite being a small team it has always been a pleasure to work with you. I especially appreciate the time spent with Jorge Armando Benitez. Your help with computing issues was always invaluable as was your availability to discuss issues about Colombia. I am indebted to Andres Florez. Thanks for showing me that dedication and discipline are necessary to achieve my goals and for pushing me through the very intense times of the Z' analysis. I will always be inspired by your successful career.

I would like to thank the highly ionizing particles team: Katarina Bendtz, Akshay Katre, Wendy Taylor, David Milstead and Philippe Mermod. It was a long journey in which we had to navigate through many hurdles without much support from other ATLAS groups, but brick by brick we built the analysis. Special thanks to Katarina. Our long discussions made the rough times more bearable.

I would like to thank the TRT team. It is fair to say that my computing skills and passion for the detector performance come from the time spent on all the projects I worked on during my service work. Special thanks to all those at CERN and to those involved with the ATLAS experiment. The great performance of the detector can only be the result of the hard work of a great team.

Thanks to Andrea Capra, I really appreciate the time we spent thinking about the trajectory of an electron in the field of a monopole and the simulation you developed for this purpose. Thanks to Eric Davidson. The three years we shared the apartment were definitely the best I had in Toronto. I never felt so comfortable anywhere else. Also, I would like to thank David McKevy, you are full of good thoughts. Spending time with you always cheered me up.

There are two very special people I would like to thank. Champ, you have become like a brother to me. Thanks for letting me into your life. I am sure the adventures will continue...life with you is always an adventure anyway. Paola, your charisma is unbeatable, your passion for teaching is remarkable. I am sure you will become a great educator. Thanks for being there for me.

Si no hubiera sido por el apoyo de mi familia a lo largo de mi juventud, nunca habría logrado llegar hasta donde lo he hecho. Muchas gracias a todos. Gracias mami y papi por permitirme tener una educación de la más alta calidad y dejarme decidir mi camino. Angela, te agradezco por siempre ser mi enlace con ustedes. Sin ti, la comunicación habría sido muy difícil. Ha sido doloroso haberlos dejado por tantos años y verlos crecer desde lejos.

Claire, there are no words to describe how grateful I am to you for all the support and love during this time. I will let my future actions show you how important it is for me to have you by my side, even if we are actually a few thousand kilometres away. You have made me a better person and I continuously learn from you how to improve. As you will soon complete your graduate studies, I would like to wish you a future full of success. Never let anything or anyone stop you. This world is in urgent need of more people like you.

Table of Contents

List of Tables

List of Figures

Chapter 1

Introduction

This section briefly introduces the Standard Model of particle physics and the physics of high-energy colliders. The theoretical status of magnetic monopoles is described with emphasis on the results that motivate their experimental searches. A review of the most common detection techniques and the results of the most relevant experimental searches is also presented.

1.1 The Standard Model of particle physics

The Standard Model (SM) of particle physics is the theory that describes three of the four known fundamental forces. These are the electromagnetic, weak and strong interactions. The SM is a gauge theory invariant under transformations of the group $SU(3)_{\mathrm{C}} \times SU(2)_{\mathrm{L}} \times U(1)_{\mathrm{Y}}$, where the $SU(3)_{\mathrm{C}}$ describes the strong interaction between particles that possess colour charge, and $SU(2)_{\mathrm{L}} \times U(1)_{\mathrm{Y}}$ describes the electroweak interactions. It was the product of many contributions, with particular merit to those from S. L. Glashow [1], S. Weinberg [2] and A. Salam [3], which set the foundations of the theory of electroweak interactions and led to the discovery of its force carriers, the Z and $W^{\pm}$ bosons.

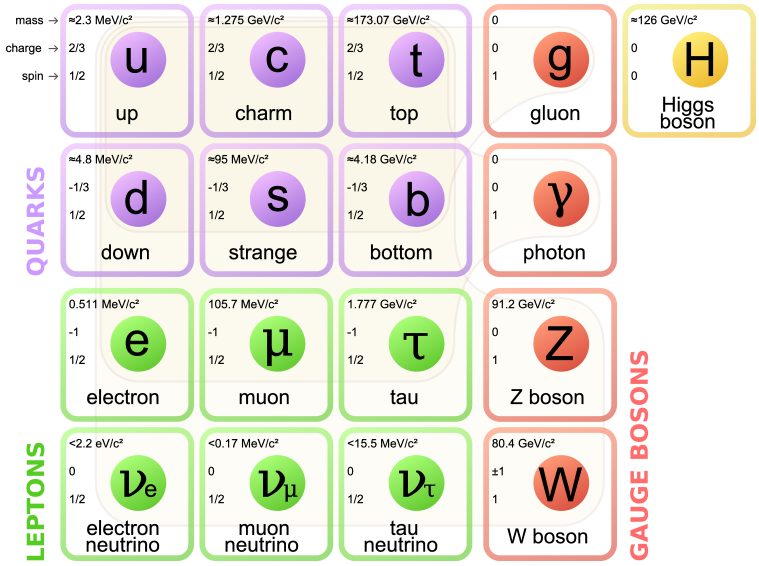

Figure 1.1: Particle content of the SM model of particle physics [4]. The values of spin, electric charge and approximate mass are also shown.

1.1.1 Particle content of the Standard Model

The particle content of the SM consists of the most fundamental constituents of matter known to date, divided in two main categories: fermions and bosons. Fermions are particles that obey the Fermi exclusion principle and have half-integer spin, in units of $\hbar$. Fermions include leptons and quarks. Bosons, on the other hand, have integer spin. Most bosons in the SM are vector bosons of spin-1 that represent the force carriers of the interactions, i.e., the photon (γ), the Z and $W^{\pm}$ bosons, and the gluon (g). Only the recently discovered Higgs boson (H) is a spin-0 scalar. Leptons and quarks possess weak isospin and hypercharge, interacting weakly and electromagnetically, except for the neutrinos, which are electrically neutral. In addition to the weak interaction, quarks are subject to the strong interaction, mediated by the gluons, as they possess colour charge.

Three lepton families or generations have been observed in nature comprising the charged electron (e),[1] muon (μ) and tau (τ) leptons and their respective neutrinos ($\nu_{e,\mu,\tau}$). In the quark sector, three generations have been observed as well; each contains one down-type

[1]Historically, the electron has been noted as e, a symbol shared with the magnitude of the electron's electric charge. In this section the symbol e may be used for the electron; in the remaining sections and chapters it will only represent the magnitude of the electric charge of the electron.

and one up-type quark. The down-type quarks of the three generations are known as down (d), strange (s) and bottom (b), while the up-type quarks are known as up (u), charm (c) and top (t). A summary of the SM particles, including their associated spin, electric charge and approximate mass is shown in Fig. 1.1. Each one of the particles mentioned above has been observed to have an associated antiparticle, which differs only in the sign of the intrinsic additive quantum numbers, e.g, electric charge (for non-neutral particles), colour charge, lepton number.

1.2 Physics of proton–proton high energy collisions

The highest-energy particle accelerator currently in operation is the Large Hadron Collider, which collides protons at energies in the TeV scale. Protons are baryons composed of two u and one d quarks, which are known as the valence quarks. The high mass of the proton, with respect to that of its valence quarks, is mostly due to the binding energy. Inside the proton, valence quarks exchange gluons, which in turn may decay into quark–antiquark pairs, known as *sea* quarks, and recombine into gluons. Collectively, the valence quarks, sea quarks and gluons that form the proton are known as partons. When protons collide, partons, one from each proton, interact via the interactions described by the SM. In an inelastic collision, the interaction between these two constituents of the proton is known as the hard scatter.

1.2.1 The underlying event

In addition to the hard scatter, additional processes take place involving the remnants of the colliding protons. This is known as the underlying event. The partons involved in the hard scatter and the byproducts of the interaction may also contribute to the underlying event via initial and final state radiation. Although the underlying event mostly consists of low-momentum-transfer processes involving the strong interaction, in some cases there may be multiple parton interactions in which more than one parton from each proton participate in hard scatter processes. The presence of the underlying event generates an increase in the

charged-particle density in the detector, which has an effect on the measurements performed by particle detectors in high-energy proton–proton collisions [5, 6].

Initial and final state radiation

In hadron colliders, the interacting partons possess colour charge leading to the spontaneous emission of gluons before the hard scatter takes place. This process is known as initial state radiation. On the other hand, the byproducts of a hard scatter may also radiate before hadronization occurs. This is known as final state radiation.

1.2.2 Multiple collisions in an event

In order to increase the probability of a hard scatter in a collision, dense bunches of particles are used. This may lead to multiple collisions in a bunch crossing, with a number of them being actual hard-scatter interactions while others correspond to a pion exchange between protons. Protons may collide elastically in what is known as a non-diffractive collision, or may collide inelastically in a single- or double-diffractive collision in which one or both protons dissociate into a mixture of particles. A third type of inelastic collision may also occur: the central-diffractive collision in which the final state particles are produced in the detector central region while the protons remain intact. These three inelastic processes account for about 25–30% of the total inelastic cross section [7]. The additional inelastic collisions that take place when two bunches of protons collide are known as pileup.

1.3 Magnetic monopoles

Elementary particles in nature have been observed to be electrically charged or neutral. Only elementary particles that possess non-neutral electric charge have been observed to interact electromagnetically.[2] This interaction occurs between electrically charged particles and electromagnetic fields, of which the photon is the quantum mechanical representation.

[2]Composite particles such as light neutral mesons have radiative decay modes. However, these decay modes are a consequence of the interaction between the electrically charged constituents of the composite particles.

1.3.1 Magnetic monopoles and electromagnetism

The classical theory of electromagnetism, which describes the dynamics of electrically charged particles and electromagnetic fields, is contained in Maxwell's equations

$$\begin{aligned} \vec{\nabla}\cdot\vec{E} &= \frac{\rho_e}{\epsilon_0}, \qquad \vec{\nabla}\times\vec{E} = -\frac{\partial\vec{B}}{\partial t}, \\ \vec{\nabla}\cdot\vec{B} &= 0, \qquad \vec{\nabla}\times\vec{B} = \mu_0\epsilon_0\frac{\partial\vec{E}}{\partial t} + \mu_0\vec{j}_e, \end{aligned} \tag{1.1}$$

where $\vec{E}$ and $\vec{B}$ are the electric and magnetic fields, respectively, ρ_e the electric charge density, and $\vec{j}_e$ the electric current density. In Maxwell's equations, only electric charge densities and electric current densities appear as sources of electric and magnetic fields. The absence of a magnetic charge or a magnetic current density is not a prediction of the theory but a result of experimental observation. In fact, Maxwell's equations can be written in a form that includes both the electric and magnetic components:

$$\begin{aligned} \vec{\nabla}\cdot\vec{E} &= \frac{\rho_e}{\epsilon_0}, \qquad \vec{\nabla}\times\vec{E} = -\frac{\partial\vec{B}}{\partial t} - \mu_0\vec{j}_m, \\ \vec{\nabla}\cdot\vec{B} &= \mu_0\rho_m, \qquad \vec{\nabla}\times\vec{B} = \mu_0\epsilon_0\frac{\partial\vec{E}}{\partial t} + \mu_0\vec{j}_e, \end{aligned} \tag{1.2}$$

with ρ_m and $\vec{j}_m$ the magnetic charge and current densities, respectively. A region of space with magnetic charge density, ρ_m, has an integrated magnetic charge, g, giving rise to a magnetic monopole. Monopoles can also be considered to be point particles with magnetic charge density $\rho_m = g\delta(\vec{x})$. Maxwell's equations in the form of Eq. (1.2) are symmetric under the following duality transformation:

$$\begin{pmatrix} \vec{E} \\ c\vec{B} \end{pmatrix} = \begin{pmatrix} \cos\xi & \sin\xi \\ -\sin\xi & \cos\xi \end{pmatrix} \begin{pmatrix} \vec{E}' \\ c\vec{B}' \end{pmatrix}, \qquad \begin{pmatrix} c\rho_e \\ \rho_m \end{pmatrix} = \begin{pmatrix} \cos\xi & \sin\xi \\ -\sin\xi & \cos\xi \end{pmatrix} \begin{pmatrix} c\rho'_e \\ \rho'_m \end{pmatrix}, \tag{1.3}$$

where c is the speed of light and ξ is the transformation parameter.

This symmetry raises a fundamental question about the point of defining electric and magnetic charges (and their corresponding current densities) if a simple transformation can relate them. It makes no sense to define electric and magnetic charge individually. However, one can define the ratio of magnetic to electric charge,

$$\frac{\rho_m}{c\rho_e} = \frac{-(c\rho'_e)\sin\xi + \rho'_m\cos\xi}{(c\rho'_e)\cos\xi + \rho'_m\sin\xi}, \tag{1.4}$$

and assume that it is the same for all particles. Under this assumption, a duality transformation can be chosen such that $\xi = 0$ and $\frac{\rho_m}{c\rho_e} = 0$. Although taking this ratio as zero may seem an arbitrary choice, experimental measurements on the magnetic charge of matter have shown that $g < 10^{-26} g_{\mathrm{D}}$ and $g < 10^{-24} g_{\mathrm{D}}$ for nucleons and electrons, respectively [8], where g_{D} is the Dirac magnetic charge.[3] Thus, the generalized form of Maxwell's equations (Eq. (1.2)) becomes the known magnetic monopole-free form of Eq. (1.1).

The observation of a magnetic monopole in nature would restore symmetry in Maxwell's equations, leading to the case in which the fields transform as $\vec{E} \to \vec{B}$ and $\vec{B} \to -\vec{E}$, and the sources as $c\rho_e \to \rho_m$ and $\rho_m \to -c\rho_e$, for $\xi = \pi/2$.

1.3.2 Dirac monopoles

During the first half of the twentieth century, Dirac tried to establish whether magnetic monopoles could be accommodated within the existing framework of electromagnetism and quantum mechanics. His efforts lead to a prediction of great relevance for physics: the existence of magnetic monopoles is compatible with quantum mechanics and explains the observed quantization of electric charge [9, 10].

The Dirac string

The existence of a magnetic monopole of magnetic charge g requires the formulation of an electromagnetic vector potential, $\vec{A}$, from which a divergent magnetic field of the form

$$\vec{B}(\vec{r}) = \vec{\nabla} \times \vec{A} = \frac{\mu_0 g}{4\pi r^2} \hat{r}, \tag{1.5}$$

can be obtained. Dirac proposed the vector potential of an infinitely thin solenoid extending from $-\infty$ to the origin as a solution. However, this potential, given by

$$\vec{A}(\vec{r}) = \frac{\mu_0 g (1 - \cos\theta)}{4\pi r \sin\theta} \hat{\phi}, \tag{1.6}$$

[3] The magnetic charge, g, is commonly expressed in terms of the Dirac charge, g_{D}, which is considered as the elementary magnetic charge. See Sec. 1.3.2 on the Dirac monopole and the charge quantization condition.

is not defined along $\theta = \pi$. This singularity, known as the Dirac string, poses no problem as it is invisible, since the actual observable in classical electrodynamics is $\vec{B}$, and $\vec{\nabla} \times \vec{A}$ gives a field of the same form as that of Eq. (1.5).

Other vector potential configurations that do not include singularities have been proposed [11]. For instance, a vector potential that is defined separately for each hemisphere could avoid singularities:

$$\vec{A}(\vec{r}) = \begin{cases} \dfrac{\mu_0 g(1-\cos\theta)}{4\pi r \sin\theta}\hat{\phi}, & 0 \leq \theta \leq \dfrac{\pi}{2}, \\ -\dfrac{\mu_0 g(1+\cos\theta)}{4\pi r \sin\theta}\hat{\phi}, & \dfrac{\pi}{2} \leq \theta \leq \pi. \end{cases} \tag{1.7}$$

This set of vector potentials also yields the magnetic field of a monopole. It is important to note that no assumption on the spin of the monopole has been made so far. Thus, both fermion-like and boson-like particles are Dirac monopole candidates. Also, in Dirac's theory of magnetic monopoles the mass of the monopole is not specified.

Charge quantization condition

In classical electrodynamics, the physical observables correspond to the electric and magnetic fields, $\vec{E}$ and $\vec{B}$. The scalar and vector potentials are just defined as mathematical tools. However, in quantum electrodynamics, these potentials acquire a much more relevant role and their presence has physical consequences. This is clearly evident in the Aharonov–Bohm effect [12], in which electrically charged particles in the presence of an electromagnetic vector (or scalar) potential, but no electric or magnetic field, experience a phase change that leads to physically observable quantum mechanical interference effects. An electrically charged particle must therefore experience the presence of the Dirac string from the vector potential in Eq. (1.5).

A point particle with electric charge q going around the Dirac string describing an infinitesimally small loop will experience a change in its wave function's phase given by

$$\Delta\phi = \frac{q}{\hbar}\int \vec{A}\cdot d\vec{l} = \lim_{\theta\to\pi}\frac{q}{\hbar}\frac{\mu_0 g(1-\cos\theta)}{4\pi r\sin\theta}\int_0^{2\pi} r\sin\theta d\phi = \frac{\mu_0 q g}{\hbar}. \tag{1.8}$$

The presence of the Dirac string is thus, in principle, detectable. In order to make the string undetectable, as would be expected from a real monopole, the phase change has to be a multiple of 2π. This requirement leads to a result of great importance: the existence of a magnetic monopole requires the quantization of charge. This result, known as the Dirac quantization condition, can be written as

$$qg = \frac{nh}{\mu_0}, \tag{1.9}$$

where n is a non-negative integer.

It must be noted that Dirac's quantization condition can be obtained by considering the vector potential of Eq. (1.7) and requiring that the difference between the phase shifts induced by the vector potentials of both hemispheres at $\theta = \pi/2$ be a multiple of 2π [11]. Another way to derive Dirac's quantization condition is to quantize the angular momentum of a system of an electrically charged particle and a magnetic monopole [13]. The fact that the charge quantization is achieved in several scenarios with magnetic monopoles reinforces the importance of Dirac's results.

Electric charge has been observed in nature quantized in units of the electron electric charge, e [14], which is also the lowest absolute non-zero electric charge observed in nature.[4] Thus, Eq. (1.9) can be rewritten in terms of e and the fine structure constant $\alpha = \frac{\mu_0 e^2 c}{4\pi\hbar}$, and in the lowest case, $n = 1$, the elementary magnetic charge, known as the Dirac charge g_{D}, can be obtained:

$$g = \frac{n}{2\alpha}(ce) \quad \xrightarrow{n=1} \quad g_{\mathrm{D}} = \frac{(ce)}{2\alpha}. \tag{1.10}$$

An important result can be derived from Eq. (1.10): the Dirac charge, g_{D}, is roughly equivalent to 68.5 times the elementary electric charge, e.[5]

Schwinger monopoles

Decades after Dirac's prediction of magnetic monopoles as a way to understand charge quantization, Julian Schwinger revised the theory, in particular, he studied its relativistic

[4] Strongly interacting particles, such as quarks, possess fractional electric charges of $\pm\frac{1}{3}e$ and $\pm\frac{2}{3}e$. However, their observation is restricted to bound states of quarks with electric charge quantized in units of e.

[5] In SI units the magnetic charge is expressed in A·m and the electric charge in A·s. In Gaussian units both magnetic and electric charge are given in esu.

invariance [15]. As a result, he found that the vector potential that represents a solution for a magnetic monopole field is given by

$$\vec{A}(\vec{r}) = -\frac{\mu_0 g}{4\pi r}\cot\theta\hat{\phi}. \tag{1.11}$$

This vector potential leads to a quantization condition that restricts the integer n to even values only, i.e.,

$$qg = \frac{2nh}{\mu_0}. \tag{1.12}$$

This discrepancy appears from the use of a vector potential with an infinite discontinuity or string along $\theta = 0$ and $\theta = \pi$, as opposed to the semi-infinite string used by Dirac. The minimum magnetic charge of monopoles in Schwinger's theory thus possesses twice the Dirac charge, g_{D}, which also has an impact on the magnitude of the magnetic coupling, as described below.

Schwinger's work also considered particles that carry both electric and magnetic charge [16]. The existence of such particles, known as dyons, leads to the following generalized quantization condition:

$$q_1 g_2 - q_2 g_1 = \frac{2nh}{\mu_0}, \tag{1.13}$$

where q_1, g_1 and q_2, g_2 are the electric and magnetic charges of the two dyons.

Magnetic coupling to the photon

The strength of the coupling between the photon and the electron is given by the fine structure constant, α. In analogy, a magnetic coupling constant, α_m, which determines the strength of the coupling of magnetic monopoles to the photon, can be defined by substituting $g^2 = (ng_{\mathrm{D}}/c)^2$ for e^2, as shown in Fig. 1.2. This leads to

$$\alpha = \frac{\mu_0 e^2 c}{4\pi\hbar} \quad \xrightarrow{e\to g = n g_{\mathrm{D}}/c} \quad \alpha_m = \frac{\mu_0 g_{\mathrm{D}}^2}{4\pi\hbar c} n^2. \tag{1.14}$$

A direct consequence of the quantization condition of Eq. (1.10) is that the strength of the magnetic coupling is at least four orders of magnitude greater than that of the fine structure constant. For instance, for $n = 1$, the magnetic coupling constant is $\alpha_m \approx 34.24$. Such large coupling values along with the quantization condition have strong implications in the understanding of the production of monopoles and their interactions with matter.

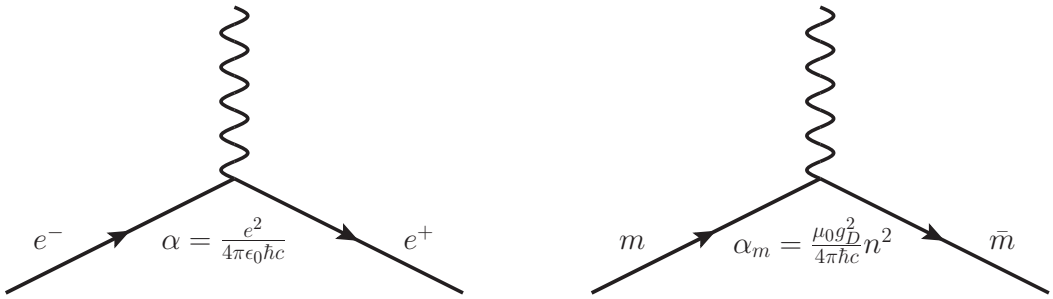

Figure 1.2: Feynman diagram depicting the interaction vertices between electrons and photons (left) and magnetic monopoles and photons (right). The magnetic coupling is defined in analogy to the fine structure constant.

1.3.3 Production of Dirac monopoles

A monopole–anti-monopole pair would be subject to a strong attractive potential at the moment of its creation. Thus, monopoles could only be sought in atomic processes involving energies of at least 500 MeV, as estimated by Dirac [10]. Such energy regimes have been accessible at particle colliders for several decades now. The large magnitude of the magnetic coupling limits the reliability of perturbative pair production cross section predictions at colliders since higher-order contributions diverge. Therefore, only production models at first order are assumed in scenarios with energies accessible by the current particle accelerators.

Drell-Yan production of monopoles

In searches for monopoles produced at hadron colliders, the leading-order Drell-Yan process [17] is the most commonly used model. In this scenario, a quark and an antiquark from the colliding hadrons interact via a Z boson or a photon producing a lepton pair. In order to accommodate monopoles in the Drell-Yan mechanism, only a virtual photon is considered as no assumption on the weak interaction of monopoles is made. Although Drell-Yan production is normally for fermion pair production, spin-0 particles can also be produced. Figure 1.3 shows the Feynman diagrams of monopole–anti-monopole production assuming the Drell-Yan mechanism for spin-0 (left) and spin-$1/2$ (right) monopoles. The monopole coupling to the photon used in this scenario corresponds to that described in Sec. 1.3.2, formulated in analogy to the fine structure constant and proportional to n^2, with $g = ng_{\mathrm{D}}$.

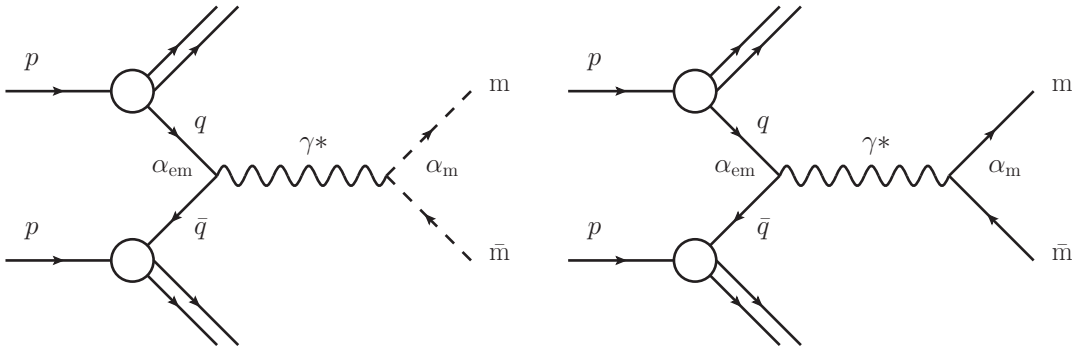

Figure 1.3: Feynman diagrams for pair production of spin-0 (left) and spin-1/2 (right) monopoles assuming the Drell-Yan production mechanism in which the production of monopoles is only mediated by a photon.

The Drell-Yan production model has been used as the benchmark in direct searches for monopoles at particle colliders, thus this model was used in the interpretation of the results of this search.

Monopole production via photon fusion

Additional leading-order spin-1/2 monopole production mechanisms in proton collisions have been proposed, e.g., monopole production via photon fusion [18]. Figure 1.4 shows the Feynman diagrams of the processes that contribute to the monopole production from photon fusion. The predicted cross section of this production mechanism at a centre-of-mass energy of 8 TeV is comparable to that of the Drell-Yan case and about 50 times larger at a centre-of-mass energy of 14 TeV, making it a very important scenario to consider at the Large Hadron Collider in Run 2. The production cross section of monopoles from photon fusion has been calculated for spin-0 and spin-1 monopoles as well [19]. This production mechanism has never been considered in direct searches for magnetic monopoles at particle colliders, including this work.

1.3.4 Monopoles as topological defects

Monopoles are predicted by grand unified theories (GUTs) in which the $U(1)$ group of electromagnetism is embedded in a larger compact non-Abelian group. This was shown

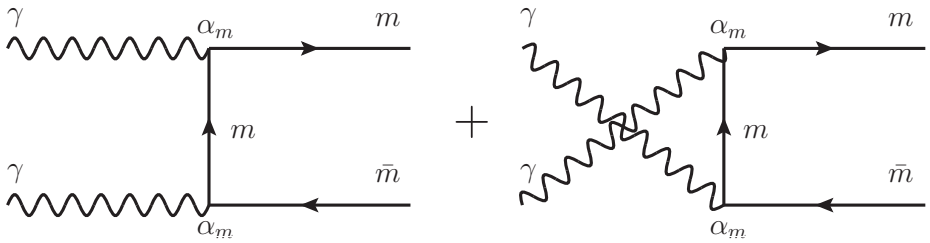

Figure 1.4: Feynman diagrams for pair production of spin-1/2 monopoles from photon fusion.

independently by 't Hooft [20] and Polyakov [21]. This is also the case of the SM, which consists of a $SU(2)_L \times U(1)_Y$ symmetry that breaks down to the $U(1)$ symmetry of electromagnetism, giving rise to electroweak monopoles. However, it has been argued that such a symmetry group does not admit monopole solutions when it undergoes spontaneous symmetry breaking [22, 23].

In GUT models, the minimum of the scalar potential is degenerate. The symmetry of the vacuum is broken when the vacuum state of the scalar field assumes a specific direction. However, GUT models admit another solution in which the direction of the scalar field is coupled to the spatial direction. This solution is known as the hedgehog configuration:

$$\phi^a = v\frac{r^a}{r}, \quad a = 1, 2, 3. \tag{1.15}$$

This solution is topologically stable despite not corresponding to the absolute minimum of the scalar potential [20]. Equation (1.15) leads to a solution of the non-Abelian electromagnetic gauge potential, which represents the Coulomb-like non-Abelian field of a point particle from which the Dirac string vector potential can be extracted [24].

Charge quantization in GUT models

In Dirac's theory of magnetic monopoles, charge quantization is a consequence of the existence of monopoles. In GUT models the charge quantization condition arises if the U(1) group of electromagnetism is embedded into a semi-simple non-Abelian group of higher rank. These are in fact two ways of seeing the same situation. In GUT models where the U(1) group of electromagnetism is a subgroup of a higher rank semi-simple group that undergoes spontaneous symmetry breaking, there are monopole solutions. In GUT models,

the non-Abelian analog of Dirac's charge quantization condition reads just as Eq. (1.9) and thus the minimum magnetic charge of GUT monopoles is the Dirac charge, g_{D}.

Monopole mass in GUT models

Unlike Dirac's theory of magnetic monopoles, GUT models have led to a prediction of the mass of the monopole. This is obtained as the energy of the monopole configuration at rest, which classically corresponds to the monopole mass. The energy of the monopole configuration is composed of the energy of the Abelian field outside the monopole core, R_c, which is related to the reciprocal of the mass of the vector boson of the model $R_c \sim (m_X)^{-1} \sim (ev)^{-1}$, and the energy of the scalar field inside the core [24]. The monopole mass predicted by the GUT models is then approximately $M \approx 137 m_X$. The mass of the vector boson in GUT models is of the same order as the unification scale, i.e., 10^{16} GeV [25]. Thus, the mass of magnetic monopoles predicted by GUT models is of order 10^{18} GeV, well outside the reach of particle colliders.

Monopoles in electroweak models

Magnetic monopoles within the framework of the SM are believed not to exist [22,23]. However, it has been proposed that monopole-like solutions are possible in the SM electroweak sector [26]. These solutions, known as electroweak monopoles, obey Schwinger's charge quantization condition (Eq. 1.12) and thus have a minimum magnetic charge of $2g_{\mathrm{D}}$.

Unlike GUT monopoles, electroweak monopoles do not have a well-defined mass in the theory, just like Dirac monopoles. However, recent developments predict a monopole mass of order 4—10 TeV [27]. Such monopoles could be produced at hadron colliders.

1.4 Passage of monopoles through matter

Magnetic monopoles interact with electromagnetic fields in a similar manner as electrically charged particles. The force that a particle with electric and magnetic charge experiences

in the presence of an electromagnetic field is described by the Lorentz force

$$\vec{F} = q\left(\vec{E} + \vec{v} \times \vec{B}\right) + g\left(\vec{B} - \vec{v} \times \frac{\vec{E}}{c^2}\right), \tag{1.16}$$

with q and g the electric and magnetic charges, respectively. Due to the large electric charge equivalent of the Dirac charge ($g_{\mathrm{D}} \approx 68.5(ce)$), the interaction of a magnetic monopole with an electric field is at least one order of magnitude stronger than that of a particle with the electron charge. Conversely, an electron in an atomic orbital would experience the magnetic field of a moving monopole of charge g with a strength βg, where β is the monopole velocity relative to the speed of light. The appearance of the β factor in the interaction strength, as indicated by the Lorentz force formula in Eq. (1.16), has strong implications in the behaviour of the stopping power for magnetically charged particles.

1.4.1 Energy loss by ionization

The energy losses by ionization of electrically charged particles are described by the Bethe-Bloch formula given by

$$-\frac{dE}{dx} = \frac{4\pi e^4 z^2 N_e}{m_e c^2 \beta^2}\left[\ln\left(\frac{2m_e c^2 \beta^2 \gamma^2}{I}\right) - \beta^2 - \frac{\delta}{2}\right], \tag{1.17}$$

where z is the charge of the projectile particle in units of e and βc its velocity, $m_e c^2$ the electron rest mass, N_e and I are the electron density and mean ionization energy of the material, and δ is a density effect correction that becomes relevant for ultrarelativistic particles.

Magnetic monopoles ionize the medium through which they travel, depositing large amounts of energy due to the strength of the interaction of orbiting electrons with the magnetic field of monopoles. As a first approach, a simple substitution of βg for ze can be done in order to study the interaction of monopoles with matter using formulas originally intended for interactions between particles that possess electric charge, e.g., Eq. (1.17).

The energy losses of monopoles consist of two regimes: a high-momentum transfer or close-interaction regime, which has been modelled by Kazama, Yang and Goldhaber (KYG) by solving the Dirac's equation of an electron in the magnetic field of a monopole [28],

and a low-momentum transfer or distant-interaction regime, modelled using the dipole approximation. Ahlen has put together a stopping-power[6] formula based on the first-order Born approximation that takes into account both close- and distant-interaction regimes with an accuracy of about 3% for monopoles with $\beta \gtrsim 0.2$ and $\gamma \lesssim 100$ [29]. The monopole energy losses by ionization are thus given by

$$-\frac{dE}{dx} = \frac{4\pi e^2 g^2}{m_e c^2} N_e \left[\ln\left(\frac{2m_e c^2 \beta^2 \gamma^2}{I}\right) + \frac{k(g)}{2} - \frac{1}{2} - \frac{\delta}{2} - B(g) \right], \tag{1.18}$$

where $g = n g_{\mathrm{D}}$, $k(g)$ is the KYG correction given by

$$k(g) = \begin{cases} 0.406 & |n| \leq 1, \\ 0.346 & |n| \geq 1.5, \end{cases} \tag{1.19}$$

which arises from the relativistic cross section calculated in Ref. [28], and $B(g)$ is the Bloch correction given by

$$B(g) = \begin{cases} 0.248 & |n| \leq 1, \\ 0.672 & |n| \geq 1.5, \end{cases} \tag{1.20}$$

which accounts for higher order effects for low-energy collisions in which the monopole velocity approaches the orbital velocity of the electron. This stopping-power formula is valid for relativistic factors $\gamma \lesssim 100$, beyond which spin effects and contributions from the internal structure of nuclei become important.

At very low velocities, i.e., $\beta < 0.01$, the energy losses of monopoles are described by [30]

$$-\frac{dE}{dx} = (45 \ \ \mathrm{GeVcm^{-1}}) n^2 \beta, \tag{1.21}$$

with $n = g/g_{\mathrm{D}}$. This formula is just a lower limit on the energy losses as interactions with the electron spin are not modelled. For velocities in the range $0.01 < \beta < 0.1$, shell effects may play a role. However, such corrections are small and the stopping power is modelled by interpolating between the predictions of Eq. (1.18) and Eq. (1.21).

The energy losses by ionization of monopoles are considered independent of spin as the energy involved in spin-flip transitions is negligible in the ranges considered. The monopole

[6]The stopping power corresponds to $-dE/dx$. Both names are used interchangeably in the literature and herein.

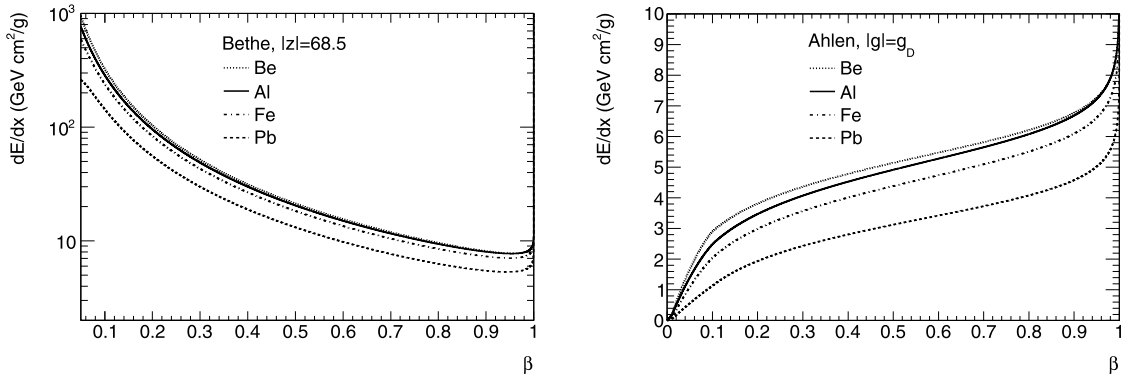

Figure 1.5: Energy loss per unit length, dE/dx, by an electrically charged particle with $|z| = 68.5$ (left) and a magnetic monopole of charge $|g| = 1.0g_{\mathrm{D}}$ (right) as a function of the particle velocity, β, for different materials [31].

spin only becomes important at very low velocities, for which ionization has ceased due to the β dependence of the magnetic field that the electron experiences [29].

Based on the stopping-power formulas for magnetically and electrically charged particles (Eqs. (1.17) and (1.18)), it can be seen that energy losses by ionization of a magnetic monopole of charge $|g| = 1.0g_{\mathrm{D}}$ are four orders of magnitude higher than those of an electrically charged particle with $|z| = 1$. A comparison between the dominant terms of Eq. (1.18) and Eq. (1.17) shows the main difference between the interactions of electrically and magnetically charged particles with matter. The absence of a dependence on the reciprocal of the projectile velocity squared, $1/\beta^2$, in Eq. (1.18) means that magnetically charged particles deposit more of their kinetic energy at high velocities than electrically charged particles. At low velocities, electrically charged particles deposit most of their kinetic energy, resulting in what is known as a Bragg peak towards the end of their trajectory. On the other hand, monopole energy losses decrease with decreasing monopole velocity. Figure 1.5 shows the energy losses by ionization by an electrically charged particle of charge $|z| = 68.5$ (left) and a magnetic monopole of charge $|g| = 1.0g_{\mathrm{D}}$ (right) as a function of the particle velocity, β, for different materials.

1.4.2 Energy loss by bremsstrahlung and pair production

Magnetic monopoles passing through a medium may interact with the nuclei. Such collisions would cause the monopole to accelerate, radiating photons and thus losing some kinetic energy. The radiated photons may then produce an electron–positron pair in the presence of an atomic nucleus in a process known as pair production. The process by which a charged particle gives off a photon in the presence of nuclei is known as bremsstrahlung and accounts for part of the energy losses of monopoles due to radiation, as described by [32]:

$$-\frac{dE_{\text{rad}}}{dx} = \begin{cases} \dfrac{16}{3}\dfrac{NZ^2e^2}{\hbar c}\dfrac{g^4}{mc^2}, & \beta \ll 1, \\ \dfrac{16}{3}\dfrac{NZ^2e^2}{\hbar c}\dfrac{g^4}{mc^2}\gamma \ln\left(\dfrac{233m}{Z^{1/3}m_e}\right), & \gamma \gg 1, \end{cases} \tag{1.22}$$

where m is the monopole mass, N and Z are the atomic density and number of the material such that $N_e = ZN$. The ratio of energy losses by bremsstrahlung to energy losses by ionization (Eq. (1.18)) can be written as

$$-\frac{dE_{\text{rad}}}{dE_{\text{ion}}} = \begin{cases} \dfrac{4}{3\pi}\dfrac{Zg^2}{\hbar c}\dfrac{m_e}{m}\dfrac{1}{\lambda}, & \beta \ll 1, \\ \dfrac{4}{3\pi}\dfrac{Zg^2}{\hbar c}\dfrac{m_e}{m}\dfrac{1}{\lambda}\gamma \ln\left(\dfrac{233m}{Z^{1/3}m_e}\right), & \gamma \gg 1, \end{cases} \tag{1.23}$$

where λ represents the factor multiplying the leading term of Eq. (1.18). It is important to note that for a monopole of mass in the TeV range and charge $|g| = 1.0g_{\text{D}}$ the energy losses by bremsstrahlung are at least three orders of magnitude lower than the energy losses by ionization in the range $\gamma < 10$, which corresponds to realistic scenarios for production at the Large Hadron Collider.

The magnetic field of a fast travelling monopole develops a transverse electric field component that goes as

$$\vec{E}_{\perp} = -\gamma\vec{\beta} \times \vec{B}, \tag{1.24}$$

and resembles a beam of photons under the equivalent photon approximation [33]. These quasi-real photons may decay into electron–positron pairs in the presence of the field of a nucleus or, to a lesser extent, an orbiting electron, contributing to the monopole energy

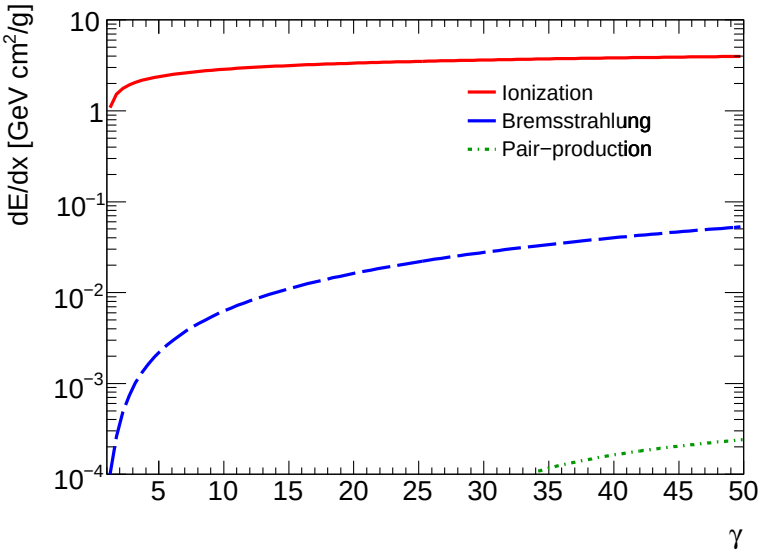

Figure 1.6: Energy loss per unit distance, dE/dx, for a magnetic monopole of charge $|g| = 1.0g_{\mathrm{D}}$ and mass 1000 GeV in argon. Three energy loss mechanisms are shown: ionization (solid-red line), bremsstrahlung (dashed-blue line) and pair production (dotted-green line) [35].

losses. The energy of these photons, however, is not high enough to make energy losses by pair production significant for realistic scenarios with relativistic factors $\gamma < 10$. Such an energy loss mechanism is relevant in the case of ultrarelativistic monopoles in cosmic radiation [34].

Figure 1.6 shows the energy losses of a monopole of mass 1000 GeV and charge $|g| = 1.0g_{\mathrm{D}}$ in argon for the three different mechanisms discussed above: ionization, bremsstrahlung and pair production. The contribution to the total energy losses from bremsstrahlung and pair production in the range $\gamma < 10$ are negligible. Thus, it can be concluded that the signature of a monopole produced at a particle collider would be dominated by ionization of the traversed medium.

1.5 Monopole detection methods

The prediction of magnetic monopoles by Dirac [9] as an explanation to charge quantization led to a number of searches involving several detection techniques. Later on, with the

prediction of 't Hooft-Polyakov [20, 21] monopoles in GUT models, the interest in such particles grew even stronger.

Detection methods cover a range of techniques and technologies, mostly taking advantage of the large ionization produced by monopoles as they pass through matter. In addition to a highly ionizing signature, monopoles accelerate in the presence of magnetic fields in a way that differs from that of particles with electric charge. Thus, monopoles could be detected as anomalous tracks in detectors immersed in magnetic fields. The detection of the divergent magnetic flux of a monopole, which would be the ultimate signature, setting it apart from other highly ionizing particles possessing electric charge, remains the most sensitive technique for monopoles that become bound in matter.

The existence of monopoles can also be tested indirectly by searching for deviations from known physics processes that could be associated to interactions involving monopoles. For instance, in SM processes in which photons, to which monopoles couple strongly, are present, deviations from SM predictions may be observed.

This section describes some of the most common detection methods used in direct and indirect searches for magnetic monopoles.

1.5.1 Direct detection methods

Monopoles would be detected directly when they interact with matter. The charge quantization condition (Eq. (1.10)) predicts that the Dirac charge, g_{D}, is approximately equivalent to $68.5(ce)$. With such an electric charge equivalent, monopoles behave as highly ionizing particles. The energy losses of monopoles in a medium are therefore large and it is expected that they quickly deposit all their kinetic energy and become trapped in the material, binding to atomic nuclei. Detection methods have been developed to detect the presence of magnetic monopoles bound in matter and their passage through some active material. Several detection techniques are described in this section. The list, although not exhaustive, contains the most commonly used methods along with references to some of the experimental searches that have used them.

Monopoles bound in matter

Monopoles may have been produced in the early universe during a phase transition as described in Sec. 1.3.4. Such monopoles may be freely accelerated by galactic magnetic fields, some maybe even to relativistic speeds, while others may have become trapped in interstellar matter, binding to nuclei with energies of order 100 keV [36]. Monopoles predicted by GUT models bound in matter are expected to be found, among other possibilities, in meteorites [37], lunar rocks [38] and in the earth's crust [39].

Another type of monopole can also be found trapped in matter: those produced at particle colliders. A monopole produced in a high-energy collision will require some kinetic energy to make it past the first layers of inactive material before reaching active parts of the detector. Thus, the probability of stopping in, for instance, the beampipe is high. Materials surrounding the interaction points of high-energy particle colliders are also possible sources of trapped monopoles [40, 41].

The most common method for detecting magnetic monopoles trapped in matter consists of passing a sample of material, such as rocks or parts of a decommissioned particle detector, through a superconducting loop coupled to a superconducting quantum interference device (SQUID) magnetometer. A monopole would generate an increase in the magnetic flux through the loop, inducing a persistent current in the system. A magnetic dipole, on the other hand, would not induce a net current upon full passage through the loop. SQUID magnetometers can detect variations in magnetic flux as small as a quantum of magnetic flux $\phi_0 = h/2e$. In comparison, the total magnetic flux of a monopole with charge $g = g_{\mathrm{D}}$ is $\phi_g = \mu_0 g_{\mathrm{D}} = h/e$. Thus, a monopole of charge g_{D} would have a total flux of two units of quantum magnetic flux.

Although the induction technique has been used primarily for detection of monopoles bound in matter, it has also been implemented to measure the flux of monopoles in cosmic rays. One famous experimental result is that of Cabrera [42] who, using a SQUID magnetometer, measured a single candidate whose signal is consistent with the expected signal from a monopole with charge g_{D}.

Another technique for detection of monopoles bound in matter consists of applying a

strong magnetic field on the matter sample in order to extract trapped monopoles. Such monopoles once extracted would be detected by using a complementary method [43].

High ionization by monopoles

As described in Sec. 1.4.1, monopoles are highly ionizing particles with energy losses about four orders of magnitude larger than those of a particle with unit electric charge. Most particle detectors with capabilities to measure dE/dx are designed with singly electrically charged particles in mind. Therefore, the passage of a monopole through such a detector would produce a distinct signature. Fast moving monopoles lose large amounts of energy by ionization, producing copious amounts of energetic δ-rays. This results in a large amount of charge collected or light produced, depending on the detection mechanism, which can be interpreted as a highly ionizing particle. Unfortunately, the energy losses of very slow monopoles ($\beta < 0.01$) are not very well understood and it is expected that they become bound to atomic nuclei [44].

Based on ionization only, the signature of a monopole is not unique since heavy objects with large electric charge, (hypothetical objects or heavy nuclei) may yield a similar signal [45]. The measurement of energy losses by ionization is fundamental to most detection methods. Detectors that measure dE/dx comprise semiconductor trackers, drift chambers and scintillators, among others.

Heavy etching on nuclear track detectors

Plastic foils or nuclear track detectors (NTD) to identify highly ionizing particles are widely used in searches for magnetic monopoles in cosmic rays [46,47] and produced at high-energy particle colliders [48–50]. Plastic foils are placed surrounding the interaction points at colliders in order to minimize the amount of material in which monopoles could become trapped. When highly ionizing particles pass through a NTD, the plastic is damaged in a way that reveals the value of the energy loss rate, dE/dx, which is closely related with the magnitude of the electric or magnetic charge. The damage is created by the high ionization and the non-ionizing energy losses due to displacement of atoms from the lattice [51].

In order to make evident the damage created by the passage of a monopole, NTD foils are etched by soaking them in a chemical bath that dissolves the damaged section of the foil. The energy loss rate of the particle, dE/dx, can be determined from the geometry of the resulting etch pit cones, which are studied under a microscope.

The NTD technology was used by Price *et al.* [52] in a balloon-borne experiment intended to study objects with large electric charge in cosmic rays. The authors of Ref. [52] claimed to have observed evidence for a moving magnetic monopole with charge $2g_{\rm D}$. The results were later reinterpreted as consistent with a slow ($\beta \approx 0.4$) massive particle, a fast ($0.7 \lesssim \beta \lesssim 0.9$) antinucleus with $Z/\beta = -114$, or an ultrarelativistic ($\beta \gtrsim 0.99$) superheavy element with $110 \lesssim Z \lesssim 114$ [53].

Anomalous tracks in magnetic fields

The interactions of monopoles with magnetic fields are described by Eq. (1.16). Unlike electrically charged particles that experience a force in a plane perpendicular to the direction of the magnetic field, monopoles are accelerated along the field. In order to measure the momentum of charged particles, tracking detectors are usually immersed in a known magnetic field. Algorithms for track reconstruction generally assume that particles possess electric charge and no magnetic charge, so that the momentum of the particle can be determined from the track curvature. Magnetically charged particles, though, would follow trajectories in a different plane, producing anomalous tracks. For instance, a particle tracker immersed in a solenoid magnet that produces a field in the direction of the z-axis would typically record tracks that follow spirals that approximate to circumferences in the $r-\phi$ plane and straight lines in the $r-z$ plane. On the other hand, a monopole would follow a parabolic trajectory (assuming no energy losses) in the $r-z$ plane and a straight line in the transverse $r-\phi$ plane.

The actual trajectory of a monopole in a magnetic field differs from a perfect parabola as the energy losses are considerable. Nevertheless, parametrizations of the expected trajectory can be used in order to improve the detection efficiency. This technique has been used in multiple searches at particle colliders [54, 55]. It must be noted that due to the copious

amount of δ-rays produced by monopoles along their trajectory, track reconstruction algorithms may have difficulties recognizing a pattern associated to a monopole-like particle in high-granularity tracking detectors.

Other detection methods

In addition to the detection methods described above, there are a number of other techniques used in monopole searches. In most cases, a combination of detection methods is used. Some of them are listed below.

Time of flight Monopoles are expected to be heavy. GUT models predict monopoles of mass $\sim 10^{16}$ GeV and lower mass limits from production at colliders imply that monopoles must have a mass of at least hundreds of GeV (see Sec. 1.6). Therefore, monopoles are expected to travel at non-relativistic velocities, which allows the use of time-of-flight detectors. This technique has been used in triggering of monopoles [56, 57].

Cherenkov radiation Fast moving monopoles in cosmic rays can produce large amounts of Cherenkov radiation leading to a clear signature [58]. In addition, even for monopoles travelling at a velocity below the threshold for Cherenkov radiation, the production of large amounts of energetic δ-rays, which produce Cherenkov light, occurs [59].

Nuclear emulsions Nuclear emulsions have been used to detect the passage of monopoles. Tracks are recorded in thick emulsions and later developed. Results that could be interpreted as possible evidence of monopoles in cosmic rays were obtained with this technique [60].

1.5.2 Indirect detection methods

The existence of monopoles can be detected indirectly through the effect that they may have in higher order contributions to known SM processes. For instance, the decay of a Z boson produced at a particle collider could be mediated by monopoles, as shown in Fig. 1.7. This process is well known when the particle involved is an electron as it is highly suppressed

in the SM. Thus, a contribution from monopoles may be measured at particle colliders. The reliability of results obtained using indirect methods is subject to discussion. The magnitude of the magnetic coupling to the photon makes perturbation theory inapplicable. Therefore, other approaches have to be used in the indirect detection of monopoles.

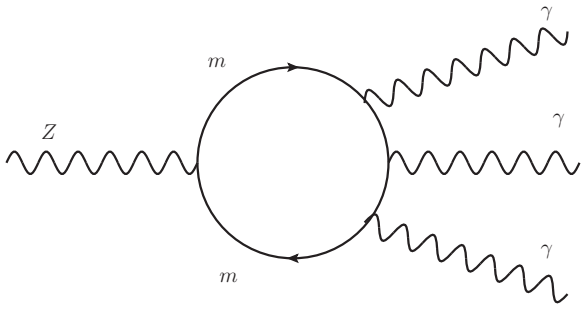

Figure 1.7: Feynman diagram of the process $Z \to \gamma\gamma\gamma$, which can be mediated by fermions and hypothetically by magnetic monopoles.

1.6 Previous experimental searches

The field of experimental searches for magnetic monopoles has been very active despite the null results so far. The motivations are strong enough to encourage scientists to ingeniously build experiments combining different technologies to achieve their purpose. Searches for magnetic monopoles cover three main areas: monopoles in cosmic rays, monopoles bound in matter and production of monopoles in high-energy collisions at particle accelerators. In the absence of conclusive evidence of the existence of monopoles experimental searches report upper limits on the monopole flux in cosmic rays, on the density of monopoles trapped in matter and on the production cross section assuming a specific production mechanism. Only a limited number of experiments have observed events that could be interpreted as magnetic monopoles. A complete list of all the searches performed so far can be found in Ref. [61]. The most relevant searches will be summarized in this section.

1.6.1 Observation of monopole-like events

Several observations of events that could be interpreted as magnetic monopoles have been made. The interpretation of the experimental results has been reassessed in some cases or is not conclusive to claim the observation of a magnetic monopole. All the observations of monopole-like events have been made by experiments studying cosmic rays.

Price *et al.* (1975) An experiment consisting of multiple layers of NTD foils complemented with a layer of nuclear emulsion and a layer of Cherenkov radiator coupled to a fast film was launched on a balloon to study heavy cosmic rays with $Z \geq 60$. An event consistent with a monopole of charge $2g_{\mathrm{D}}$ and mass greater than 200 GeV travelling downwards to earth was observed [52]. However, this observation was later reassessed when possible errors in the interpretation of the data from the NTD foils and the nuclear emulsion became apparent. The observed signature is believed to be from either a slow massive particle, a fast antinucleus or an ultrarelativistic heavy element [53].

Cabrera (1982) An experiment based on the induction method was set up to detect monopoles in cosmic rays in such a way that the passage through the superconducting coils of a particle with charge g_{D} would be measured as a total flux of $8\phi_0$. The experiment consisted of four coils, which along with the $2\phi_0$ flux associated with a single Dirac charge accounts for the $8\phi_0$. One event with magnitude $8\phi_0$ was recorded in a total exposure time of 151 days. The event could not be associated with a spurious detector response and remains the best candidate for an observation of magnetic monopoles to date [42].

Anderson *et al.* (1983) A set of nuclear emulsion plates were placed in a Pb-Hg shield 1370 m underground, such that cosmic rays and local radiation would be completely avoided. After developing the emulsion, seven tracks were observed that could not be associated to expected background from α particles. A possible interpretation of the results is that monopoles may bind to uranium nuclei naturally occurring in the surroundings of the experimental site. Under the strong magnetic field the uranium

nuclei would be sufficiently distorted to undergo fission [60].

Caplin *et al.* (1986) The observation of an unexplained event was made using an experiment dedicated to detect monopoles. Based on the induction technique, this setup would record a total magnetic flux of $2\phi_0$ when a monopole of charge g_{D} passes through it. An event with a total flux of $0.83\phi_0$ was observed, and in the absence of obvious explanations leading to an experimental failure, the event remains as a possible monopole event [62].

1.6.2 Searches for cosmic monopoles

During the phase transition described by GUT models in which the symmetry of the scalar field broke down, magnetic monopoles must have been created. The density of these cosmological monopoles should have diminished as monopole–anti-monopole annihilation occurred. GUT models predict a monopole density that is comparable with the baryon density [63], leading to the *cosmological monopole problem*, which results in a conflict between cosmology and GUT models. Due to the large mass of GUT monopoles, a density comparable to that of baryons would yield a closed universe, contrary to the observations of an expanding open universe. This problem is solved by assuming that the universe went through an inflationary period (see Ref. [44] and references therein). The resulting monopole abundance is then reduced to a level consistent with the experimental observations, and possibly even too low for an observation to ever happen. Nevertheless, the search for cosmic monopoles is a very active field.

Cosmological monopoles are expected to have masses near the unification scale (of order $\sim 10^{16}$ GeV). Therefore, they are subject to the gravitational attraction of galaxies in addition to their magnetic fields. Depending on the mass of the monopole one interaction is dominant. For monopoles of mass greater than 10^{16} GeV, which is far too heavy to be produced at high-energy colliders, the gravitational attraction becomes the dominant interaction by which they gain kinetic energy. Lighter monopoles, on the other hand, gain kinetic energy mostly by interacting with the magnetic field of galaxies.

A cosmological monopole would be accelerated to a galactic infall velocity of about

$\beta = 10^{-3}$. The interactions with matter of a monopole moving at such a velocity would be too weak to be efficiently detected using techniques relying on high ionization. Also, based on Eq. (1.21), the range of such a monopole in rock would be about 10^9 km and therefore it would not stop to become trapped in terrestrial material. The accelerating effect that the galactic magnetic field, of strength $B \approx 3 \times 10^{-10}$ T, would have on a cosmological monopole over the coherence length of about $L \approx 10^{19}$ m results in a velocity of

$$v = \left(\frac{2g_{\mathrm{D}}BL}{m}\right) \approx 10^{-2}c. \tag{1.25}$$

Due to the low speeds at which cosmological monopoles would move, most experimental searches are sensitive to lower mass monopoles that would attain a higher velocity in the galactic magnetic field and thus lose enough energy by ionization to be detected. Only experiments that use the induction technique are sensitive to monopoles of all speeds and therefore all masses as this search method depends only on the magnetic flux produced by a magnetic pole.

Based on the energy that the galactic magnetic field would give to a cosmic monopole, Parker set upper limits on the flux of cosmic monopoles [64, 65]. In order for the galactic field not to be fully depleted in a period of 10^8 years, the flux of monopoles should be of order $\sim 10^{-15}$ cm^{-2}s^{-1}sr^{-1}. These phenomenological considerations result in a limit that varies between 10^{-15} cm^{-2}s^{-1}sr^{-1} for mass $\lesssim 10^{17}$ GeV and 10^{-13} cm^{-2}s^{-1}sr^{-1} for mass $\approx 10^{20}$ GeV. It sets a stringent upper limit that has been superseded by only a fraction of the experiments searching for monopoles in cosmic rays [61, 65].

The MACRO experiment at the Gran Sasso laboratory was optimized for detecting monopoles with a remarkably wide range of velocities, covering $4 \times 10^{-5} < \beta < 1$ [66]. A combination of detection techniques was used to achieve sensitivity in such a wide range. Layers of liquid scintillator sensitive to particles as slow as $\sim 10^{-4}c$ were used to detect slow moving monopoles. Streamer tubes filled with a mixture of helium and n-pentane were used to record the signatures of highly ionizing monopoles in the range $\beta > 10^{-3}$. In addition, NTD foils were used to detect tracks produced by monopoles in various velocity ranges. No monopole events were observed by MACRO. The combination of several analyses using the different detection methods led to an upper limit on the flux of monopoles of charge

$|g| = 1.0g_{\rm D}$ of 1.4×10^{-16} cm^{-2}s^{-1}sr^{-1}. This result was the first to produce limits below the Parker limit covering such a wide range of monopole velocities.

The RICE experiment located at the south pole was originally designed to detect ultra-high energy neutrinos [58]. However, it had the capability to detect relativistic monopoles in the range $\gamma \gtrsim 10^7$ with a sensitivity maximal for monopoles with $\gamma \gtrsim 10^8$. In order to achieve such relativistic factors, monopoles have mass in a intermediate range, i.e., $m \lesssim 10^8$ GeV. The RICE detection technique consisted of an array of radio antennas, which detect the Cherenkov radiation produced by the cascades initiated by ultrarelativistic particles in ice. The RICE experiment did not observe events consistent with magnetic monopoles of charge $|g| = 1.0g_{\rm D}$. An upper limit on the monopole flux of order 10^{-18} cm^{-2}s^{-1}sr^{-1} for monopoles with $\gamma \geq 10^8$ was obtained. This result exceeded the previous limit by MACRO by two orders of magnitude in its range of sensitivity. In addition to the RICE experiment, the ANITA-II experiment also searched for ultra-relativistic monopoles using a balloon-borne antenna to detect Cherenkov radiation produced in ice [67]. This experiment was sensitive to monopoles of charge $|g| = 1.0g_{\rm D}$ in the range $\gamma \geq 10^{10}$. In the absence of an observation, an upper limit on the monopole flux was set to 10^{-19} cm^{-2}s^{-1}sr^{-1}.

The ANTARES experiment was located in the western Mediterranean sea at a depth of 2475 m [59]. It consisted of an array of photomultiplier tubes, which detect Cherenkov radiation produced by muons and electrons travelling through deep sea water. The ANTARES detector was sensitive to up-going monopoles in the intermediate mass range $m \lesssim 10^8$ GeV that have lost a significant amount of energy after passing through the Earth, i.e., $\beta > 0.625$. The Cherenkov radiation resulting from the large number of δ-rays produced by monopoles is the signal of interest. One event was observed by ANTARES, which was consistent with the background-only hypothesis. Upper limits on the monopole flux were set to 1.3×10^{-17} cm^{-2}s^{-1}sr^{-1} for monopoles of charge $|g| = 1.0g_{\rm D}$ in the range $\beta > 0.625$.

The IceCube experiment is sensitive to relativistic magnetic monopoles in the range $\beta \geq 0.51$ [68, 69]. Located at the south pole, it can detect monopoles travelling through ice at speeds below the Cherenkov threshold but producing large amounts of energetic δ-rays. The Cherenkov light produced by these electrons is collected by photomultiplier

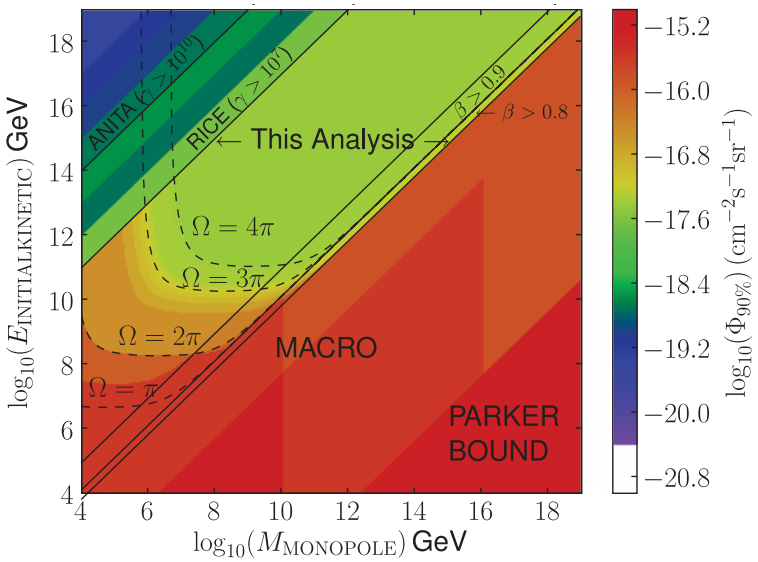

Figure 1.8: Upper limits on monopole flux at Earth's surface for monopoles of charge $|g| = 1.0 g_{\mathrm{D}}$ as a function of the monopole kinetic energy and mass for various searches by neutrino experiments [68].

tubes. A monopole event would be four orders of magnitude brighter than a muon event. No such event was observed and an upper limit on the monopole flux was set at 1.55×10^{-18} cm^{-2}s^{-1}sr^{-1}. Figure 1.8 shows a summary of the upper limits on monopole flux at Earth's surface for monopoles of charge $|g| = 1.0 g_{\mathrm{D}}$ as a function of the monopole initial kinetic energy and mass. This summary includes results by some of the neutrino experiments sensitive to monopoles described above.

Searches for monopoles in cosmic rays include mostly monopoles with masses lower than that of GUT monopoles, i.e., $m \lesssim 10^{16}$ GeV. However, the most stringent limits on monopole flux have been obtained for GUT monopoles that are accelerated gravitionally to velocities in the range $10^{-5} < \beta < 0.04$. An upper limit on the monopole flux ranging from 6×10^{-28} cm^{-2}s^{-1}sr^{-1} to 7×10^{-20} cm^{-2}s^{-1}sr^{-1} for monopoles of mass $m > 10^{17}$ GeV was obtained by the Super-Kamiokande experiment [70]. This search differs from all the other neutrino observatories in that it does not attempt to detect the passage of monopoles through the active volume of the detector. Instead, the search focuses on a predicted excess of neutrinos from the sun arriving with an energy of 29.79 MeV. These low-energy neutrinos are expected to be produced in the sun when monopoles accumulate and catalyze proton

decays. The mechanism by which the proton decays is known as the Callan–Rubakov process [71, 72].

1.6.3 Searches for monopoles bound in matter

A number of searches for monopoles trapped in matter have been performed setting upper limits on the monopole density for magnetic charges in various ranges. Most of these searches use the induction technique and have found no evidence of monopoles in meteorites, ferromagnetic materials and polar volcanic rocks, among other materials. The most stringent upper limits on monopole density have been set to 2.0×10^{-7} g^{-1} for charges $|g| > 0.6g_{\rm D}$ and mass between 10^{14}–10^{17} GeV [73]. Other searches have set mass-independent limits on the monopole density of 6.9×10^{-6} g^{-1} for charges $|g| > g_{\rm D}/3$ [37] and 9.8×10^{-5} g^{-1} for charges $|g| \geq 1.0g_{\rm D}$ [39].

1.6.4 Searches for production of monopoles at colliders

Magnetic monopoles have been sought at high-energy colliders for decades. However, the monopoles that could be produced at colliders are restricted to masses within the energy reach of the accelerators. Therefore, none of the current collider searches is sensitive to GUT monopoles, not even to those in the intermediate mass range since the maximum energy achieved by a collider is 13 TeV. The most relevant searches for monopoles have been performed using data collected at e^+e^-, $p\bar{p}$, e^+p and pp colliders. These searches have used a number of techniques to capture the signatures of monopoles as will be described below.

Indirect searches for monopoles at colliders

Searches for magnetic monopoles have also been performed at colliders based on their indirect effects. The L3 experiment at the LEP collider searched for the decay process $Z \to \gamma\gamma\gamma$, which is highly suppressed in the SM [74]. The existence of monopoles that couple to the Z boson would enhance the cross section of this process. The observations were consistent with the QED background expectation leading to a branching ratio limit

of BR($Z \to \gamma\gamma\gamma$) $< 0.8 \times 10^{-5}$, which results in a lower limit on the monopole mass of 520 GeV.

The D0 experiment also performed an indirect search with data from the Tevatron at $\sqrt{s} = 1.8$ TeV [75]. In this search, the production of two high transverse energy photons in elastic and inelastic collisions was considered. No events passed the selection criteria. Therefore, lower mass limits of 610, 870 and 1580 GeV were obtained for spin-0, spin-1/2 and spin-1 monopoles of charge $|g| = 1.0 g_{\mathrm{D}}$.

Searches at e^+e^- colliders

Two experiments searched for monopoles produced in e^+e^- collisions $\sqrt{s}$ =91.1 GeV at the LEP collider. The MODAL experiment [49] was a dedicated experiment that used NTD foils around one of the LEP interaction points. Monopoles are expected to produce tracks through the foils that fulfill certain criteria to be deemed as highly ionizing. No monopole-like tracks in the NTDs were found. In 1992, MODAL set limits on the production cross section assuming pair production with the Drell-Yan mechanism. This later became the benchmark model for most of the searches at colliders. An upper production cross section limit was set to 70 pb. The second experiment, using NTD foils wound around the beampipe and other parts of the OPAL detector [48], achieving an almost 4π coverage, was able to produce a more stringent cross section limit of 0.3 pb, assuming the Drell-Yan mechanism. Due to the energy limitations of LEP, both experiments were only able to rule out monopoles of mass $m < 45$ GeV. These results apply to monopoles of charge $|g| = 1.0 g_{\mathrm{D}}$ and $|g| = 2.0 g_{\mathrm{D}}$.

The limits from LEP were later exceeded by OPAL at LEP2 with data from e^+e^- collisions at $\sqrt{s}$ =206.3 GeV [76]. The detection techniques of this search varied from that of previous searches at LEP. OPAL made use of its jet chamber to identify high ionization deposits and trajectories that bent in a plane parallel to its solenoidal magnetic field. In the absence of an observation, upper limits on production cross section were set to 0.05 pb for monopoles of charge $|g| = 1.0 g_{\mathrm{D}}$ and masses in the range 45–102 GeV, assuming Drell-Yan production. It can be concluded that the combination of the results from all LEP and LEP2

searches effectively excludes monopoles of mass $m < 102$ GeV.

Monopoles at HERA

After the searches at LEP and LEP2, the H1 experiment collected data at the HERA e^+p collider at $\sqrt{s}$ =300 GeV. The beampipe of H1 was examined to search for monopoles produced in collisions that became trapped in it [40]. The induction technique was used to detect the magnetic flux of monopoles through a superconducting coil coupled to a SQUID magnetometer. No persistent currents consistent with a monopole signal were detected. This search assumed a production process different from previous searches since Drell-Yan production does not occur in e^+p collisions. Pair production of monopoles through photon–photon interactions was assumed. Two specific models were taken into account: spin-0 monopoles produced in elastic collisions and spin-1/2 monopoles produced in inelastic collisions. This search considered the effect of the solenoidal magnetic field in which the beampipe was immersed to determine the acceptance of the search. The upper limits on production cross section are mass- and charge-dependent as this search was sensitive to charges 0.1–6.0g_{D}. Upper limits vary from 0.06 pb to 2 pb in the mass range 5–140 GeV.

Direct searches at $p\bar{p}$ colliders

At the Tevatron, three direct searches for magnetic monopoles produced in $p\bar{p}$ collisions have been performed. Analysis of samples from the D0 and CDF detectors exposed to the byproducts of collisions at $\sqrt{s}$ =1.8 TeV, including the D0 beampipe and part of the CDF forward electromagnetic calorimeter, when passed through a superconducting coil coupled to a SQUID magnetometer, led to new upper limits on production cross section [41]. The production model assumed by this search was the Drell-Yan mechanism. The upper production cross section limits obtained are 0.6, 0.2, 0.07 and 0.2 pb for charges 1.0, 2.0, 3.0 and 60g_{D}, respectively. From these cross section limits the corresponding lower mass limits are 265, 355, 410 and 375 GeV, respectively. Two additional searches were performed by the CDF experiment using data from collisions at $\sqrt{s}$ =1.96 TeV [56, 57]. A different approach was used in these searches in which a dedicated time-of-flight trigger sensitive to

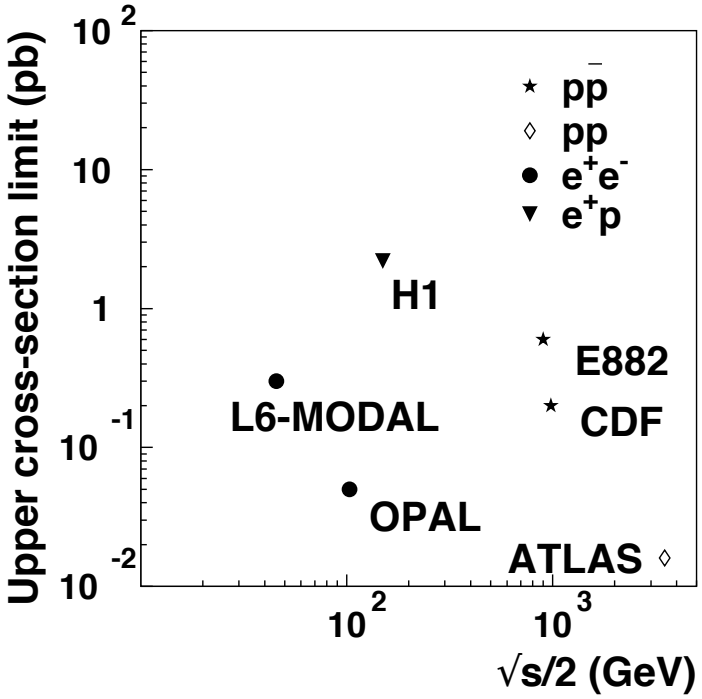

Figure 1.9: Summary of upper limits on production cross section as a function of $\sqrt{s}/2$ for several experiments that used data collected at different types of colliders [61].

monopoles with $\beta > 0.2$ was used. The selected events were analyzed using the outer central tracker, in which large ionization and a trajectory consistent with a magnetically charged particle was expected. No monopole events were observed by either search and therefore upper cross section limits were set to about 10^{-2} pb, assuming the Drell-Yan mechanism for monopoles of charge $|g| = 1.0 g_{\mathrm{D}}$. Lower mass limits were set to 476 GeV [57].

Monopoles at the LHC

The collider search that has produced the most competitive limits so far was performed by the ATLAS experiment with data from pp collisions at $\sqrt{s}$ =7 TeV [77]. This search used several ATLAS subdetectors, combining the measurements from the transition radiation tracker and the electromagnetic calorimeter in order to identify highly ionizing monopoles with mass in the range 200–1500 GeV. No monopole events were observed by ATLAS in the selected dataset. This search was able to produce model independent results using fiducial regions of high and uniform event selection efficiency, setting upper limits on production

cross section of about 2 fb for monopoles of charge $|g| = 1.0 g_{\mathrm{D}}$ and mass in the range 200–1500 GeV. In addition, assuming the Drell-Yan production mechanism, upper cross section limits varying from about 0.2 pb to 0.02 pb for masses from 200 GeV to 1200 GeV were obtained. A lower mass limit of 862 GeV was obtained assuming the Drell-Yan mechanism. The work presented in this dissertation builds on the knowledge and techniques developed for the search at ATLAS using data from pp collisions at 7 TeV.

Figure 1.9 presents a summary of the upper limits on production cross section obtained by searches performed by several experiments with data from different types of particle colliders.

Chapter 2

The LHC and ATLAS

This chapter introduces the Large Hadron Collider and the ATLAS detector, in particular, the Transition Radiation Tracker and the calorimeters, which play an important role in the detection of magnetic monopoles. A brief description of the ATLAS trigger scheme and computing infrastructure is also included.

2.1 The Large Hadron Collider

The Large Hadron Collider (LHC) [78] is the highest-energy particle collider ever built, allowing frontiers of experimental high-energy physics to be pushed to new regimes. The LHC is part of CERN's accelerator complex, which delivers beams of particles to a number of experiments that study the fundamental laws of physics. Designed as a discovery machine, the LHC proved so in 2012 when the observation of a new particle consistent with the Standard Model scalar boson was announced. A diagram of CERN's accelerator complex is shown in Fig. 2.1. The LHC has been designed to collide particles in three configurations: proton–proton (pp), proton–lead ion (p+Pb) and lead ion–lead ion (Pb+Pb). Protons are produced from a bottle of hydrogen gas by stripping the hydrogen atoms of their electrons, and then accelerated though a chain that comprises linear and circular accelerators. Before injection into the LHC, protons split in two beams that circulate in opposite directions

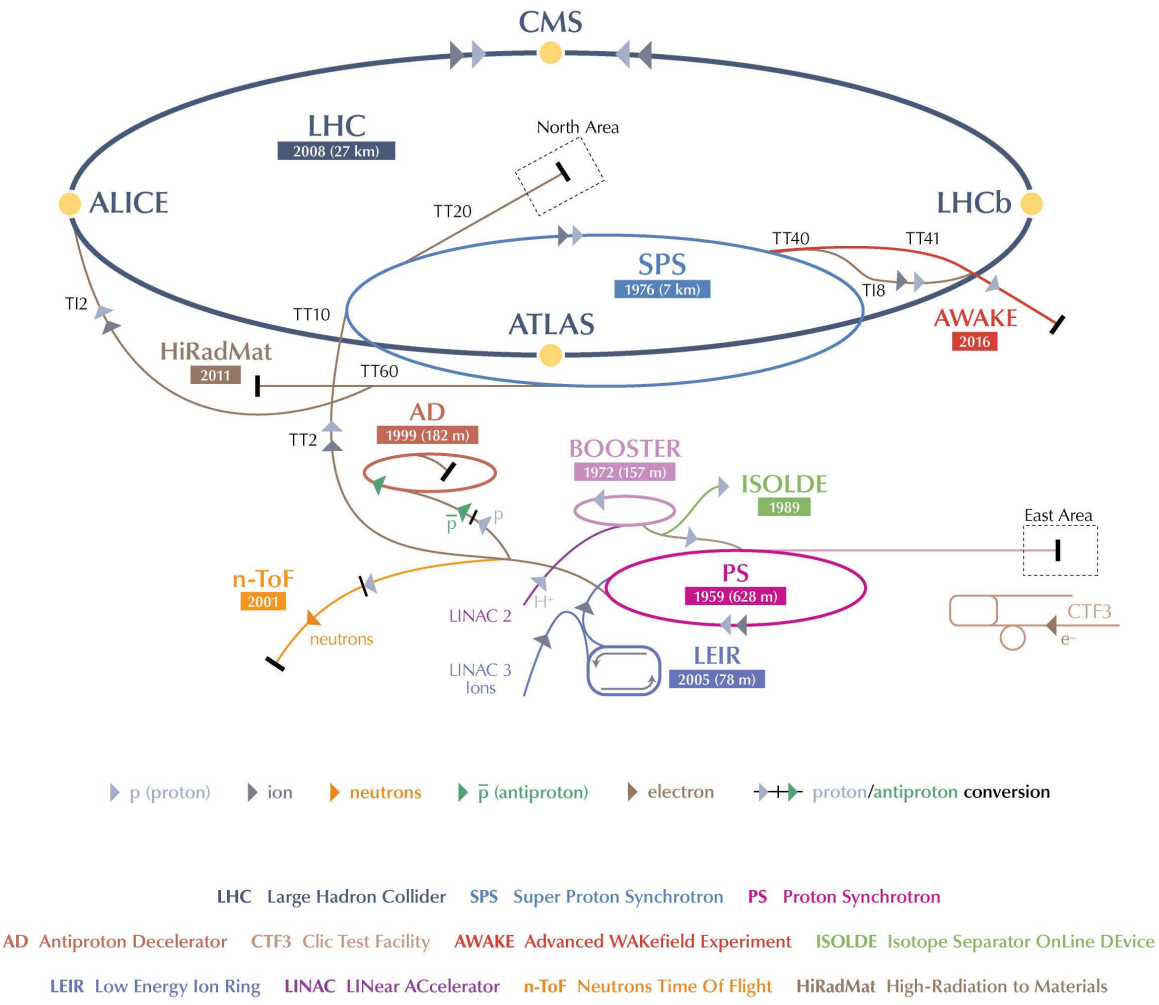

Figure 2.1: CERN's accelerator complex [79].

colliding at four interaction points where the main LHC experiments are located: ATLAS, ALICE, CMS, and LHCb.

The LHC is a circular collider that accelerates bunches of protons in a 27 km ring producing collisions at a centre-of-mass energy of $\sqrt{s} = 7$ TeV and $\sqrt{s} = 8$ TeV during the 2011 and 2012 runs, respectively. These two years along with the first two years of operation, 2009 and 2010, in which collisions were produced at a centre-of-mass energy of $\sqrt{s} = 0.9$ TeV and $\sqrt{s} = 2.36$ TeV, respectively, are known as Run 1.

2.1.1 LHC performance in Run 1

The operating conditions of the LHC during Run 1 pp collisions changed significantly from 2010 through 2012. Apart from the increase in centre-of-mass energy, the spacing between proton bunches was reduced from 250 ns in 2010 to 50 ns in 2011 and 2012, which, combined with high intensity ($1.6 - 1.7 \times 10^{11}$ protons per bunch in 2012), gave an instantaneous luminosity peaking at 7.7×10^{33} cm^{-2}s^{-1} in 2012. As a consequence, the observed average number of collisions per bunch crossing ($\langle\mu\rangle$), otherwise known as pileup, by ATLAS and CMS was around 12 in 2011 and 20 in 2012. Table 2.1 summarizes the integrated luminosity delivered by the LHC during the years 2010 through 2012. A more comprehensive status report on the LHC operation during Run 1 can be found in Ref. [80].

Year	$\sqrt{s}$ [TeV]	Integrated luminosity [fb^{-1}]
2010	7	0.04
2011	7	6.1
2012	8	23.1

Table 2.1: Centre-of-mass energy and integrated luminosity delivered by the LHC during the years 2010 - 2012.

2.2 The ATLAS detector

The ATLAS detector is a multipurpose particle detector located at one of the LHC interaction points with a layout that resembles that of a cylinder [81]. Figure 2.2 shows a three-dimensional rendering of the ATLAS detector layout.

The ATLAS detector is centred about the nominal interaction point, which is the origin of the coordinate system in which the z direction is defined by the direction of the beam, and the x-y plane is transverse to the beam with the x-axis pointing to the centre of the LHC ring and the y-axis pointing upwards. The ATLAS detector is symmetric about the z-axis with the azimuthal angle ϕ measured around the beam axis and the polar angle θ measured from the beam axis. These two angles are expressed in radians hereafter. It also has forward-backward symmetry with respect to the interaction point. The pseudorapidity

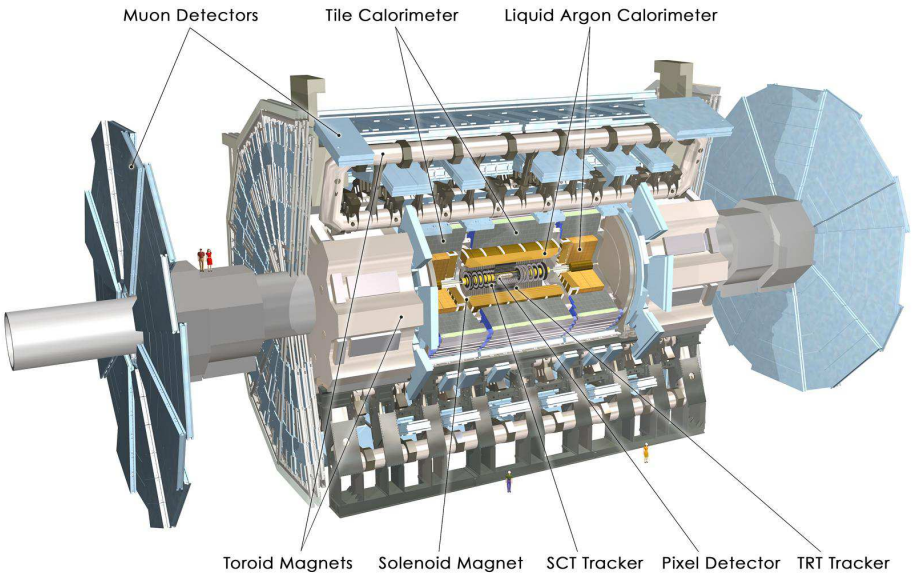

Figure 2.2: Full three-dimensional rendering of the ATLAS detector (copyright © CERN).

is defined as

$$\eta = -\ln\left(\tan\frac{\theta}{2}\right). \tag{2.1}$$

The ATLAS detector comprises a charged particle tracker, known as the Inner Detector (ID), immersed in a 2 T magnetic field produced by a thin superconducting solenoid, an electromagnetic (EM) calorimeter, a hadronic calorimeter (HCal), and a muon spectrometer (MS) immersed in a toroidal magnetic field produced by three superconducting toroidal magnets (one barrel and two end-caps).

During Run 1 the ID was composed of three independent subsystems: the Pixel detector, the Semiconductor Tracker (SCT) and the Transition Radiation Tracker (TRT). The ID provides momentum measurements for charged particles with a transverse momentum (p_{T})[7] greater than approximately 0.5 GeV within the pseudorapidity range $|\eta| < 2.5$. In addition, the ID is capable of providing electron identification for charged particle tracks within $|\eta| < 2.0$. The two innermost subsystems, the Pixel and SCT, use silicon sensors while the outer TRT is a Xe-based drift chamber composed of straw tubes. Figure 2.3 shows a side

[7]The transverse momentum p_{T} is defined as the momentum in the plane transverse to the beam axis.

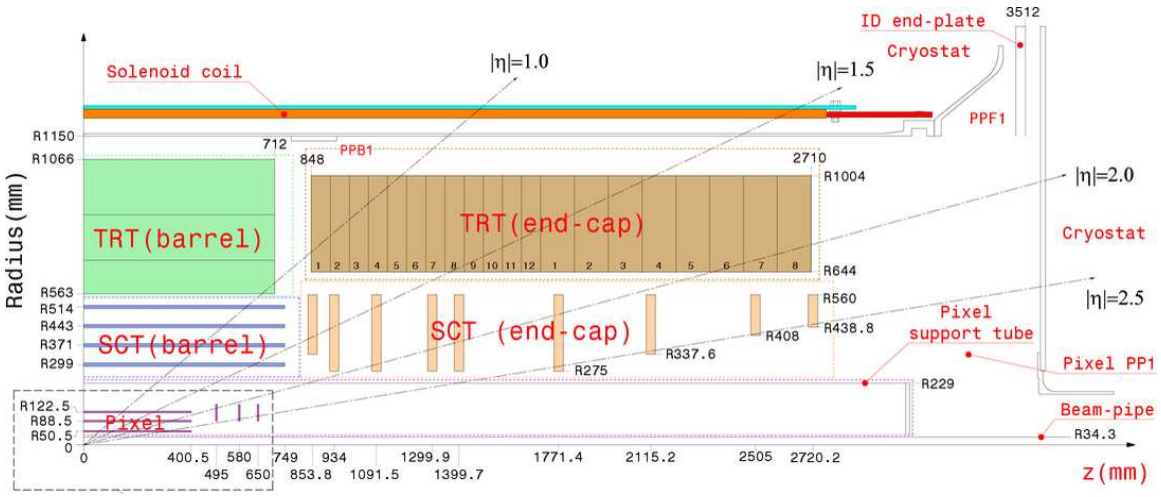

Figure 2.3: Side view of the Inner Detector. The ID has azimuthal symmetry and forward-backward symmetry with respect to the nominal interaction point. The labels PP1, PPB1 and PPF1 indicate the patch-panels for the ID services [81].

view of the barrel and end-cap regions of the ID.

The ATLAS calorimeter consists of several sampling detectors with full azimuthal coverage and symmetry. The EM calorimeter is the closest to the interaction point, providing energy measurement and particle identification for electrons and photons. The next layer is a hadronic calorimeter that measures the energy of particle jets. A cut-away view of the ATLAS calorimeter system can be seen in Fig. 2.4.

The muon spectrometer uses the deflection of muon tracks in a magnetic field generated by three large superconducting toroid magnets to perform momentum measurements in the pseudorapidity range $|\eta| < 2.7$. The MS uses four different technologies for two main purposes: precision tracking and triggering. The monitored drift tubes and the cathode strip chambers provide the precision tracking while the resistive-plate chambers and the thin-gap chambers offer triggering capabilities in the pseudorapidity range $|\eta| < 2.4$. Figure 2.5 shows a cut-away view of the MS with its four different subsystems.

2.2.1 The Pixel detector

The Pixel detector is the innermost silicon tracker whose main purpose is to make measurements with a spatial resolution of $r - \phi \times z = 5 \times 115$ μm in the barrel and $r - \phi \times r =$

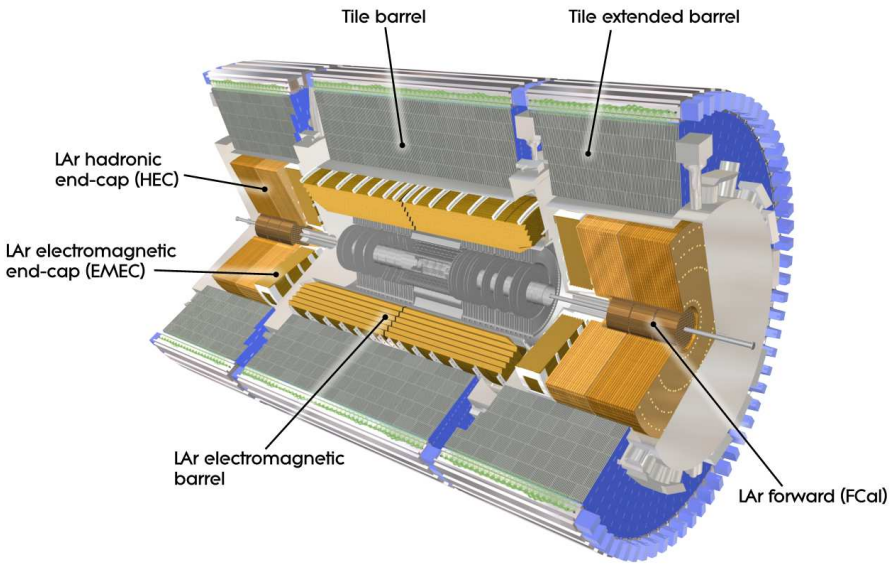

Figure 2.4: Cut-away view of the ATLAS calorimeter system showing the liquid argon detectors in yellow and the plastic scintillators in grey [81].

5×115 μm in the end-caps [82]. The Pixel detector contributes to the measurement of the transverse and longitudinal impact parameters, which allow for reconstruction of primary vertices. In particular, the innermost layer is of great importance for identification of jets of particles from b-quark decays.

The Pixel detector provides tracking in the pseudorapidity range $|\eta| < 2.5$ with full coverage in ϕ. The active region consists of a central barrel, comprising three radial layers, and two end-caps with three layers or disks each. It consists of 50 μm$\times$400 μm silicon sensors, adding up to approximately 80 million readout channels. The readout electronics of the Pixel sensors allow for dE/dx measurements by integrating the time during which the collected charge is above a given threshold [83].

2.2.2 The Semiconductor tracker

The SCT is a silicon detector surrounding the Pixel detector [81]. The SCT modules consist of two micro-strip sensors, which are paired such that there is one sensor on each side. The bottom and top sensors are misaligned by an angle of 40 mrad in order to achieve high

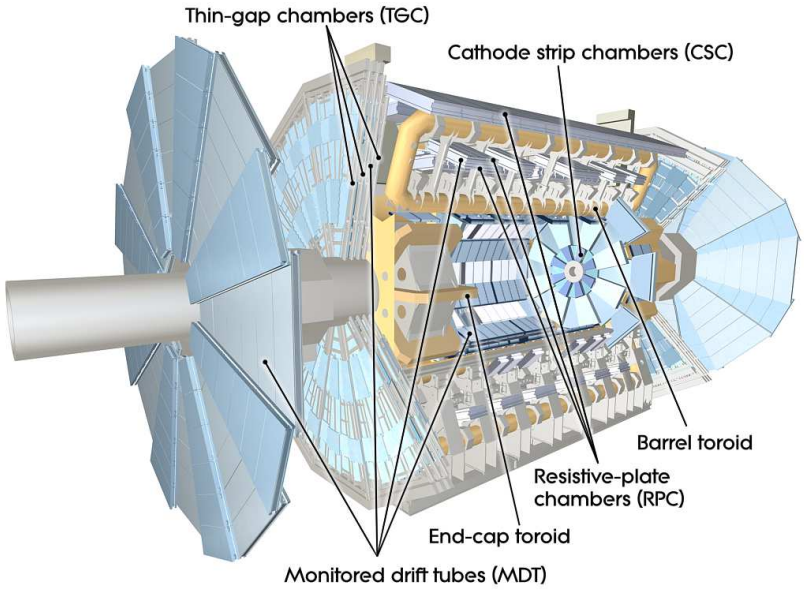

Figure 2.5: Cut-away view of the ATLAS muon spectrometer system showing the four different subsystems [81].

precision in the z-axis using fewer modules than the Pixel detector. The SCT provides coverage in the pseudorapidity range $|\eta| < 2.5$ with a central barrel composed of four radial layers and two end-caps made up of 9 disks each. The SCT has about 6 million readout channels.

2.2.3 The Transition Radiation Tracker

The TRT is a drift chamber composed of straw tubes of 4 mm diameter with a gold-plated tungsten wire (anode) of 31 μm diameter at the centre. The active gas of the TRT is a Xe-based mixture, which absorbs transition radiation X-rays produced by electrons. The TRT is a drift chamber in the proportional regime, i.e., the amount of charge collected is proportional to the energy deposition in the chamber. Thus, it can be used to perform $\mathrm{d}E/\mathrm{d}x$ measurements [84]. The potential difference between the cathode (straw wall) and the anode is kept at approximately 1600 V. The TRT is divided into three elements: one central barrel covering the pseudorapidity range $|\eta| < 1.06$ and two end-caps covering $0.77 < |\eta| < 2.0$. In the barrel, the straws have a length of 144 cm and are aligned with the

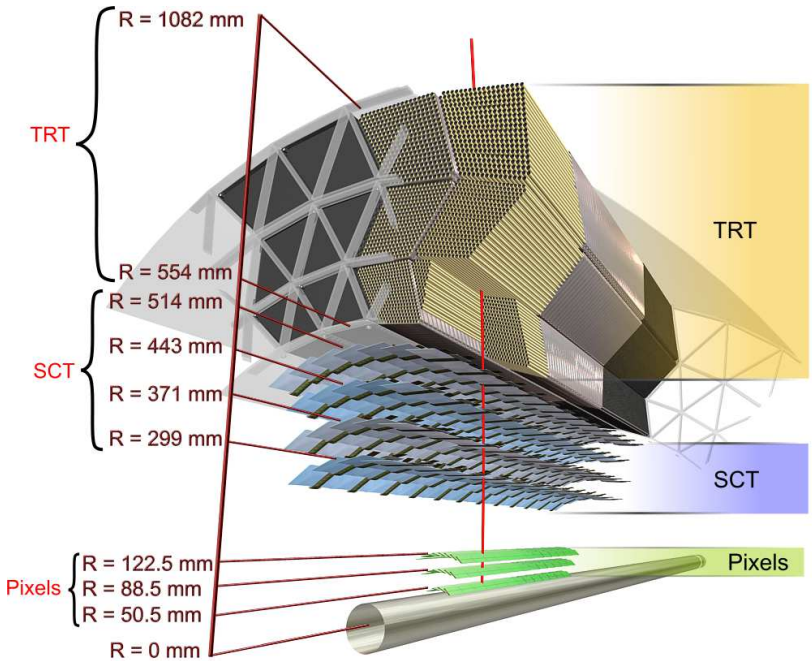

Figure 2.6: Section of the ID barrel (copyright © CERN).

beam line in radial layers. The number of straws per layer increases with the radial distance from the beam line. The barrel straws have a glass insert at $\eta = 0$ that effectively separates the readout of one straw into two individual channels. Straws in the nine innermost layers of the barrel are divided into three segments, with the central part not read out. This reduces the active part of such straws to only the two segments at the extremes [85].[8] A section of the ID barrel showing the geometry of the TRT barrel is shown in Fig. 2.6.

In the TRT end-cap the straws of length 37 cm are oriented radially. The straws are organized in disks grouped into two types of wheels. Type A wheels are those closer to the interaction point, each one comprising eight disks of straws separated by 8 mm in z; there are 12 type A wheels. The outer type B wheels, of which there are eight, are also composed of eight disk of straws, but unlike the type A wheels, these are spaced by 15 mm. Figure 2.7 shows a section of the ID end-cap showing the geometry of the TRT end-cap.

The space between TRT straws is filled with a radiator material made of polypropylene in the form of fibres in the barrel and of foils in the end-caps. Electrons with a momentum

[8]The length of the active segments of straws in the nine innermost layers in the barrel is 31.2 cm, significantly shorter than the 72 cm long active segments of the straws in the outer layers.

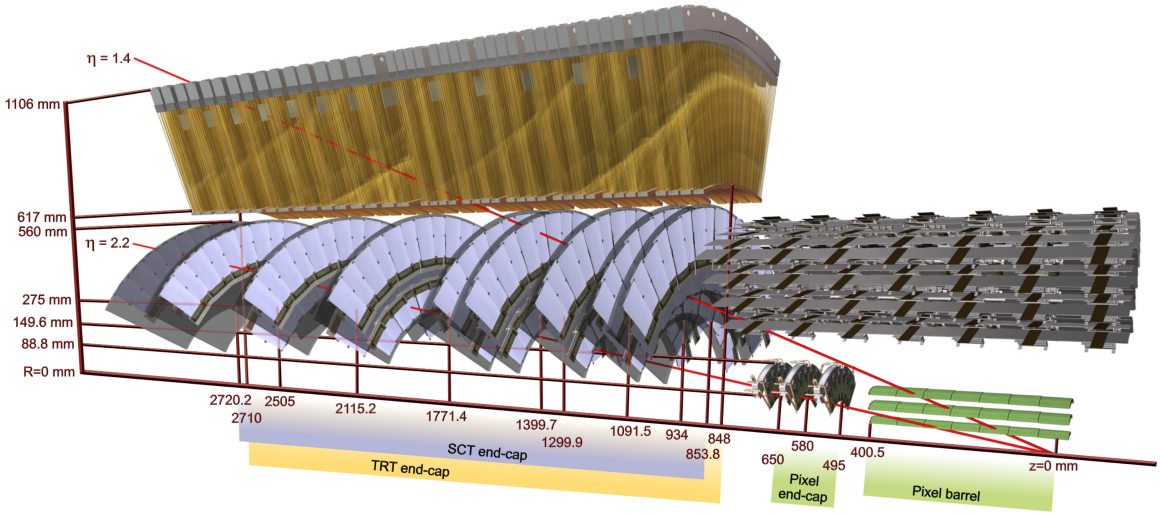

Figure 2.7: Cross section of the ID end-cap (copyright © CERN).

above 1 GeV produce transition radiation photons with energies between 5 and 30 keV as they traverse the interfaces between air and radiator material. These transition radiation photons are absorbed by the Xe-based gas mixture.

Readout of the TRT

The charge from ionization of the active gas mixture is collected by means of the 1.6 kV electric field. The lighter electrons drift to the central anode while the heavier ions drift to the straw walls. Electrons from ionization liberated at the point of closest approach to the anode are the first to be collected, and their drift time is used to reconstruct the charged particle trajectories. The collection time of ions can extend beyond 75 ns.

The signal pulses are discriminated by a front-end chip called the ASDBLR[9] that also amplifies, shapes and restores the baseline. The ASDBLR receives input from eight individual straws [86]. This front-end chip has two discriminating thresholds: a 300 eV low threshold (LT) used for track reconstruction purposes and a 6 keV high threshold (HT) for electron identification. A second front-end chip called the DTMROC,[10] which measures the drift time when a trigger accept signal is received, uses 8 bits per 25 ns time slice, the

[9] Amplitude shaper discriminator baseline restorer chip
[10] Drift time measurement and readout chip

design spacing between colliding proton bunches, to transmit the LT information from the ASDBLR. This corresponds to a time binning of 3.125 ns [86]. For each 3.125 ns bin, a bit is set to one if the signal was above the low threshold during the corresponding time window. The HT signal from the ASDBLR is processed once per 25 ns time slice, thus only one bit is transmitted every 25 ns. Similarly to the LT signal case, the HT bit is set to one if the signal was above the high threshold at any point during the 25 ns time slice. After a trigger accept signal is received, the DTMROC encodes the information corresponding to three 25 ns time slices, for a readout window of 75 ns, in the following way: for each 25 ns time slice, the earliest "most significant bit" carries the HT information and the next eight bits carry the LT information with the latest being the least significant bit. In total, there are 27 bits for each 3×25 ns window: three HT bits and 24 LT bits. The DTMROCs receives the input from two ASDBLR chips (16 straws) and transmit a digitized signal. Figure 2.8 shows an example of the digitization of a TRT signal pulse by the DTMROC. The digitized TRT data is read out by the read-out drivers (ROD), which reduce the size of the event data, formatting them to fulfill bandwidth constraints. The data is then transmitted to a readout buffer before being sent for Level-2 trigger reconstruction (see Sec. 2.2.6). The TRT comprises a total of over 350 000 individual channels.

The time measured by the DTMROCs—time from the start of the 75 ns readout window or, equivalently, trigger accept signal to the first LT bit high—is relative to the central ATLAS clock. However, the drift time should be measured with respect to the time of passage of the particle through the straw. Thus, a time known as T_0 is subtracted from the measured time to obtain the actual drift time. The time T_0 corresponds to the time that it takes a particle travelling at the speed of light to reach the straw. The corrected drift time $T_{\text{drift}} = T_{\text{measured}} - T_0$ is used to determine the drift radius, which represents the distance of closest approach to the central wire. Based on the measured drift radii, the reconstructed output of the TRT are drift circles [87].

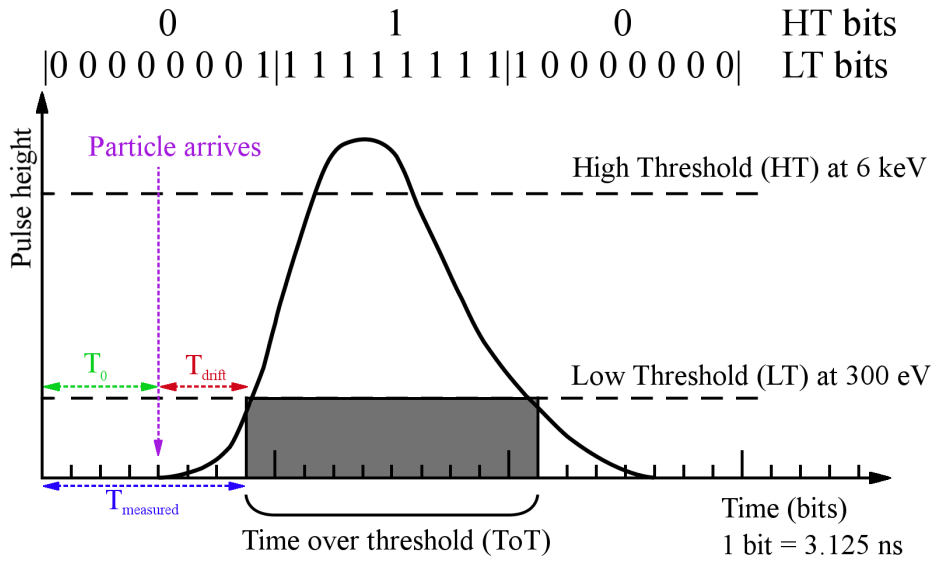

Figure 2.8: TRT signal pulse in a 75 ns read-out window. Values of low- and high-threshold bits are shown for the example pulse. Each bit corresponds to a time bin of 3.125 ns.

2.2.4 Calorimetry at ATLAS

The ATLAS calorimeter provides high resolution energy measurements with pseudorapidity coverage in $|\eta| < 4.9$ and full coverage in ϕ. The calorimeter can be divided into two main categories: an EM calorimeter closer to the interaction point, right outside the solenoid magnet enclosing the ID, and a hadronic calorimeter. The two main technologies used in the calorimeter are liquid argon (LAr) and scintillating tiles. The LAr technology is used by the EM calorimeter barrel and end-caps, the hadronic calorimeter end-caps, and the forward calorimeter. Only the hadronic barrel and extended barrel use the scintillating tile technology. The combination of EM and hadronic calorimeters fulfill all the physics performance requirements for which they were designed, i.e., large acceptance and full azimuthal coverage with uniform response, precise energy measurements, and good particle identification of electrons versus jets and photons versus π^0 [81].

The electromagnetic LAr calorimeter

The EM LAr calorimeter [88] is the closest to the interaction point, surrounding the solenoid magnet. It comprises one central barrel covering the pseudorapidity range $|\eta| < 1.475$

Granularity $\Delta\eta \times \Delta\phi$ versus $\lvert\eta\rvert$				
Layer	Barrel		End-cap	
Presampler	0.025×0.1	$\lvert\eta\rvert < 1.52$	0.025×0.1	$1.5 < \lvert\eta\rvert < 1.8$
First layer	0.025/8×0.1	$\lvert\eta\rvert < 1.40$	0.050×0.1	$1.375 < \lvert\eta\rvert < 1.425$
	0.025×0.025	$1.40 < \lvert\eta\rvert < 1.475$	0.025×0.1	$1.425 < \lvert\eta\rvert < 1.5$
			0.025/8×0.1	$1.5 < \lvert\eta\rvert < 1.8$
			0.025/6×0.1	$1.8 < \lvert\eta\rvert < 2.0$
			0.025/4×0.1	$2.0 < \lvert\eta\rvert < 2.4$
			0.025×0.1	$2.4 < \lvert\eta\rvert < 2.5$
			0.1×0.1	$2.5 < \lvert\eta\rvert < 3.2$
Second layer	0.025×0.025	$\lvert\eta\rvert < 1.40$	0.050×0.025	$1.375 < \lvert\eta\rvert < 1.425$
	0.075×0.025	$1.40 < \lvert\eta\rvert < 1.475$	0.025×0.025	$1.425 < \lvert\eta\rvert < 2.5$
			0.1×0.1	$2.5 < \lvert\eta\rvert < 3.2$
Third layer	0.025×0.1	$\lvert\eta\rvert < 1.52$	0.025×0.1	$1.5 < \lvert\eta\rvert < 1.8$

Table 2.2: Granularity of the EM LAr calorimeter versus $|\eta|$ [81].

($|\eta| < 1.52$ including the presampler barrel), and two end-caps in $1.375 < |\eta| < 3.2$. The EM calorimeter is a LAr detector with accordion-shaped lead absorbers and copper electrodes. In the region $|\eta| < 1.8$, a presampler detector, consisting of an active LAr layer of 1.1 cm in depth in the barrel region and 0.5 cm in the end-cap regions, is used to correct for the energy lost by electrons and photons deeper in the calorimeter. The EM LAr calorimeter has two to four layers as the presampler and the third layer cover only the pseudorapidity range $|\eta| < 1.8$. Each layer has a different depth and is divided into cells in ϕ-η. The segmentation of each layer is different and may depend on the pseudorapidity. Table 2.2 describes the granularity of the EM LAr calorimeter versus $|\eta|$ for all the four layers. Figure 2.9 shows a wedge of the EM calorimeter near $\eta = 0$, where the four layers can be seen. It is important to note the large differences in depth and segmentation. The total depth of the barrel region at $\eta = 0$ is $24X_0$[11] and can be as deep as $38X_0$ in the end-caps. The second layer plays a very important role in the measurement of electrons and photons, since the electromagnetic cascade fully develops in it.

Electrons and ions from ionization of LAr by charged particles are collected by an applied voltage between the copper plates. This voltage is η-dependent, varying between 1000 V

[11]The radiation length, X_0, is defined as the average distance over which an electron passing through a material has lost all but $1/e$ of its energy solely due to radiation losses.

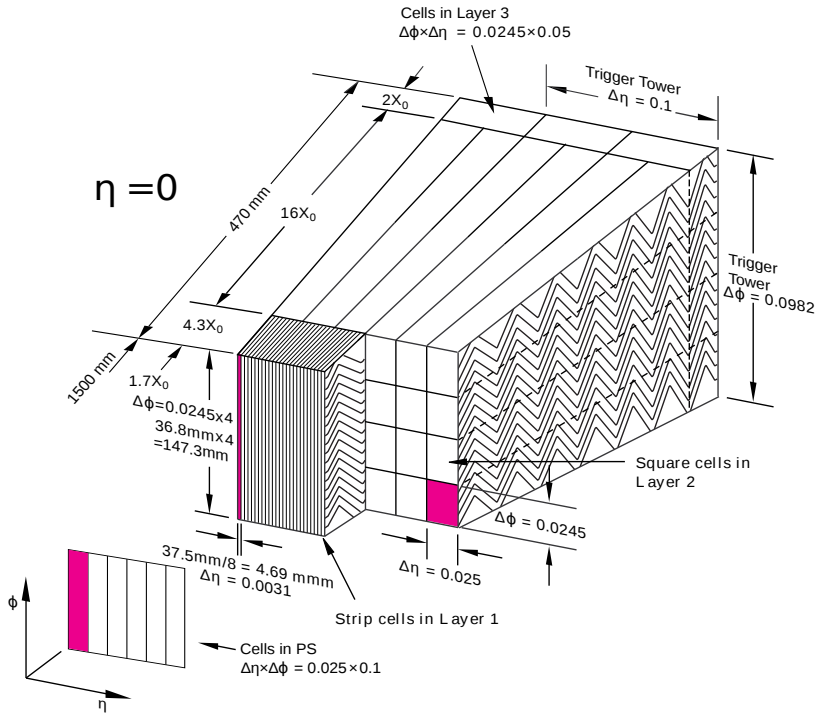

Figure 2.9: Section of the EM LAr calorimeter at $\eta = 0$. The granularity and depth of each layer are indicated [89].

and 2500 V in the end-cap regions and fixed to 2000 V in the barrel region. The copper electrodes are grouped into readout cells. Shaping, digitization and transmission of the calorimeter signals is performed by the front-end electronics. The shaping of the pulses removes the long tail from the detector response time. Sampling of the shaped signal is performed every 25 ns, as can be seen in Fig. 2.10. The long detector response of the EM LAr calorimeter makes it sensitive to contamination from collisions from the adjacent bunch crossings [90].

The hadronic tile calorimeter

In the region $|\eta| < 1.7$, hadronic calorimetry is performed via plastic scintillating tiles as the active medium and steel absorbers [91]. The tile calorimeter comprises one central barrel covering the pseudorapidity region $|\eta| < 1$ and two extended barrels covering $0.8 < |\eta| < 1.7$, all located outside the EM LAr calorimeter. The scintillating tiles are arranged radially

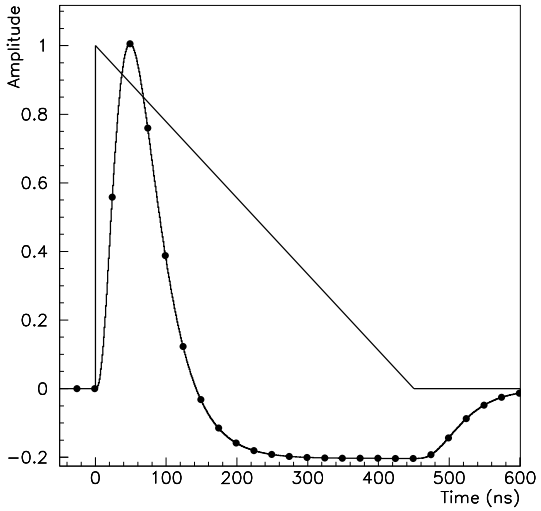

Figure 2.10: Amplitude as a function of time for a triangular pulse in a cell of the EM LAr calorimeter and output of the front-end electronics after shaping. The solid black points represent the sampling points every 25 ns [90].

pointing inwards to the beam axis, as shown in Fig. 2.11. Light produced in the scintillating tiles is collected by wavelength-shifting fibres coupled to either side of the tiles, and read out by two different photomultiplier tubes. This redundancy ensures response uniformity.

2.2.5 The muon spectrometer

Muons are the only charged particles expected to reach the outermost part of the ATLAS detector where the MS is located. In addition to providing charged particle tracking, the MS triggers on events that contain muon-like signals [81]. The MS is immersed in a toroidal magnetic field produced by a central magnet in the pseudorapidity region $|\eta| < 1.4$ and by two end-cap toroid magnets in $1.6 < |\eta| < 2.7$. The MS comprises a number of subsystems that perform the two main tasks. The Monitored Drift Tubes and Cathode Strip Chambers provide precision measurements while the Resistive Plate Chambers and Thin-Gap Chambers are part of the muon trigger system.

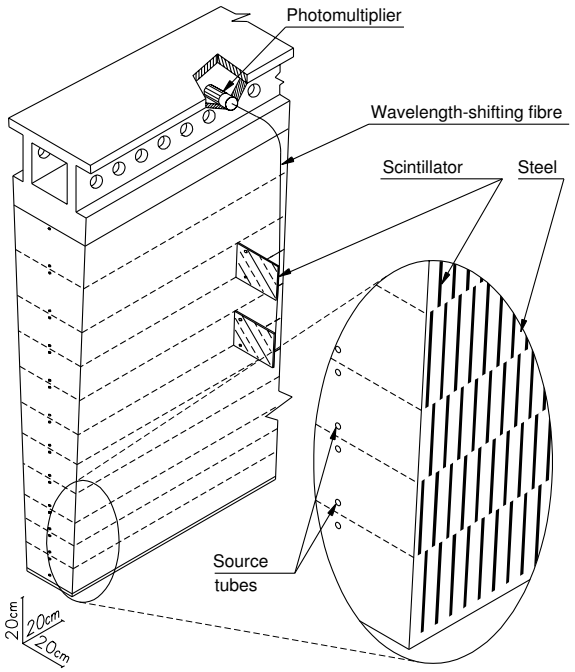

Figure 2.11: View of a tile calorimeter module corresponding to a ϕ wedge, with the steel absorber, scintillating tiles and radioactive source used for calibration [81].

2.2.6 ATLAS trigger system

The ATLAS trigger system is divided into three levels ranging from events selection based on energy depositions in the calorimeters and the MS at the lowest level to event selection using fully reconstructed physics objects at the highest level. Level-1 consists of hardware triggers that select events with signatures from high-p_{T} muons, electrons, photons, jets, τ-leptons decaying hadronically, and transverse missing energy, $E_{\mathrm{T}}^{\mathrm{miss}}$. The Level-1 trigger uses the calorimeters as well as subsystems of the MS such as the Resistive Plate Chambers in the barrel and the Thin-Gap Chambers in the end-cap. The maximum rate that can be handled by the Level-1 trigger is 75 kHz.

At Level-2, partial reconstruction of events selected by the Level-1 trigger is performed based on Regions of Interest (RoI) defined by energy deposition in the calorimeters or hits in the MS that indicate the possible existence of trigger objects in the event. The trigger rate after L2 selection is reduced to below 3.5 kHz.

The final stage in the trigger system, the Event Filter (EF), uses full offline reconstruc-

tion and analysis of the event to select events at a rate of approximately 200 Hz. At this level, the use of the full detector granularity and precision, along with particle identification tools, ensure high trigger selection efficiency.

Regions of interest in the calorimeter

In the ATLAS calorimeter, Level-1 RoIs are defined by transverse energy depositions in a region of size $\Delta\eta \times \Delta\phi = 0.4 \times 0.4$ divided into trigger towers of size $\Delta\eta \times \Delta\phi = 0.1 \times 0.1$. The core of the RoI is defined as the central $\Delta\eta \times \Delta\phi = 0.2 \times 0.2$ region. Each RoI has two energy components, electromagnetic and hadronic, that can be used as discriminants in order to select events with specific topologies. Event selection is performed using flags based on transverse energy thresholds, and multiplicity of trigger objects, among others. For instance, an event can be selected if the total transverse energy in the RoI is above a threshold, while the energy contained in the hadronic calorimeter in the $\Delta\eta \times \Delta\phi = 0.2 \times 0.2$ core and the energy outside the RoI core are below a given threshold [92]. The previous example shows a Level-1 trigger designed for selecting isolated electrons or photons that deposit most of their energy in the EM calorimeter. Figure 2.12 shows the trigger towers along with the core and isolation rings used by electron and photon Level-1 triggers.

2.2.7 Computing infrastructure

The ATLAS experiment demands a large computing infrastructure in order to achieve successful collision data collection and analysis. Collected data must be processed, reconstructed and stored after being selected by the EF. In addition, Monte Carlo simulation of numerous Standard Model processes and new physics signatures must be done to allow for analysis of the collected data.

In order to satisfy these requirements, the ATLAS experiment takes advantage of the World LHC Computing Grid (WLCG) [93]. The WLCG, or simply "the grid," is a multi-tier system in which the data, real and simulated, is distributed to computing centres around the world in order to optimize the available resources.

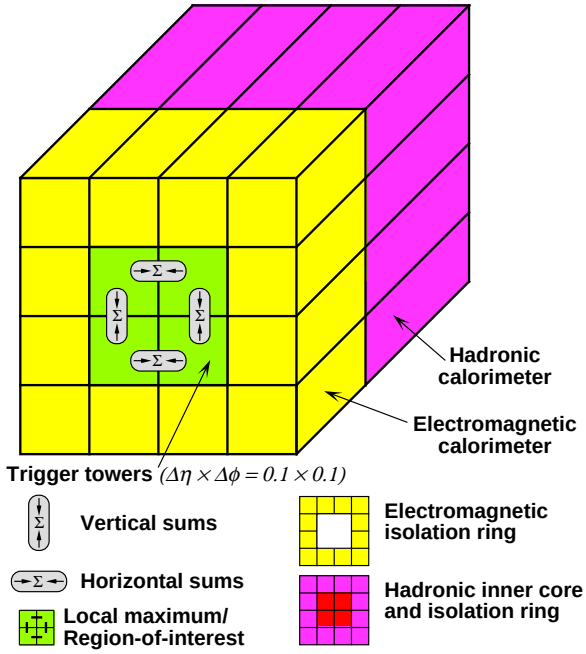

Figure 2.12: Trigger towers and RoI core and isolation rings used by electron and photon Level-1 triggers [81].

The computing grid

Tier-0 is the first layer of the systems in which data collection, reconstruction of raw data, detector calibration and alignment are performed. It consists of about 1000 cores and is based at the CERN analysis facility and Wigner Research Centre for Physics where all the reconstructed data is stored. Tier-1 facilities, of which there are about ten worldwide, including the TRIUMF tier-1 in Canada, reprocess the data with improved calibrations and store a fraction of the reconstructed collision data. Tier-2 sites dedicate most of their resources to generation of simulated Monte Carlo data and user physics analysis. In addition, replicas of derived data formats are stored at tier-2 centres. The last stage in this tiered architecture is tier-3, which is a collection of private computing clusters to which users download further derived data formats to perform physics analysis.

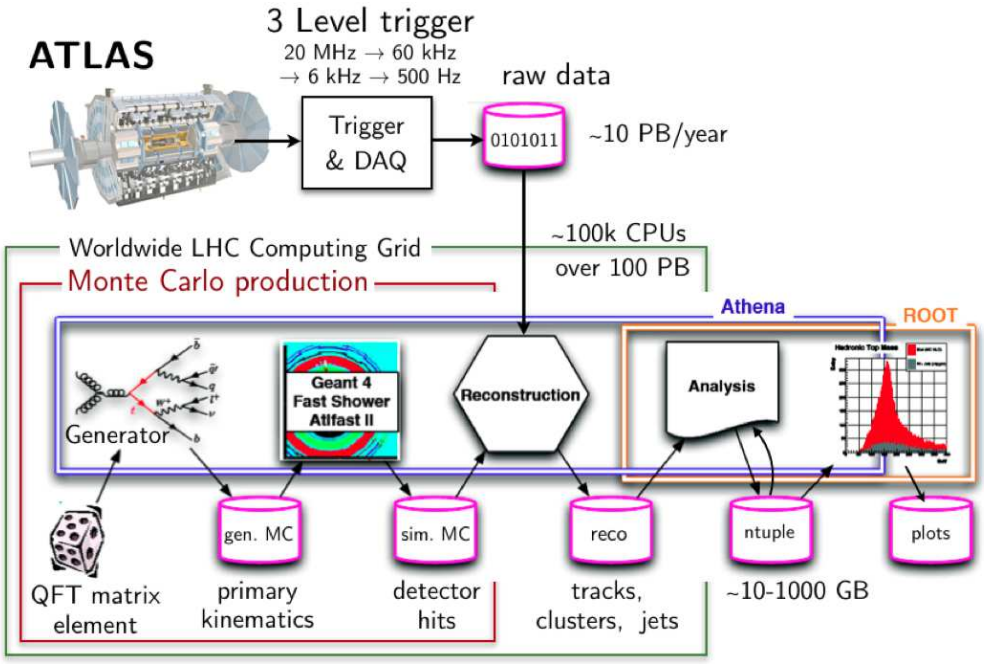

Figure 2.13: Graphical depiction of the ATLAS event data model from generation of simulated events and collection of collision data to physics analysis results [94].

Event data model in ATLAS

Collision data events that are selected by the trigger system are stored in a raw format containing byte streams before reconstruction. The equivalent format for simulated data is known as raw data object (RDO). Reconstruction is performed with the ATLAS software known as Athena, which integrates a number of software tools for data manipulation and analysis. The output of the reconstruction is stored in event summary data (ESD) format. Data files in this format are kept at tier-0 with a fraction of them replicated to tier-1. Data in ESD format are reduced in order to produce more manageable files to be processed with the ROOT analysis framework [95] that is used for user analysis. This final stage can be performed with the Athena software or a combination of the Athena software and ROOT [96]. Figure 2.13 shows the event data model from generation of events and data collection to final physics analysis results.

Chapter 3

Performance of the Transition Radiation Tracker

This chapter presents studies on the performance of the TRT during Run 1 with a detailed comparison of simulation and data from the 2011 and 2012 runs at energies of $\sqrt{s} = 7$ TeV and $\sqrt{s} = 8$ TeV, respectively. Special emphasis is made on studies performed using electrons from J/ψ and Z decays.

3.1 Summary of TRT performance of Run 1

The TRT provides measurements with a nominal spatial resolution of 130 μm. These spatial position measurements, known as TRT hits, are used by the track fitting software to calculate the curvature of the trajectory of charged particles. From this, the transverse momentum can be obtained. TRT hits are obtained by reconstructing drift circles, which represent the radius of closest approach to the anode wire of the charged particle crossing the TRT straw.

The TRT hits are classified in two main categories: LT hits used for tracking and HT hits used for electron ID. Since all TRT pulses that give a signal above the HT level must have passed the low threshold too, all HT hits are also LT hits. In addition to these

categories, LT *hits on track* (hits associated to a fitted track) can be further classified in *precision hits* and *tube hits*. A precision hit is a TRT drift circle that lies within $2\sigma_r$ of a fitted track predicted position, with σ_r the expected position resolution. If a TRT drift circle lies beyond $2\sigma_r$ of the fitted track predicted position, it is declared as a tube hit and the drift radius is set to zero (corresponding to the centre of the straw) and its error set to $4/\sqrt{12}$ mm. A *hole* is declared when there is a missing TRT hit in a straw expected to be crossed by a charged particle, based on the fitted track.

The performance of the TRT can be studied by analyzing parameters such as the position residuals, the straw efficiency and the HT hit probability. The position residual is defined as the difference between the measured drift radius and the distance of closest approach of the fitted track to the central wire. The expected position resolution, σ, is obtained from the standard deviation of a Gaussian fit of the position residual distribution.

Electron ID is an important component of the TRT performance. The probability of a particle producing a HT hit depends on the momentum of the particle and the amount of radiator material traversed. The distribution of the radiator material varies along the detector, with the end-cap type-B wheels having the largest amount of radiator material. The material distribution in the ID is shown in Fig. 3.1.

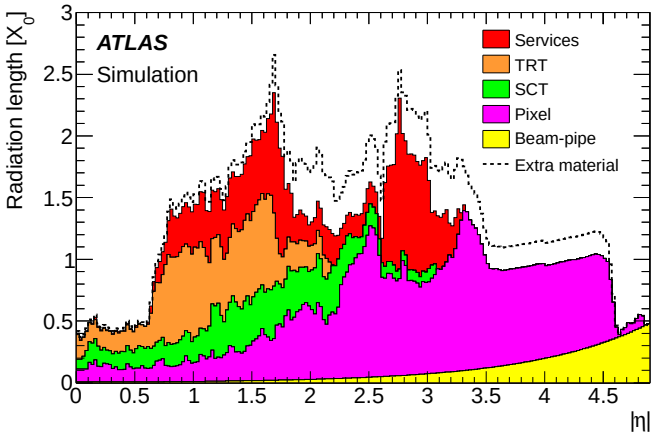

Figure 3.1: Material distribution in radiation lengths X_0 in the ID as a function of the absolute pseudorapidity $|\eta|$ averaged over ϕ [97].

3.1.1 Dataset

The TRT performance studies used two datasets: one from the 2011 *pp* run with low instantaneous luminosity and another from the 2012 *pp* run with a higher instantaneous luminosity. Period D from 2011 comprises data collected during the last two weeks of April 2011 with maximum average number of interactions per bunch crossing of about $\langle\mu\rangle$=7. This dataset was selected in order to minimize contamination from additional collisions in the same bunch crossing. Period B from 2012 comprises data from the the first month of data taking with maximum average number of interactions per bunch crossing of about $\langle\mu\rangle$=25 as can be seen in Fig. 3.2. This dataset allows the study of the TRT performance for cases with increased number of collisions in the same bunch crossing occur. The performance studies used samples of muons and electrons to cover the cases of minimum ionizing particles and particles that produce transition radiation. I performed the studies using electrons and contributed to the studies using muons. Therefore, emphasis is made on the description of the studies involving electrons.

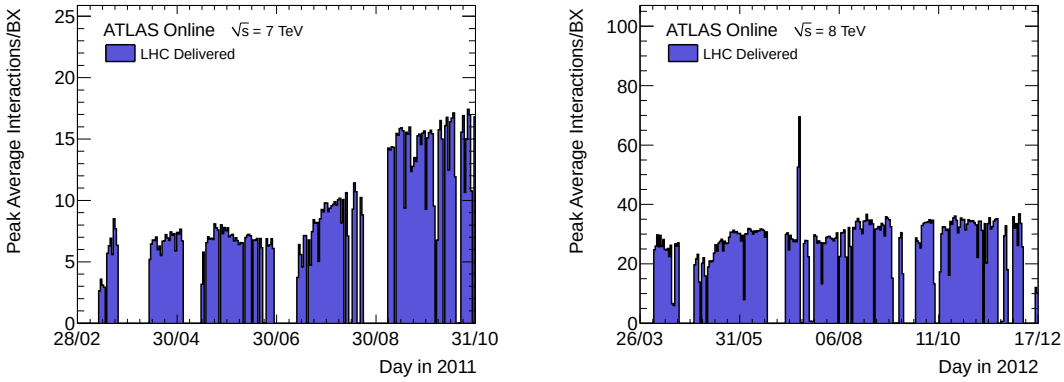

Figure 3.2: Peak average number of interactions per bunch crossing per day during the 2011 (left) and 2012 (right) *pp* run at $\sqrt{s}$ =7 TeV and $\sqrt{s}$ =8 TeV, respectively. Period D of 2011 corresponds to collision data collected from April 14, 2011 to April 28, 2011, and period B of 2012 corresponds to collision data collected in early 2012.

3.1.2 Monte Carlo samples for performance studies

In order to study the performance of the TRT, electron–positron pairs and $\mu^+\mu^-$ pairs from Z boson and J/ψ decays are used. A simulated sample of electron–positron pairs from Z boson decays, produced at $\sqrt{s}$ =7 TeV and $\sqrt{s}$ =8 TeV with the ALPGEN [98] generator interfaced with PYTHIA [99] for hadronization and parton shower generation, is used. Events in this sample have a minimum electron transverse momentum $p_{\mathrm{T}} > 20$ GeV. In order to study low p_{T} electrons, an additional sample with electron–positron pairs from J/ψ meson decays was used. The J/ψ mesons in this sample were produced at $\sqrt{s} = 7$ TeV and $\sqrt{s} = 8$ TeV with the PYTHIA [99] generator.

Simulated MC samples have been processed with the ATLAS simulation software up to the GEANT4 simulation stage, i.e., simulated energy deposits in the detector still have to be converted into digital signals and then reconstructed into physics analysis objects.

3.1.3 Straw efficiency

The straw efficiency measures the probability of a LT hit from a charged particle passing through a straw. This efficiency depends on the distance of closest approach of the charged particle to the anode wire. The straw efficiency is given by

$$\epsilon_{\mathrm{straw}} = \frac{n_{\mathrm{hits}}}{n_{\mathrm{hits}} + n_{\mathrm{holes}}}, \tag{3.1}$$

where n_{hits} is the number of hits on track and n_{holes} is the number of holes on the same track. This efficiency is calculated as a function of the fitted track-to-wire distance. In order to study the TRT straw efficiency, muons from Z boson and J/ψ meson decays were used. Muons from collision data were selected from two different datasets including low-luminosity data from the 2011 run from collisions at $\sqrt{s} = 7$ TeV and high-luminosity data from the 2012 run at $\sqrt{s} = 8$ TeV. These two datasets allow for studies of the straw efficiency in low and high pileup conditions. Simulated muons were obtained from samples of Z decays generated with SHERPA and J/ψ decays generated with PYTHIA [99] and centre-of-mass energies of $\sqrt{s} = 7$ TeV and $\sqrt{s} = 8$ TeV. Figure 3.3 shows the straw efficiency as a function of the track-to-wire distance for hits on track in the TRT barrel (left) and

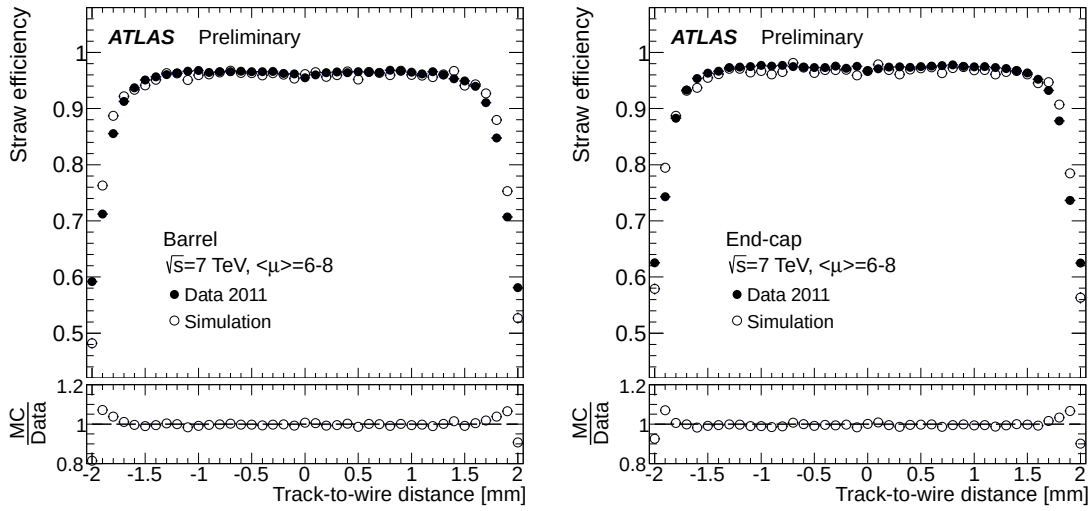

Figure 3.3: Straw efficiency as a function of the track-to-wire distance for TRT hits on track in the TRT barrel (left) and end-cap (right) regions using simulated and collision data with low pileup, $6 < \langle\mu\rangle < 8$, at a centre-of-mass energy of $\sqrt{s} = 7$ TeV [100].

end-cap (right) regions using simulated and collision data with low pileup, $6 < \langle\mu\rangle < 8$, at a centre-of-mass energy of $\sqrt{s}$ =7 TeV. The straw efficiency is uniform and greater than 95% for track-to-wire distances up to ± 1.5 mm, after which the straw efficiency drops due to straw-edge effects where the ionization path is shorter.

The straw efficiency can also be studied as a function of the fitted track pseudorapidity η. For this purpose, the straw efficiency as a function of the track-to-wire distance is sliced in pseudorapidity bins and the straw efficiency averaged over all the track-to-wire distance values in the range $(-2, 2)$. Figure 3.4 shows the straw efficiency as a function of the fitted track pseudorapidity η for muons in low (left) and high (right) pileup conditions from collisions at $\sqrt{s} = 7$ TeV and $\sqrt{s} = 8$ TeV, respectively. A slight decrease in straw efficiency is observed at the TRT barrel–end-cap transition region $0.77 < |\eta| < 1.06$ where the straws are arranged in two different ways and at the edges of the TRT acceptance $|\eta| \sim 2$. Nevertheless, TRT straw efficiency is high across all η ranges, and very important, the straw efficiency remains high in high-luminosity conditions with pileup in the range $25 < \langle\mu\rangle < 30$.

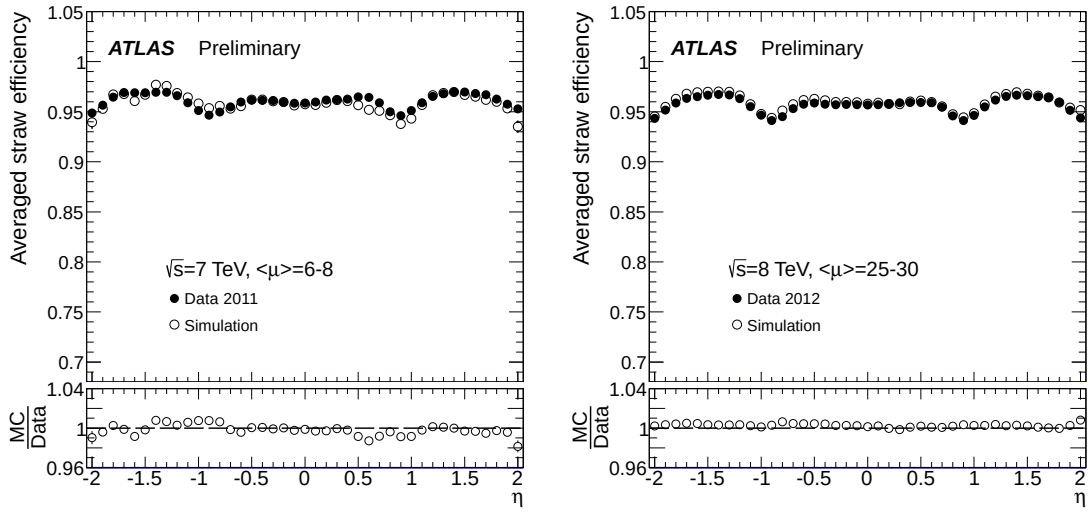

Figure 3.4: Average straw efficiency as a function of the reconstructed muon track pseudorapidity η for muons in low (left) and high (right) pileup conditions from collisions at $\sqrt{s} = 7$ TeV and $\sqrt{s} = 8$ TeV, respectively [100].

3.1.4 High-threshold hit probability

The fraction of HT hits on track is a powerful discriminator for electron identification. A typical HT hit produced by an electron has energy contributions from ionization of the TRT active gas and absorption of transition radiation photons in the X-ray range, the latter being the dominant contribution while only about 25% of the total comes from ionization produced by the electron. This yields an energy deposition above the ≈ 6 keV high threshold. On the other hand, a minimum ionizing particle would only lose energy through ionization, depositing about 2.5 keV in a straw.

The intensity of the transition radiation produced by a particle crossing the interface between two media is given by [101]

$$S = \frac{\alpha\hbar}{3}\frac{(\omega_1 - \omega_2)^2}{\omega_1 + \omega_2}\gamma, \tag{3.2}$$

where α is the fine structure constant, ω_1 and ω_2 are the plasma frequencies of the two media, and $\gamma = E/m$ the relativistic factor in natural units. The amount of transition radiation produced per interface transition is in general low ($S \approx 10^{-2}\gamma$ eV), therefore the use of multiple interfaces increases the amount of radiation significantly. This is the case

of the TRT, which uses a material made of polypropylene fibres. The opening angle with respect to the particle trajectory at which the radiation is emitted is in general small and goes as $\theta \approx 1/\gamma$. Thus, the radiation produced by a charged particle is expected to interact with the same straws as the charged particle. For ultrarelativistic particles the energy is mostly emitted in the X-ray region [101].

High-threshold hit probability for minimum ionizing particles

In order to study the probability for minimum ionizing particles to produce TRT HT hits, muons from J/ψ and Z decays are used in order to cover a wide kinematic regime 5 GeV $< p <$ 60 GeV. Muon pairs were required to have an angular separation of $\Delta R = \sqrt{(\Delta\phi)^2 + (\Delta\eta)^2} > 0.3$, and transverse momentum $p_{\mathrm{T}} > 5$ GeV. Muons from J/ψ decays are selected with a trigger requiring two muons with transverse momentum $p_{\mathrm{T}} > 4$ GeV and restricted to the invariant mass range 3.0 GeV $< m_{\mu^+\mu^-} <$ 3.2 GeV. Muon pairs from Z decays are selected using a single muon trigger with a transverse momentum requirement of $p_{\mathrm{T}} > 18$ GeV and restricted to the reconstructed invariant mass range 75 GeV $< m_{\mu^+\mu^-} <$ 105 GeV. Muons with momentum $p \approx 60$ GeV are below the threshold needed for producing transition radiation (~ 60 GeV corresponding to a Lorentz γ-factor of $\sim$600). Since muons in the selected momentum range do not produce significant transition radiation, their HT hit probability should be independent of the amount of radiator material and its distribution in the detector. Figure 3.5 shows the HT probability for muons as a function of the muon track pseudorapidity η for muons from J/ψ decays with momentum 5 GeV $< p <$ 20 GeV (left) and muons from Z decays with momentum $p <$ 60 GeV (right). The HT hit probability for minimum ionizing particles is below 10% and fairly independent of the particle γ-factor in the range $\gamma < 600$. An increase in the HT hit probability is observed in the TRT barrel–end-cap transition region $0.77 < |\eta| < 1.06$ where the straws are arranged in two different ways.

The geometry of the TRT is such that the TRT barrel comprises 73 radial layers, with layer one being the innermost. Layers 1-9 are the inner short straws [85]. In the TRT end-caps, there are 160 straw disks or layers, with Layer 1 being the nearest to the interaction

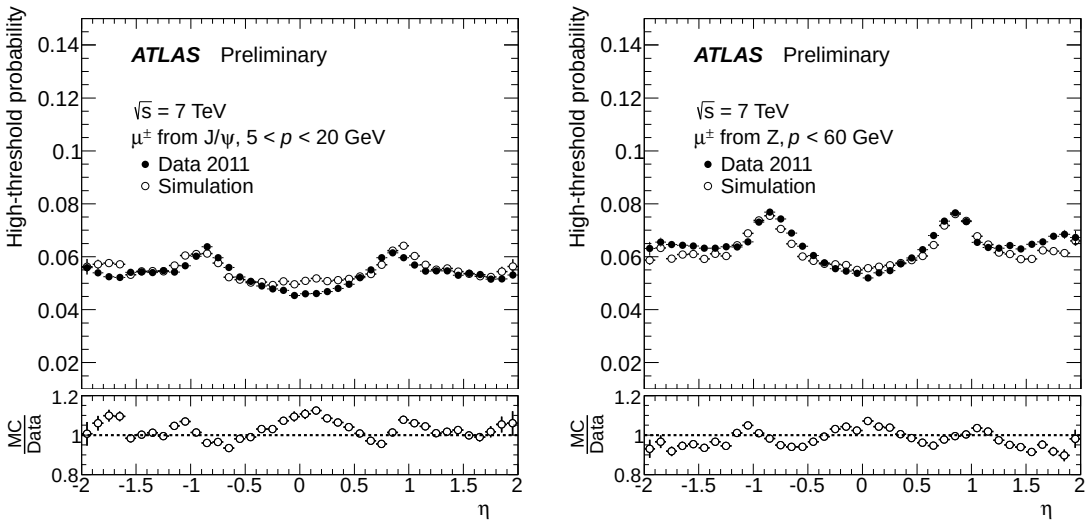

Figure 3.5: High-threshold hit probability for muons as a function of the muon track pseudorapidity η for muons from J/ψ decays with momentum 5 GeV $< p <$ 20 GeV (left) and muons from Z decays with momentum $p <$ 60 GeV (right) produced in low luminosity collisions with $3 < \langle\mu\rangle < 9$ at $\sqrt{s} = 7$ TeV [100].

point. Minimum ionizing particles such as muons with γ-factor $\gamma < 600$ should not produce significant transition radiation. Therefore, the HT hit probability should be independent of the amount of radiator material in the detector. Figure 3.6 shows the HT hit probability as a function of the straw layer in the TRT barrel (left) and end-cap (right) for muons from Z decays with momentum $p <$ 60 GeV produced in low luminosity collisions with $3 < \langle\mu\rangle < 9$ at $\sqrt{s} = 7$ TeV.

3.1.5 High-threshold hit probability for electrons

Electrons passing through the TRT with a momentum above ~ 0.5 GeV (γ-factor ~ 1000) produce transition radiation when they cross the gas–radiator material interface. This transition radiation, in the X-ray range, is then absorbed by the Xe-based gas mixture. Transition radiation photons of up to 30 keV are the dominant contribution to the energy deposited in the TRT straws by electrons. A large fraction of HT hits on track is then a signature of electrons in the TRT and plays an important role in the particle identification in the ATLAS detector. In order to study the probability for electrons to produce a TRT

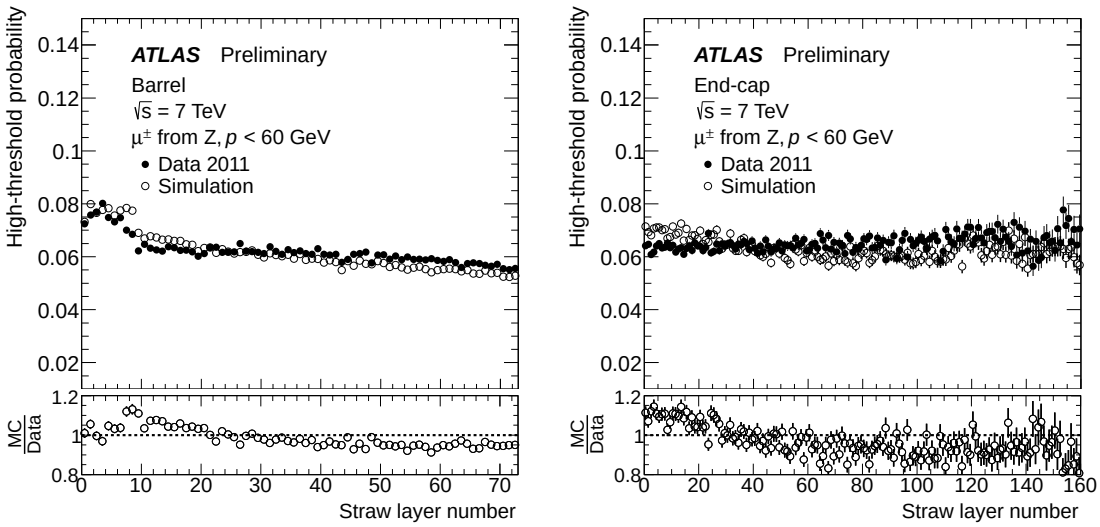

Figure 3.6: High-threshold hit probability for muons as a function of the straw layer in the TRT barrel (left) and end-cap (right) for muons from Z decays with momentum $p < 60$ GeV produced in low luminosity collisions with $3 < \langle\mu\rangle < 9$ at $\sqrt{s} = 7$ TeV [100].

HT hit on track, electrons from J/ψ and Z decays produced in low luminosity conditions at $\sqrt{s} = 7$ TeV are selected, covering a large momentum range from $p = 5$ GeV up to approximately 200 GeV. Two different selection criteria have been used to filter only events that correspond to electrons from Z and J/ψ decays.

Electrons from J/ψ decays

In order to select events with low momentum electrons, at least one of the following triggers is required to be passed:

- `EF_e9_tight_e5_tight_Jpsi`,
- `EF_2e5_tight_Jpsi`,
- `EF_e5_tight_e4_etcut_Jpsi_TRT`,
- `EF_e5_tight_e4_etcut_Jpsi_SiTrk`,
- `EF_e5_tight_e9_etcut_Jpsi`,
- `EF_e5_tight_e4_etcut_Jpsi`.

These triggers are specific for selecting electrons from J/ψ decays. In addition to the trigger requirement, the electrons must be labelled as `Medium++` and have a minimum

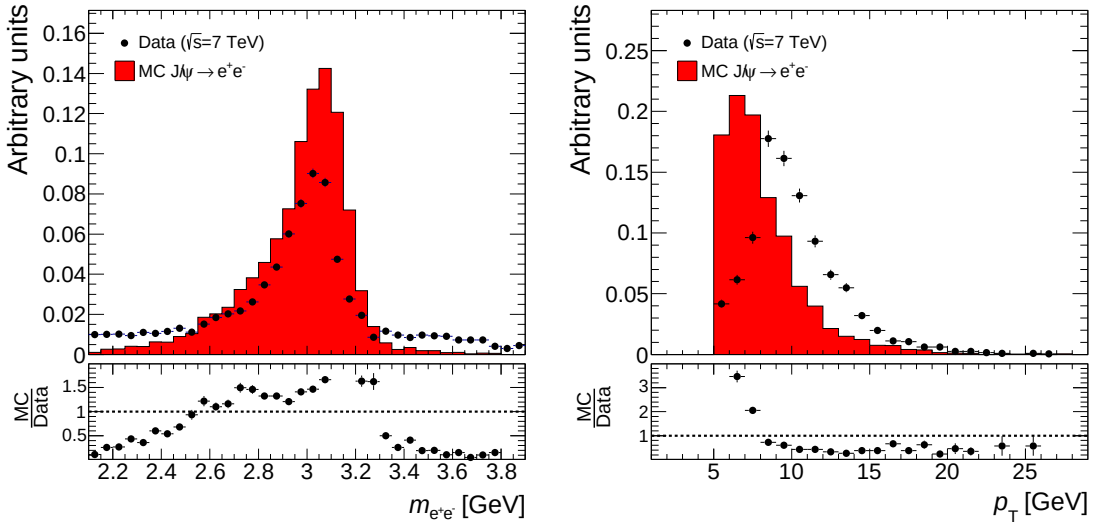

Figure 3.7: Reconstructed invariant mass $m_{e^+e^-}$ (left) and transverse momentum p_{T} (right) of electrons from J/ψ decays in collision data and MC. Only events within the mass window 2.9 GeV $< m_{ee} <$ 3.2 GeV are used for this study.

transverse momentum of $p_{\mathrm{T}} > 5$ GeV. The label `Medium++` represents a series of selection criteria that ensure high electron selection efficiency while rejecting background from jets that fake electrons and electron–positron pairs from photon conversions. Among the `Medium++` selection criteria there are calorimeter-based discriminants such as the ratio of the transverse energy deposited in the hadronic calorimeter to the transverse energy deposited in the electromagnetic calorimeter, limiting the amount of hadronic leakage allowed, measurements of the lateral particle shower shape, and energy deposition dispersion in the first layer of the electromagnetic calorimeter. In addition, there are some tracking requirements: there must be at least one hit in the Pixel detector and at least one hit in the STC. The transverse impact parameter, i.e., the radial distance from the beam line, must be less than 1 mm. The absence of TRT requirements on the track quality of the electron ensure that these studies are not biased by the electron identification selection criteria [102].

Electrons with $p_{\mathrm{T}} > 5$ GeV identified as `Medium++` must have a b-layer hit (a hit in the innermost layer of the Pixel detector) and be within the TRT pseudorapidity acceptance $|\eta| < 2.0$. The final selection criteria are related to the electron–positron pair reconstructed invariant mass $m_{e^+e^-}$ and their separation $\Delta R = \sqrt{(\Delta\phi)^2 + (\Delta\eta)^2}$. Only events with a

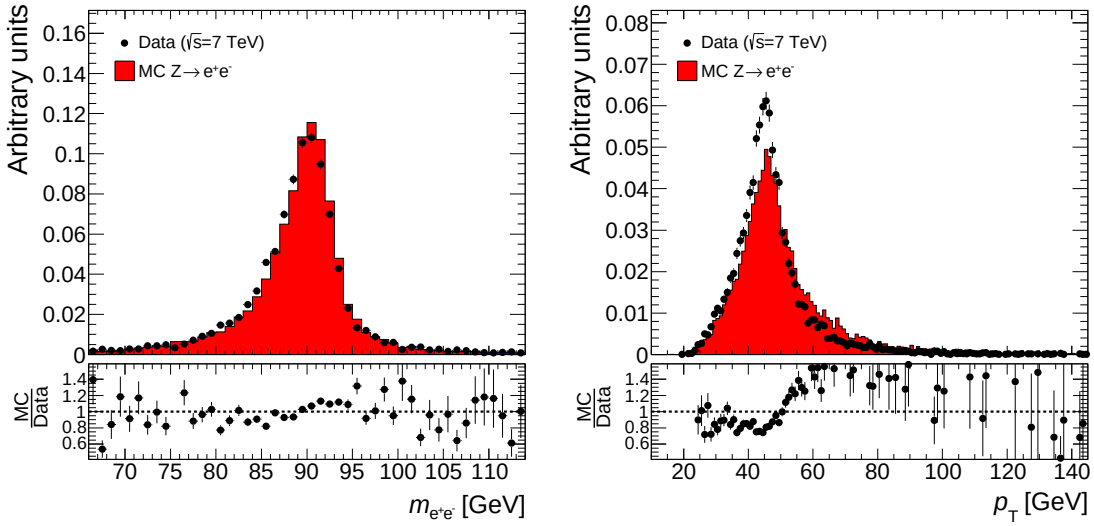

Figure 3.8: Reconstructed invariant mass $m_{e^+e^-}$ (left) and transverse momentum p_{T} (right) of electrons from Z decays. Only events within the mass window 75 GeV $< m_{e^+e^-} <$ 105 GeV are used for this study.

reconstructed invariant mass in the window 2.9 GeV $< m_{ee} <$ 3.2 GeV are selected in order to find agreement with the measured J/ψ mass of 3096.916 $\pm$ 0.011 MeV [61]. Finally, the electron–positron pair must have a separation $\Delta R > 0.2$. Both electrons from J/ψ decays are used for the study of the TRT performance. Figure 3.7 shows the reconstructed invariant mass $m_{e^+e^-}$ and transverse momentum p_{T} of the electrons from J/ψ decays. The performance of the TRT and the accuracy of its simulation are studied using known particles in specific momentum ranges. Therefore, it is not necessary to find perfect agreement between collision data and MC—it is sufficient to select electrons in the same momentum range.

Electrons from Z boson decays

In order to study electrons of higher momentum, electron–positron pairs from Z decays are selected using the tag-and-probe method in which one electron (the tag) is identified using very high quality requirements while the other (the probe) uses looser quality requirements. Only the probe electrons are used for the study of the performance of the TRT. Only events that passed the `EF_e20_medium` or the `EF_e22_medium` triggers are kept. These triggers

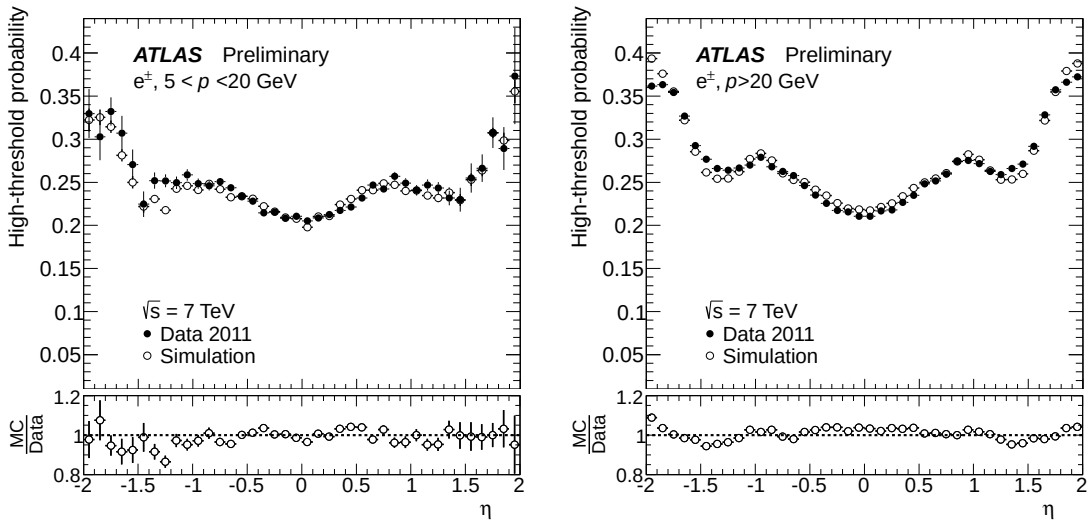

Figure 3.9: High-threshold hit probability for electrons as a function of track pseudorapidity η for electron pairs from J/ψ and Z decays with momentum 5 GeV $< p <$ 20 GeV (left) and $p >$ 20 GeV (right) produced in low luminosity collisions with $3 < \langle\mu\rangle < 9$ at $\sqrt{s} = 7$ TeV [100].

require an energy deposition in the calorimeter of at least 20 GeV or 22 GeV and an ID track geometrically matched to the energy deposition in the calorimeter.

The tag electron must have a transverse momentum $p_{\mathrm{T}} > 22$ GeV, be identified as a `Tight++` electron [102], and be geometrically matched to the object that passed the trigger. Electrons identified as `Tight++` must fulfill all the requirements of a `Medium++` electron [102] and some additional criteria. The energy contained in the calorimeter in a cone of radius $\Delta R = 0.2$ around the direction of the electron, subtracting the electron energy, must be less than 6 GeV. There must be an ID track geometrically matched to the electron calorimeter cluster. The sum of the transverse momentum of all tracks in a cone of radius $\Delta R = 0.4$ around the electron ID track, excluding the electron track, must be less than 6% of the electron transverse energy. Additional criteria requires at least 14 TRT hits on track and a fraction of more than 30 % TRT HT hits on track.

The probe electron must have a transverse momentum $p_{\mathrm{T}} > 15$ GeV and be identified as `Loose++` [102]. This identification requirement corresponds to calorimeter only discriminants ensuring that no bias on the TRT track quality is present on the probe electron.

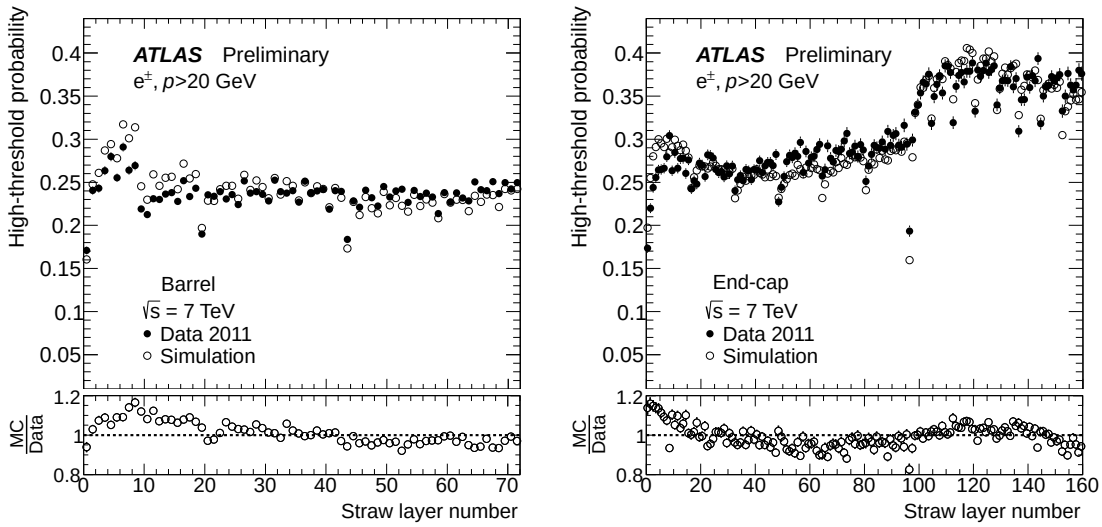

Figure 3.10: High-threshold hit probability for electrons as a function of the straw layer in the TRT barrel (left) and end-cap (right) for electron pairs from J/ψ and Z decays with momentum $p > 20$ GeV produced in low luminosity collisions with $3 < \langle\mu\rangle < 9$ at $\sqrt{s} = 7$ TeV [100].

Electron–positron pairs must have opposite charge, have a separation $\Delta R > 0.3$ and the reconstructed invariant mass should be in within 75 GeV $< m_{e^+e^-} <$ 105 GeV, which contains the measured value of $m(Z) = 91.1876 \pm 0.0021$ GeV [61]. Figure 3.8 shows the reconstructed invariant mass $m_{e^+e^-}$ and transverse momentum p_{T} of the electrons from Z decays.

Figure 3.9 shows the probability to produce a TRT HT hit on track for electrons from J/ψ decays (left) with momentum 5 GeV $< p <$ 20 GeV and electrons from Z decays (right) with momentum $p > 20$ GeV in low-luminosity conditions with $3 < \langle\mu\rangle < 9$ at $\sqrt{s} = 7$ TeV. The HT hit probability is about 21% in the central region and increases to about 35% at high $|\eta|$. The significant variations in TRT HT hit probability account for the varying amount of radiator material an electron traverses as a function of its pseudorapidity. Figure 3.10 shows the TRT HT hit probability for electrons from J/ψ and Z decays with momentum $p > 20$ GeV produced in low-luminosity conditions with $3 < \langle\mu\rangle < 9$ at $\sqrt{s} = 7$ TeV as a function of the straw layer in the TRT barrel (left) and end-cap (right). The TRT end-caps comprise type A wheels that cover the straw layer numbers 1 to 96

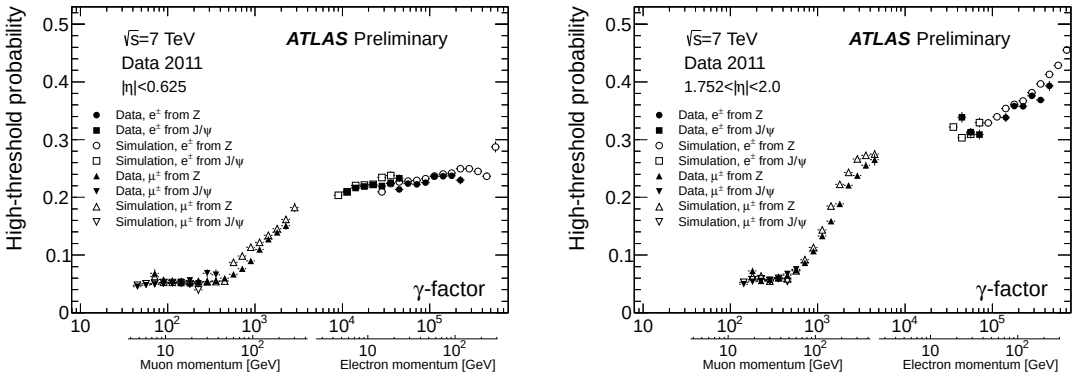

Figure 3.11: High-threshold hit probability for electrons and muons from J/ψ and Z decays as a function of the relativistic γ factor for tracks with $|\eta| < 0.625$ (left) corresponding to the TRT barrel region and $1.752|\eta| < 2.0$ (right) corresponding to the end-cap wheels type B. Data (solid symbols) and simulation (open symbols) are shown for low luminosity running during 2011 [100].

and type B wheels that span from straw layer number 97 to 160. An increased amount of radiator material is found in between layers of type B wheels, with respect to type A wheels, due to the greater spacing between straw layers. The extra radiator material is reflected as an increase in the TRT HT hit probability for electrons in end-cap straw layer numbers 97 and beyond.

High-threshold hit probability as a function of γ-factor

The intensity of the emission of transition radiation by electrically charged particles is proportional to the relativistic γ factor, as seen in Eq. (3.2). Figure 3.11 shows the HT hit probability for electrons and muons from J/ψ and Z decays, covering a range of γ values from approximately 50 to 5×10^5. It is clear that the HT hit probability increases with γ and has a turn-on point at around $\gamma = 600$. At very high γ values the production of transition radiation reaches a maximum [101], causing the HT hit probability to stabilize, as can be seen in the central pseudorapidity region. In the high-pseudorapidity region, although the production of transition radiation reaches a maximum at high γ, the greater amount of radiator material available causes the HT hit probability to continue rising. In addition, Figs. 3.9 and 3.10 show that the amount of radiator material has a significant

impact in the amount of radiation emitted. This is confirmed in Fig. 3.11 where the HT hit probabilities are higher at higher absolute pseudorapidity values.

Chapter 4

Simulation of monopole interactions with the ATLAS detector

This chapter describes expected signatures of magnetic monopoles in ATLAS, the generation of simulated signal monopole events, the simulation of monopole interactions with the detector, and the reconstruction of physics objects used in this search. In addition, Standard Model processes that may mimic monopole signatures (i.e, background) are discussed.

4.1 Expected signatures of monopoles in ATLAS

Monopole interactions with matter differ from those of particles such as photons, electrons, muons and hadrons with unit electric charge commonly used in measurements and searches at particle colliders. The main differences, as described in Sec. 1.4, are the high ionization produced by monopoles due to the high equivalent electric charge, the absence of an inverse squared β dependence in the energy losses by ionization (Eq. (1.18)), and the dominance of ionization over pair production and bremsstrahlung as energy loss mechanisms. These

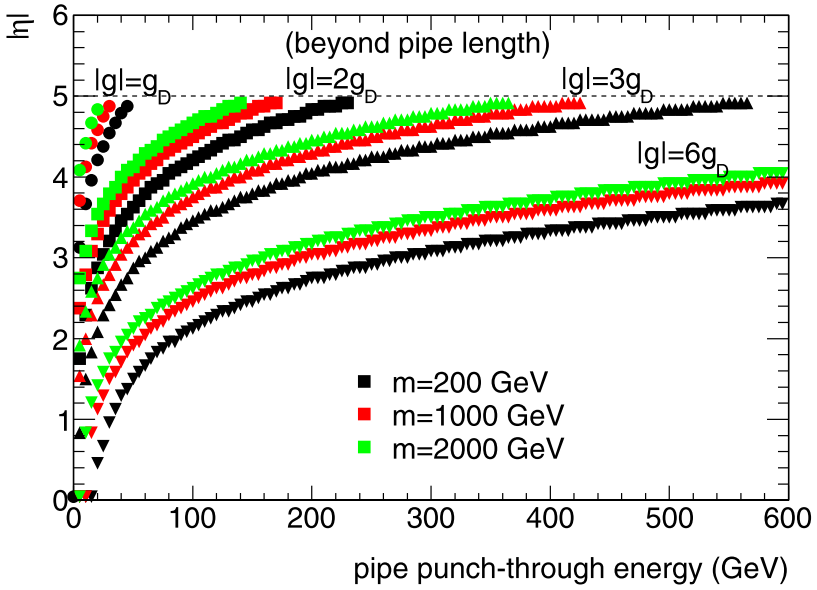

Figure 4.1: Kinetic energy below which monopoles become trapped in the ATLAS beampipe as a function of absolute pseudorapidity, $|\eta|$, for various charges and masses [31].

determine the particular signature of monopoles in the ATLAS detector and become very relevant in two subdetectors: the TRT and the LAr EM calorimeter.

4.1.1 High ionization in the Inner Detector

The beryllium beampipe surrounding the interaction point is the first piece of material that monopoles must traverse before entering the ID. The density of solid-state beryllium is three orders of magnitude higher than that of gaseous Xenon, the base gas of the TRT, and comparable with that of LAr, the active material of the EM calorimeter. Therefore, the energy losses are significant, causing monopoles with low kinetic energy to stop and become trapped in the material. The kinetic energy below which a monopole would become trapped in the ATLAS beampipe for monopoles of various charges as a function of absolute pseudorapidity can be found in Fig. 4.1. In summary, monopoles of charge $2g_{\mathrm{D}}$ (the highest charge considered herein) need about 10 GeV of kinetic energy to punch through the ATLAS beampipe when produced within $|\eta| \leq 2$, the limit of acceptance of the TRT.

In all three subsystems, the Pixel, the SCT and the TRT, the amount of charge collected by the readout electronics is proportional to the ionization produced in the active materials.

This is fundamental to understand the response of the ATLAS detector to monopoles.

Monopoles in the Pixel detector

The performance of silicon detectors is affected by the passage of highly ionizing particles. The high-density cloud of electron–hole pairs created by the particle creates a space charge effect that nullifies the external electric field. As a consequence, the collection of the charge from ionization occurs after a time delay. In addition, due to the high ionization density, recombination effects cause the collected charge to be less than the total created [103].

The Pixel detector, however, fails to detect monopoles for a different reason. The charge signal collected by the detector elements is compared against a threshold and the time-over-threshold is measured with an accuracy of eight bits. The threshold has been calibrated so that a minimum ionizing particle will produce a time-over-threshold count of 30. When the time-over-threshold count exceeds the overflow at 255, the data from the sensor is lost. Thus, due to the very large ionization exceeding the overflow, the signal of monopoles is lost [83].

Monopoles in the SCT

The SCT readout electronics, unlike the pixel detector, do not overflow for large energy depositions. Thus, a measurable signal is produced by monopoles passing through the SCT strips. Due to the high ionization density produced by monopoles along with energetic δ-electrons, regions in the SCT with a high density of hits may be found. These hits can be used to reconstruct electrically charged particle-like tracks along the trajectory of the monopole. Figure 4.2 shows an event display of a simulated monopole event of charge $|g| = 2g_{\mathrm{D}}$ in the ATLAS detector. The ID is the central dark grey area. There is a region of high density of tracks in the ID pointing almost vertically, aligned with a region in the TRT with a large number of HT hits (red dots) and an energy deposition in the EM calorimeter (green). Note that these ID tracks are reconstructed from SCT hits only and do not have a TRT extension. This effect is explained in Sec. 5.2.1.

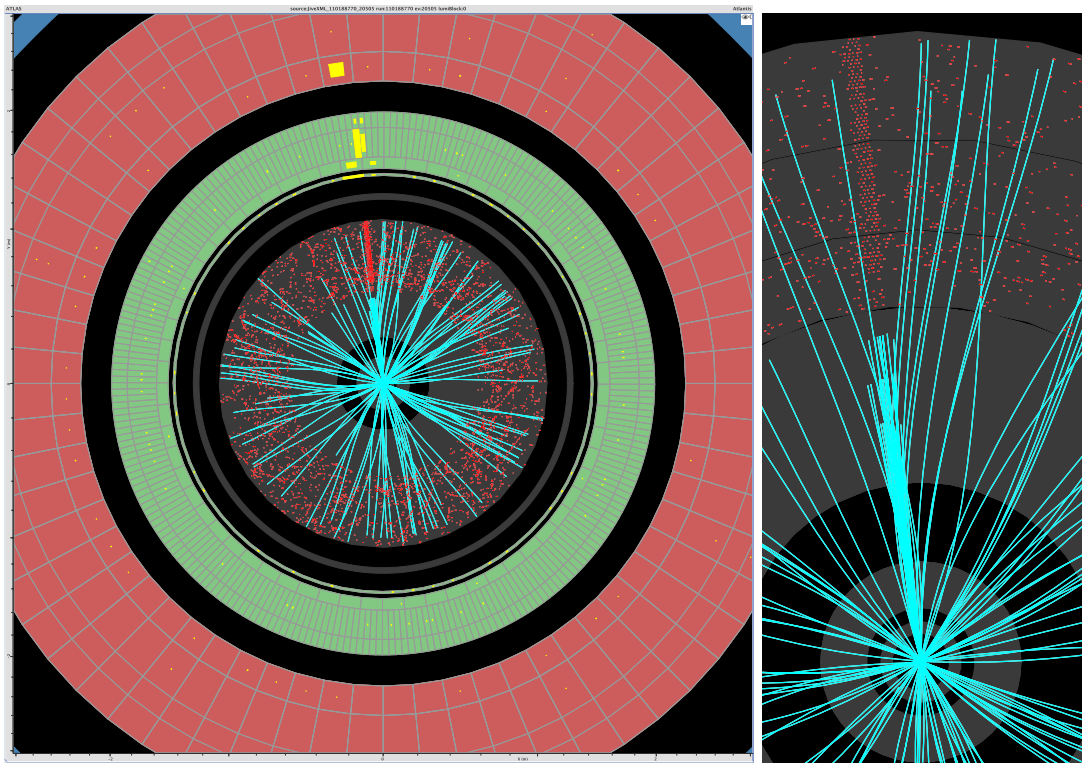

Figure 4.2: Event display of a monopole of charge $|g| = 2g_{\mathrm{D}}$ in the ATLAS detector. Note the large density of tracks in the ID (dark grey central area) with no TRT extension. The TRT HT hits are represented as red dots. The EM and hadronic calorimeters are green and red, respectively.

Monopoles in the TRT

Magnetic monopoles ionize the Xe-based gas mixture in the TRT straws with an energy deposition usually three to four orders of magnitude higher than that of a minimum ionizing particle; this is enough to exceed the 6 keV high threshold. Unlike the pixel detector, the TRT front-end electronics produce a measurable signal regardless of the magnitude of the energy deposition. Thus, monopoles create TRT HT hits in the straws traversed.

As described in Sec. 1.5.1, close collisions between monopoles and atoms from the absorbing material give rise to high-energy δ-rays. In the mass and energy ranges considered in this search, δ-rays can be produced with energies ranging from 0.1 MeV to over 100 MeV. For example, a monopole of mass 500 GeV with kinetic energy of 300 GeV would produce δ-rays with a maximum kinetic energy of approximately 2 MeV. Although, electrons with

momentum less than 1 GeV are very unlikely to produce transition radiation, they may continue to propagate and ionize the gas mixture in the TRT straws. In the presence of the 2 T solenoidal magnetic field, the trajectory of a δ-ray bends with a radius of curvature of the order of millimetres. For instance, a δ-ray with kinetic energy of 2 MeV would have a radius of curvature of 4 mm. The maximum propagation range from the monopole trajectory for such an electron would be twice the radius of curvature, i.e., 8 mm. A single δ-ray with a kinetic energy of a few MeV would only deposit about 2 keV in a straw – not enough to exceed the high threshold–as it loses its energy mainly through ionization [61, Chapter 32]. It is the energy deposition by several δ-rays in the same straw that exceeds the high threshold.

The signature of monopoles in the TRT is, thus, a swath of TRT HT hits of width approximately ± 4 mm along the monopole trajectory. This can be seen in Fig. 4.2 for a simulated monopole event of charge $|g| = 2.0 g_{\mathrm{D}}$. Unlike minimum ionizing particles with a HT hit probability of about 10% and electrons with a HT hit probability between 30% and 40% [100], monopoles produce on average more than 70% HT hits in a region of width ± 4 mm along their trajectory.

4.1.2 Energy deposition in the calorimeter

Prior to entering the EM calorimeter monopoles have to pass through the inner wall of the cryostat enclosing the solenoid magnet and the EM calorimeter. The solenoid magnet, which is present only in the barrel region, accounts for approximately 0.66 radiation lengths at normal incidence, or about a third of the material in front of the EM calorimeter [81].

Shape of energy deposition

As described in Sec. 2.2.4, the EM calorimeter comprises a thin presampler and three main layers. The presampler, first and third layer are thin in comparison with the second layer, which is 16 radiation lengths in depth.

Ionization is the dominant mechanism by which monopoles lose their kinetic energy as explained in Sec 1.4. Since the bremsstrahlung and pair-production phenomena are highly

suppressed, there is no formation of electromagnetic cascades in the LAr EM calorimeter, rather, just a narrow cluster of energy deposition. Minimum ionizing particles, such as muons and pions, also traverse the EM calorimeter without radiating, depositing some of their kinetic energy in a narrow cluster. However, unlike monopoles, the energy deposition of minimum ionizing particles is uniform along their trajectory and is about 3 GeV in total.

Monopoles ionize the LAr, depositing most of their energy in the innermost layers where they travel at higher velocities. Therefore, energy depositions in the presampler and EM1 are very relevant in defining the signature of a monopole in the calorimeter. The energy losses of monopoles are very low at low velocities, allowing them to slowly penetrate to outer layers such as EM3 and even the hadronic calorimeter, depending on the initial energy of monopoles and the amount of material traversed along their trajectory. Lower mass monopoles with high kinetic energies may produce δ-rays in the EM calorimeter that are energetic enough to propagate and radiate, broadening the shape of the energy deposition.

Electrons and photons also deposit most of their energy in the LAr EM calorimeter. There are, however, major differences in the shape of the energy deposition with respect to monopoles. Electrons pass through the thin presampler without initiating an electromagnetic cascade, which only starts in EM1 and fully develops in EM2, possibly ending in EM3 or even leaking some energy into the hadronic calorimeter. Thus, most of the energy deposition from electrons occurs in EM2 where the particle shower is mostly contained. A similar situation occurs for photons, which initiate an electromagnetic cascade slightly later than electrons.

Penetration depth

The penetration depth of monopoles is highly dependent on the magnetic charge since the energy loss increases with g^2. The calorimeter is the sensitive part of ATLAS responsible for triggering, therefore, the likelihood of reaching it determines the sensitivity to monopoles of this search. Monopoles of charge $0.5g_{\mathrm{D}}$ can make it to the central region of the EM calorimeter with as little as 50 GeV of kinetic energy, while monopoles of charge $1.0g_{\mathrm{D}}$ and $2.0g_{\mathrm{D}}$ need about 100 GeV and 600 GeV of kinetic energy, respectively. Such high

minimum kinetic energy requirements limit the sensitivity to high-charge monopoles produced using realistic kinematic models in which regions above 500 GeV in the kinetic energy spectrum correspond to very low production cross sections.

Low EM calorimeter energy threshold Level-1 triggers are necessary to select events with highly ionizing monopoles that tend to stop early in the calorimeter. However, since these low threshold triggers are designed to select events with electrons and photons that deposit their energy in the EM calorimeter, these triggers usually apply a requirement that would reject monopoles that deposit energy in the hadronic calorimeter. Monopoles of charge $0.5g_{\mathrm{D}}$ and at least 300 GeV of kinetic energy are able to penetrate to the central region of the hadronic calorimeter, while monopoles of charge $1.0g_{\mathrm{D}}$ need at least 1300 GeV of kinetic energy to reach the same part of the detector. Monopoles of charge $g \geq g_{\mathrm{D}}$ would not reach the hadronic calorimeter for kinetic energies below 3000 GeV. A complete study on the penetration depth of highly ionizing particles can be found in Ref. [31].

4.2 Simulation of monopoles in the ATLAS detector

In order to study the interactions of monopoles with the ATLAS detector, it is necessary to generate simulated monopole events which are then processed using a GEANT4-based ATLAS detector simulation. This includes the equations of motion for magnetically charged particles and the model of production of δ-rays by highly ionizing particles. Energy deposits are digitized and reconstruction of physics objects is performed using the Athena software.

The uncertainties on the appropriate way to model the production of monopole–antimonopole pairs at colliders motivates the inclusion of model-independent studies covering a wide range of masses. Also, Dirac's quantization condition (Eq. (1.9)) predicts that the fundamental magnetic charge is g_{D} while Schwinger's quantization condition (Eq. (1.12)) predicts $2g_{\mathrm{D}}$. Therefore, monopoles of mass 200, 500, 1000, 1500, 2000 and 2500 GeV, and magnetic charges $|g|$ =$0.5g_{\mathrm{D}}$, $1.0g_{\mathrm{D}}$, $1.5g_{\mathrm{D}}$ and $2.0g_{\mathrm{D}}$ are included in this search. Although fractional magnetic charges are not predicted by the theories, there is no reason not to search for them, and historically they have been included in previous searches (see Sec. 1.6). All the simulated samples used in this analysis were produced as part of the `mc12c` production

campaign, which reproduces the running conditions of the LHC and ATLAS detector during the 2012 data taking period. The GEANT4 simulation of the `mc12c` production campaign was performed using the transform[12] `AtlasG4_trf` with the `ATLAS-GEO-21-02-02` version of the simulateed detector geometry implemented in GEANT4 [104], the conditions tag `OFLCOND-MC12-SIM-00` [105], which contains information relevant to the detector running conditions, and the GEANT4 physics list `QGSP_BERT` [106]. In the `mc12c` production campaign digitization and reconstruction (see Secs. 4.2.3 and 4.2.4) were performed using a single transform, `DigiMReco_trf`. This transform takes as input all the necessary configurables such as the GEANT4 detector geometry and offline conditions tags (`ATLAS-GEO-21-02-02` and `OFLCOND-MC12b-SDR-01` [107]), ATLAS software database release (`DBRelease-26.9.1`), pileup profile distribution and trigger menu database configuration.

Digitization and reconstruction of simulated monopole samples of charge $2.0g_{\mathrm{D}}$ require high amounts of available memory due to the high ionization levels. Memory limitations arose during this stage of the Monte Carlo production. Although access to high-memory queues was granted for the production of these samples, it was not possible to digitize and reconstruct them in full. In all cases, at least 50% of the number of events in each sample were processed successfully. No obvious bias was introduced to the digitized and reconstructed monopole samples as the computing jobs would fail or succeed in a random manner, which appeared to be related to the conditions of the machines to which the jobs were assigned.

4.2.1 Event generation

Simulated monopole events are generated in two types of samples: single monopole events allowing for a model-independent search and spin-1/2 pair-produced monopoles assuming the Drell-Yan mechanism. Although monopoles are predicted by models with masses in the TeV scale (see Sec. 1.3), their production mechanism is not well understood. This is mainly a consequence of the large magnetic coupling to the photon. The Drell-Yan production mechanism is used as a benchmark model that offers a scenario with realistic

[12] In the Athena software, transforms are scripts that execute the algorithms necessary to perform a transformation from a data format to another in the data production chain.

kinematics for monopoles produced in pp collisions at the LHC.

Single particle production

Single particle monopole samples are generated with flat kinetic energy, ϕ and η distributions in the ranges 10 GeV $< E^{\text{kin}} <$ 3000 GeV, $-\pi < \phi < \pi$ and $-3 < \eta < 3$, respectively. These samples have 50 000 events with equal number of monopoles and anti-monopoles.

In the absence of a hard scattering process, no electrically charged particles from the underlying event are present in the single monopole samples. However, additional proton–proton interactions are overlaid to simulate pileup events, as described in Section 4.2.3.

Drell-Yan production

Pair-produced spin-1/2 monopoles in proton-proton collisions at a centre-of-mass energy of 8 TeV using Drell-Yan kinematics are produced with the Monte Carlo leading-order matrix element generator MadGraph5 [108]. The parton distribution function (PDF) CTEQ6L1 [109] is used with the AU2 tune [110]. Samples of 22 000 events were generated for each mass and charge combination.

A requirement on the minimum transverse momentum, p_{T}, of the generated particles is imposed to ensure that only monopoles energetic enough to reach the EM calorimeter are simulated, thus optimizing usage of computing resources. The exact requirement is mass- and charge-dependent and was obtained from trigger efficiency curves by finding the transverse momentum at which the efficiency becomes non-zero. These trigger efficiency curves can be found in App. A. In order to keep a conservative approach, the minimum p_{T} was chosen about 50 to 100 GeV below the turn-on. See Sec. 5.1 for more on the trigger used in this search. Table 4.1 summarizes the production cross sections and generator-level minimum-p_{T} requirements for each mass and charge point included in this search.

The generated four-vectors are processed by the Monte Carlo generator Pythia 8 [111], which adds momentum smearing, parton shower and hadronization effects, and decays of the byproducts of the simulated proton-proton collisions. The generated events are processed by Pythia until 20 000 events have been successfully simulated.

Charge $\|g\|$	Mass [GeV]	Cross section [pb]	p_{T} cut [GeV]	Cross section [pb] after p_{T} cut
$0.5g_D$	200	37.6	0	37.6
	500	0.600	50	0.582
	1000	6.71×10^{-3}	150	6.08×10^{-3}
	1500	1.33×10^{-4}	200	1.19×10^{-4}
	2000	2.24×10^{-6}	250	1.95×10^{-6}
	2500	1.97×10^{-8}	300	1.62×10^{-8}
$1.0g_D$	200	150.	150	53.5
	500	2.40	200	1.52
	1000	2.69×10^{-2}	250	2.03×10^{-2}
	1500	5.33×10^{-4}	300	4.19×10^{-4}
	2000	8.95×10^{-6}	350	6.81×10^{-6}
	2500	7.86×10^{-8}	400	5.58×10^{-8}
$1.5g_D$	200	339.	250	37.1
	500	5.41	300	2.08
	1000	6.05×10^{-2}	350	3.56×10^{-2}
	1500	1.20×10^{-3}	400	7.73×10^{-4}
	2000	2.01×10^{-5}	450	1.28×10^{-5}
	2500	1.77×10^{-7}	550	9.28×10^{-8}
$2.0g_D$	200	602.	500	4.37
	500	9.62	550	0.729
	1000	1.08×10^{-1}	650	2.05×10^{-2}
	1500	2.14×10^{-3}	700	5.78×10^{-4}
	2000	3.58×10^{-5}	750	1.01×10^{-5}
	2500	3.15×10^{-7}	800	7.98×10^{-8}

Table 4.1: Cross sections of Drell-Yan produced spin-1/2 monopoles in proton-proton collisions at $\sqrt{s} = 8$ TeV and generator-level minimum-p_{T} requirements.

Dedicated samples to simulate pileup were generated with Pythia 8 using the PDF MSTW2008LO with the A2MSTW2008LO tune [112, 113] for minimum-bias processes at the LHC.

4.2.2 Simulation

A Geant4 [114] version of the ATLAS detector geometry and material density distribution was used to simulate the interactions between the generated magnetic monopoles and the detector material. Interactions between the ATLAS detector and other particles from the

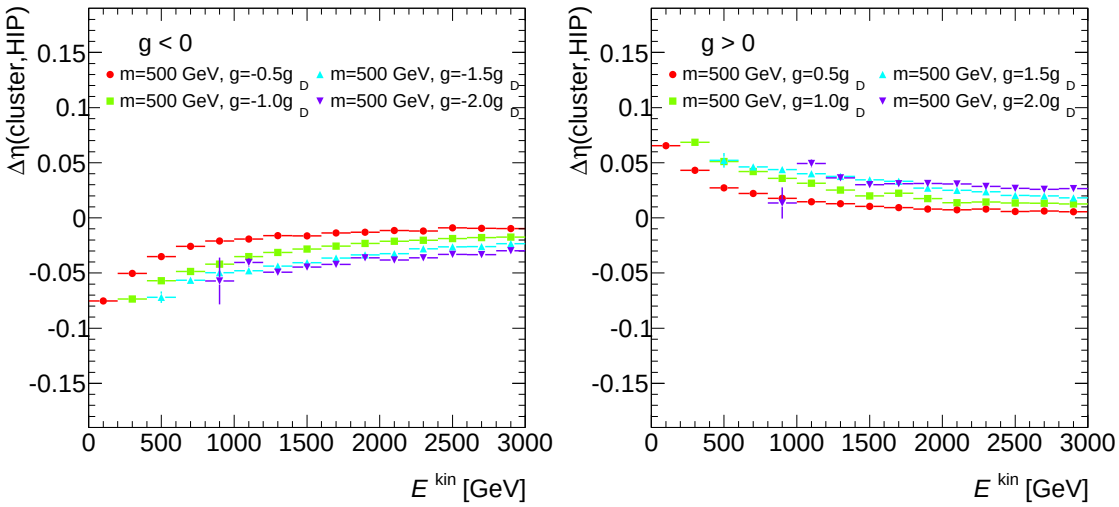

Figure 4.3: Profile histogram of the difference between pseudorapidity η of the calorimeter cluster and the monopole's truth η for monopoles of mass 500 GeV and various charges as a function of the monopole truth kinetic energy E^{kin}. High charge monopoles with low E^{kin} values do not possess enough energy to penetrate to the calorimeter, and therefore are not reflected in these plots.

underlying event or pileup collisions are also simulated. The ATLAS geometry version `ATLAS-GEO-21-02-02` was used. This is the default of the `mc12c` production campaign.

Prior to 2010, the simulation of the passage of magnetically charged particles through matter was not described in the GEANT4 simulation of the ATLAS detector. Therefore, the custom simulation package, `Simulation/G4Extensions/Monopole`, was developed. This package instantiates the correct equations of motion for magnetically charged particles in electromagnetic fields (Eq. 1.16), computes the energy deposition by monopoles with integer and fractional magnetic charges in units of g_{D} (Eq. 1.18) taking into account the generation of δ-rays, and propagates monopoles in time. The Monopole simulation package is based on that developed for the search for monopoles in 2011 data [77].

Monopole interactions with the magnetic field

The ID is enclosed in a solenoid magnet producing a field of 2 T parallel to the beam axis. The trajectory of an electrically charged particle bends in the $r-\phi$ plane perpendicular to the magnetic field while magnetically charged particles are accelerated (or decelerated) along

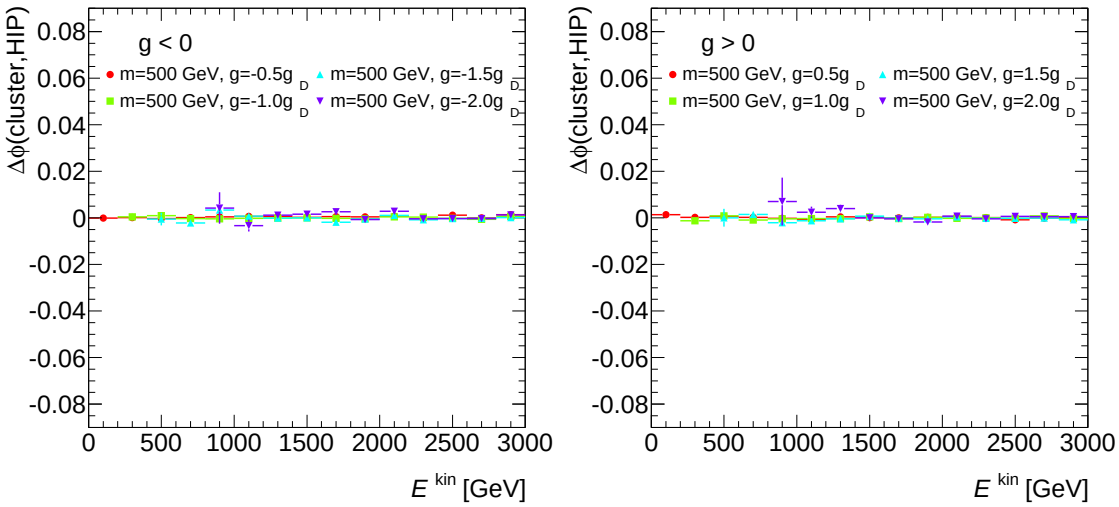

Figure 4.4: Profile histogram of the difference between azimuthal angle, ϕ, of the calorimeter cluster and the monopole's truth ϕ for monopoles of mass 500 GeV and various charges as a function of the monopole truth kinetic energy E^{kin}. High charge monopoles with low E^{kin} values do not possess enough energy to penetrate to the calorimeter, and therefore are not reflected in these plots.

the direction of the magnetic field in the $r-z$ plane. Such an acceleration along the direction of the field causes the reconstructed calorimeter cluster produced by the monopole to be misaligned in η with respect to the original orientation of the generated particle, η_{truth}. This can be seen in Fig. 4.3 for monopoles of mass 500 GeV and various charges. As expected, positively charged monopoles bend in a direction opposite to negatively charged monopoles. Higher charge monopoles experience a stronger interaction with the field causing a greater bending. Lower kinetic energy monopoles bend more in η as their momentum is lower. On the other hand, monopole trajectories are unaffected in the $r-\phi$ plane. As a consequence, the ϕ coordinates of the calorimeter cluster and the original monopole are the same. This is shown in Fig. 4.4.

Energy deposition by monopoles

Energy losses by ionization of magnetically charged particles are described by Eq. 1.18. This equation is implemented in the Monopole simulation package. Figure 4.5 shows the energy losses through ionization by magnetic monopoles of mass 1000 GeV and various charges as

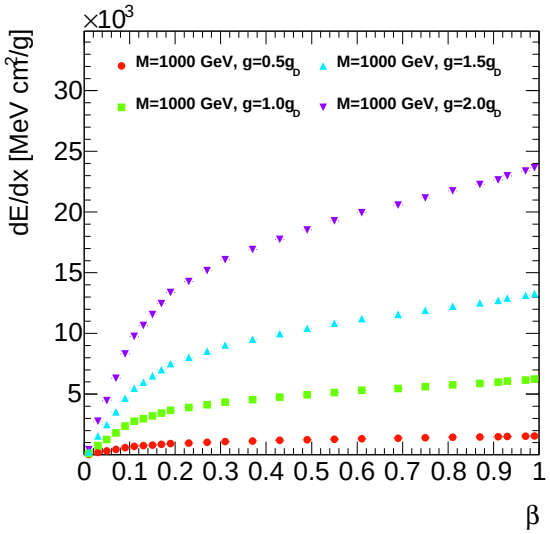

Figure 4.5: Energy losses by ionization for monopoles of mass 1000 GeV and various charges as a function of speed-of-light fraction β.

a function of the monopole's speed-of-light fraction β. Equation 1.18 also predicts that the energy losses are proportional to g^2. Figure 4.5 is consistent with this dependence. It must be noted that, unlike electrically charged particles that deposit most of their kinetic energy at low β, monopoles deposit more energy at high β. This means that magnetically charged particles do not produce a Bragg peak. This is shown in Fig. 4.6 where the Bragg curve in LAr of a magnetic monopole of mass 1000 GeV, charge $|g| = 1.0g_{\mathrm{D}}$ and initial kinetic energy $E^{\mathrm{kin}} = 1000$ GeV is compared to that of an electrically charged particle of the same mass and charge $|z| = 68.5$ (the electric equivalent of g_{D}).

The KYG and Bloch corrections described in Sec. 1.4 exist for multiples of the Dirac charge only. This search, however, includes fractional charges. Therefore, the values of the KYG, $k(g)$, and Bloch, $B(g)$, corrections used in this search are

$$k(g) = \begin{cases} 0.406, & |n| \leq 1 \\ 0.346, & |n| \geq 1.5 \end{cases} \quad \text{and} \quad B(g) = \begin{cases} 0.248, & |n| \leq 1 \\ 0.672, & |n| \geq 1.5, \end{cases} \tag{4.1}$$

respectively. The energy losses by ionization of magnetically charged particles are simulated by the class `G4mplAtlasIonisation`.

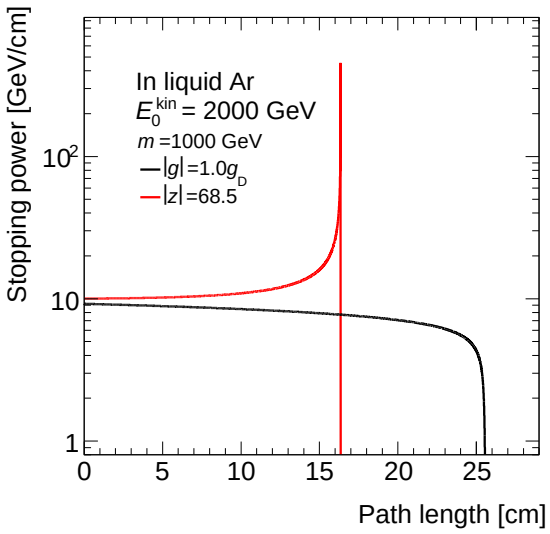

Figure 4.6: Bragg curves in LAr for a magnetic monopole of mass 1000 GeV, charge $|g| = 1.0g_{\mathrm{D}}$ and initial kinetic energy $E^{\mathrm{kin}} = 2000$ GeV, and for an electrically charged particle of the same mass and charge $|z| = 68.5$.

Production of δ-rays

Electrons from inner shells of the atoms of the ATLAS detector material are knocked off by monopoles. These electrons are known as δ-rays or δ-electrons and usually have a kinetic energy of a few keV, significantly more than the energy of an electron from ionization. The δ-ray production model described in Ref. [115] is implemented in the class `G4mplAtlasIonisationWithDeltaModel`. The energy with which the δ-rays are produced is directly subtracted from the monopole's kinetic energy. Energy losses by ionization of δ-rays are simulated using the default GEANT4 classes.

Time propagation of monopoles in ATLAS

Unlike electrically charged particles, the kinetic energy of a magnetic monopole is changed by the solenoidal magnetic field as it is accelerated. In order to correctly propagate monopoles in time, the monopole equation of motion has to be integrated over the changing velocity at each step.

Propagation in time of monopoles has been validated in the TRT and the calorimeter.

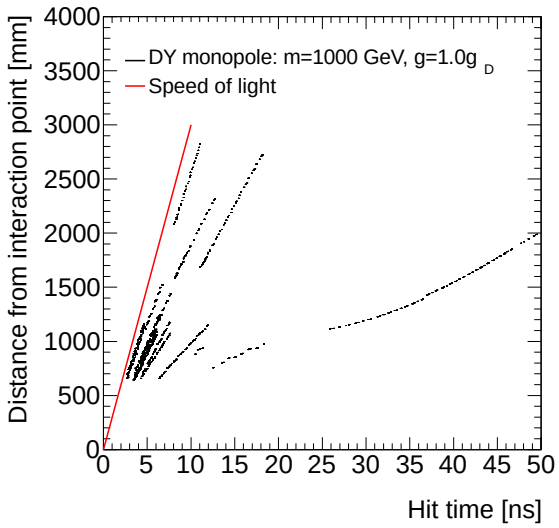

Figure 4.7: TRT hit distance from the interaction point as a function of time for magnetic monopoles of mass 1000 GeV and charge $|g| = 1.0g_{\mathrm{D}}$ from ten events randomly chosen in a simulated sample. The red line shows the hit distance vs time expected for a particle travelling at the speed of light.

Figure 4.7 shows the distance from the interaction point of TRT hits produced by monopoles as a function of the hit time. Each line represents a pair-produced spin-1/2 monopole; there are in total ten monopoles in this figure. Note that all monopoles travel through the TRT at a speed lower than the speed of light. This figure, along with the TRT geometry described in Fig. 2.3, shows which monopoles go through the TRT barrel, end-cap and transition region. Also, the accelerating effect of the magnetic field can be observed for one monopole trajectory.

In the ATLAS calorimeter, cluster times are reconstructed as the weighted average of the calorimeter cells in the cluster using the square of the energy deposition in the cell as the weight. Time information from presampler cells is not included in the time calculation. The time of calorimeter clusters with energy deposition in the presampler only is, therefore, set to zero. Figure 4.8 shows the cluster time for monopoles of mass 1000 GeV (left) and 2500 GeV (right). As expected, heavier monopoles travel on average at lower speeds than lighter monopoles, arriving at the EM calorimeter later. Figure 4.9 shows the average cluster time of monopoles of mass 1000 GeV and various charges as a function of the

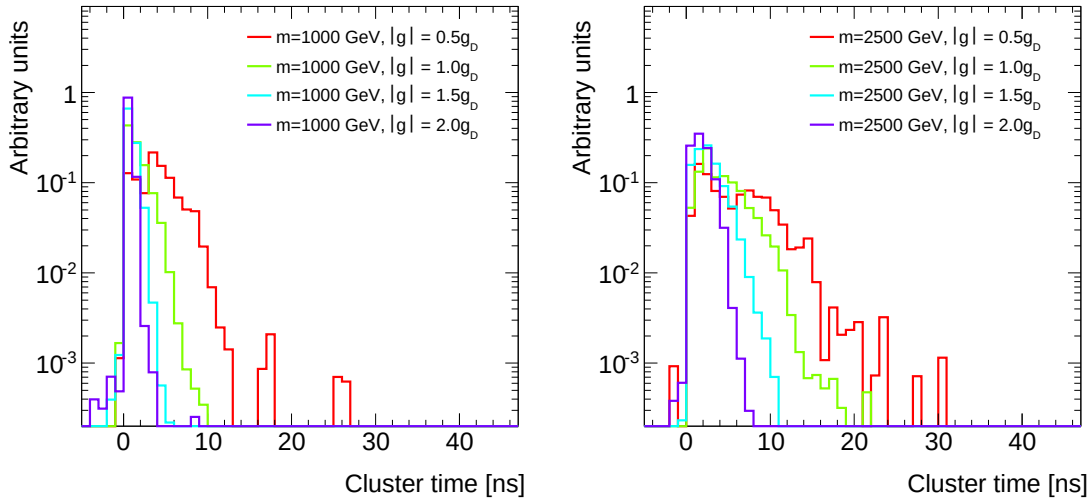

Figure 4.8: Reconstructed time of calorimeter clusters produced by single monopoles of mass 1000 GeV (left) and 2500 GeV (right), and various charges.

generated monopole's β. In order to exclude geometrical effects, only monopoles generated in the central region, $|\eta| < 0.3$, have been included in this figure. As the magnetic charge increases, only monopoles generated with $\beta \approx 1$ have enough kinetic energy to reach the EM calorimeter before stopping.

Figure 4.10 shows the average cluster time as a function of the cluster η for single monopoles of various masses and charges. Large η dependences are observed as the magnetic charge decreases. Since monopoles of lower charge are generated with a broader β spectrum than that of monopoles of higher charge (e.g., monopoles of mass 1000 GeV and charge $|g| = 2.0g_{\mathrm{D}}$ are mostly generated with $\beta \approx 1$), the geometrical effects reflecting the amount of detector material before the EM calorimeter become more obvious as the charge decreases.

Recombination effects in liquid argon

Charged particles passing through the EM calorimeter ionize the LAr. Electrons from ionization are collected by means of an electric field applied between the copper electrodes, and the energy deposition is deduced from the charge collected in each calorimeter cell. In the case of monopoles, the ionization density is very high, allowing for electron-ion pairs to

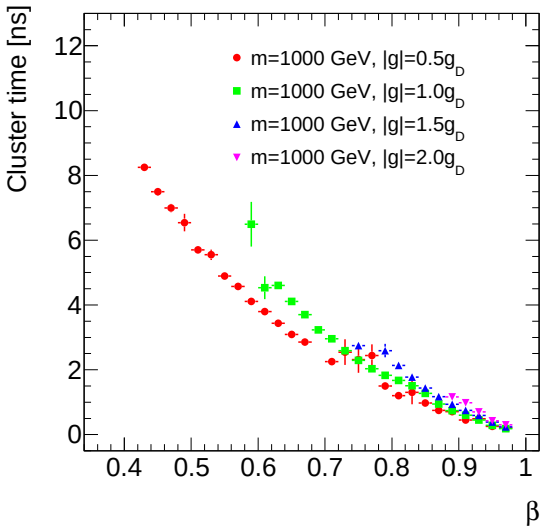

Figure 4.9: Average calorimeter cluster time for single monopoles of mass 1000 GeV and various charges generated in $|\eta| < 0.3$ as a function of the monopole speed β.

recombine before they can be collected. This recombination effect leads to an underestimate of the measured energy.

Birks' law [116, 117] describes this phenomenon by relating the actual deposited and collected charge in the calorimeter, and has been implemented in ATLAS in the form

$$E_{\text{vis}} = E_0 \frac{1 + \frac{A'k}{E_D}}{1 + \frac{k}{\rho E_D}\frac{\mathrm{d}E}{\mathrm{d}x}}, \tag{4.2}$$

where E_{vis} is the visible energy in the calorimeter, E_0 the actual deposited energy and $\mathrm{d}E/\mathrm{d}x$ the energy deposited per unit length. The recombination effects depend on the external electric field, E_D, and the density of the LAr, ρ. In the EM calorimeter the drift electric field is assumed to be uniform with a magnitude of 10 kV/cm. The Birks' "constant" $k = 0.0486$ (kV/cm)(g/cm^2)MeV^{-1} has been measured by the ICARUS TPC collaboration [118]. The normalization parameter A' is set to 1.51.

A correction to Birks' law was developed using heavy-ion data in order to explain the recombination effects for very high $\mathrm{d}E/\mathrm{d}x$ values as the ICARUS measurement only describes well the recombination effects by particles with single electric charge [119].

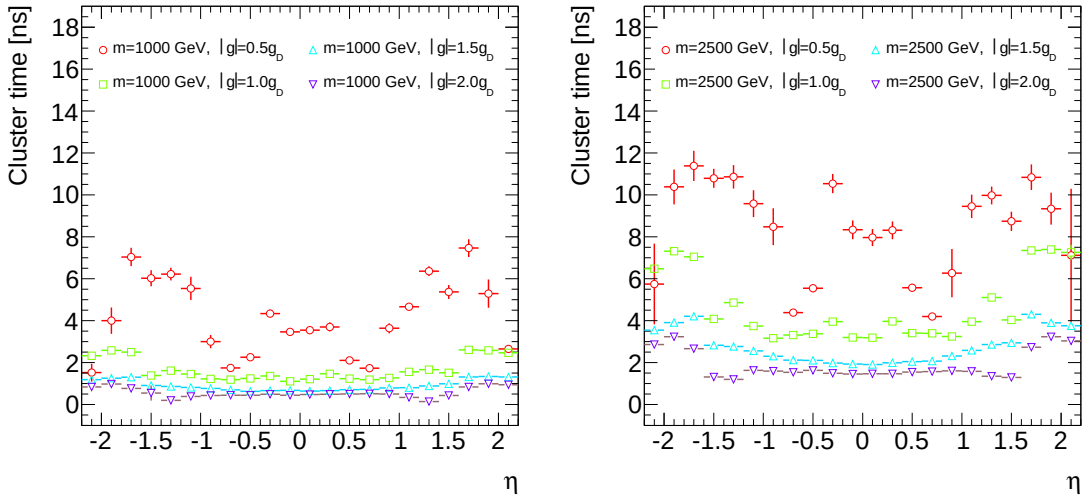

Figure 4.10: Average calorimeter cluster time for single monopoles of mass 1000 GeV (left) and 2500 GeV (right), and various charges as a function of the cluster η.

4.2.3 Digitization of simulated signal

Simulated Monte Carlo samples are digitized using the ATLAS software. At this stage, simulated energy depositions are converted to simulated digital signals that resemble the output from the detector electronics. Digitization of simulated monopole signals is done using the Athena software.

It is during the digitization stage that additional collisions are overlaid to simulate the pileup conditions of the collected data. Simulated monopole samples are digitized using the default pileup profile of the `mc12b/mc12c` production campaign. Since collisions and simulated data do not have perfectly matching pileup profiles, a pileup reweighing is performed at analysis level to account for these differences. Figure 4.11 shows the pileup profile distributions of the collision data used in this search and the simulated data samples. The high instantaneous luminosity of the LHC gives rise to two types of pileup: in-time pileup from collisions in the same bunch crossing, and out-of-time pileup from collisions from the previous or next bunch crossing. To account for both in-time and out-of-time pileup, a quantity $\langle\mu\rangle$ has been defined as the number of interactions per bunch crossing averaged per luminosity block. A luminosity block is usually around a minute or two of

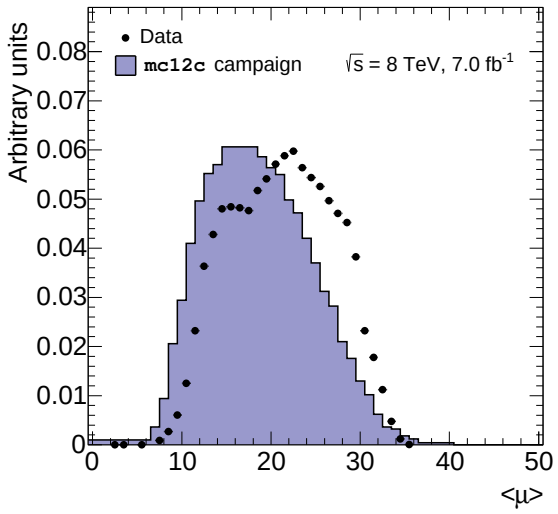

Figure 4.11: Pileup profiles for the collision dataset used in this search and the `mc12c` production campaign used for the simulated monopole samples.

data taking.

The `mc12c` pileup profile has been designed to emulate the conditions of the entire 2012 run. However, the dataset used in this search is just a subset of the full 2012 dataset and its pileup profile therefore differs, as observed in Fig. 4.11. Due to complications with the production of signal samples of monopoles of charge $2.0g_{\mathrm{D}}$, centrally produced official samples have a pileup profile that is truncated at $\langle\mu\rangle$=18. This will be shown later to not be a problem due to the very high ionization produced by such monopoles.

4.2.4 Event reconstruction

Digital signals from the ATLAS detector electronics and digitized simulated samples are reconstructed on a event-by-event basis. Physics objects such as charged leptons, photons, particle jets and missing transverse energy are identified at this stage from reconstructed charged particle tracks and clusters of energy deposition in the calorimeter. Two basic reconstructed objects are used in this search: TRT drift circles and calorimeter clusters of topologically connected energy deposits. Reconstruction of simulated monopole samples is done using the default ATLAS software.

TRT hits and drift circles

As described in Sec. 2.2.3, the digital signals from the TRT front-end boards comprise 27 bits that span 75 ns (in 2012 the bunch spacing was 50 ns). The 27-bit readout contains the data of three 25 ns (bunch spacing at design luminosity) slices, i.e., nine bits per slice. The first bit in each slice is set to one if the TRT high threshold was exceeded while the remaining eight bits contain the TRT LT information, each one representing an interval of approximately 3.125 ns [86]. See Fig. 2.8 in Sec. 2.2.3.

Drift circles are reconstructed using the leading edge of the low-threshold component of the signal, i.e., the first high bit in the 75 ns interval, which represents the drift time of the electrons from ionization produced at the point of closest approach of the particle passing through the straw. Not all reconstructed drift circles are kept. As part of the TRT hit processing at the reconstruction stage an out-of-time pileup suppression algorithm is used to reject TRT hits likely coming from neighbouring bunch crossings. Hits with a trailing edge (last bit high) less than 11 ns are associated to the previous bunch crossing and rejected, and hits with a leading edge greater than 60 ns are associated to the next bunch crossing and rejected. Only TRT drift circles that are not rejected as out-of-time pileup are considered as TRT LT hits. If a HT bit is high, the drift circle is also classified as a TRT HT hit.

In this search the position of the centre of the straw that recorded a hit and the discriminator output (LT or HT hit) are of more relevance than the actual precision measurement provided by the TRT drift circles.

Calorimeter topological clusters

Clusters of energy deposition in the calorimeter are commonly used to measure the energy of electrons, photons and jets. It is impossible to measure the energy of a monopole using only the calorimeter, due to the large energy losses before reaching it. Thus, rather than using the magnitude of the energy deposition in the search for monopoles, the shape of the calorimeter cluster is used. Topological clusters are used for this purpose as they are reconstructed in an energy density-based approach. In particular the `CaloCalTopoClusters`

are used [120].

A topological cluster in ATLAS is a calorimeter object that is built based on the signal-to-noise ratio of the cells that form it. Thus, the number of cells making up the cluster is variable. The expected noise level is an η-dependent quantity defined as the quadratic sum of the electronics noise at zero luminosity and the noise at high luminosity, which is dominated by pileup [120].

Topological clusters are seeded by calorimeter cells for which the absolute-energy-to-noise ratio is above four. Neighbouring cells in all directions, i.e., cells in the same and neighbouring longitudinal layers, are added to the cluster if their absolute energy to noise ratio is above two. When a cell is a neighbour to two different clusters, these are merged. Finally, all neighbouring cells to those already added to the cluster are added so that the tails of electromagnetic cascades and jets are not lost.

An additional step for splitting topological clusters is performed as it is very common in ATLAS events to have overlapping particles. Local maxima are found by requiring that the energy deposition in the cell be above 500 MeV and that at least four cells be included in the cluster, all with energy deposition less than the local maximum. Each local maximum will yield one cluster formed using the same algorithm just explained. At the boundary between two clusters, cells can be shared among them. The energy of the shared cells, however, is weighed so that no double counting of the energy is done.

One particularity of the cluster-splitting algorithm is that local maxima are restricted to cells in the second and third layers of the EM calorimeter. Local maxima from the presampler, first layer of the EM calorimeter and hadronic calorimeter are only used if they do not overlap in η and ϕ with maxima found in the second and third layers of the EM calorimeter.

Trigger reconstruction

Simulation of ATLAS triggers is performed at the reconstruction stage. The trigger reconstruction runs over the simulated samples the same algorithms used online for data collection. This search uses a dedicated trigger for highly ionizing particles that was deployed

during the last part of the 2012 run. This trigger was not part of the ATLAS software release used for the `mc12c` official production. Therefore, a dedicated release, `TrigMC-17.2.11.2.1`, containing the dedicated trigger and compatible with the `mc12c` production campaign, was built to digitize and reconstruct all simulated samples used in this search. The Monte Carlo trigger database used was `MC_pp_v4_tight_prescales` [121].

4.3 Possible background signals

A number of simulated Monte Carlo samples of Standard Model processes have been re-processed to include the dedicated trigger. Due to the scale of the computing resources needed to process all Standard Model processes that would be necessary to study all possible background sources, only a limited number were made available to this search. These include electron–positron pairs from Drell-Yan production, electrons from W boson decays and high-p_{T} multijet events.

4.3.1 High-energy electrons

Electrons with momentum above 10 GeV produce transition radiation in the TRT in the form of X-rays. Photon absorption by the Xe-based gas mixture combined with the ionization produced by the electrons generate TRT HT hits along their trajectories. The probability of finding a TRT HT hit on a track produced by an electron is about 30%. This probability increases in the TRT end-caps where there is a larger amount of radiator material [100]. The amount of radiation emitted is proportional to the Lorentz factor $\gamma = E/m$.

The electromagnetic cascade generated by high-energy electrons with energy around the TeV scale is suppressed due to an increase of the formation length of the bremsstrahlung photon [122]. Due to the very small longitudinal momentum transfer from the electron to the nuclei of the detector material, the uncertainty principle $\delta x \delta p \geq \hbar/2$ dictates that the distance over which the bremsstrahlung photon forms must be long. In addition to this effect, bremsstrahlung is further suppressed due to creation of electron–positron pairs

from partially formed photons. The formation length can thus approach a radiation length. Due to this bremsstrahlung suppression, high-energy electrons would be indistinguishable from minimum ionizing particles in the first layer of the EM calorimeter, creating a narrow cluster of energy deposition. The full cascade only develops in the deeper second layer.

Simulated Monte Carlo samples of electrons from W boson decays, and Drell-Yan produced electron–positron pairs binned in invariant mass from 20 to 3000 GeV were used to study the performance of the selection criteria against possible background signals from electrons.

4.3.2 High-p_{T} jets

Events with high-p_{T} jets from collisions with strong interactions may be a source of background. Such jets are generally contained in a narrow cone and have a high degree of colinearity [123]. Electrically charged particles from high-p_{T} jets may overlap and deposit energy in the same TRT straws. If the number of overlapping particles is high enough, a TRT HT hit will be registered.

Collimated jets from high-p_{T} multijet events, mainly composed of minimum ionizing particles and neutral pions, may produce narrow energy depositions. Jets, however, penetrate to the hadronic calorimeter, something that only occurs for very energetic monopoles.

Simulated Monte Carlo samples of strong 2-to-2 processes with minimum momentum transfer of 1000 GeV were used to study the performance of the selection criteria for possible background signals from high-p_{T} multijet events.

Chapter 5

Reconstruction of magnetic monopoles in ATLAS

This chapter describes the reconstruction of magnetic monopoles based on the signatures in the ATLAS detector. A description of the trigger used is followed by the definition of the variables used for reconstruction of monopole candidates. Studies on the performance of the selection variables are also presented in this chapter.

5.1 Monopole trigger

The majority of experimental measurements and searches in proton-proton collisions at the LHC experiments use triggers that select events with Standard Model objects such as charged leptons, particle jets from processes involving the strong interaction and missing transverse energy, which can be associated to neutrinos escaping the detectors undetected. However, in some searches for physics beyond the Standard Model, the use of triggers that select unconventional signatures may be required.

In this search a dedicated trigger has been used to select events with monopole-like signatures. This trigger is based on the interactions described in Sec. 4.1. In particular, a

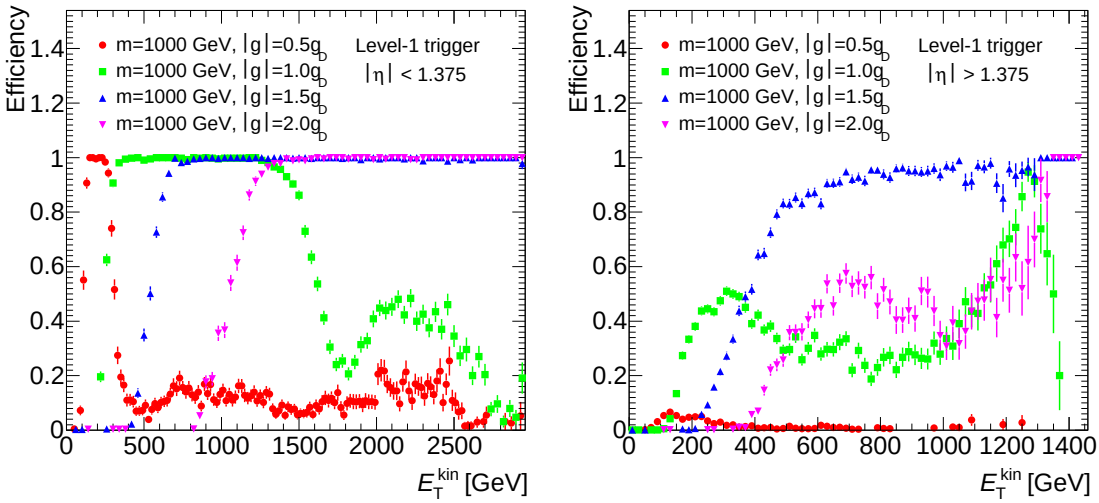

Figure 5.1: Level-1 `EM18VH` trigger efficiency for monopoles of mass 1000 GeV and various charges as a function of the monopole transverse kinetic energy, $E_{\mathrm{T}}^{\mathrm{kin}}$, for generated monopole in pseudorapidity ranges $|\eta| < 1.375$ (left) and $|\eta| > 1.375$ (right).

region in the TRT with a large fraction of HT hits is used as a powerful discriminant to select highly ionizing particles like magnetic monopoles. This trigger, known as the HIP or HIP TRT trigger, is a dedicated Level-2 trigger seeded by a electron–photon Level-1 trigger that requires energy deposition in the EM calorimeter.

5.1.1 Region of interest in the electromagnetic calorimeter

In the absence of any ID-based Level-1 trigger, the innermost part of the ATLAS detector that can be used to select monopole events is the EM calorimeter. Monopoles are highly ionizing particles, with energy losses several orders of magnitude greater than those of minimum ionizing particles. Thus, the probability of reaching the EM calorimeter, let alone depositing large amounts of energy, is low. It then becomes very important to use the lowest energy threshold Level-1 trigger available to avoid the loss of monopoles that stop early in the calorimeter, depositing only a small amount of energy.

At Level-1, calorimeter RoIs are defined as regions of size $\Delta\eta \times \Delta\phi = 0.4 \times 0.4$. The dedicated HIP trigger is seeded by the Level-1 `EM18VH` trigger [124], which has a variable minimum transverse energy threshold that varies between 18 and 20 GeV, depending on the

η coordinate. Since this Level-1 trigger was developed for selecting events with electrons or photons, the maximum amount of energy deposition in the hadronic calorimeter is restricted by applying a "hadronic veto." Regions of interest with more than 1 GeV deposited in the hadronic calorimeter in the $\Delta\eta \times \Delta\phi = 0.2 \times 0.2$ core of the RoI are rejected. The sensitivity of this search is mainly determined by the probability of reaching the EM calorimeter and passing the `EM18VH` trigger.

Figure 5.1 shows the `EM18VH` trigger efficiency as a function of the transverse kinetic energy, $E_{\mathrm{T}}^{\mathrm{kin}} = E^{\mathrm{kin}} \sin\theta$, of the generated monopoles in the EM calorimeter barrel and end-cap regions. Due to the requirement on the maximum energy deposition in the hadronic calorimeter, the trigger efficiency drops at higher $E_{\mathrm{T}}^{\mathrm{kin}}$ values.

They key advantage of the HIP trigger is that it ensures the highest efficiency for monopoles among the triggers currently available. This is achieved in part due to the absence of any other requirements on the energy deposition in the calorimeter apart from those mentioned above. Standard electron and photon triggers in ATLAS usually require, at Level-2, energy deposition in the second layer of the EM calorimeter since shower-shape variables based on information from this layer are used. The use of such Level-2 variables would reduce the sensitivity of the search by failing to select monopoles that stop in the presampler and the first layer. The HIP trigger does not use Level-2 trigger calorimeter clusters and therefore retains acceptance for monopoles that would not be accepted by standard electron and photon triggers.

5.1.2 Region of high ionization in the TRT

Events that pass the Level-1 `EM18VH` trigger are tested at Level-2 for high ionization in the TRT, one of the main signatures of monopoles. A narrow region of TRT HT hits is expected along the monopole trajectory, which should be in line with the energy deposition in the calorimeter.

Based on the direction of the RoI identified the Level-1 `EM18VH` trigger, a wedge in the TRT of size $\Delta\phi = \pm 0.1$ is defined. This matches the size in ϕ of the Level-1 RoI. The wedge is divided into 20 bins of equal size. The bin with the highest number of TRT HT

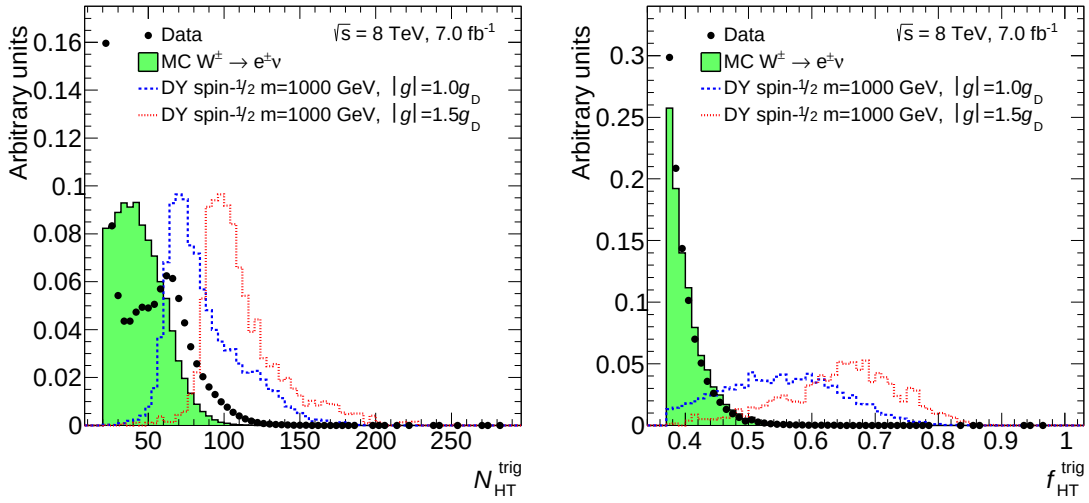

Figure 5.2: Number of TRT HT hits $N_{\mathrm{HT}}^{\mathrm{trig}}$ (left) and fraction of HT hits $f_{\mathrm{HT}}^{\mathrm{trig}}$ (right) in a narrow wedge of size $\Delta\phi = \pm 0.015$ for 7 fb^{-1} of data collected with the trigger, an expected background process and two typical monopole samples.

hits becomes the centre of a narrower wedge of size $\Delta\phi = \pm 0.015$. This narrow wedge constitutes the expected TRT region traversed by the monopole.

In order to discriminate signal from background, the number of TRT LT and HT hits is counted and the fraction of HT hits computed. Figure 5.2 shows the number of TRT HT hits, $N_{\mathrm{HT}}^{\mathrm{trig}}$, and the fraction of HT hits, $f_{\mathrm{HT}}^{\mathrm{trig}}$, in the narrow wedge of size $\Delta\phi = \pm 0.015$. The Level-2 trigger requires a minimum number of TRT HT hits $N_{\mathrm{HT}}^{\mathrm{trig}} > 20$ and fraction of HT hits $f_{\mathrm{HT}}^{\mathrm{trig}} > 0.37$. These requirements ensure a high trigger efficiency for signal monopoles while achieving a good background rejection, as suggested by Fig. 5.2. The $N_{\mathrm{HT}}^{\mathrm{trig}}$ distribution for collision data shows a double peak structure as it comprises events with electrons with a TRT HT hit probability of about 30%[13] and multijet events that can have a large charged particle multiplicity in the narrow wedge of $\Delta\phi = \pm 0.015$, producing a large number of TRT HT hits.

The Level-2 component of the HIP trigger is highly efficient with respect to Level-1. The inefficiency introduced by the Level-2 TRT requirements occurs for monopoles found near the turn-on point of the Level-1 trigger and is more significant for lower charges. Figure 5.3

[13]This probability yields an average of about ten TRT HT hits on track for electrons.

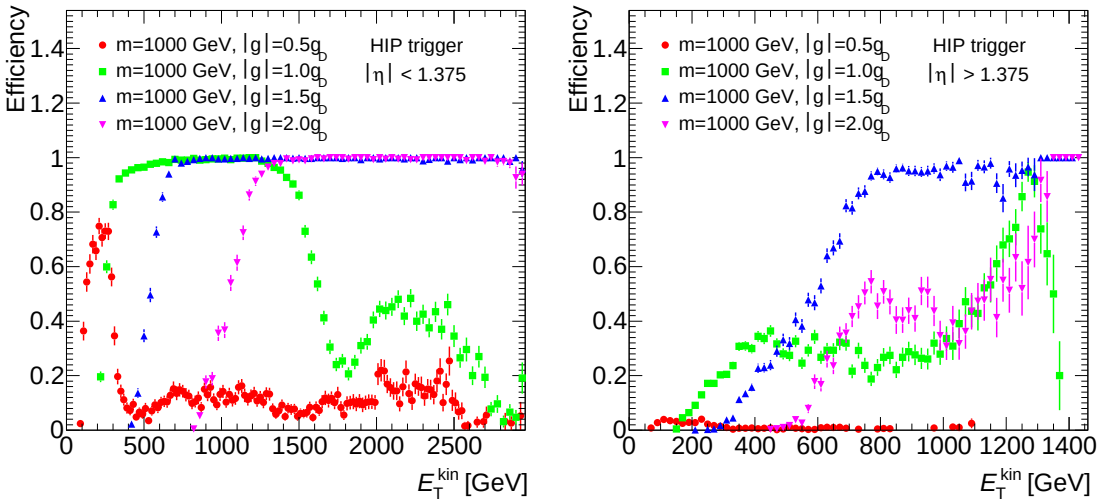

Figure 5.3: Dedicated HIP trigger efficiency for monopoles of mass 1000 GeV and various charges as a function of the monopole transverse kinetic energy, $E_{\mathrm{T}}^{\mathrm{kin}}$, for generated monopole pseudorapidity $|\eta| < 1.375$ (left) and $|\eta| > 1.375$ (right).The efficiency represents the combined efficiency of the Level-1 and Level-2 triggers.

shows the dedicated HIP trigger efficiency (Level-1 and Level-2 efficiencies combined) for monopoles of mass 1000 GeV and various charges as a function of the monopole transverse kinetic energy, $E_{\mathrm{T}}^{\mathrm{kin}}$.

Trigger efficiencies for pair-produced spin-1/2 monopoles generated using the Drell-Yan model can be found in Table 5.1. The very low trigger efficiencies for pair-produced spin-1/2 monopoles of charge $|g| = 2.0g_{\mathrm{D}}$ motivate their exclusion from this search. The efficiency for the mass 1000 GeV charge $|g| = 2.0g_{\mathrm{D}}$ sample is missing due to complications during the official MC production that prevented its successful completion.

5.2 Reconstruction of magnetic monopoles

This search uses data from the electron–photon stream, which comprises events selected by electron and photon triggers. The dedicated trigger is considered as a photon trigger as it uses the `EM18VH` Level-1 trigger and has no additional tracking requirements at Level-2 or event filter. In order to reduce the size of the collision data files and background MC from the electron-photon stream, these are processed using a software filter that selects

Spin-1/2	$\|g\| = 0.5g_D$	$\|g\| = 1.0g_D$	$\|g\| = 1.5g_D$	$\|g\| = 2.0g_D$
200 GeV	23.90 ± 0.30	3.84 ± 0.14	0.16 ± 0.03	0.002 ± 0.006
500 GeV	36.19 ± 0.34	15.87 ± 0.26	1.23 ± 0.09	0.03 ± 0.02
1000 GeV	33.97 ± 0.33	24.62 ± 0.30	3.74 ± 0.13	—
1500 GeV	32.55 ± 0.33	23.59 ± 0.30	3.60 ± 0.13	0.11 ± 0.03
2000 GeV	25.43 ± 0.31	18.11 ± 0.27	2.83 ± 0.12	0.06 ± 0.02
2500 GeV	16.57 ± 0.26	11.32 ± 0.23	1.71 ± 0.09	0.03 ± 0.02

Table 5.1: HIP TRT trigger efficiencies in percentages for spin-1/2 monopoles pair-produced with the Drell-Yan model. The uncertainties on the trigger efficiencies are statistical. The efficiency for the mass 1000 GeV charge $|g| = 2.0g_{\mathrm{D}}$ sample is missing due to complications during the official MC production that prevented its successful completion.

events that passed certain triggers and fulfilled specific conditions. The RPVLL (R-parity violating and long-lived particles) filter used for this purpose selects, among others, events that passed the dedicated HIP trigger.

The last step in the data size reduction chain is the production of a format for offline analysis with the ROOT framework. Private ROOT ntuples contain preselected monopole candidates that passed a set of preselection criteria that is highly efficient for monopole events that passed the dedicated trigger. These preselection criteria are roughly optimized based on the trigger used and the expected signature of a monopole. Samples of simulated monopole events do not need to be processed using the RPVLL filter as their size is small enough for storage and data analysis; the reduction to private ROOT ntuples is performed directly on them.

A monopole candidate is defined, from an event passing the HIP trigger, as a region in the TRT with a large fraction of TRT HT hits associated with a calorimeter cluster, as described in Ch. 4. Preselected monopole candidates saved to private ROOT ntuples for further analysis fulfill the following two requirements: a calorimeter cluster with transverse energy greater than 16 GeV (this requirement ensures that the preselected cluster corresponds to the RoI identified by the Level-1 `EM18VH` trigger), a TRT region with a number, N_{HT}, and fraction, f_{HT}, of TRT HT hits in a narrow road exceeding 9 and 0.4, respectively (see Sec. 5.2.1 for the description of the TRT hit counting algorithm used to determine N_{HT} and f_{HT}). Calorimeter clusters and TRT regions that do not meet these criteria are discarded.

Offline reconstruction of preselected magnetic monopoles in events selected by the HIP TRT trigger is performed using the energy deposition in two detectors only: the TRT and the calorimeter. The output of the TRT contains information about two different energy thresholds, making it a great discriminant for monopoles. The SCT, on the other hand, does not have an output with information on the ionization produced by the incident particle. As mentioned in Sec. 4.1.1, the signal of monopoles in the Pixel detector would be lost due to the length of the time-over-threshold overflowing the maximum number of bits allowed. Therefore, the TRT is the only ID sub-detector used for the reconstruction of monopoles in events that passed the trigger. Energy deposits in the EM calorimeter are used to select monopole candidates based on the amount and shape of the energy deposition while energy deposits in the hadronic calorimeter are used to ensure that inefficiencies introduced by the Level-1 trigger are accounted for.

5.2.1 Monopole reconstruction in the TRT

In order to identify regions in the TRT with high energy deposition from monopoles and associated δ-rays, an algorithm to count the TRT hits was developed based on that used in the search for magnetic monopoles in the 2011 ATLAS dataset [77]. It is important to note that no ID tracks with TRT extension have been observed in simulated monopole events. A possible explanation for this is that the pattern finding algorithm of the track reconstruction fails to identify TRT extensions due to the large number of TRT hits in a broad region.[14]

High-threshold hit counting algorithm

Using the orientation of the calorimeter cluster, a wedge-shaped region in the TRT of size $\Delta\phi = \pm 0.05$ centred on the cluster's azimuthal angle ϕ_{clust} is defined. Within this region a smaller region is determined using information from the TRT HT hits only.

The peak $(\Delta\phi)_{\text{max}}$ of the distribution $\Delta\phi = \phi_{\text{HT}} - \phi_{\text{clust}}$ of TRT HT hits in the wedge

[14]The region of high ionization density is expected to be broad with respect to the usual signature of charged particles such as electrons. However, this high ionization density region is in itself narrow, with a width of the order of one cm

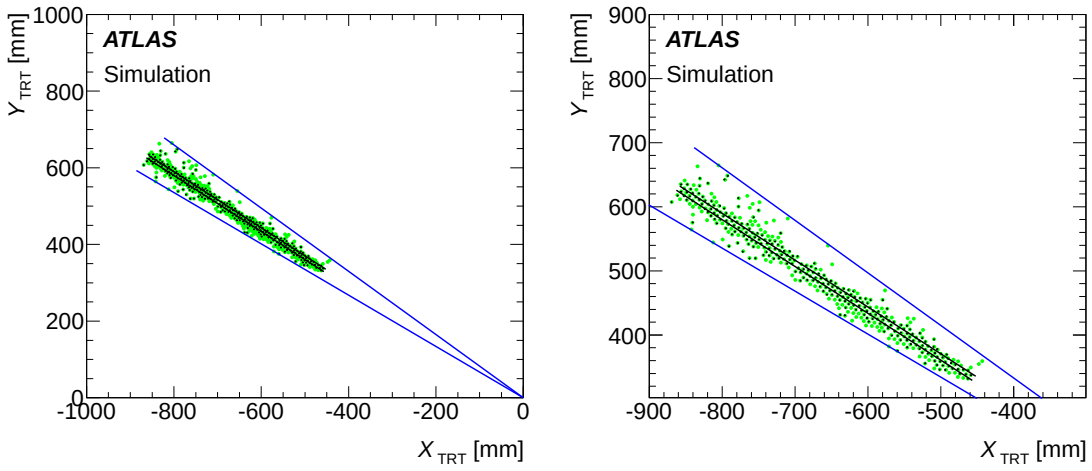

Figure 5.4: An example of a simulated monopole trajectory and the TRT region constructed for the hit counting in the barrel in the transverse plane. The blue lines represent the wedge of size $\Delta\phi = \pm 0.05$ and the black lines depict the limits of the ± 4 mm rectangular road. Straws with TRT LT hits are coloured green and straws with TRT HT hits have black markers overlaid. The right plot is a closeup of the rectangular road [77].

of size $\Delta\phi = \pm 0.05$ is determined, and a narrower wedge of size $\Delta\phi = \pm 0.01$ centred on $\phi = \phi_{\text{clust}} + (\Delta\phi)_{\text{max}}$ is defined. Based on the TRT HT hits in this narrower wedge, the average value $\phi_{\text{HT}}^{\text{avg}}$ is obtained. This value $\phi_{\text{HT}}^{\text{avg}}$ is used in the construction of a region in the TRT along the monopole trajectory in which the fraction of HT hits is computed and used as a discriminating variable.

In the TRT barrel, where only information on the r and ϕ coordinates of the TRT hits is available, a rectangular road of width ± 4 mm centred on $\phi_{\text{HT}}^{\text{avg}}$ is built. This road is sufficiently wide to include two TRT straws (a TRT straws are 4 mm in diameter). Also, the maximum range of a typical δ-ray falls within the width of the rectangular road, as mentioned in Sec. 4.1.1. In the TRT end-cap, where only z and ϕ information is available, a different type of road has to be constructed. A wedge-shaped road of size $\Delta\phi = \pm 0.006$ centred on $\phi_{\text{HT}}^{\text{avg}}$ is defined. The angular width of this road is chosen so that it is ± 4 mm at the inner radius of the TRT end-cap wheels. An example of the rectangular road constructed for a simulated monopole trajectory in the TRT barrel is presented in Fig. 5.4.

The numbers of TRT hits and TRT HT hits are counted in the road in order to calculate

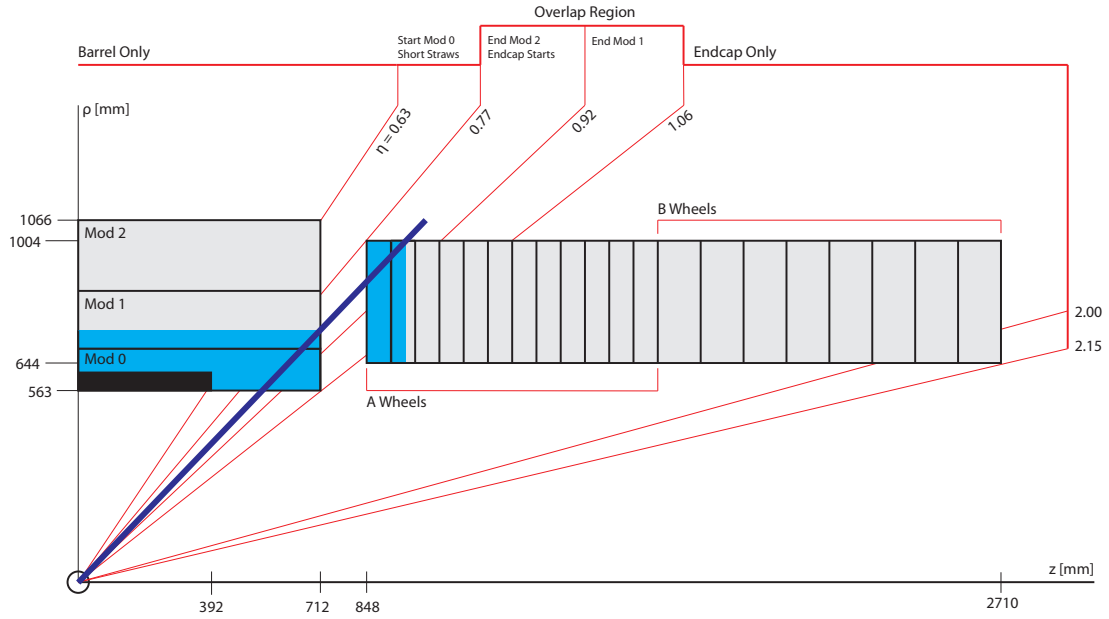

Figure 5.5: Graphic depiction of the TRT hit counting algorithm for a monopole in the TRT barrel–end-cap transition region (blue line). The blue shaded areas represent the straws in the barrel and the end-cap included in the hit counting algorithm [35].

the fraction of TRT HT hits over all hits, f_{HT}. The geometry of the TRT is such that it is only possible to know on which side, i.e., $\eta < 0$ or $\eta > 0$, the hit occurred. The information of the exact η coordinate of the hit is not available. Thus, all hits on the same side of the TRT as the calorimeter cluster are counted. In the region $|\eta| < 0.1$, it is difficult to know through which side of the detector the monopole passed due to the propagation of δ-rays and the possible bending of the monopole trajectory in the solenoidal magnetic field. Therefore, the fraction of TRT HT hits is calculated independently in both positive and negative barrels, and the maximum is taken as f_{HT} provided there are at least ten TRT hits on the corresponding side. If no side has at least ten TRT hits, hits on both sides of the TRT barrel are included in the calculation of f_{HT}. Similarly, in the barrel–end-cap transition region, $0.77 < |\eta| < 1.06$, the fraction of TRT HT hits is calculated independently in both barrel and end-cap, and the maximum is taken as f_{HT} provided there are at least ten TRT hits on the corresponding detector element. If no detector element has at least ten TRT hits, hits in both the barrel and the end-cap are counted and included in the

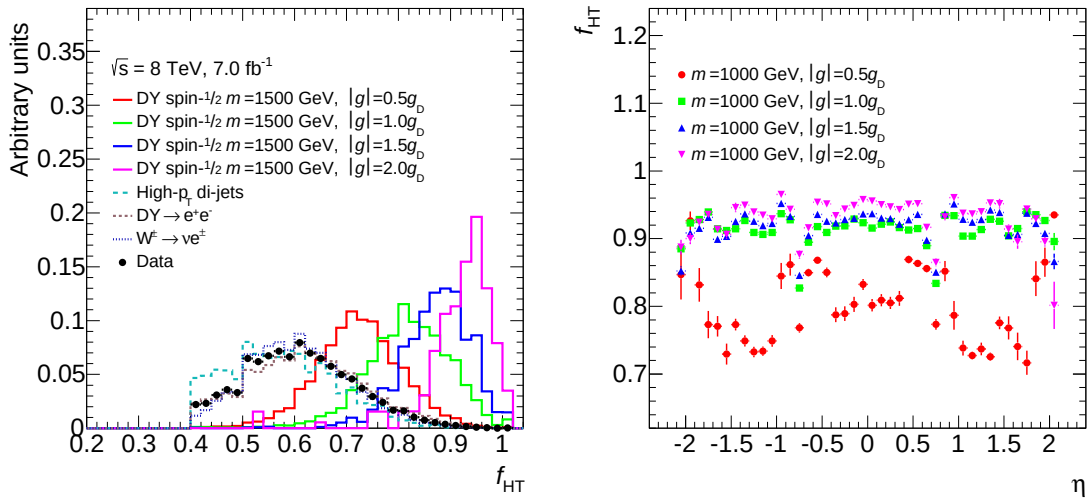

Figure 5.6: Left: Distribution of the fraction of TRT HT hits, f_{HT}, for spin-1/2 Drell-Yan monopoles of mass $m = 1500$ GeV and various charges. Collision data and background MC samples are also shown. Right: Distribution of the fraction of TRT HT hits, f_{HT}, as a function of calorimeter cluster pseudorapidity for single monopoles of mass $m = 1000$ GeV and various charges.

computation of f_{HT}. Figure 5.5 depicts the TRT hit counting algorithm for a monopole in the TRT barrel–end-cap transition region. The blue shaded areas represent the straws in the barrel and end-cap expected to have TRT HT hits.

Performance of the fraction f_{HT} as a discriminating variable

As mentioned in Secs. 4.1.1 and 4.3, a large fraction of TRT HT hits, as produced by highly ionizing monopoles and associated δ-rays, can also be observed in events with electrons and overlapping minimum ionizing particles. However, based on the TRT HT hit probability for electrons and muons [100], it is expected that f_{HT} takes higher values for monopoles. Figure 5.6 (left) shows the distribution of f_{HT} for spin-1/2 Drell-Yan monopoles of mass $m =$ 1500 GeV and various charges. The fraction f_{HT} is higher for higher charge monopoles as the ionization energy deposit is greater. The preselection requirement $f_{\mathrm{HT}} > 0.4$ described above is highly efficient for monopole events. The fraction TRT HT hits, f_{HT}, as a function of calorimeter cluster pseudorapidity for monopoles of mass $m = 1000$ GeV and various charges is shown in Fig. 5.6 (right).

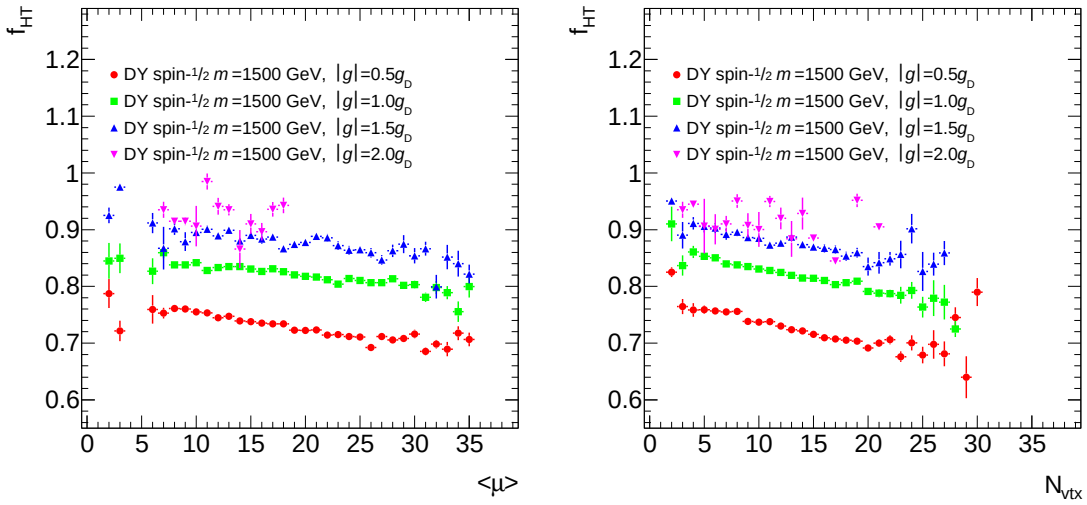

Figure 5.7: Profile histogram of the fraction of TRT HT hits, f_{HT}, as a function of the average number of interactions per bunch crossing $\langle\mu\rangle$ (left) and the number of primary reconstructed vertices N_{vtx} (right) for pair-produced spin-1/2 monopoles of mass $m = 1500$ GeV and various charges. The histogram for charge $|g| = 2.0g_{\mathrm{D}}$ is truncated at $\langle\mu\rangle$=18 due to complications with the official production of the MC samples.

The narrow width of the roads used in the hit counting algorithm ensures robustness against pileup since charged particles from additional collisions mainly produce TRT LT hits. A larger number of TRT LT hits in the road makes the fraction f_{HT} take lower values as the number of TRT HT hits produced by a monopole is expected not to change with pileup. Figure 5.7 shows the profile histogram of the fraction of TRT HT hits f_{HT} as a function of the average number of interactions per bunch crossing $\langle\mu\rangle$ (left) and the number of primary reconstructed vertices N_{vtx} (right). As the average number of interactions per bunch crossing increases, the fraction f_{HT} drops by a maximum of 5%. Therefore, it can be considered as robust against pileup, ensuring that discriminating power is maintained despite the changing instantaneous luminosity conditions during one run of data taking.

Removal of overlapping calorimeter clusters

Several calorimeter clusters with transverse energy $E_{\mathrm{T}} > 16$ GeV may be matched to the same region in the TRT with a high fraction of TRT HT hits. Such is the case when the topological clustering algorithm returns clusters that are very close in η and in ϕ, typically

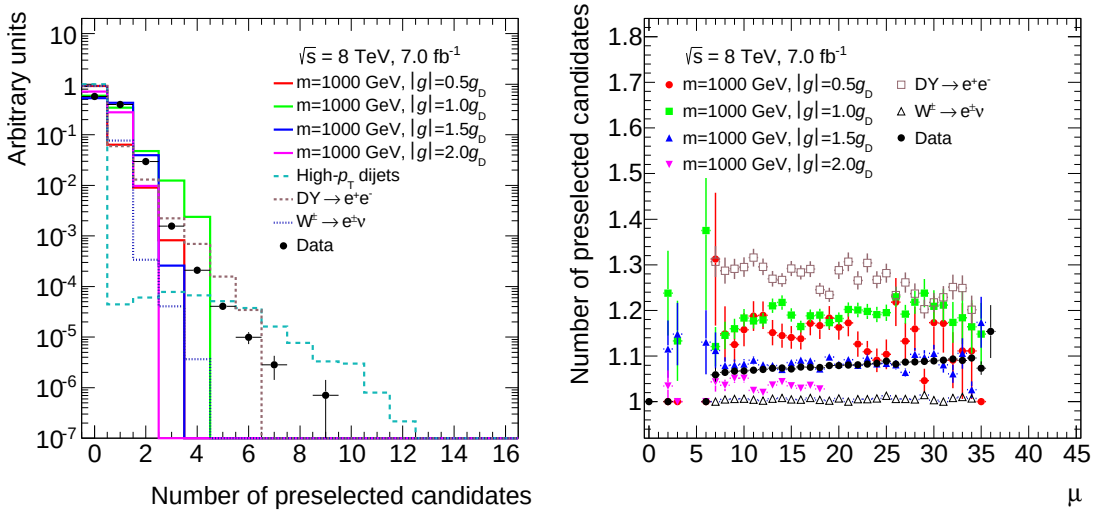

Figure 5.8: Number of preselected monopole candidates (left) and profile histogram of the number of preselected monopole candidates as a function of pileup $\langle\mu\rangle$ (right), in single monopole events of various charges and mass $m = 1000$ GeV. Collision data and background MC samples are also shown. The profile histogram of the number of preselected monopole candidates as a function of $\langle\mu\rangle$ only includes events in which at least one monopole candidate has been preselected.

within $\Delta\eta \times \Delta\phi = 0.1 \times 0.1$. Figure 5.8 shows the number of preselected monopole candidates per event for single particle monopoles of mass $m = 1000$ GeV and various charges, background MC samples and collision data. In single monopole events, only one preselected candidate per event is expected. It is observed, however, that a fraction of single monopole events have more than one preselected candidate. These additional preselected candidates do not originate from clusters created by charged particles from pileup events since the average number of preselected candidates per event in events with at least one preselected candidate is fairly uniform across all $\langle\mu\rangle$ values in the samples. Thus, the preselected candidate multiplicity is an effect of the clustering algorithm, which splits topological clusters when more than one maximum of energy deposition is found. Multiple maxima can be produced when the energy deposition is large and associated with energetic δ-rays that propagate in the LAr calorimeter and radiate. This can be seen in Fig. 5.9 where higher charge monopole events are associated with a set of clusters with a larger standard deviation of the pseudorapidity coordinate η.

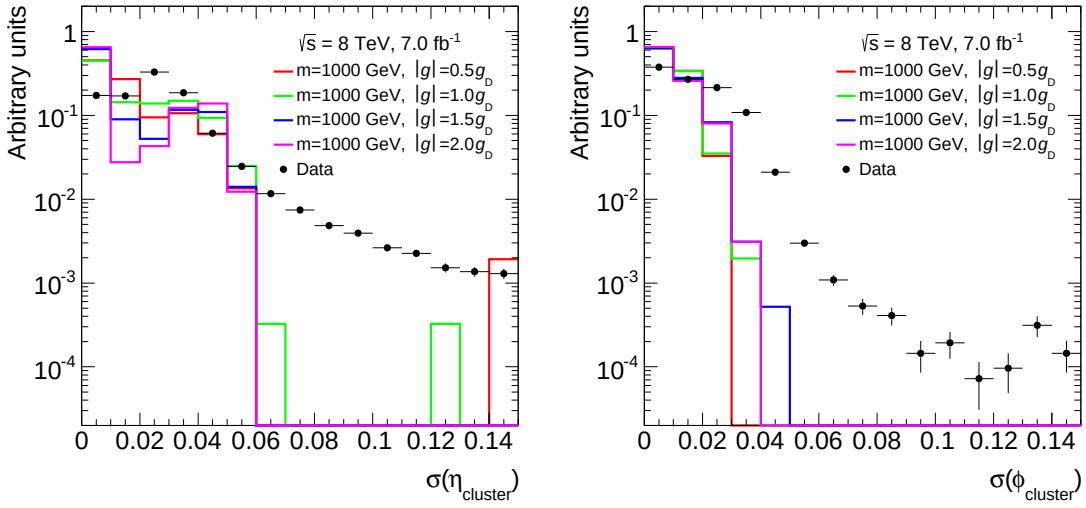

Figure 5.9: Standard deviation of the distribution of the angular coordinates η (left) and ϕ (right) of calorimeter clusters from preselected monopole candidates from single monopole events with more than one preselected candidate for various signal MC samples. Collision data are also shown.

Multiple monopole candidates in single monopole events is an undesirable situation as it means that the same TRT region has been used in the formation of more than one preselected monopole candidate. In order to identify which calorimeter clusters have been associated to the same TRT region, their η and ϕ information is used. A set of clusters is defined as associated to the same TRT region if the standard deviations of the pseudorapidity and azimuthal angle satisfy $\sigma(\eta_{\text{cluster}}) < 0.1$ and $\sigma(\phi_{\text{cluster}}) < 0.05$, respectively. These distributions can be seen in Fig. 5.9. These selection criteria ensure that only clusters associated with the same TRT region are taken into account in the overlap removal.

In order to ensure that there is only one calorimeter cluster associated to each TRT region with a large fraction of TRT HT hits, the cluster with the highest summed energy deposition in the presampler and EM1 is selected. This criterion is based on the expected signature of a monopole in the calorimeter, which must deposit a large fraction of its energy early in the calorimeter. Energetic δ-rays emitted along the monopole trajectory may penetrate to EM2 and be reconstructed as a cluster without energy deposition the presampler or EM1.

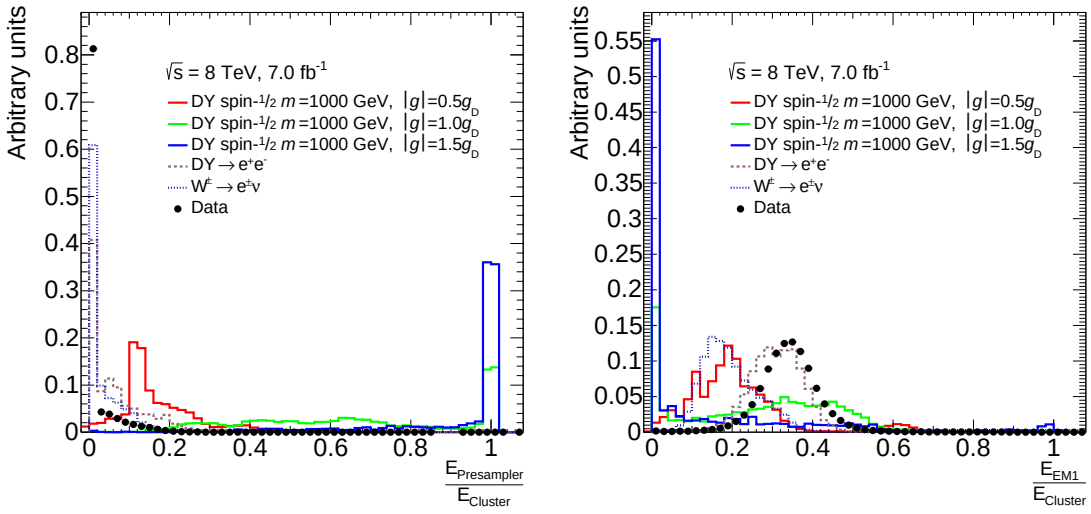

Figure 5.10: Fraction of cluster energy deposited in the presampler (left) and EM1 (right) for spin-1/2 monopoles of mass 1000 GeV and various charges. Collision data and background MC processes containing electrons are also shown.

5.2.2 Monopole reconstruction in the LAr electromagnetic calorimeter

The Level-1 trigger requires a minimum transverse energy deposition of 18 to 20 GeV in the calorimeter. A similar requirement is applied as part of the monopole reconstruction: calorimeter clusters are required to have a minimum transverse energy deposition in the LAr EM calorimeter, i.e., the summed transverse energy in the presampler, EM1, EM2 and EM3 must be $E_{\mathrm{T}}^{\mathrm{EM}} > 16$ GeV. In addition, only calorimeter clusters in the pseudorapidity ranges $|\eta| < 1.375$ and $1.52 < |\eta| < 2.0$ are considered. The requirement $|\eta| < 2.0$ is based on the TRT coverage, which defines the Level-2 dedicated trigger acceptance. Clusters in the LAr calorimeter barrel–end-cap transition region, $1.375 < |\eta| < 1.52$, are rejected to ensure robustness of the final selection variables (see Sec. 6.4.1).

The EM calorimeter was designed to measure the energy of electrons and photons. The electromagnetic cascades produced by these particles develop fully in EM2, the deepest layer, making it a crucial layer for their measurement. However, due to the suppression of bremsstrahlung and the highly ionizing nature of monopoles, which leads to an early stop in the calorimeter, the presampler and EM1 are the most relevant layers in this search. This is the case in particular, when pair-produced spin-1/2 monopoles are considered, as the kinetic

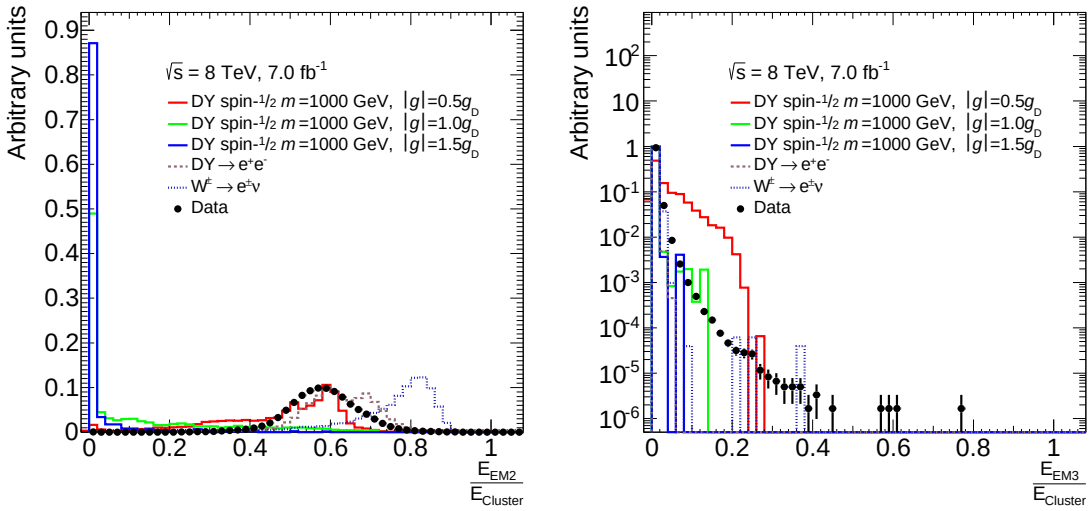

Figure 5.11: Fraction of cluster energy deposited in EM2 (left) and EM3 (right) for spin-1/2 monopoles of mass 1000 GeV and various charges. Collision data and background MC processes containing electrons are also shown.

energy spectrum of the generated monopoles is much softer than in the single monopole case. Figures 5.10 and 5.11 show the fraction of the cluster energy deposited in each layer for spin-1/2 monopoles of various charges. It must be noted that for charges $|g| \geq 1.0g_{\mathrm{D}}$ a significant faction of the energy is deposited in the first layers. For lower charges, such as $|g| = 0.5g_{\mathrm{D}}$, a significant fraction of the energy is deposited in EM2. A very small fraction of the energy is deposited in the outermost layer, EM3, in all cases. Electrons, on the other hand, do not deposit a significant amount of energy in the presampler; most of the energy deposition occurs in the deeper layer EM2.

The transverse energy deposition by monopole candidates in the EM calorimeter must be at least 16 GeV, thus, based on the large fraction of the cluster energy deposited in the presampler and EM1, it is required that monopole candidates deposit at least 5 GeV in the presampler or EM1. The "or" operator is necessary as the presampler only covers the range $|\eta| < 1.8$. Also, lower charge monopoles may not deposit 5 GeV in the presampler in some cases due to the shallow depth of this layer. This requirement rejects background candidates that fulfill $E_{\mathrm{T}}^{\mathrm{EM}} > 16$ GeV but do not have a significant energy deposition in the presampler or EM1. Figures 5.12 and 5.13 show the energy deposited by monopoles of

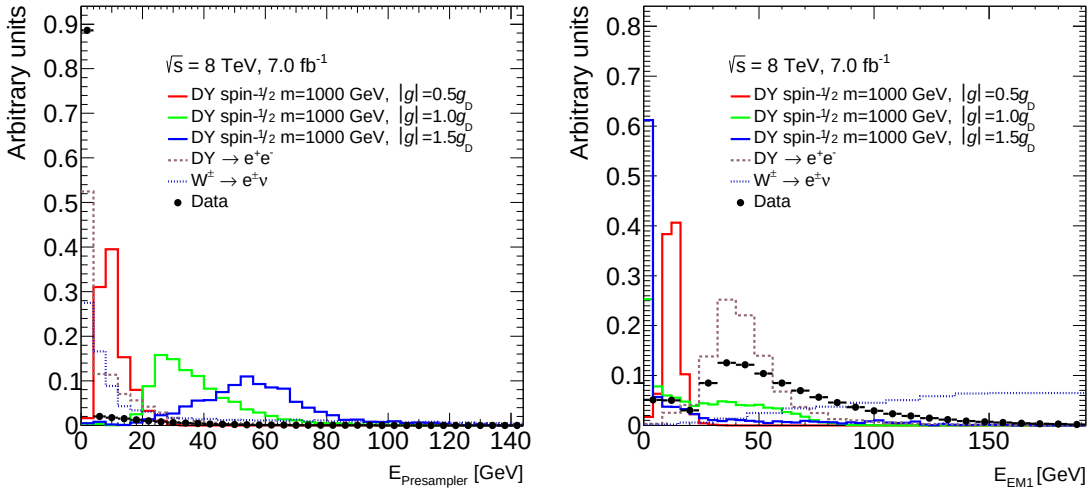

Figure 5.12: Energy deposition in the presampler (left) and EM1 (right) for monopoles of mass 1000 GeV and various charges. Collision data and background MC processes containing electrons are also shown.

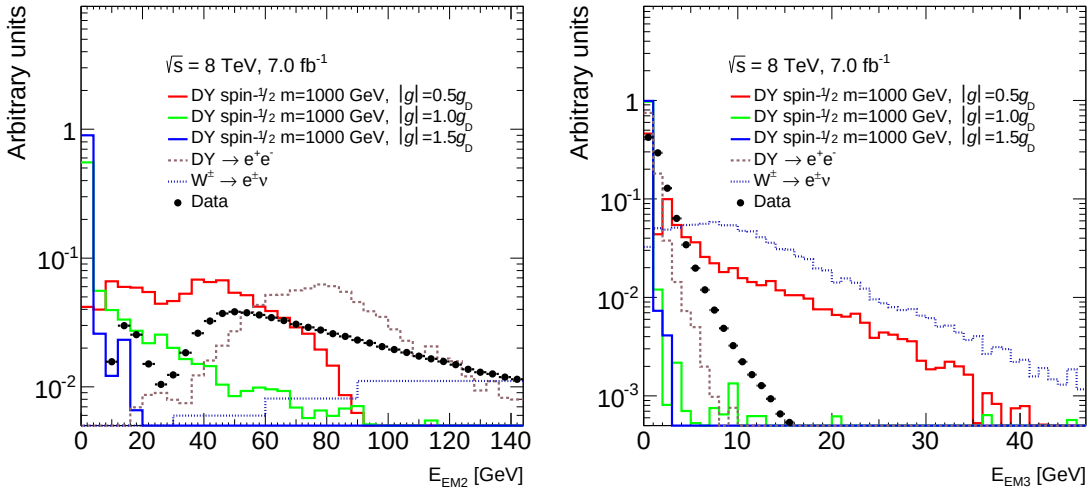

Figure 5.13: Energy deposition in EM2 (left) and EM3 (right) for monopoles of mass 1000 GeV and various charges. Collision data and background MC processes containing electrons are also shown.

mass 1000 GeV and various charges in each layer of the EM calorimeter. It can be seen that a requirement on the minimum energy deposition in the presampler or EM1 of 5 GeV would not significantly affect the selection efficiency for monopole events.

5.2.3 Hadronic energy deposition

The Level-1 trigger used as a seed by the dedicated HIP trigger rejects regions of interest with a transverse energy deposition in the hadronic calorimeter greater than 1 GeV. In order to ensure that all inefficiencies introduced by the Level-1 trigger hadronic veto are properly accounted for, the monopole reconstruction algorithm rejects calorimeter clusters with energy deposition in the hadronic calorimeter exceeding 1 GeV. The energy deposition in the hadronic calorimeter is defined as the energy contained in the cluster cells belonging to the tile calorimeter barrel and extended barrel. These two regions effectively cover the range $|\eta| < 1.7$, allowing background from multijet events to fulfill this criterion despite energy being deposited in the hadronic calorimeter end-cap, which extends beyond $|\eta| = 1.7$.

5.2.4 Lateral dispersion of energy deposition

A calorimeter cluster with very low lateral energy dispersion due to the highly suppressed electromagnetic cascade is the main signature of a monopole in the EM calorimeter. In order to measure the lateral dispersion, several variables were studied. The energy-weighted cluster size, σ_{R}, based on the variable used in the search in 2011 data [77], was extended to the presampler, EM1 and EM2. This variable was shown to be non-optimal due to losses in signal–background discriminating power arising from the coarse segmentation in the presampler (see App. B). A second variable that measures the fraction of the cluster energy deposited in the highest energy cells was therefore designed. This variable, named w (it stands for width for historical reasons), is constructed and optimized for the three innermost layers of the EM calorimeter. The dispersion w_i for each layer is defined as

$$w_i = \frac{\sum_n^N E_n^i}{E_{\mathrm{total}}^i}, \tag{5.1}$$

where E_n^i is the n-th highest energy cell in layer i, where the index i represents the presampler, EM1 or EM2, and $N = 2, 4, 4$ is the number of highest energy cells included in the calculation of w_i for the presampler, EM1 and EM2, respectively. The dispersion in each layer, w_i, is only computed if the total cluster energy in the layer is $E_{\mathrm{total}}^i > 5$ GeV. This requirement ensures that only layers traversed by the monopole candidate are taken into

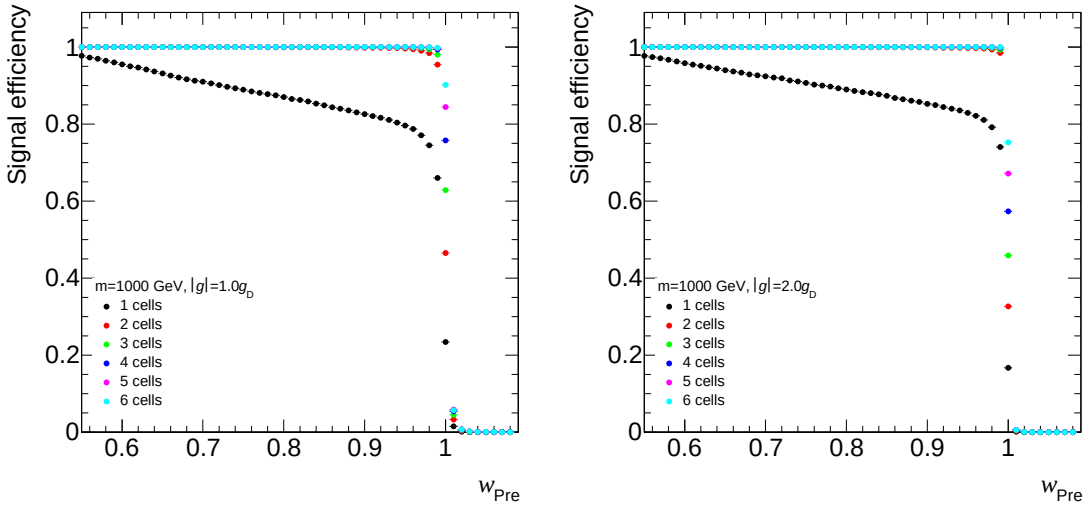

Figure 5.14: Signal efficiency as a function of w_{Pre} in the presampler for single monopoles of mass $m = 1000$ GeV, and charge $g = 1.0g_{\mathrm{D}}$ (left) and $g = 2.0g_{\mathrm{D}}$ (right). Different cases have been considered in which one to six cells are included in the calculation.

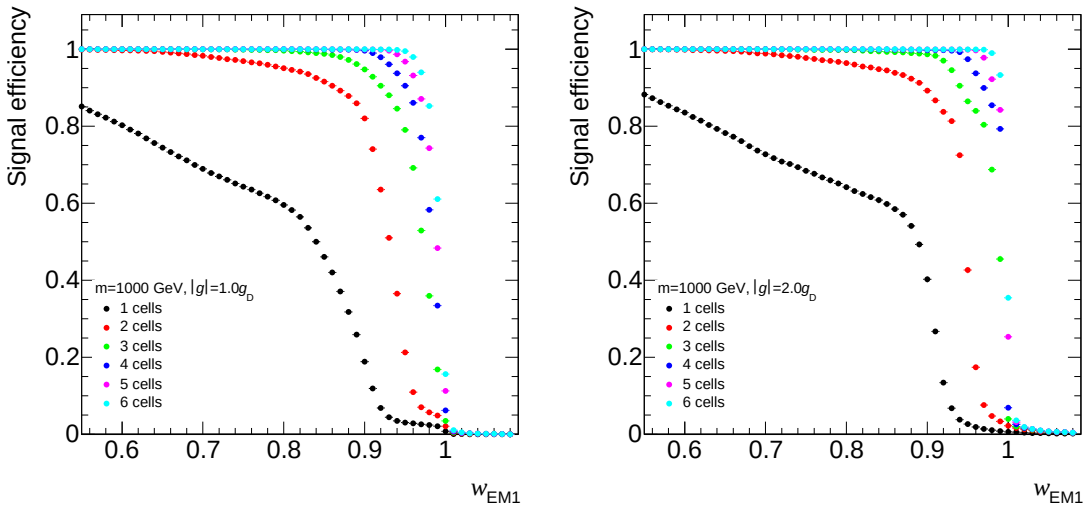

Figure 5.15: Signal efficiency as a function of w_{EM1} in EM1 for single monopoles of mass $m = 1000$ GeV, and charge $g = 1.0g_{\mathrm{D}}$ (left) and $g = 2.0g_{\mathrm{D}}$ (right). Different cases have been considered in which one to six cells are included in the calculation.

account.

The number of cells included in the calculation of w_i was optimized to account for the differences in granularity between the three innermost calorimeter layers. A compromise between signal efficiency, defined as the fraction of signal monopole candidates that pass

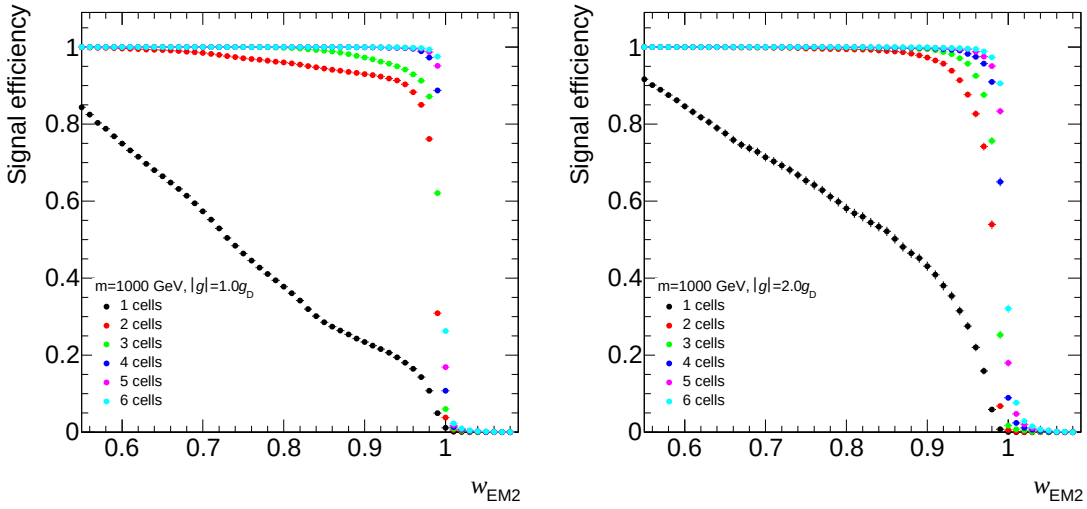

Figure 5.16: Signal efficiency as a function of w_{EM2} in EM2 for single monopoles of mass $m = 1000$ GeV, and charge $g = 1.0g_{\mathrm{D}}$ (left) and $g = 2.0g_{\mathrm{D}}$ (right). Different cases have been considered in which one to six cells are included in the calculation.

a selection cut on w_i, and signal–background discrimination was achieved in this process. Figures 5.14 to 5.16 show the signal efficiency for single monopoles of charge $|g| = 1.0g_{\mathrm{D}}$ and $|g| = 2.0g_{\mathrm{D}}$ and mass $m = 1000$ GeV as a function of a cut on w_i. Figure 5.17 shows the square root of the number of candidates from background MC events from electrons from $W^{\pm}$ decays and Drell-Yan electron–positron pair production that pass a cut on w_i. In order to maximize the signal–background discrimination, it is necessary to choose the minimum number of cells per layer to include in the calculation of w_i. By doing so, clusters with minimal lateral dispersion peak at one while broad energy depositions will peak at lower values. In the absence of an electromagnetic cascade, an EM calorimeter cluster produced by a monopole is expected to have very low lateral dispersion and thus its associated w_i's peak at one.

The discrimination power of w_i as a function of the number of cells and the cut on w_i can be estimated by measuring the sensitivity of w_i to a monopole signal. The sensitivity used in this optimization is described in Ref. [125] and is defined by the expression

$$\frac{\epsilon(t)}{a/2 + \sqrt{B(t)}}, \tag{5.2}$$

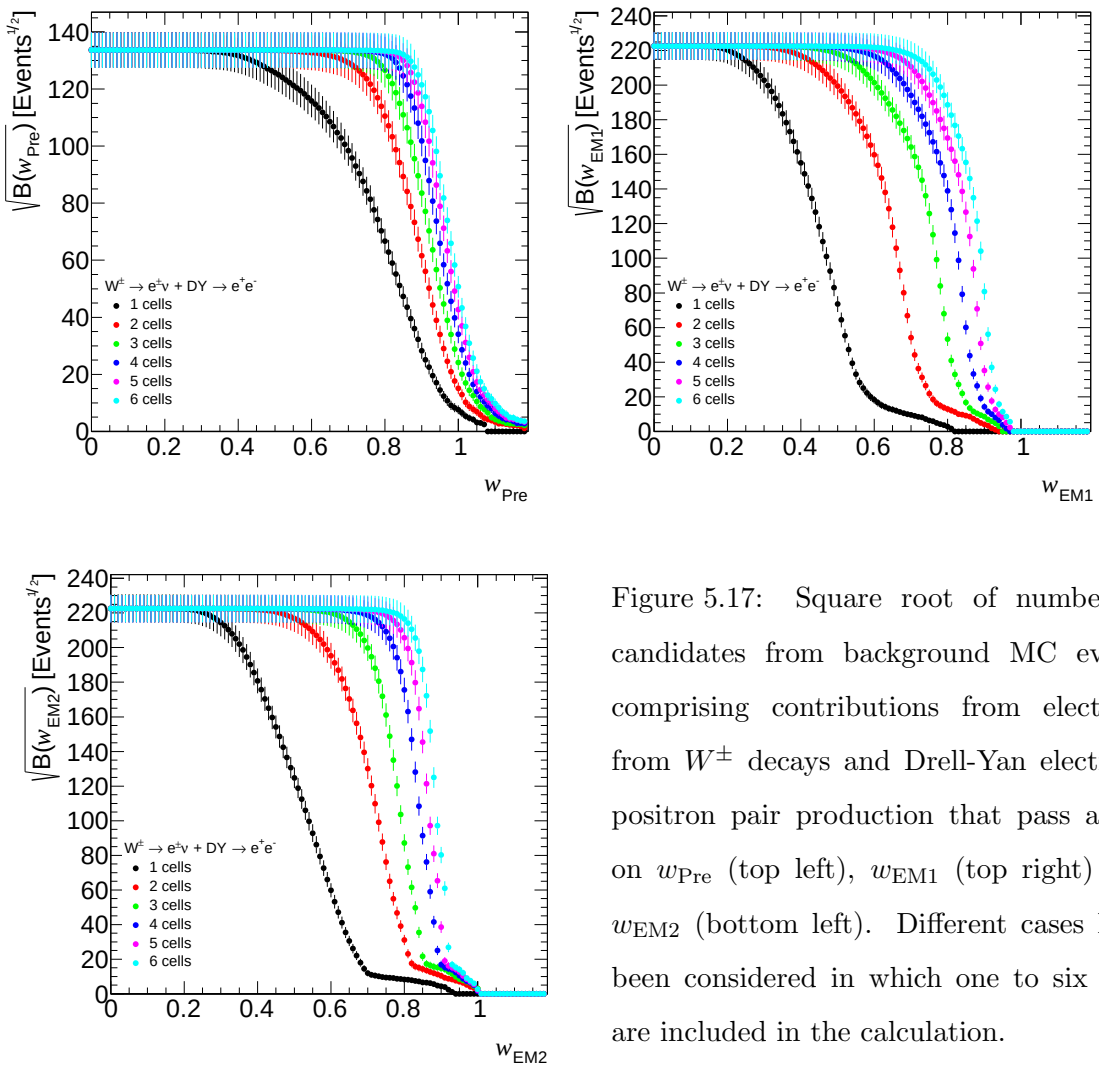

Figure 5.17: Square root of number of candidates from background MC events comprising contributions from electrons from $W^{\pm}$ decays and Drell-Yan electron–positron pair production that pass a cut on w_{Pre} (top left), w_{EM1} (top right) and w_{EM2} (bottom left). Different cases have been considered in which one to six cells are included in the calculation.

where $\epsilon(t)$ is the signal efficiency, defined as the number of candidates that pass the selection criterion t with respect to the total number of preselected candidates, a is the number of standard deviations corresponding to one-sided Gaussian tests at significance 95% (in this case, 2σ was chosen), and $B(t)$ is the number of background events satisfying the selection criterion t. This definition of sensitivity suits this search as it is independent of the (unknown) cross section of the signal, unlike other "significance-like" definitions such as $S/\sqrt{B}$ and $S/\sqrt{S+B}$. In this case the monopole signal efficiency has been compared against background from events containing electrons from $W^{\pm}$ boson decays and Drell-

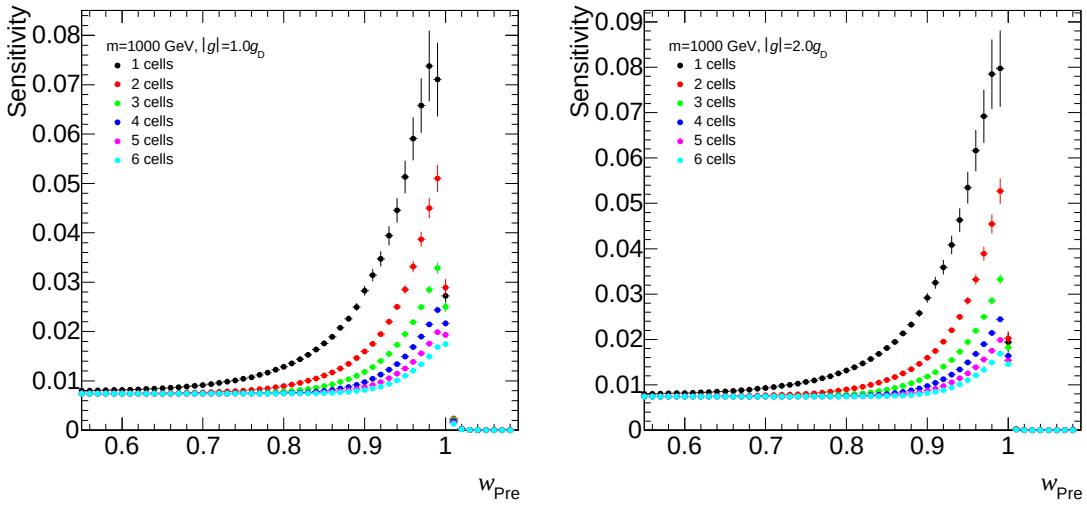

Figure 5.18: Sensitivity as a function of w_{Pre} in the presampler for single monopoles of mass $m = 1000$ GeV and charges $g = 1.0g_{\mathrm{D}}$ (left) and $g = 2.0g_{\mathrm{D}}$ (right). Different cases have been considered in which one to six cells are included in the calculation.

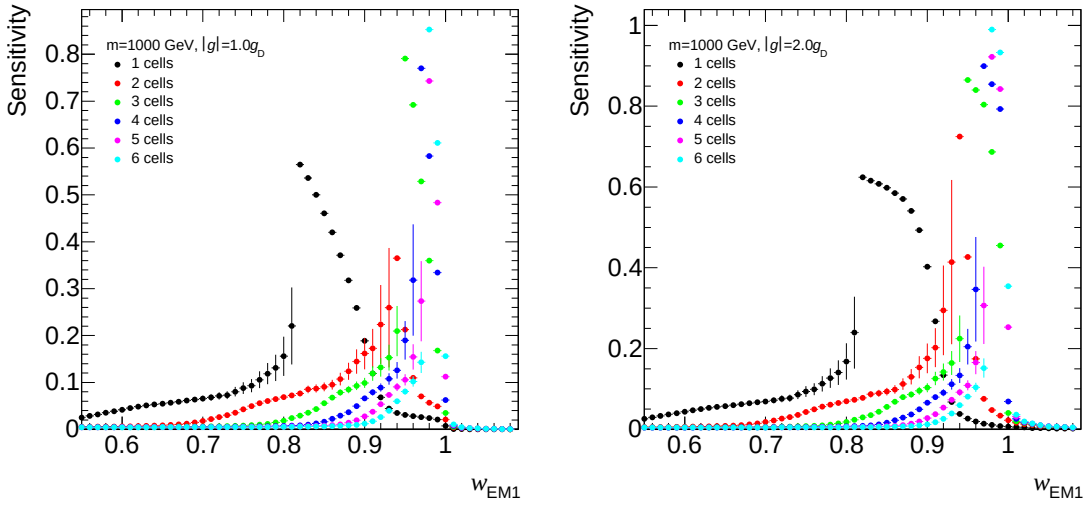

Figure 5.19: Sensitivity as a function of w_{EM1} in EM1 for single monopoles of mass $m = 1000$ GeV and charges $g = 1.0g_{\mathrm{D}}$ (left) and $g = 2.0g_{\mathrm{D}}$ (right). Different cases have been considered in which one to six cells are included in the calculation.

Yan production of electron–positron pairs since electrons are expected to generate narrower energy depositions in the calorimeter than jets from strong interactions. Figures 5.18 to 5.20 show the sensitivity as a function of a cut on w_i for different numbers of cells. The ideal number of cells to include in the calculation of w_i is found when the sensitivity is maximal

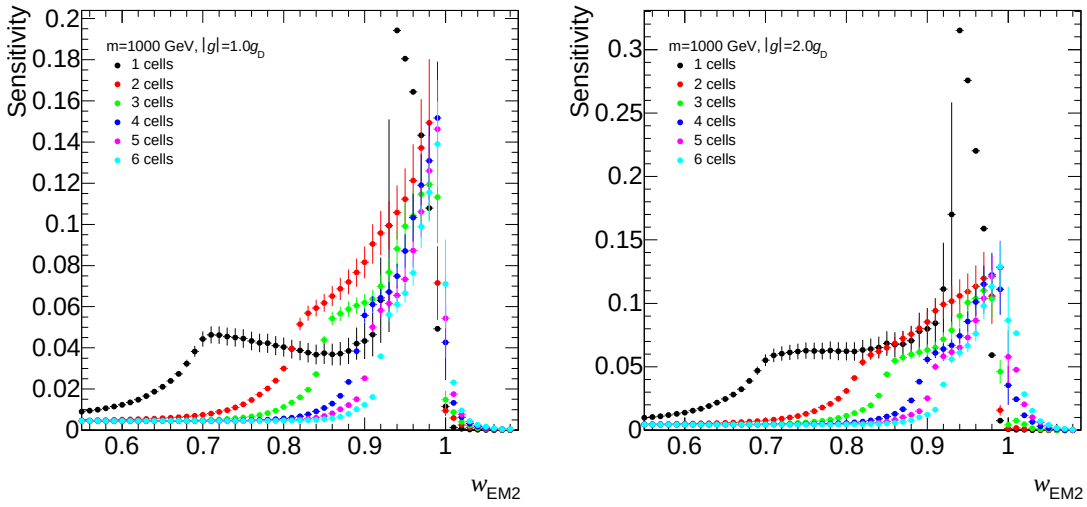

Figure 5.20: Sensitivity as a function of w_{EM2} in EM2 for single monopoles of mass $m = 1000$ GeV and charges $g = 1.0g_{\mathrm{D}}$ (left) and $g = 2.0g_{\mathrm{D}}$ (right). Different cases have been considered in which one to six cells are included in the calculation.

so long as the efficiency is kept high for values of w_i between 0.9 and 0.96. Values of w_i lower than 0.9 may increase the background while values higher than 0.96 may make the search sensitive to large systematic uncertainties on the event selection efficiency.

From Figs. 5.14 and 5.18 it can be seen that for the presampler, the computation of w_{Pre} using a single cell offers the best sensitivity. Unfortunately, the signal efficiency is much lower than for the cases in which more than one cell is included. Based on this, w_{Pre} is calculated using the two highest energy cells. For EM1, as shown in Figs. 5.15 and 5.19, high sensitivity is achieved using four cells, which peaks at high w_{EM1}, while keeping a high signal efficiency. Therefore, four cells are used for the calculation of w_{EM1}. Finally, Figs. 5.16 and 5.20 show that in EM2, very high signal efficiency is achieved by including four or more cells in the calculation of w_{EM2}. Thus, four cells are chosen as it yields a higher sensitivity.

Figure 5.21 shows the distributions of w_i for single monopoles of mass $m = 1000$ GeV and various charges, along with collision data and background MC samples. The coarse segmentation of the presampler is reflected in the lower discrimination power observed for w_{Pre}. Nevertheless, the expected backgrounds deposit very little energy in the presampler

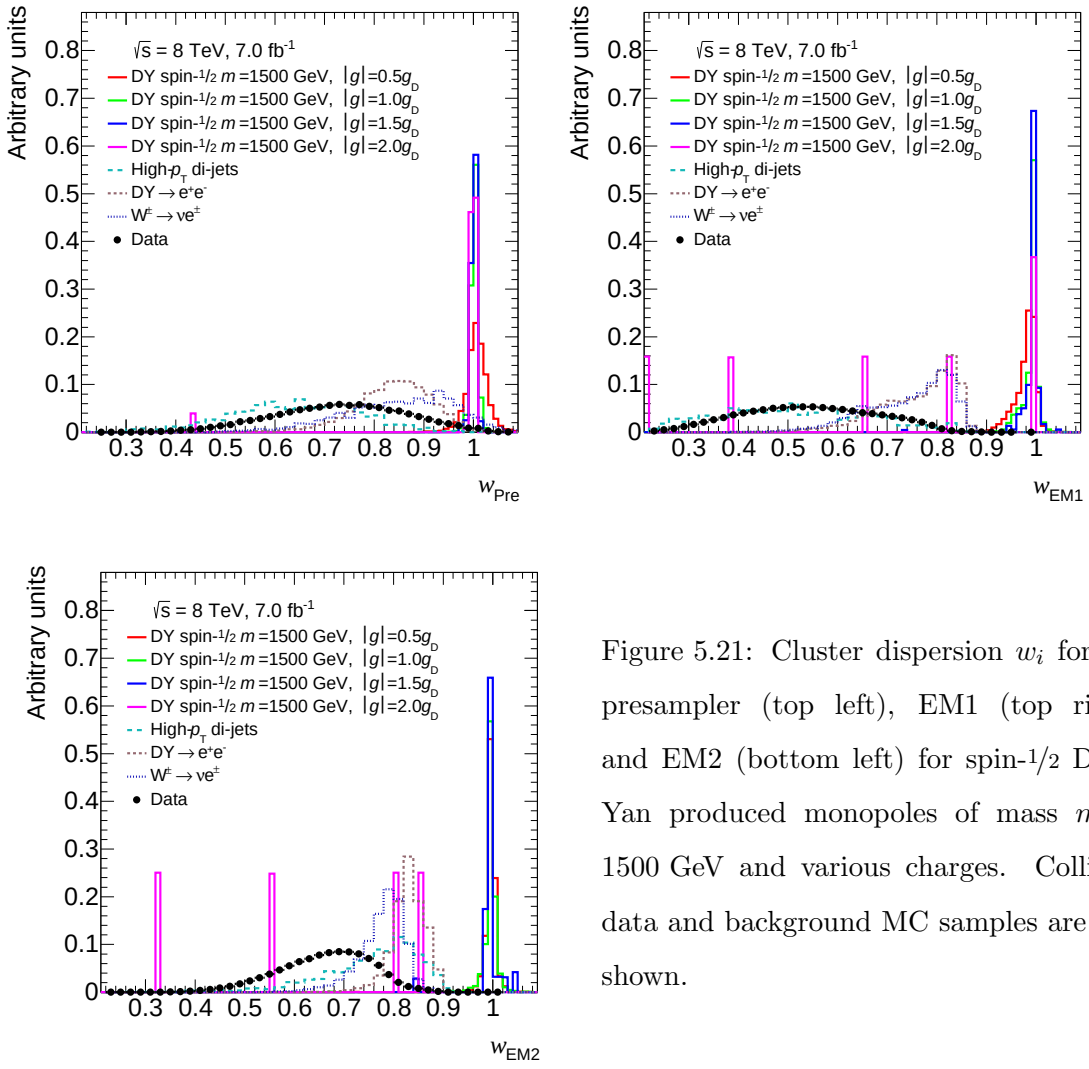

Figure 5.21: Cluster dispersion w_i for the presampler (top left), EM1 (top right) and EM2 (bottom left) for spin-1/2 Drell-Yan produced monopoles of mass m = 1500 GeV and various charges. Collision data and background MC samples are also shown.

and, in many cases, not even the 5 GeV necessary to define w_{Pre}. The layers EM1 and EM2 have a finer segmentation, allowing for a better discriminating power, in particular in EM1 in which multijet events take much lower values of w_{EM1}.

The measurement of the calorimeter cluster energy dispersion used in this search is the average of the individual w_i. This average includes only those w_i that have been defined, i.e., the total cluster energy in the layer $E_i > 5$ GeV,

$$w = \frac{\sum_i w_i}{N_{\mathrm{defined}}}. \tag{5.3}$$

Figure 5.22 (left) shows the distribution of w for monopoles of mass m = 1000 GeV and

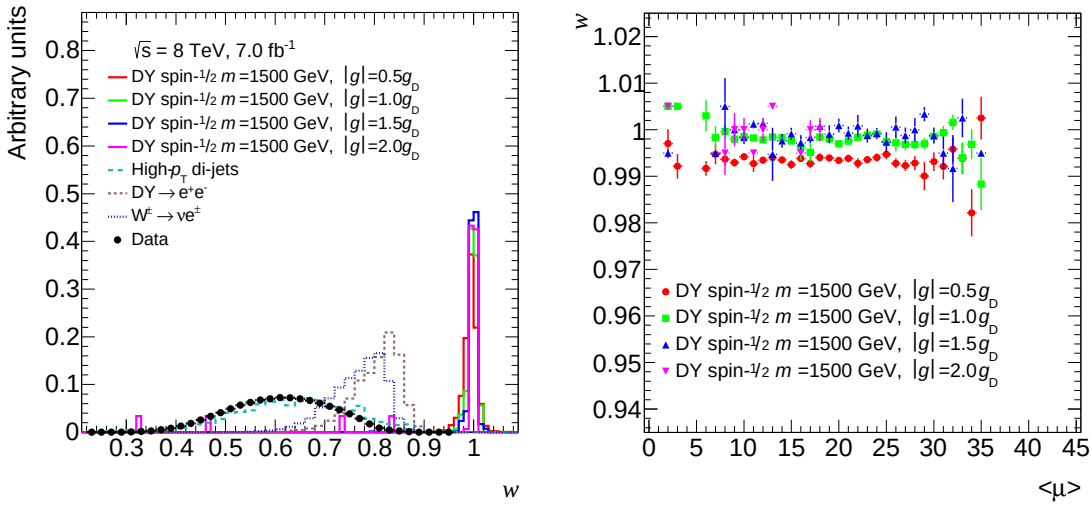

Figure 5.22: Cluster dispersion w (left) and profile histogram of its dependence on pileup $\langle\mu\rangle$ (right) for spin-1/2 Drell-Yan produced monopoles of mass $m = 1500$ GeV and various charges. Collision data and background MC are also shown.

various charges. The combination of w_i offers an excellent discriminating power between monopole signal and background.

As with the fraction of TRT HT hits, f_{HT}, it is important that the cluster dispersion w is robust against pileup, i.e., the measured lateral dispersion does not change significantly with changing pileup conditions. In the EM calorimeter, out-of-time pileup must be considered since the typical readout time of the electronics is greater than the 50 ns spacing between bunches of protons during the 2012 pp run. The quantity $\langle\mu\rangle$ takes into account both the in-time and out-of-time pileup. Therefore, the dispersion w must be very robust against it. This can be seen in Fig. 5.22 (right), which shows remarkable robustness to background from additional collisions.

The cluster dispersion w can be affected by δ-rays that are energetic enough to radiate, e.g., δ-rays with a energy above 20 MeV. In such case, the energy deposition will have a greater lateral dispersion. Figure 5.23 shows that the degradation of the w variable is more significant for lower mass monopoles. The maximum energy of a δ-ray produced by a

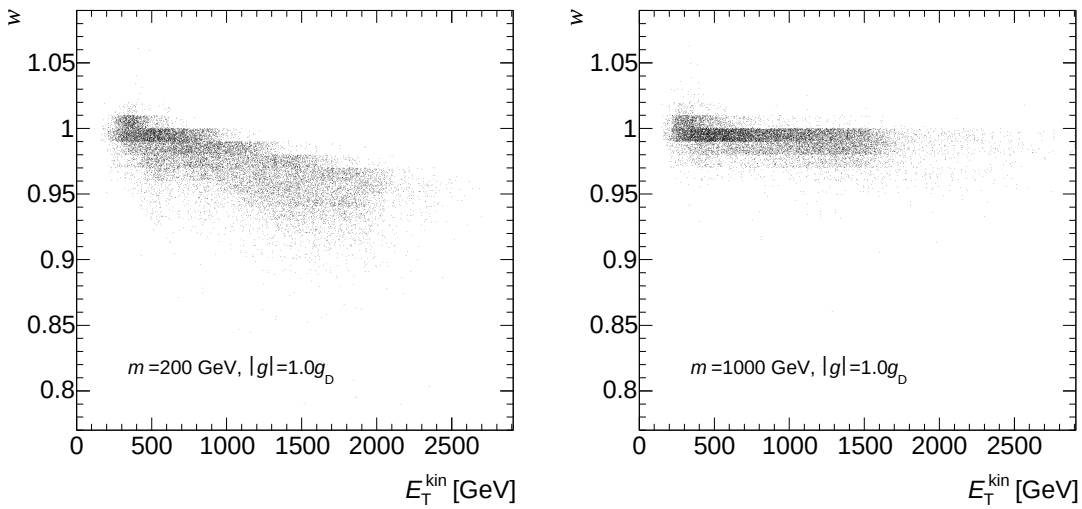

Figure 5.23: Cluster dispersion w as a function of truth monopole $E_{\mathrm{T}}^{\mathrm{kin}}$ for single monopoles of charge $|g| = 1.0g_{\mathrm{D}}$ and masses $m = 200$ GeV (left) and $m = 1000$ GeV (right).

monopole is described by

$$E_{\delta}^{\mathrm{max}} = 2m_e c^2 \frac{E_{\mathrm{mon}}^{\mathrm{kin}}}{m_{\mathrm{mon}}} \left(\frac{E_{\mathrm{mon}}^{\mathrm{kin}}}{m_{\mathrm{mon}}} + 2 \right), \tag{5.4}$$

from where it can be deduced that lighter monopoles yield more energetic δ-rays. For instance, a mass 200 GeV monopole with kinetic energy 1000 GeV would produce δ-rays with a maximum kinetic energy of 36 MeV. Electrons with such energy are in the bremsstrahlung regime in liquid argon. Thus, δ-rays produced by lower mass monopoles in the calorimeter may have sufficient energy to propagate and radiate, generating an electromagnetic cascade that affects the measurement of the lateral dispersion of the energy deposition, causing a degradation of w.

Chapter 6

Search for magnetic monopoles in 2012 8 TeV data

This chapter describes the search for magnetic monopoles in data from proton-proton collisions at $\sqrt{s} = 8$ TeV with the ATLAS detector. A description of the dataset is followed by a summary of the event selection criteria. The event selection efficiencies are presented and a background estimate is performed using collision data. Finally, the systematic uncertainties on the signal event selection efficiency are discussed in detail.

6.1 Data sample

This search for magnetic monopoles was performed using a dataset of pp collisions at $\sqrt{s} = 8$ TeV collected at the ATLAS detector with the HIP trigger during the 2012 run, comprising periods G, H, J and L, which span from eary October through November. The data have been required to fulfill quality criteria by selecting only luminosity blocks present in the good run list `PHYS_Standard All_Good` [126]. Good quality requirements include LHC stable beams, all ATLAS subsystems operational and good data quality flags from each subsystem. The total integrated luminosity of the dataset is 7.0 fb^{-1} with an uncer-

tainty of 2.8% [127] (see Sec. 6.5). Details on the run condition stability can be found in App. C.

Data from the electron–photon stream, of which the HIP trigger is part, is saved in ESD format. These data are then further reduced by selecting events that pass some criteria. This is performed by the `RPVLL_DESD` filter, which contains the DESD HIP filter whose purpose is to select events that pass the HIP trigger.

6.2 Event selection criteria

The selection of events with monopole candidates exploits their unique signature in the ATLAS detector. As described in Ch. 5, the reconstruction of magnetic monopoles relies heavily on two subdetectors: the TRT and the LAr EM calorimeter. The event selection is performed in three stages, starting from a preselection of monopole candidates in events that passed the HIP trigger, followed by a tight selection that discriminates monopole candidates based on the expected signature of monopoles in the calorimeter, and finally, selection of candidate events based on the shape of the energy deposition in the LAr EM calorimeter and the ionization in the TRT.

6.2.1 Signal region definition

The signal region was defined using the f_{HT} and w discriminating variables described in Secs. 5.2.1 and 5.2.2. In order to optimize the cut values that define the signal region, the sensitivity of the search was maximized using the formula from Eq. (5.2). The background contributions have been obtained from pseudo-data randomly generated in the $w - f_{\mathrm{HT}}$ phase space from the individual one-dimensional distributions of f_{HT} and w in collision data. In order to exclude the possibility of generating data points from the signal region in the pseudo-data, only candidate events with $w < 0.8$ were used to generate the one-dimensional f_{HT} distribution and candidate events with $f_{\mathrm{HT}} < 0.6$ were used to generate the one-dimensional w distribution. Figure 6.1 (left) shows the two-dimensional f_{HT} versus w distribution for the generated pseudo-data. By construction, the generated pseudo-data

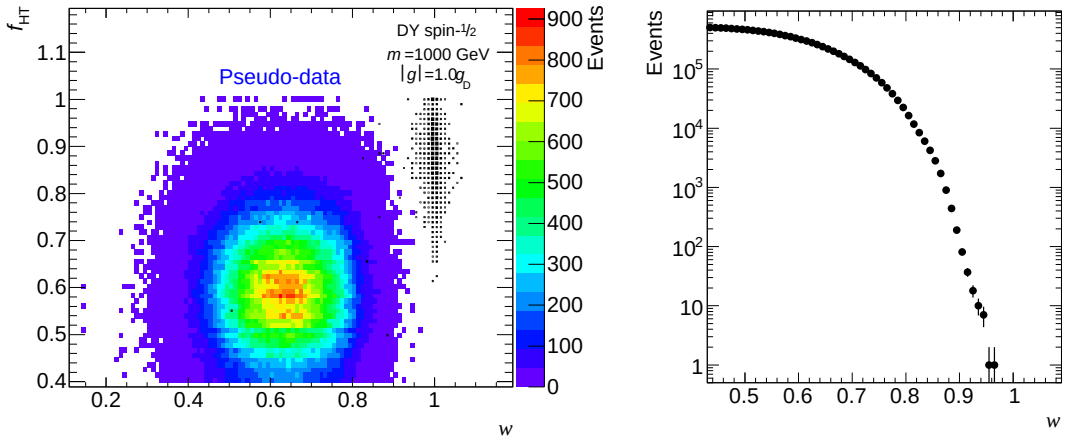

Figure 6.1: Left: Pseudo-data generated from individual one-dimensional distributions of f_{HT} and w. The signal region is excluded by using low-f_{HT} and low-w control regions to generate the pseudo-data. Spin-1/2 monopoles of mass 1000 GeV and charge $|g| = 1.0g_{\mathrm{D}}$ produced with the Drell-Yan model are also shown. Right: Number of events in pseudo-data above a cut on w.

is uncorrelated. This is proven by calculating the Pearson correlation coefficient, which returns a negligible correlation of 0.07% between selection variables.

The efficiency $\epsilon(t)$ is the event selection efficiency for the signal samples after the requirements on f_{HT} and w. The number of background events, $B(t)$, corresponds to the number of simulated MC background events after the requirements on f_{HT} and w. As mentioned earlier in Sec. 5.2.4, this approach for maximizing the sensitivity of a search is independent of the cross section of the signal. This is ideal in order to optimize the signal region using single particle monopole samples with uniform kinematical distributions and spin-1/2 Drell-Yan produced monopoles whose production cross section is known, but not fully reliable.

Due to the excellent discriminating power of w, as shown in Fig. 5.22, the expression from Eq. (5.2) is maximal for values $w > 0.97$ where there are no contributions to $B(t)$ from the pseudo-data events, as shown in Fig. 6.1 (right). As a direct consequence of the absence of background in $w > 0.97$, the sensitivity is maximal for $f_{\mathrm{HT}} > 0.4$, i.e., the signal region would include all candidates above $w > 0.97$ since all candidates with $f_{\mathrm{HT}} < 0.4$ are rejected at the preselection stage. Thus, a selection criterion $f_{\mathrm{HT}} < 0.4$ is too loose

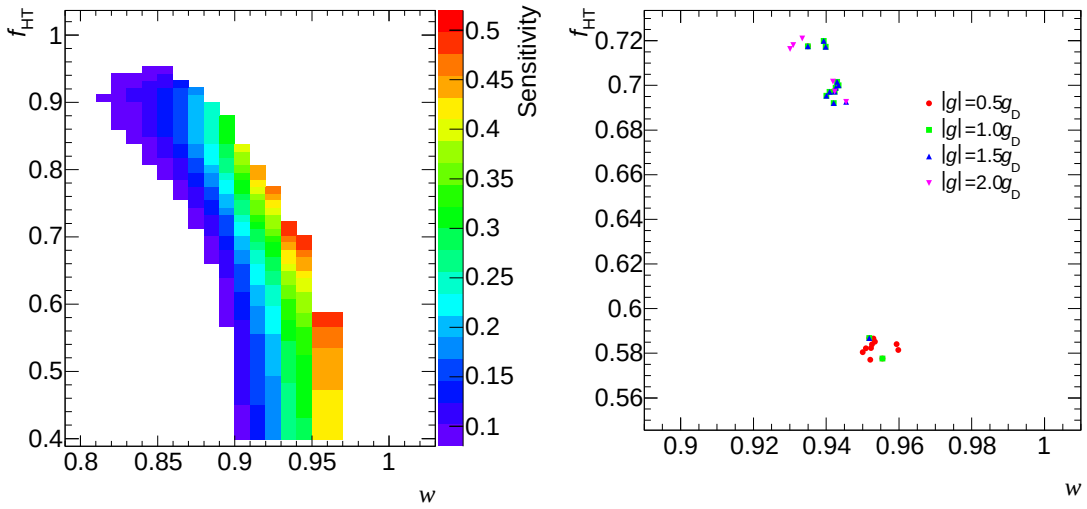

Figure 6.2: Sensitivity $\epsilon(t)/(a/2+\sqrt{B(t)})$ as a function of f_{HT} and w for spin-1/2 monopoles of mass 1000 GeV and charge $|g| = 1.0g_{\mathrm{D}}$ (left), and points of maximal sensitivity for monopoles of masses and charges for which the search is sensitive (right).

and is equivalent to not applying any additional selection. It must be kept in mind that this optimization is performed with pseudo-data obtained from control regions away from where the signal is expected, i.e., $w < 0.8$ for the generation of pseudo-data for f_{HT}, and $f_{\mathrm{HT}} < 0.6$ for the generation of pseudo-data for w. Therefore, it is only representative of a limited subset of the actual dataset used in the search. The use of a signal region defined by $w > 0.97$ and $f_{\mathrm{HT}} > 0.4$ would therefore expose the search to possible background events with $f_{\mathrm{HT}} \approx 0.4$. In addition, the stability of the search may be compromised if the w cut is too close to the bulk of the w distribution for the signal as the systematic uncertainties on the event selection efficiency may blow up. Some of the systematic uncertainties are related to the energy measurements in the EM calorimeter, afecting the measurement of the lateral dispersion, w, as described in Sec. 6.5.

A small modification to the optimization is performed in order to avoid exposing the search to backgrounds at low-f_{HT} values close to $f_{\mathrm{HT}} = 0.4$ due to the very loose optimal cut for f_{HT}. It is required that there be at least one background event in the signal region. Figure 6.2 shows the sensitivity (left), as defined in Eq. (5.2), as a function of f_{HT} and w for a sample of Drell-Yan produced monopoles of mass 1000 GeV and charge $|g| = 1.0g_{\mathrm{D}}$.

The maximum of the sensitivity is used to select the cut values defining the signal region. Also in Fig. 6.2, the points of maximal sensitivity are shown (right) for all mass and charge points for which the search is sensitive; this includes both single monopole samples and spin-1/2 Drell-Yan produced monopoles. As a compromise between the optimal values for all signal samples, the signal region is defined by the following two requirements:

- $f_{\mathrm{HT}} \geq 0.7$,
- $w \geq 0.94$.

In order to perform an event-based search, only one monopole candidate per event is kept. In the case of multiple candidates in the event, which is expected for pair-produced monopoles, the one closest to the signal region is kept, i.e., the candidate with highest f_{HT}. Table 6.1 presents a summary of the event selection criteria used in this search.

Preselection	Trigger	HIP trigger `EF_g_nocut_hiptrtL2`
	Calorimeter	`CaloCalTopoCluster` Cluster transverse energy $E_{\mathrm{T}} > 16$ GeV
	TRT	Number of HT hits in narrow region $N_{\mathrm{HT}} > 9$ Fraction of HT hits in narrow region $f_{\mathrm{HT}} > 0.4$
Tight selection	Overlap removal	One EM calorimeter cluster per TRT region
	Calorimeter	EM transverse energy $E_{\mathrm{T}}^{\mathrm{EM}} > 16$ GeV $E_{\mathrm{Pre}} > 5$ GeV or $E_{\mathrm{EM1}} > 5$ GeV Cluster pseudorapidity $\lvert\eta\rvert < 1.375$ or $1.52 < \lvert\eta\rvert < 2.0$ Energy in hadronic calorimeter $E_{\mathrm{HCal}} < 1$ GeV
	TRT	Only one candidate per event is selected: maximum f_{HT}
Final selection	TRT	Fraction of HT hits in narrow region $f_{\mathrm{HT}} \geq 0.7$
	Calorimeter	Cluster energy dispersion $w \geq 0.94$

Table 6.1: Summary of the event selection criteria.

6.3 Event selection efficiency

The event selection criteria is highly efficient for signal events that pass the HIP trigger. Tables 6.2 and 6.3 present the numbers of monopole candidates and events with at least one monopole candidate for two typical samples. The main inefficiency comes from the HIP trigger, in particular from the Level-1 component, which requires that the monopole reach

Selection	Candidates	Rel. eff.	Total eff.	Events	Rel. eff.	Total eff.
All	—	—	—	50000	—	—
HIP trigger	—	—	—	20326	40.65	40.65
Preselection	24263	—	—	20278	99.76	40.56
Overlap removal	20281	83.59	83.59	20278	100.00	40.56
$E_{\mathrm{T}}^{\mathrm{EM}} > 16$ GeV	20278	99.99	83.58	20276	99.99	40.55
$E_{\mathrm{Pre}} > 5$ GeV OR $E_{\mathrm{EM1}} > 5$ GeV	20276	99.99	83.57	20274	99.99	40.55
$\lvert\eta\rvert < 1.375$ OR $1.52 < \lvert\eta\rvert < 2.0$	18319	90.35	75.50	18318	90.35	36.64
Hadronic veto $E_{\mathrm{HCal}} \leq 1$ GeV	17276	94.30	71.20	17274	94.30	34.55
Max f_{HT} candidate	17274	99.99	71.19	17274	100.00	34.55
$w \geq 0.94$	17239	99.79	71.05	17239	99.79	34.48
$f_{\mathrm{HT}} \geq 0.7$	17082	99.09	70.40	17082	99.09	34.16

Table 6.2: Numbers of monopole candidates and events with at least one monopole candidate after requiring each selection criterion for single monopoles of mass 1000 GeV and charge $|g| = 1.0g_{\mathrm{D}}$. Relative efficiencies with respect to the previous selection criterion and absolute efficiencies with respect to the total number of preselected monopoles or total number of events in the sample are also presented in percentages.

the EM calorimeter depositing at least 18 GeV. Events with monopoles of charge $|g| = 0.5g_{\mathrm{D}}$ fail to pass the HIP trigger when they reach the barrel or extended barrel of the hadronic calorimeter depositing more than 1 GeV. Events with such characteristics are rejected by the Level-1 trigger. Tables for all samples can be found in App. D.

Selection	Candidates	Rel. eff.	Total eff.	Events	Rel. eff.	Total eff.
All	—	—	—	26502	—	—
HIP trigger	—	—	—	6526	24.62	24.62
Preselection	11253	—	—	6503	99.65	24.54
Overlap removal	10877	96.66	96.66	6503	100.00	24.54
$E_{\mathrm{T}}^{\mathrm{EM}} > 16$ GeV	10794	99.23	95.92	6503	100.00	24.54
$E_{\mathrm{Pre}} > 5$ GeV OR $E_{\mathrm{EM1}} > 5$ GeV	10787	99.94	95.86	6503	100.00	24.54
$\lvert\eta\rvert < 1.375$ OR $1.52 < \lvert\eta\rvert < 2.0$	10310	95.58	91.62	6242	95.97	23.55
Hadronic veto $E_{\mathrm{HCal}} \leq 1$ GeV	10286	99.77	91.41	6242	100.00	23.55
Max f_{HT} candidate	6242	60.68	55.46	6242	100.00	23.55
$w \geq 0.94$	6222	99.69	55.29	6222	99.69	23.48
$f_{\mathrm{HT}} \geq 0.7$	6193	99.53	55.04	6193	99.53	23.37

Table 6.3: Numbers of monopole candidates and events with at least one monopole candidate after requiring each selection criterion for spin-1/2 Drell-Yan produced monopoles of mass 1000 GeV and charge $|g| = 1.0g_{\mathrm{D}}$. Relative efficiencies with respect to the previous selection criterion and absolute efficiencies with respect to the total number of preselected monopoles or total number of events in the sample are also presented in percentages.

A summary of the event selection efficiencies for all the spin-1/2 Drell-Yan monopole

Drell-Yan spin-1/2 monopole event selection efficiencies [%]				
Mass [GeV]	$\|g\| = 0.5g_{\mathrm{D}}$	$\|g\| = 1.0g_{\mathrm{D}}$	$\|g\| = 1.5g_{\mathrm{D}}$	$\|g\| = 2.0g_{\mathrm{D}}$
200	22.30 ± 0.29	3.51 ± 0.13	0.14 ± 0.03	—
500	33.50 ± 0.33	14.86 ± 0.25	1.16 ± 0.09	—
1000	27.82 ± 0.32	23.37 ± 0.30	3.64 ± 0.13	—
1500	23.65 ± 0.30	22.15 ± 0.29	3.53 ± 0.13	—
2000	16.68 ± 0.26	16.52 ± 0.26	2.79 ± 0.12	—
2500	9.79 ± 0.21	9.76 ± 0.22	1.61 ± 0.09	—

Table 6.4: Event selection efficiency for spin-1/2 monopoles produced assuming the Drell-Yan model. Uncertainties are statistical only. Monopoles of charge $|g| = 2.0g_{\mathrm{D}}$ produced assuming the Drell-Yan model are excluded from the search due to very low trigger efficiency.

mass and charge combinations is presented in Table 6.4. Spin-1/2 monopoles of charge $|g| = 2.0g_{\mathrm{D}}$ produced with the Drell-Yan model are excluded from the search as the trigger efficiency is too low, thus they are excluded from the summary. Single monopole samples of charge $|g| = 2.0g_{\mathrm{D}}$ are not excluded from the search and are used for model-independent results.

6.3.1 Event selection efficiency maps

The event selection efficiency can be presented as two-dimensional maps in the kinetic energy, E^{kin}, versus pseudorapidity, η, phase space, where E^{kin} and η are associated with the generated monopoles.

The amount of material before the EM calorimeter barrel region ($|\eta| < 1.375$) is roughly proportional to $(\sin\theta)^{-1}$ while before the end-cap region ($|\eta| > 1.52$) it is roughly proportional to $(\cos\theta)^{-1}$. Therefore, in order to account for the material in front of the EM calorimeter, event selection efficiency maps are defined in terms of the generated monopole's transverse kinetic energy, $E_{\mathrm{T}}^{\mathrm{kin}} = E^{\mathrm{kin}} \sin\theta$. Figure 6.3 shows the event selection efficiency map for single particle monopoles of mass 1000 GeV and charges $|g| = 1.0g_{\mathrm{D}}$ (left) and $|g| = 2.0g_{\mathrm{D}}$ (right). Efficiency maps for the remaining single monopole samples used in the search can be found in App. E.

In the EM calorimeter end-cap regions, event selection efficiency maps can be defined in terms of the longitudinal kinetic energy, $E_{\mathrm{L}}^{\mathrm{kin}} = E^{\mathrm{kin}} \cos\theta$, to account for the amount

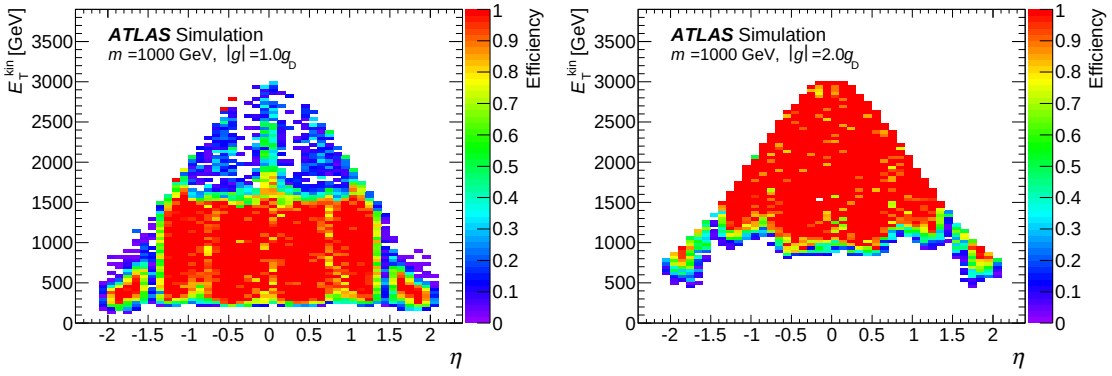

Figure 6.3: Event selection efficiency as a function of the transverse kinetic energy, $E_{\mathrm{T}}^{\mathrm{kin}}$, and pseudorapidity, η, for single particle monopoles of mass 1000 GeV and charges $|g| = 1.0g_{\mathrm{D}}$ (left) and $|g| = 2.0g_{\mathrm{D}}$ (right) [45].

of material before the EM calorimeter. This approach is used in the definition of fiducial regions of high and uniform event selection efficiency, which are necessary for the model independent results (see Sec. 6.3.3).

6.3.2 Extrapolation to spin-0 pair produced monopoles

The theory of magnetic monopoles proposed by Dirac does not impose any constraints on the spin of the monopole [24]. Similarly, the spin of the so-called electroweak monopole is not determined by the theory [26,27]. Therefore, there is no reason to restrict the search for magnetic monopoles to spin-1/2 particles only. The interactions of monopoles with matter are spin independent and thus so are their energy losses through the ATLAS detector. This situation can be exploited to extend the search to spin-0 monopoles produced assuming the Drell-Yan model without the need for full GEANT4 simulation of the ATLAS detector and reconstruction with the ATLAS software.

Extrapolation of model independent single particle results to spin-0 monopoles requires event selection efficiency maps of fully simulated and reconstructed single monopoles in the transverse kinetic energy, $E_{\mathrm{T}}^{\mathrm{kin}}$, versus pseudorapidity, η, space. The probability of selecting an event with a monopole candidate can be extracted from this map for any production model.

In addition to the single monopole efficiency maps, the event generator-level four-vectors of spin-0 monopoles assuming Drell-Yan production are necessary to calculate the event selection efficiency for the model. The event selection efficiency associated to each spin-0 monopole in every generated event is extracted from the event selection efficiency maps for the corresponding mass and charge using the generated monopole's transverse kinetic energy, $E_{\mathrm{T}}^{\mathrm{kin}}$, versus pseudorapidity, η, values. Each monopole is then passed with a probability equal to its associated selection efficiency. For models in which monopoles are pair produced, an event is deemed as passed when at least one of the generated monopoles in the event was successfully passed by the extrapolation algorithm. The event selection efficiency is calculated as the number of generated events that passed over the total number of generated events. More details on this method and its validation can be found in Ref. [128].

Charge $\|g\|$	Mass [GeV]	Cross sec. [pb]	$\sigma^{\text{spin-0}}/\sigma^{\text{spin-1/2}}$	Charge $\|g\|$	Mass [GeV]	Cross sec. [pb]	$\sigma^{\text{spin-0}}/\sigma^{\text{spin-1/2}}$
$0.5g_D$	200	3.08	8.19×10^{-2}	$1.5g_D$	200	27.7	8.17×10^{-2}
	500	3.91×10^{-2}	6.52×10^{-2}		500	0.352	6.51×10^{-2}
	1000	3.14×10^{-4}	4.68×10^{-2}		1000	2.82×10^{-3}	4.66×10^{-2}
	1500	4.52×10^{-6}	3.40×10^{-2}		1500	4.07×10^{-5}	3.39×10^{-2}
	2000	5.39×10^{-8}	2.41×10^{-2}		2000	4.85×10^{-7}	2.41×10^{-2}
	2500	3.31×10^{-10}	1.68×10^{-2}		2500	2.98×10^{-9}	1.68×10^{-2}
$1.0g_D$	200	12.33	8.22×10^{-2}	$2.0g_D$	200	49.3	8.18×10^{-2}
	500	0.156	6.50×10^{-2}		500	0.626	6.50×10^{-2}
	1000	1.25×10^{-3}	4.65×10^{-2}		1000	5.02×10^{-3}	4.65×10^{-2}
	1500	1.81×10^{-5}	3.40×10^{-2}		1500	7.23×10^{-5}	3.38×10^{-2}
	2000	2.16×10^{-7}	2.41×10^{-2}		2000	8.63×10^{-7}	2.41×10^{-2}
	2500	1.33×10^{-9}	1.69×10^{-2}		2500	5.30×10^{-9}	1.68×10^{-2}

Table 6.5: Cross section of Drell-Yan produced spin-0 monopoles in proton-proton collisions at $\sqrt{s} = 8$ TeV and ratios with respect to Drell-Yan produced spin-1/2 monopoles.

Direct comparison of the production cross sections of spin-0 and spin-1/2 monopoles (see Tables 6.5 and 4.1, respectively) produced with the Drell-Yan model show that production of spin-1/2 monopoles is more likely by a factor of approximately ten for particles of mass 200 GeV up to a factor of approximately 60 for particles of mass 2500 GeV. The kinematics of Drell-Yan spin-0 monopoles also differ from those of spin-1/2. In order to conserve angular momentum, Drell-Yan spin-0 monopoles cannot be produced at rest. This implies that the transverse kinetic energy spectrum is harder than that of Drell-Yan produced spin-1/2 monopoles [128].

The extrapolated event selection efficiencies for spin-0 monopoles produced assuming the Drell-Yan model are presented in Table 6.6. The event selection efficiencies for spin-0 monopoles are higher due to the harder spectrum. Monopoles with higher transverse momentum are more likely to penetrate to the EM calorimeter and deposit enough energy to exceed the Level-1 threshold. The efficiencies obtained for spin-0 monopoles of charge $|g| = 2.0g_{\mathrm{D}}$ are below 1%, motivating their exclusion from the search, similarly to spin-1/2 monopoles produced with the Drell-Yan method.

Drell-Yan spin-0 monopole event selection efficiencies [%]				
Mass [GeV]	$\|g\| = 0.5g_{\mathrm{D}}$	$\|g\| = 1.0g_{\mathrm{D}}$	$\|g\| = 1.5g_{\mathrm{D}}$	$\|g\| = 2.0g_{\mathrm{D}}$
200	42.5 ± 0.3	10.0 ± 0.2	0.40 ± 0.04	0.01 ± 0.01
500	53.8 ± 0.3	34.8 ± 0.3	4.1 ± 0.1	0.11 ± 0.02
1000	44.3 ± 0.3	51.1 ± 0.3	11.4 ± 0.2	0.39 ± 0.04
1500	36.5 ± 0.3	49.7 ± 0.3	13.8 ± 0.2	0.43 ± 0.04
2000	30.9 ± 0.3	41.6 ± 0.3	10.9 ± 0.2	0.32 ± 0.04
2500	22.9 ± 0.3	30.8 ± 0.3	6.9 ± 0.2	0.12 ± 0.02

Table 6.6: Event selection efficiency for spin-0 monopoles produced assuming the Drell-Yan model obtained with the extrapolation method from single particle event selection efficiency maps. Uncertainties are statistical only.

6.3.3 Selection efficiency in fiducial regions

The large coupling of magnetic monopoles to the photon prevents the use of perturbative methods to calculate the production cross section and kinematics of monopoles at the LHC. This introduces large uncertainties to the understanding of the production model. A model-independent search for monopoles is therefore of major importance.

In order to provide results that are model independent, fiducial regions of high and uniform event selection efficiency were obtained using single particle monopole samples. These regions can be used to study different monopole production models by taking into account their kinematics. Fiducial regions were obtained for each mass and charge combination as a function of the monopole kinetic energy and pseudorapidity. The size of the region as a function of the kinetic energy depends on two factors: the minimum energy required to penetrate to the EM calorimeter, which is related to the amount of material before the

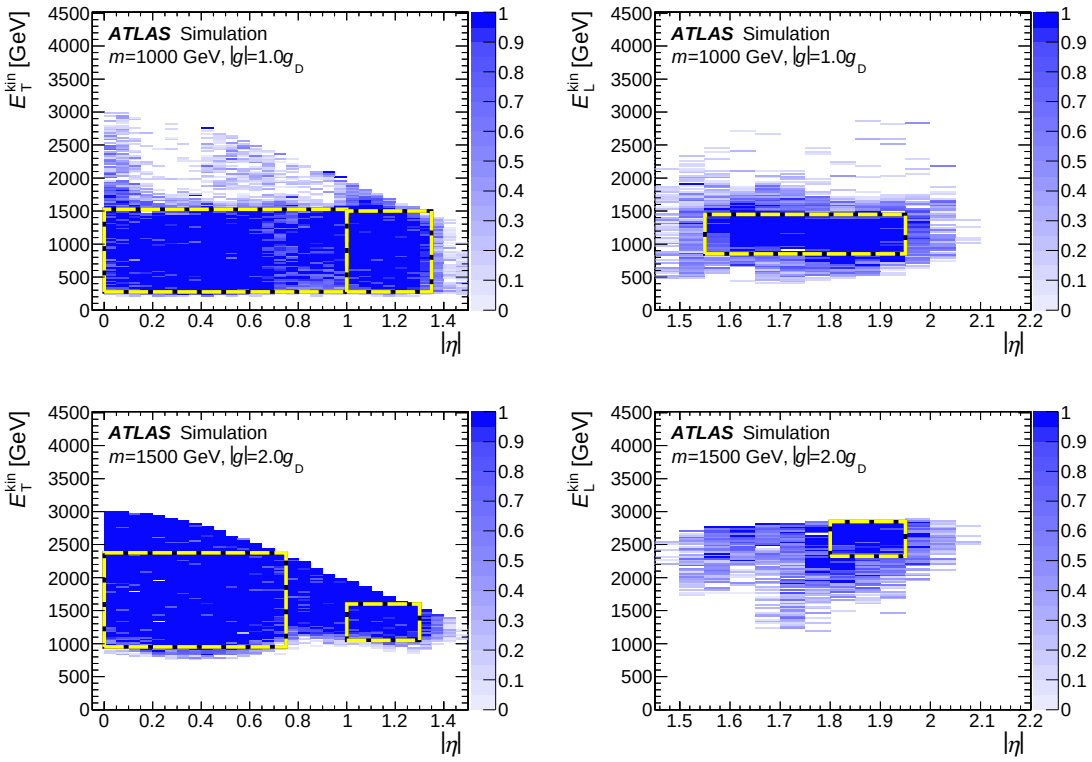

Figure 6.4: Event selection efficiency as a function of absolute pseudorapidity, $|\eta|$, and monopole kinetic energy, $E_{\mathrm{T}}^{\mathrm{kin}}$ or $E_{\mathrm{L}}^{\mathrm{kin}}$, with fiducial regions of high and uniform event selection efficiency overlaid for single monopoles of mass 1000 GeV and charge $|g| = 1.0g_{\mathrm{D}}$ (top row) and mass 1500 GeV and charge $|g| = 2.0g_{\mathrm{D}}$ (bottom row). Three fiducial regions have been defined to account for the detector geometry and material before the EM calorimeter.

EM calorimeter, and the maximum energy before penetrating to the hadronic calorimeter, which would cause the Level-1 trigger to reject the event.

Based on the distribution of the amount of material before the EM calorimeter, as explained in Sec. 6.3.1, a total of three regions were obtained in the absolute pseudorapidity ranges $|\eta| < 1$, $1 < |\eta| < 1.375$ and $1.52 < |\eta| < 2.0$. The division of the EM calorimeter barrel region into two separate regions accounts for inefficiencies introduced by the detector geometry of the TRT, as the TRT barrel–end-cap transition region spans across $0.77 < |\eta| < 1.06$. The fiducial regions in the EM calorimeter barrel region ($|\eta| < 1$ and $1 < |\eta| < 1.375$) are defined as a function of the transverse kinetic energy, $E_{\mathrm{T}}^{\mathrm{kin}}$, while the fiducial region in the EM calorimeter end-cap region ($1.52 < |\eta| < 2.0$) is defined as a function of the

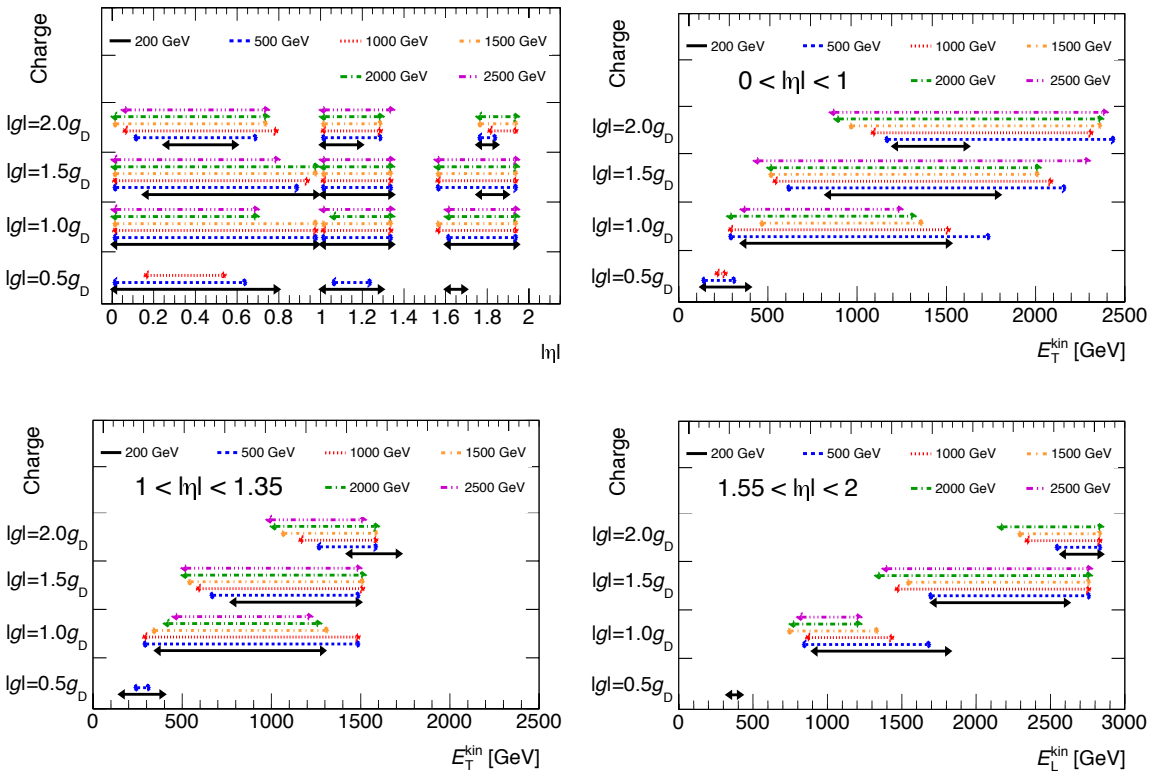

Figure 6.5: Boundaries of the fiducial regions of high and uniform event selection efficiency for single monopoles. The pseudorapidity boundaries (top left) are presented for three $|\eta|$ slices and the transverse or longitudinal kinetic energy boundaries are presented individually for the fiducial regions in $|\eta| < 1$ (top right), $1 < |\eta| < 1.375$ (bottom left) and $1.52 < |\eta| < 2.0$ (bottom right).

longitudinal kinetic energy, $E_{\mathrm{L}}^{\mathrm{kin}}$.

An algorithm was implemented to identify the largest rectangles in the $E_{\mathrm{T}}^{\mathrm{kin}}$ or $E_{\mathrm{L}}^{\mathrm{kin}}$ versus $|\eta|$ space for which the average selection efficiency was greater than 90% with a standard deviation lower than 12.5%. Figure 6.4 shows examples of the event selection efficiency maps with the fiducial regions obtained for single monopoles of mass 1000 GeV and charge $|g| = 1.0g_{\mathrm{D}}$ and mass 1500 GeV and charge $|g| = 2.0g_{\mathrm{D}}$ overlaid.

The size of the region is dependent on the charge and mass of the monopole and, in some cases, no fiducial region was found. This situation occurs for monopoles of charge $|g| = 0.5g_{\mathrm{D}}$ that often pierce through the EM calorimeter reaching the hadronic calorimeter causing the rejection of the event. Figure 6.5 shows the fiducial regions for all mass and charge points.

$\lvert g\rvert = 0.5 g_{\mathrm{D}}$						
mass [GeV]	$E_{\mathrm{T,min}}^{\mathrm{kin}}$	$E_{\mathrm{T,max}}^{\mathrm{kin}}$	$E_{\mathrm{T,min}}^{\mathrm{kin}}$	$E_{\mathrm{T,max}}^{\mathrm{kin}}$	$E_{\mathrm{L,min}}^{\mathrm{kin}}$	$E_{\mathrm{L,max}}^{\mathrm{kin}}$
	$0.0 < \lvert\eta\rvert < 0.8$		$1.0 < \lvert\eta\rvert < 1.3$		$1.6 < \lvert\eta\rvert < 1.7$	
200	125	400	150	400	325	425
	$0.0 < \lvert\eta\rvert < 0.65$		$1.05 < \lvert\eta\rvert < 1.25$		$— < \lvert\eta\rvert < —$	
500	125	325	225	325	—	—
	$0.15 < \lvert\eta\rvert < 0.55$		$— < \lvert\eta\rvert < —$		$— < \lvert\eta\rvert < —$	
1000	200	275	—	—	—	—

Table 6.7: Fiducial regions for monopoles of charge $|g| = 0.5 g_{\mathrm{D}}$. The units of $E_{\mathrm{T}}^{\mathrm{kin}}$ and $E_{\mathrm{L}}^{\mathrm{kin}}$ are GeV. The entries are blank for mass and charge points for which no fiducial region of high and uniform event selection efficiency was found.

$\lvert g\rvert = 1.0 g_{\mathrm{D}}$						
mass [GeV]	$E_{\mathrm{T,min}}^{\mathrm{kin}}$	$E_{\mathrm{T,max}}^{\mathrm{kin}}$	$E_{\mathrm{T,min}}^{\mathrm{kin}}$	$E_{\mathrm{T,max}}^{\mathrm{kin}}$	$E_{\mathrm{L,min}}^{\mathrm{kin}}$	$E_{\mathrm{L,max}}^{\mathrm{kin}}$
	$0.0 < \lvert\eta\rvert < 1.0$		$1.0 < \lvert\eta\rvert < 1.35$		$1.6 < \lvert\eta\rvert < 1.95$	
200	350	1525	350	1300	900	1825
	$0.0 < \lvert\eta\rvert < 1.0$		$1.0 < \lvert\eta\rvert < 1.35$		$1.6 < \lvert\eta\rvert < 1.95$	
500	275	1750	275	1500	825	1700
	$0.0 < \lvert\eta\rvert < 1.0$		$1.0 < \lvert\eta\rvert < 1.35$		$1.55 < \lvert\eta\rvert < 1.95$	
1000	275	1525	275	1500	850	1450
	$0.0 < \lvert\eta\rvert < 1.0$		$1.0 < \lvert\eta\rvert < 1.35$		$1.6 < \lvert\eta\rvert < 1.95$	
1500	450	1375	325	1325	725	1350
	$0.0 < \lvert\eta\rvert < 0.7$		$1.0 < \lvert\eta\rvert < 1.35$		$1.55 < \lvert\eta\rvert < 1.95$	
2000	275	1325	400	1275	750	1225
	$0.0 < \lvert\eta\rvert < 0.7$		$1.05 < \lvert\eta\rvert < 1.35$		$1.6 < \lvert\eta\rvert < 1.95$	
2500	350	1250	450	1225	800	1225

Table 6.8: Fiducial regions for monopoles of charge $|g| = 1.0 g_{\mathrm{D}}$. The units of $E_{\mathrm{T}}^{\mathrm{kin}}$ and $E_{\mathrm{L}}^{\mathrm{kin}}$ are GeV. The entries are blank for mass and charge points for which no fiducial region of high and uniform event selection efficiency was found.

The exact numerical values that define each region can be found in Tables 6.7 to 6.10.

6.3.4 Event selection efficiency in collision data

The numbers of monopole candidates and events with at least one candidate are presented in Table 6.11. The relative and absolute efficiencies of each criterion are also presented. The absolute selection efficiency is calculated with respect to the total number of preselected

$\lvert g\rvert = 1.5g_{\mathrm{D}}$						
mass [GeV]	$E^{\mathrm{kin}}_{\mathrm{T,min}}$	$E^{\mathrm{kin}}_{\mathrm{T,max}}$	$E^{\mathrm{kin}}_{\mathrm{T,min}}$	$E^{\mathrm{kin}}_{\mathrm{T,max}}$	$E^{\mathrm{kin}}_{\mathrm{L,min}}$	$E^{\mathrm{kin}}_{\mathrm{L,max}}$
	$0.15 < \lvert\eta\rvert < 1.0$		$1.0 < \lvert\eta\rvert < 1.35$		$1.75 < \lvert\eta\rvert < 1.9$	
200	825	1800	775	1500	1700	2625
	$0.0 < \lvert\eta\rvert < 0.9$		$1.0 < \lvert\eta\rvert < 1.35$		$1.55 < \lvert\eta\rvert < 1.95$	
500	600	2175	650	1500	1675	2775
	$0.0 < \lvert\eta\rvert < 0.95$		$1.0 < \lvert\eta\rvert < 1.35$		$1.55 < \lvert\eta\rvert < 1.95$	
1000	525	2100	575	1525	1450	2775
	$0.0 < \lvert\eta\rvert < 1.0$		$1.0 < \lvert\eta\rvert < 1.35$		$1.55 < \lvert\eta\rvert < 1.95$	
1500	500	2025	525	1525	1525	2775
	$0.0 < \lvert\eta\rvert < 1.0$		$1.0 < \lvert\eta\rvert < 1.35$		$1.55 < \lvert\eta\rvert < 1.95$	
2000	500	2025	500	1525	1325	2775
	$0.0 < \lvert\eta\rvert < 0.8$		$1.0 < \lvert\eta\rvert < 1.35$		$1.55 < \lvert\eta\rvert < 1.95$	
2500	425	2300	500	1500	1325	2775

Table 6.9: Fiducial regions for monopoles of charge $|g| = 1.5g_{\mathrm{D}}$. The units of $E^{\mathrm{kin}}_{\mathrm{T}}$ and $E^{\mathrm{kin}}_{\mathrm{L}}$ are GeV. The entries are blank for mass and charge points for which no fiducial region of high and uniform event selection efficiency was found.

$\lvert g\rvert = 2.0g_{\mathrm{D}}$						
mass [GeV]	$E^{\mathrm{kin}}_{\mathrm{T,min}}$	$E^{\mathrm{kin}}_{\mathrm{T,max}}$	$E^{\mathrm{kin}}_{\mathrm{T,min}}$	$E^{\mathrm{kin}}_{\mathrm{T,max}}$	$E^{\mathrm{kin}}_{\mathrm{L,min}}$	$E^{\mathrm{kin}}_{\mathrm{L,max}}$
	$0.25 < \lvert\eta\rvert < 0.6$		$1.0 < \lvert\eta\rvert < 1.2$		— $< \lvert\eta\rvert <$ —	
200	1200	1625	1425	1725	—	—
	$0.1 < \lvert\eta\rvert < 0.7$		$1.0 < \lvert\eta\rvert < 1.3$		$1.75 < \lvert\eta\rvert < 1.85$	
500	1150	2450	1250	1600	2575	2850
	$0.05 < \lvert\eta\rvert < 0.8$		$1.0 < \lvert\eta\rvert < 1.3$		$1.75 < \lvert\eta\rvert < 1.85$	
1000	1075	2325	1150	1600	2525	2850
	$0.0 < \lvert\eta\rvert < 0.75$		$1.0 < \lvert\eta\rvert < 1.3$		$1.8 < \lvert\eta\rvert < 1.95$	
1500	950	2375	1050	1600	2325	2850
	$0.0 < \lvert\eta\rvert < 0.75$		$1.0 < \lvert\eta\rvert < 1.3$		$1.75 < \lvert\eta\rvert < 1.95$	
2000	875	2375	1000	1600	2275	2850
	$0.05 < \lvert\eta\rvert < 0.75$		$1.0 < \lvert\eta\rvert < 1.35$		$1.75 < \lvert\eta\rvert < 1.95$	
2500	850	2400	975	1525	2150	2850

Table 6.10: Fiducial regions for monopoles of charge $|g| = 2.0g_{\mathrm{D}}$. The units of $E^{\mathrm{kin}}_{\mathrm{T}}$ and $E^{\mathrm{kin}}_{\mathrm{L}}$ are GeV. The entries are blank for mass and charge points for which no fiducial region of high and uniform event selection efficiency was found.

monopoles or with respect to the total number of events selected by the HIP trigger.

Selection	Candidates	Rel. frac. of cand.	Fraction of presel. cand.	Events	Rel. frac. of events	Fraction of total events
HIP trigger	—	—	—	854130	—	—
Preselection	650465	—	—	603150	70.62	70.62
Overlap removal	606645	93.26	93.26	603150	100.00	70.62
$E_{\mathrm{T}}^{\mathrm{EM}} > 16$ GeV	600358	98.96	92.30	597761	99.11	69.98
$E_{\mathrm{Pre}} > 5$ GeV OR $E_{\mathrm{EM1}} > 5$ GeV	591627	98.55	90.95	589103	98.55	68.97
$\lvert\eta\rvert < 1.375$ OR $1.52 < \lvert\eta\rvert < 2.0$	501304	84.73	77.07	499544	84.80	58.49
Hadronic veto $E_{\mathrm{HCal}} \leq 1$ GeV	498993	99.54	76.71	497401	99.57	58.23
Max f_{HT} candidate	497401	99.68	76.47	497401	100.00	58.23
$w \geq 0.94$	3	10^{-6}	10^{-6}	3	10^{-6}	10^{-6}
$f_{\mathrm{HT}} \geq 0.7$	0	0.00	0.00	0	0.00	0.00

Table 6.11: Numbers of monopole candidates and events with at least one monopole candidate after requiring each selection criterion in the collision data. Also shown are the relative fraction of candidates and events with respect to the previous selection criterion and fraction of candidates and events with respect to the total number of preselected monopoles candidates or total number of events selected by the HIP trigger.

6.4 Two-dimensional sideband data-driven background estimation

The HIP trigger has been designed to select events that passed the Level-1 trigger, which requires energy deposition in the EM calorimeter, and have a large fraction of TRT HT hits. This trigger is very effective at selecting signal events in which a monopole penetrates to the EM calorimeter. The HIP trigger rate is dominated by low transverse momentum multijet events in which close-by charged particles within a jet hit the same TRT straws generating a region of high ionization density. High transverse momentum multijet events and events containing electrons are also among those selected by the HIP trigger. The main background near the signal region, i.e., events with high ionization density in a narrow region of the TRT and a energy deposition in the EM calorimeter with very low lateral dispersion, comprises events containing high energy electrons.

Simulated MC samples of electrons from W boson decays and Drell-Yan produced electron-positron pairs were used to study the performance of the selection variables. A simulated MC sample of high transverse momentum multijet events was also used, but it

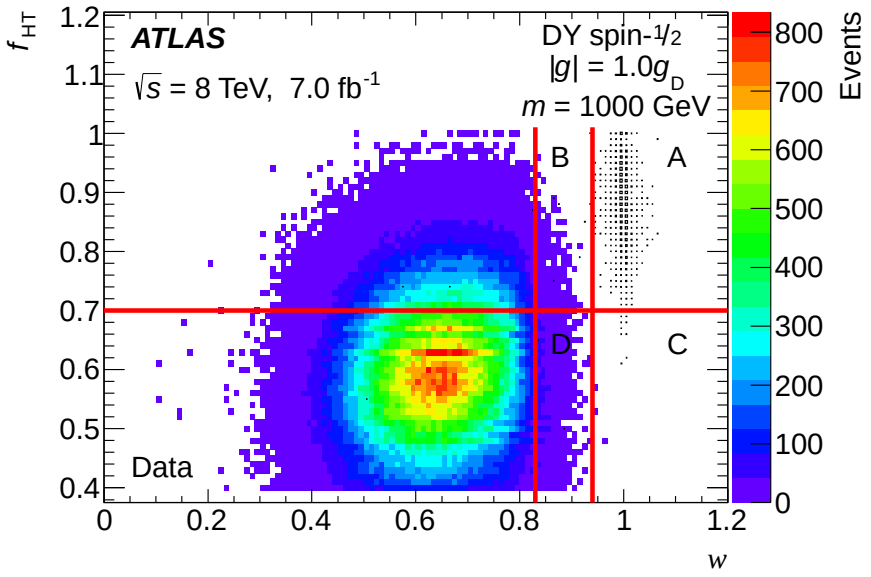

Figure 6.6: Fraction of TRT HT hits, f_{HT}, versus EM calorimeter cluster lateral dispersion, w, for candidate events after tight selection for collision data (colour) and for monopoles of mass 1000 GeV and charge $|g| = 1.0g_{\mathrm{D}}$ (boxes). The quadrants A, B, C and D used for the background estimate are also shown.

was found that its contribution to the background was negligible. Despite the availability of some MC samples, a complete set of simulated background samples that include the HIP trigger, which was deployed late in 2012, could not be reprocessed. Therefore, a MC-based background estimate was not possible.

The background estimate in the signal region was performed directly from the data collected by the trigger that passed the tight selection requirements. The two-dimensional sideband method, otherwise known as the ABCD method, was used [129]. This data-driven background estimate requires the definition of a signal region and three control regions. In this search the control and signal regions are defined in terms of the fraction of TRT HT hits, f_{HT}, and the EM cluster lateral dispersion, w. Figure 6.6 shows the candidate events in collision data after tight selection for the signal region along with the three control regions. The control regions, labelled as B, C and D, are defined by $f_{\mathrm{HT}} \geq 0.7$ and $0.83 < w < 0.94$, $f_{\mathrm{HT}} < 0.7$ and $w \geq 0.94$, and $f_{\mathrm{HT}} < 0.7$ and $0.83 < w < 0.94$, respectively. The signal region, A, is defined by $f_{\mathrm{HT}} \geq 0.7$ and $w \geq 0.94$, as detailed in Sec. 6.2.1.

The two-dimensional sideband background estimate method requires that the search use sequential requirements—in this case, w and f_{HT}. The background in the signal region is predicted by scaling the number of events in control region C (low f_{HT} and high w) using as a constant the ratio of the number of events in the low-w regions B and D, i.e.,

$$N_{\mathrm{A}}^{\mathrm{est}} = \left(\frac{N_{\mathrm{B}}}{N_{\mathrm{D}}}\right) N_{\mathrm{C}}. \tag{6.1}$$

This particular version of the method assumes no signal leakage into the control regions and no correlation between selection variables.

6.4.1 Correlation between final selection variables

The two-dimensional sideband method requires the two discriminating variables not be correlated or be only slightly correlated. In the case of f_{HT} and w, a small non-negligible correlation exists. The Pearson correlation factor between the discriminating variables in the data in the region $w < 0.94$ is 0.120. A separation of the data in pseudorapidity slices shows that the correlation in the region $|\eta| < 1.375$ is small with a correlation factor of 0.036, while in the EM calorimeter barrel–end-cap transition region, $1.375 < |\eta| < 1.52$, and in the region $1.52 < |\eta| < 2.0$, the correlation factor is 0.200 and 0.152, respectively. The large correlation in $1.375 < |\eta| < 1.52$ is the main motivation to reject monopole candidates in this region. After removing the EM calorimeter barrel–end-cap transition region, the correlation factor between the discriminating variables, f_{HT} and w, decreases to 0.094. Figure 6.7 shows the profile histograms of f_{HT} versus w in the region $w < 0.94$ for the three η slices mentioned above and the full detector excluding the EM calorimeter barrel–end-cap transition region, $1.375 < |\eta| < 1.52$.

The correlation between f_{HT} and w can be studied by analyzing the behaviour of the ratio of the number of events with $f_{\mathrm{HT}} \geq 0.7$ over the number of events with $f_{\mathrm{HT}} < 0.7$ in bins of width $\Delta w = 0.01$ as a function of w. An uncorrelated sample would yield a uniform ratio across w. Figure 6.8 shows the ratio between the number of events with $f_{\mathrm{HT}} \geq 0.7$ and $f_{\mathrm{HT}} < 0.7$ for collision data after tight selection in the region $w < 0.94$. The individual pseudorapidity slices are not correlated within statistical uncertainties. However,

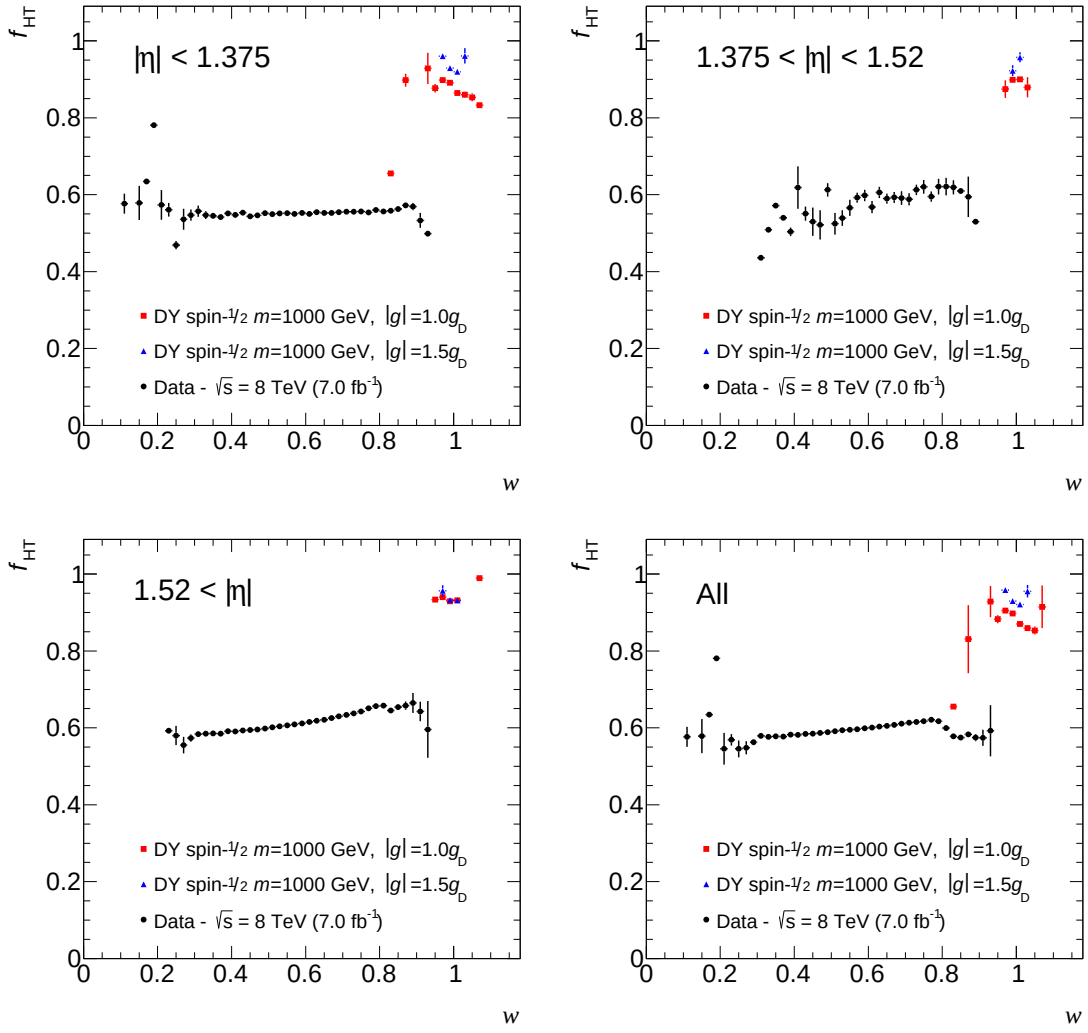

Figure 6.7: Profile histograms of f_{HT} versus w for the EM calorimeter barrel (top left), barrel–end-cap transition region (top right), end-cap (bottom left) and full detector (bottom right). Collision data and Drell-Yan produced monopoles of mass 1000 GeV and charge $|g| = 1.0g_{\mathrm{D}}$ and $|g| = 1.5g_{\mathrm{D}}$ are shown. Collision data in $w < 0.94$ only is presented. Candidate events in the EM calorimeter barrel–end-cap transition region are excluded from the full detector profile histogram. Thus, it represents the final dataset.

the combination of all the slices shows some correlation. Thus, it was concluded that the correlation is of a geometrical origin.

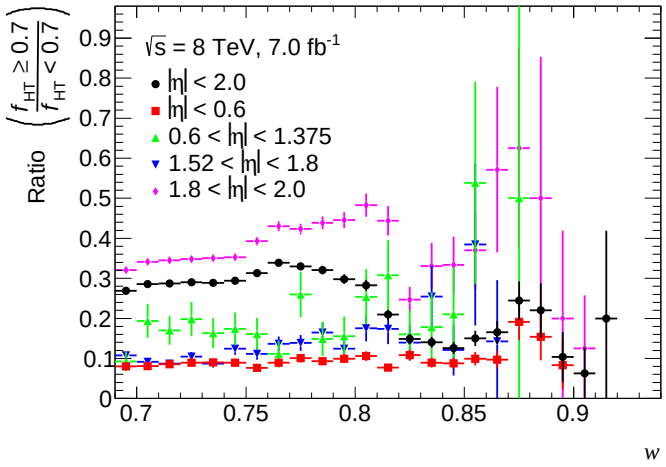

Figure 6.8: Ratio of number of events with $f_{\mathrm{HT}} \geq 0.7$ over number of events with $f_{\mathrm{HT}} < 0.7$ as a function of w in bins of width $\Delta w = 0.01$, in collision data after tight selection in the region $w < 0.94$.

6.4.2 Correction to correlation between selection variables

Due to the geometrical correlation present in the collision data, a correction has to be introduced in order to account for a possible under- or over-estimation of the true background. The correlation can be described by the correction parameter $c = (N_{\mathrm{A}} N_{\mathrm{D}})/(N_{\mathrm{B}} N_{\mathrm{C}})$ [129]. The correction parameter can be determined using data from the region $w < 0.94$ such that the background estimate in the signal region becomes

$$N_{\mathrm{A}}^{\mathrm{est}} = c \left(\frac{N_{\mathrm{B}}}{N_{\mathrm{D}}} \right) N_{\mathrm{C}}. \tag{6.2}$$

For a specific w bin, i, in Fig. 6.8, the value of the ratio in any other bin, j, with higher w could be regarded as $N_{\mathrm{A}}/N_{\mathrm{C}}$. By comparing the ratios for all w_j (all w bins with a value higher that w_i), a correlation correction factor $c_{i,j}$ can be obtained:

$$c_{i,j} = \frac{N_{\mathrm{B}}^{j} N_{\mathrm{D}}^{i}}{N_{\mathrm{B}}^{i} N_{\mathrm{D}}^{j}}. \tag{6.3}$$

A correction factor for each bin i is defined as the weighted average over all $c_{i,j}$ taking the weight as the reciprocal square of the statistical uncertainty in each bin j. Figure 6.9 shows the values of the correlation correction parameter, c_i. It can be seen that the deviation from

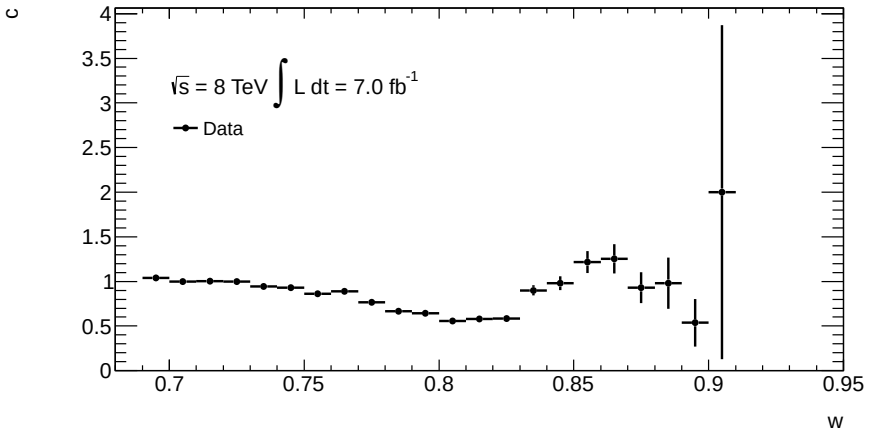

Figure 6.9: Correlation correction parameter for each bin w_i obtained as outlined in the text. The deviations from unity lead to an overall correction parameter of $c = 1.0 \pm 0.4$.

unity is no larger than 40%, leading to $c = 1.0 \pm 0.4$. This correction effectively introduces a systematic uncertainty on the background estimate.

6.4.3 Background estimate

The number of candidate events in collision data in the control regions is presented in Table 6.12. The background estimate assuming no signal leakage and accounting for an existing small correlation between the selection variables by means of a systematic uncertainty is

$$N_{\mathrm{A}}^{\mathrm{est}} = \left(\frac{N_{\mathrm{B}}}{N_{\mathrm{D}}}\right) N_{\mathrm{C}} = 0.43 \pm 0.25 \text{ (stat.)} \pm 0.17 \text{ (syst.)}. \tag{6.4}$$

The uncertainty on the background estimate is dominated by the low statistics in quadrant C.

$N_{\mathrm{A}}^{\mathrm{obs}}$	N_{B}	N_{C}	N_{D}	$N_{\mathrm{A}}^{\mathrm{est}}$
0	364	3	2527	0.43 ± 0.25 (stat.) ± 0.17 (syst.)

Table 6.12: Number of observed candidate events in collision data in quadrants A, B, C and D.

6.4.4 Background estimate using a maximum-likelihood fit

The model independent background estimate described in Sec. 6.4.3 does not account for possible signal leakages into the control regions. Although in most cases the signal leakages are of order 0.1% or negligible, for monopoles of charge $|g| = 0.5g_{\mathrm{D}}$ the signal leakage into region C can be considerably larger, reaching values of about 30%. This situation occurs when the discrimination power of f_{HT} is reduced due to the lower ionization produced by such particles. In particular, the heavier the monopole the slower it travels through the TRT producing a reduced amount of TRT HT hits in comparison with the higher charges.

Leakage into region B occurs when fast, low-mass monopoles produce copious amounts of energetic δ-rays that propagate and radiate in the EM calorimeter increasing the lateral dispersion of the calorimeter cluster, as pointed out in Sec. 5.2.4. The signal leakages into quadrants B, C and D are presented in Table 6.13.

In order to account for model-dependent leakages the background estimate is performed for each mass and charge sample by means of a maximum-likelihood fit. This is done with the RooStat framework [130] as part of the limit-setting procedure. The number of events in quadrants A, B, C, and D are modelled as

$$\begin{aligned}
\mu_A &= \sigma_{\mathrm{sig}}^{\mathrm{eff}} \cdot \mu + \mu^U, \\
\mu_B &= \sigma_{\mathrm{sig}}^{\mathrm{eff}} \cdot b\mu + \mu^U \tau_B, \\
\mu_C &= \sigma_{\mathrm{sig}}^{\mathrm{eff}} \cdot c\mu + \mu^U \tau_C, \\
\mu_D &= \sigma_{\mathrm{sig}}^{\mathrm{eff}} \cdot d\mu + \mu^U \tau_B \tau_C \cdot c_{\mathrm{corr}},
\end{aligned} \tag{6.5}$$

where μ and μ^U are the number of expected signal and background events in the signal region, $\sigma_{\mathrm{sig}}^{\mathrm{eff}}$ reflects the systematic uncertainty on the event selection efficiency for the signal, and the parameters b, c and d represent the signal leakages into the control regions B, C and D, respectively. The parameter τ_B (τ_C) is defined as the ratio of background events in control region B (C) to the number of background events in the signal region. Finally, the parameter c_{corr} represents the correlation correction factor, as explained in Sec. 6.4.2. The correlation correction factor c_{corr}, was found to be $c_{\mathrm{corr}} = 1.0 \pm 0.4$. However, instead of introducing a floating parameter into the limit-setting procedure, a fixed correlation

Single monopole	b	c	d
$\|g\| = 0.5g_{\rm D}$			
m =200 GeV	1.6	2.3	0.0
m =500 GeV	1.2	4.3	0.0
m =1000 GeV	0.6	19.5	0.1
m =1500 GeV	—	—	—
m =2000 GeV	—	—	—
m =2500 GeV	—	—	—
$\|g\| = 1.0g_{\rm D}$			
m =200 GeV	8.9	3.3	0.1
m =500 GeV	0.7	1.6	0.0
m =1000 GeV	0.2	0.8	0.0
m =1500 GeV	0.1	0.9	0.0
m =2000 GeV	0.1	1.4	0.0
m =2500 GeV	0.1	1.9	0.0
$\|g\| = 1.5g_{\rm D}$			
m =200 GeV	8.0	2.6	0.1
m =500 GeV	0.5	1.6	0.0
m =1000 GeV	0.1	0.9	0.0
m =1500 GeV	0.1	0.6	0.0
m =2000 GeV	0.1	0.7	0.0
m =2500 GeV	0.1	0.7	0.0
$\|g\| = 2.0g_{\rm D}$			
m =200 GeV	19.0	1.4	0.2
m =500 GeV	0.4	1.6	0.0
m =1000 GeV	0.1	0.6	0.0
m =1500 GeV	0.1	0.3	0.0
m =2000 GeV	0.1	0.4	0.0
m =2500 GeV	0.0	0.5	0.0

DY spin-1/2 monopole	b	c	d
$\|g\| = 0.5g_{\rm D}$			
m =200 GeV	—	—	—
m =500 GeV	0.3	3.4	0.0
m =1000 GeV	0.6	15.7	0.1
m =1500 GeV	0.7	25.5	0.2
m =2000 GeV	0.5	32.6	0.3
m =2500 GeV	0.6	34.5	0.3
$\|g\| = 1.0g_{\rm D}$			
m =200 GeV	0.2	0.5	0.0
m =500 GeV	0.2	0.1	0.0
m =1000 GeV	0.1	0.4	0.0
m =1500 GeV	0.3	1.7	0.0
m =2000 GeV	0.3	4.7	0.0
m =2500 GeV	0.1	10.8	0.0
$\|g\| = 1.5g_{\rm D}$			
m =200 GeV	0.5	1.4	0.5
m =500 GeV	0.0	0.0	0.0
m =1000 GeV	0.0	0.2	0.1
m =1500 GeV	0.0	0.3	0.0
m =2000 GeV	0.0	0.6	0.0
m =2500 GeV	0.3	4.2	0.0
$\|g\| = 2.0g_{\rm D}$			
m =200 GeV	—	—	—
m =500 GeV	—	—	—
m =1000 GeV	—	—	—
m =1500 GeV	—	—	—
m =2000 GeV	—	—	—
m =2500 GeV	—	—	—

Table 6.13: Signal leakages into quadrants B, D and D in percentages, for single (left) and Drell-Yan produced spin-1/2 (right) monopoles.

parameter was set to $c_{\rm corr} = 1.4$, the maximum upward variation. The choice of this correction parameter leads to more conservative limits. Nevertheless, the different choices of $c_{\rm corr} = 0.6$, $c_{\rm corr} = 1.0$ or $c_{\rm corr} = 1.4$ do not yield significant changes in the final results.

The free parameters of the fit are μ, μ^U, τ_B, τ_C and $\sigma_{\rm sig}^{\rm eff}$, which are determined by maximizing the likelihood function

$$L(N_A, N_B, N_C, N_D \mid \mu, \mu^U, \tau_B, \tau_C) = \prod_{i=A,B,C,D} \frac{e^{-\mu_i} \mu_i^{N_i}}{N_i!} \tag{6.6}$$

with respect to the observed number of events N_A, N_B, N_C and N_D in quadrants A, B, C and D, respectively.

6.5 Systematic uncertainties

A number of systematic uncertainties that could affect the measurement of the signal event selection efficiency have been considered, as described below. In most cases, the default ATLAS simulation software was modified to reflect the conditions that would introduce a systematic uncertainty on the signal event selection efficiency. and a new sample of 5000 events was fully simulated. This was done for each mass and charge point for both the spin-1/2 Drell-Yan and the single monopole samples. When a change in the default ATLAS simulation was not necessary, the systematic variation was introduced at the analysis level allowing the use of the full statistics available in the nominal signal samples.

The relative uncertainties for spin-1/2 and spin-0 Drell-Yan monopoles of mass 1000 GeV and charge $|g| = 1.0g_{\mathrm{D}}$ are given in Table 6.14. Tables for the full set of Drell-Yan produced monopoles can be found in App. G.

Variations of efficiencies due to different systematic uncertainties for single monopole samples are shown in Table 6.15. The systematic uncertainties for single monopoles are averaged over all mass points, as no mass dependence is expected due to the uniform kinematic distributions used for generation of the samples. The variations in event selection efficiency have been considered only within the fiducial regions defined in Sec. 6.3.3.

6.5.1 ATLAS detector material modelling

Due to the highly ionizing nature of monopoles, the event selection efficiency is sensitive to material in the detector, in particular, to material before the EM calorimeter. A version of the GEANT4 ATLAS detector geometry designed specifically for detector material studies was used to fully simulate 5000 events. This modified geometry, labelled as `ATLAS-GEO-21-06-01`, has a material increase with respect to the default detector geometry version used for the `MC12c` production campaign of 5% in the whole inner detector and 15%

Spin-1/2 $\lvert g\rvert = 1.0g_{\mathrm{D}}$	MC Stat.	Det. material	G4 range cut	Birks' high	Birks' low	$\delta-$ray	TRT Occ.	LAr xTalk	Total (UP)	Total (DOWN)
m=200 GeV	± 3.71	$\pm(2 \pm 3)$	$+(6 \pm 3)$	$+(12 \pm 3)$	$+(3 \pm 3)$	$\pm(7 \pm 3)$	$+(1 \pm 2)$	0 ± 2	$+16$	-9
m=500 GeV	± 1.69	$\pm(3 \pm 2)$	0 ± 2	$+(3 \pm 2)$	$-(7 \pm 2)$	$\pm(0 \pm 2)$	0 ± 2	$-(1 \pm 2)$	$+6$	-8
m=1000 GeV	± 1.28	$\pm(4 \pm 2)$	$-(3 \pm 2)$	$+(10 \pm 2)$	$-(10 \pm 2)$	$\pm(2 \pm 2)$	$-(1 \pm 1)$	$-(3 \pm 1)$	$+12$	-12
m=1500 GeV	± 1.33	$\pm(8 \pm 2)$	$-(2 \pm 2)$	$+(13 \pm 2)$	$-(9 \pm 2)$	$\pm(1 \pm 2)$	$+(1 \pm 2)$	$-(1 \pm 2)$	$+15$	-13
m=2000 GeV	± 1.59	$\pm(3 \pm 3)$	$-(1 \pm 3)$	$+(15 \pm 3)$	$-(9 \pm 3)$	$\pm(3 \pm 3)$	$+(2 \pm 2)$	$-(3 \pm 2)$	$+16$	-11
m=2500 GeV	± 2.21	$\pm(9 \pm 3)$	$-(10 \pm 3)$	$+(9 \pm 4)$	$-(17 \pm 3)$	$\pm(6 \pm 3)$	$+(6 \pm 2)$	$-(3 \pm 2)$	$+16$	-24

Spin-0 $\lvert g\rvert = 1.0g_{\mathrm{D}}$	MC Stat.	Det. material	G4 range cut	Birks' high	Birks' low	$\delta-$ray	TRT Occ.	LAr xTalk	Extrapolation	Total (UP)	Total (DOWN)
m=200 GeV	± 2.02	$\pm(2 \pm 3)$	$+(6 \pm 3)$	$+(12 \pm 3)$	$+(3 \pm 3)$	$\pm(7 \pm 3)$	0 ± 2	0 ± 2	-10	$+16$	-13
m=500 GeV	± 0.92	$\pm(3 \pm 2)$	0 ± 2	$+(3 \pm 2)$	$-(7 \pm 2)$	$\pm(0 \pm 2)$	0 ± 2	$-(1 \pm 2)$	-9.5	$+6$	-12
m=1000 GeV	± 0.66	$\pm(4 \pm 2)$	$-(3 \pm 2)$	$+(10 \pm 2)$	$-(10 \pm 2)$	$\pm(2 \pm 2)$	$-(1 \pm 1)$	$-(3 \pm 1)$	-8.5	$+12$	-14
m=1500 GeV	± 0.68	$\pm(8 \pm 2)$	$-(2 \pm 2)$	$+(13 \pm 2)$	$-(10 \pm 2)$	$\pm(1 \pm 2)$	$+(1 \pm 2)$	$-(1 \pm 2)$	-7.5	$+15$	-15
m=2000 GeV	± 0.80	$\pm(3 \pm 3)$	$-(1 \pm 3)$	$+(15 \pm 3)$	$-(9 \pm 3)$	$\pm(3 \pm 3)$	$+(2 \pm 2)$	$-(3 \pm 2)$	-6.5	$+16$	-13
m=2500 GeV	± 1.01	$\pm(9 \pm 3)$	$-(10 \pm 3)$	$+(9 \pm 4)$	$-(17 \pm 3)$	$\pm(6 \pm 3)$	$+(6 \pm 2)$	$-(3 \pm 2)$	-5.5	$+15$	-24

Table 6.14: Relative uncertainties on the signal efficiencies in percentages for Drell-Yan produced spin-1/2 (top) and spin-0 (bottom) monopoles of charge $\lvert g\rvert = 1.0g_{\mathrm{D}}$. The errors on the uncertainties are statistical. The total relative uncertainties are calculated as quadratic sums of the individual relative uncertainties including the 2.8% uncertainty on the luminosity measurement. Note that the δ-ray and material density uncertainties are taken as symmetric, as described in the text.

Sample	MC Stat.	Det. material	G4 range cut	Birks' high	Birks' low	$\delta-$ray	TRT Occ.	LAr xTalk	Total (UP)	Total (DOWN)
$\|g\| = 0.5g_{\mathrm{D}}$	± 1.940	± 3.58	-1.15	-1.15	-0.27	± 0.35	$+1.37$	-1.58	$+5$	-5
$\|g\| = 1.0g_{\mathrm{D}}$	± 0.289	± 0.43	$+0.42$	$+0.52$	$+0.11$	± 0.06	$+0.67$	-3.20	$+3$	-4
$\|g\| = 1.5g_{\mathrm{D}}$	± 0.231	± 0.24	$+0.27$	$+0.42$	-0.02	± 0.33	$+0.53$	-2.56	$+3$	-4
$\|g\| = 2.0g_{\mathrm{D}}$	± 0.431	± 0.85	-0.36	$+0.32$	-0.78	± 0.27	$+0.46$	-4.23	$+3$	-5

Table 6.15: Relative uncertainties on the signal efficiencies in percentages for single monopoles in fiducial regions. The total relative uncertainties are calculated as quadratic sums of the individual relative uncertainties including the 2.8% uncertainty on the luminosity measurement. Note that the δ-ray and material density uncertainties are taken as symmetric, as described in the text.

relative increase of Pixel and SCT services, i.e., 10% extra on top of the 5% in the whole inner detector. The relative systematic uncertainty, which is taken as symmetric, is shown in Table 6.14 for Drell-Yan produced monopoles and in Table 6.15 for single monopoles.

6.5.2 Geant4 range cut for δ-rays

In order to conserve computational resources, GEANT4 does not propagate low-energy δ-rays, i.e., electrons with energy below a minimum kinetic energy threshold are not simulated explicitly. In this case, the corresponding energy loss is added to the energy loss of the monopole continuously during the discrete step in the trajectory propagation. For convenience, this kinetic energy threshold is controlled in GEANT4 by the *cut in range* [131] parameter. This parameter, defined as a distance, is internally converted to an energy, which determines the minimum kinetic energy threshold for individual subsystems. For our purposes, this parameter effectively dictates the fraction of energy explicitly deposited by δ-rays relative to that deposited by the monopole. The range cut should be kept as low as possible for the best simulation precision, as more low-energy δ-rays are explicitly simulated. The default value of the range cut used in the ATLAS TRT simulation is 50 μm. For each mass and charge sample, 5000 events were fully simulated using a range cut of 25 μm in the inner detector instead of 50 μm. The efficiencies were then recomputed. The relative systematic uncertainty is shown in Table 6.14 for Drell-Yan produced monopoles and in Table 6.15 for single monopoles.

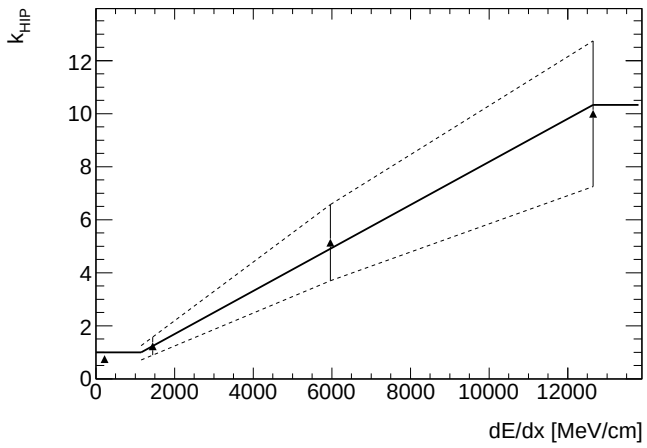

Figure 6.10: HIP correction to Birks' Law as a function of dE/dx for various heavy ions for $E_D = 7$ kV/cm [132].

6.5.3 HIP correction to Birks' Law

The precision of the HIP correction to Birks' Law is limited by the uncertainties in the experimental heavy-ion data [132] used to derive the correction. The upper (lower) systematic uncertainty on the HIP correction was obtained by fully simulating 5000 events using the upper (lower) curves given in Fig. 6.10. The efficiencies were then recomputed. The relative uncertainty is shown in Tables 6.14 for Drell-Yan produced monopoles and in Table 6.15 for single monopoles.

6.5.4 δ-ray production model

The monopole energy loss and δ-ray production models used in GEANT4 are based on Eq. 1.18, which has an associated uncertainty of about 3% [115]. The calorimeter cluster lateral dispersion, w, and the fraction of TRT HT hits in the narrow region, f_{HT}, could be sensitive to δ-ray production. The δ-ray production can be modified in the GEANT4 simulation package for monopoles. Therefore, 5000 events were fully simulated where the production of δ-rays was suppressed by 3% for all monopole mass and charge samples. The efficiencies were then recomputed. The relative uncertainty, which is taken as symmetric, is shown in Table 6.14 for Drell-Yan produced monopoles and in Table 6.15 for single

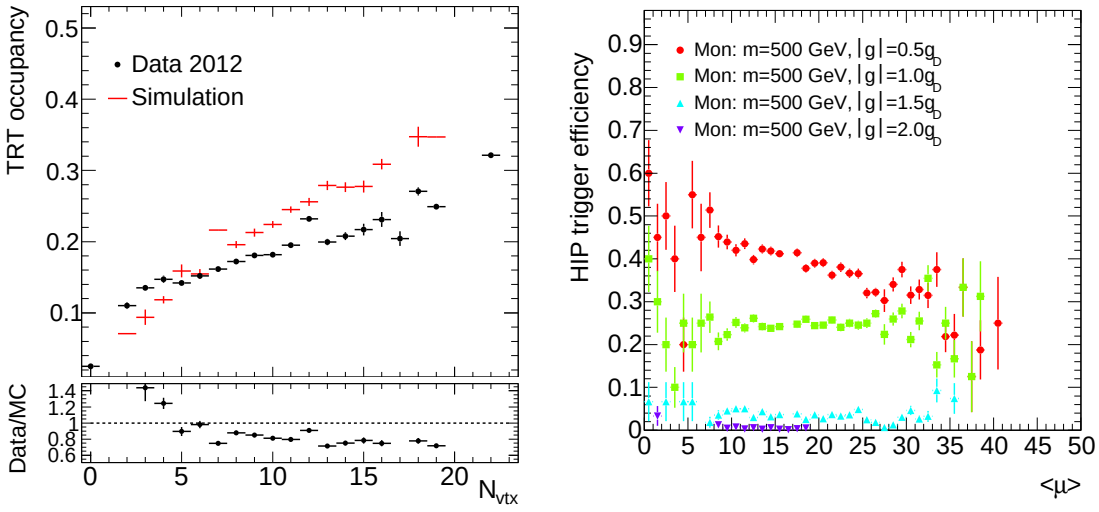

Figure 6.11: Comparison of the TRT occupancy as a function of the number of reconstructed vertices for collision data and MC (left), and HIP trigger efficiency as a function of average number of interactions per bunch crossing $\langle\mu\rangle$(right).

monopoles.

6.5.5 TRT occupancy

The accuracy of the pileup description in the simulated MC samples is an important component of this analysis as it affects the efficiency of the requirement on the fraction of TRT HT hits, f_{HT}. The occupancy is defined as the fraction of TRT channels that yield a signal, be it from actual ionization or noise, in an event. Approximately four luminosity blocks from the dataset used in the search were used to study the occupancy in data. A simulated MC sample of electrons from W decays was used to study the TRT occupancy in the simulation. Both data and MC were processed by the DESD HIP filter, ensuring that events of similar characteristics are compared.

Figure 6.11 (left) shows a comparison of the TRT occupancy as a function of the number of reconstructed vertices for collision data and MC. The TRT occupancy is underestimated in the simulation for low values of reconstructed vertices while it is overestimated for high values. To assign the corresponding systematic uncertainty, at the analysis level the number of low-threshold hits (those likely to come from pileup as opposed to the monopole or

associated δ-rays) was scaled by a factor dependent on the number of reconstructed primary vertices. This factor is determined as the ratio between data and simulation. For points not represented in Fig. 6.11 (left) the average ratio of 0.92 was used. The event selection efficiencies were then recomputed. The resulting relative uncertainty is shown in Table 6.14 for Drell-Yan produced monopoles and in Table 6.15 for single monopoles. Due to the overall overestimation of the TRT occupancy in the simulation, the resulting relative uncertainty yields a positive variation.

The efficiency of the HIP trigger in simulated data may also be affected by the accuracy of the pileup description in the Monte Carlo. Figure 6.11 (left) shows an increase of about 30% in the TRT occupancy from events with low to high pileup. This increase in occupancy as a function of pileup can be used to estimate the change in trigger efficiency due to a mismodelling of the TRT occupancy in the simulation. As can be seen in Fig. 6.11 (right), the change in trigger efficiency from low-pileup events to high-pileup events is negligible for monopoles of charge $|g| \geq 1.0 g_{\mathrm{D}}$ and about 40% for monopoles of charge $|g| = 0.5 g_{\mathrm{D}}$. Since this decrease assumes a change in TRT occupancy of 30%, a more realistic estimate of the systematic uncertainty on the trigger efficiency due to the mismodelling of the pileup is about 10%, as the actual average mismodelling of the TRT occupancy is only 8%.

6.5.6 LAr calorimeter cross-talk

This search uses a measure of the lateral energy dispersion as a calorimeter discriminant between signal and background. Signal leakage between EM calorimeter cells, known as cross-talk, may originate on the copper electrodes or through the readout electronics chain, causing three different types of cross-talk in the EM calorimeter: inductive, resistive and capacitive. Presence of cross-talk in either the ϕ or η direction would affect the determination of the energy deposition lateral dispersion.

Inductive cross-talk between neighbouring second-layer EM calorimeter cells has been studied as well as inductive cross-talk between second-layer calorimeter cells and third-layer calorimeter cells, as described in Ref. [133]. Cross-talk between neighbouring second-layer EM calorimeter cells in η is of order 1.1% and 0.6% in the barrel and end-cap outer wheel,

respectively. Cross-talk between second-layer calorimeter cells and third-layer calorimeter cells in η is of order 0.9% and 1.2% in the barrel and end-cap outer wheel, respectively. Resistive cross-talk exists between calorimeter cells in the first and second layers. This cross-talk in η is of order 0.1% in both barrel and end-cap. Capacitive cross-talk in η between calorimeter cells in the first layer is significant due to the high segmentation of the layer and is of order 7.2% and 6.3% in the barrel and end-cap outer wheel, respectively. The η cross-talk types described above have been implemented in the default ATLAS simulation.

In the ϕ direction, inductive cross-talk, i.e., cross-talk due to mutual inductance between the cells, is present. The mean cross-talk between neighbouring second-layer EM calorimeter cells in ϕ is of order 1.8% [133]. This ϕ cross-talk is not implemented in the ATLAS simulation. In order to assess the systematic uncertainty introduced by the absence of ϕ cross-talk in the ATLAS simulation, the cross-talk in the next-in-ϕ neighbour cell was assumed as 1.8% and the lateral dispersion, w, recomputed with the new energy deposition values. The event selection efficiencies were then recomputed for the signal samples. The relative systematic uncertainties are shown in Table 6.14 for Drell-Yan produced monopoles and in Table 6.15 for single monopoles.

6.5.7 Calorimeter arrival time

The Level-1 trigger becomes inefficient for energy depositions delayed by more than 10 ns due to an increasing probability to be associated to the wrong bunch crossing. A delay of less than 10 ns corresponds to $\beta > 0.37$ if the speed is constant. For the monopole charges and masses considered in this search, the requirement that the monopole reach the EM calorimeter automatically implies that the initial β is higher than 0.37. The monopole slows down as it traverses the ATLAS detector. However, this occurs mainly as monopoles enter the EM calorimeter and does not induce significant time shifts. It was concluded that there is no significant efficiency loss due to time delays of EM calorimeter signals at Level-1, and thus no systematic uncertainty is needed to account for possible inaccuracies of the modelling of inefficiencies due to timing in the simulation.

6.5.8 Extrapolation method for spin-0 monopole efficiencies

The method used to obtain the spin-0 monopole efficiencies [128] was applied to 22 000 generator-level Drell-Yan pair-produced spin-$1/2$ monopole events to predict the spin-$1/2$ efficiency. These results were then compared directly to the efficiencies obtained for fully simulated spin-$1/2$ monopole samples. The difference is assigned as a systematic uncertainty to the spin-0 Drell-Yan monopole efficiencies, in addition to the other systematic uncertainties described in this section obtained for fully simulated spin-$1/2$ monopoles. The relative uncertainty, which is taken as symmetric, is shown in Table 6.14.

6.5.9 Luminosity measurement

The uncertainty due to the luminosity measurement is 2.8%. It is derived, following the same methodology as that detailed in Ref. [127], from a preliminary calibration of the luminosity scale derived from beam-separation scans performed in November 2012. This is added in quadrature to the uncertainties given in Table 6.14 for Drell-Yan produced monopoles and in Table 6.15 for single monopoles.

Chapter 7

Interpretation of the search

The interpretation of the results of the search for magnetic monopoles is presented in this chapter. Results for a model-independent search are presented. In addition, the results are interpreted assuming pair production of monopoles of spin-0 and spin-1/2 using the Drell-Yan model. Upper limits on production cross section and lower mass limits are obtained for these models.

7.1 Cross section limits

In the absence of an observation of signal-like events in the collected data, upper limits on production cross section were obtained. Using fiducial regions of uniform and high selection efficiency with $\epsilon \geq 90\%$, defined using single monopole samples, model-independent production cross section limits were set. In addition, assuming a simplified Drell-Yan model for pair production of spin-1/2 monopoles, upper limits on production cross section were also set. Based on the results from single particle monopoles and the systematic uncertainties on the event selection efficiency obtained for Drell-Yan spin-1/2 monopoles, upper limits of production cross section were set for pair produced spin-0 monopoles assuming the Drell-Yan model.

Cross section limits were obtained using the CL_s method [134] with the RooStats framework [130]. Lower mass limits assuming Drell-Yan production were set for spin-1/2 and

spin-0 monopoles by comparing the observed limits on production cross section with the theoretical predictions.

7.1.1 The CL_s method

The limits on production cross section for monopoles obtained in this search were set using the frequentist CL_s method [134]. This method is particularly useful in searches with low sensitivity that may be affected by fluctuations in the expected background. The CL_s method is a simple normalization of the confidence level observed for the signal+background hypothesis, CL_{s+b}, to the confidence level observed for the background-only hypothesis, CL_b. This is defined as

$$CL_s = \frac{CL_{s+b}}{CL_b}, \tag{7.1}$$

where the confidence levels CL_{s+b} and CL_b are defined as

$$CL_{s+b} = P(q \geq q_{\text{obs}}|s+b) = \int_{q_{\text{obs}}}^{\infty} f(q|s+b), \tag{7.2}$$

$$CL_b = P(q \geq q_{\text{obs}}|b) = \int_{q_{\text{obs}}}^{\infty} f(q|b), \tag{7.3}$$

with $f(q|s+b)$ ($f(q|b)$) the probability distribution function of the test-statistic and q the observable variable, which in this case is the number of observed signal events, μ. For a desired confidence level, e.g., 95% ($\alpha = 0.95$), the CL_s value is given by

$$CL_s = 1 - \alpha = 0.05. \tag{7.4}$$

The test-statistic used in this search is defined as the logarithmic likelihood ratio [135], $-2\ln\lambda(\mu) = -2\ln(L(s+b)/L(b))$, with the likelihood functions $L(s+b)$ and $L(b)$ as defined in Eq. (6.6). The log likelihood is constructed for the case when $\mu \geq 0$, i.e., evidence of magnetic monopoles can only be observed as an increase in the number of events in the signal region over the expected background. Three cases are then considered:

$$-2\ln\lambda(\mu) = \begin{cases} -2\ln\frac{L(\mu,\hat{\hat{\theta}}(\mu))}{L(0,\hat{\hat{\theta}}(0))} & \hat{\mu} < 0, \\ -2\ln\frac{\mu,\hat{\hat{\theta}}(\mu))}{\hat{\mu},\hat{\theta}(\mu))} & 0 \leq \hat{\mu} \leq \mu, \\ 0 & \mu < \hat{\mu}, \end{cases} \tag{7.5}$$

where $\hat{\mu}$ and $\hat{\theta}$ are the maximum likelihood estimators of the maximized unconditional likelihood function, and $\hat{\hat{\theta}}$ is the value of θ that maximizes the likelihood for a given μ, i.e., the conditional maximum likelihood estimator. The systematic uncertainties and signal leakages are represented by θ. The presence of this nuisance parameter causes the probability distribution function of the log likelihood ratio to broaden with respect to a log likelihood ratio with fixed parameters. This is a consequence of the loss of information due to the systematic uncertainties on the event selection efficiency.

7.2 Model-independent cross section limits

The results of the search for monopoles can be interpreted in a model-independent scenario. This is achieved by defining fiducial regions in which the event selection efficiency is high and uniform for single monopoles generated with uniform pseudorapidity, azimuthal angle and kinetic energy spectra, as detailed in Sec. 6.3.3. The average event selection efficiency of the fiducial regions is 90%, which along with the integrated luminosity of the analyzed dataset, 7.0 fb^{-1}, can be used to obtain upper limits on the production cross section for single monopoles in fiducial regions.

Table 7.1 summarizes the upper limits on the number of signal events from which the upper limits on production cross section are calculated. It was found that the model-independent upper limit on production cross section is 0.5 fb^{-1}. The systematic uncertainties used for the limit setting were averaged over all the mass points for each charge, as outlined in Sec. 6.5. The minor differences between mass/charge combinations are therefore due only to the different signal leakages. Only results of mass and charge combinations for which fiducial regions were found are presented.

7.3 Cross section limits on pair-production of monopoles

This search included two specific models in which monopoles are produced in monopole–anti-monopole pairs: Drell-Yan production of spin-1/2 and spin-0 monopoles. A MC leading-order matrix element generator (MadGraph5 [108]) was used to generate the monopole

	95% CL upper limit on number of signal events				95% CL upper limit on production cross section [fb]			
Mass [GeV]	$\|g\| = 0.5g_D$	$\|g\| = 1.0g_D$	$\|g\| = 1.5g_D$	$\|g\| = 2.0g_D$	$\|g\| = 0.5g_D$	$\|g\| = 1.0g_D$	$\|g\| = 1.5g_D$	$\|g\| = 2.0g_D$
200	2.96	3.02	3.02	3.09	0.47	0.48	0.48	0.49
500	3.02	3.02	3.09	2.96	0.48	0.48	0.49	0.47
1000	3.09	3.02	3.09	2.96	0.49	0.48	0.49	0.47
1500	—	2.96	3.02	2.96	—	0.47	0.48	0.47
2000	—	3.09	3.09	3.02	—	0.49	0.49	0.48
2500	—	3.02	3.02	3.02	—	0.48	0.48	0.48

Table 7.1: Upper limits on number of signal events and production cross section at 95% confidence level for single monopoles in fiducial regions of high and uniform event selection efficiency. Only results of mass and charge combinations for which fiducial regions were found are presented.

events. Only leading-order calculations are used due to the large magnetic coupling to the photon, which makes the production process highly non-perturbative.

7.3.1 Spin-1/2 pair production cross section

Table 7.2 presents the upper limits on the number of signal events and the corresponding upper limits on production cross section of spin-1/2 monopole–anti-monopole pairs assuming the Drell-Yan mechanism. Only results for mass/charge points with an acceptance greater than 1% are shown. Figure 7.1 summarizes the cross section limits as a function of monopole mass. This search was performed using MC samples that were processed with the full ATLAS simulation, as described in Sec. 4.2.

Spin-1/2	95% CL upper limit on number of signal events				95% CL upper limit on production cross section [fb]			
Mass [GeV]	$\|g\| = 0.5g_D$	$\|g\| = 1.0g_D$	$\|g\| = 1.5g_D$	$\|g\| = 2.0g_D$	$\|g\| = 0.5g_D$	$\|g\| = 1.0g_D$	$\|g\| = 1.5g_D$	$\|g\| = 2.0g_D$
200	3.00	2.97	—	—	1.92	12.02	—	—
500	2.93	2.96	2.93	—	1.25	2.85	36.14	—
1000	3.08	2.86	2.87	—	1.58	1.75	11.28	—
1500	3.06	2.90	2.94	—	1.85	1.87	11.9	—
2000	3.06	3.02	2.79	—	2.62	2.61	14.31	—
2500	3.16	2.99	2.91	—	4.62	4.37	25.78	—

Table 7.2: Upper limits on number of signal events and production cross section at 95% confidence level for spin-1/2 monopoles assuming Drell-Yan production. Only results for mass and charge combinations for which the event selection efficiency was greater than 1% are included in the search.

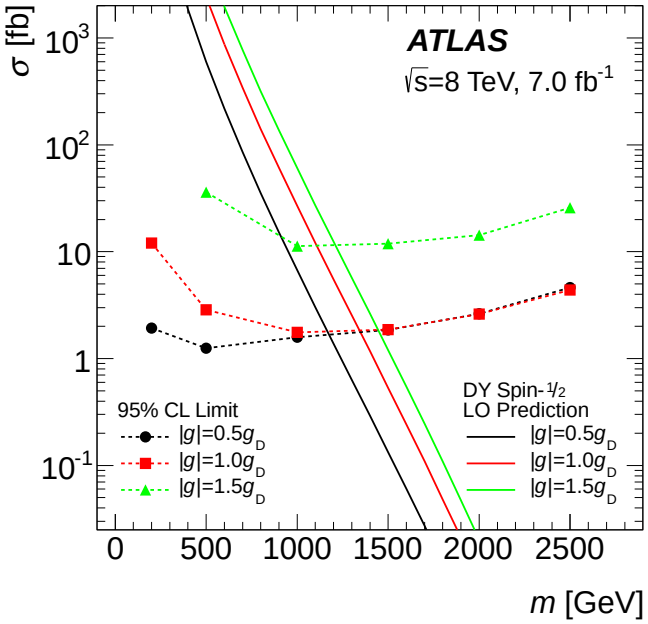

Figure 7.1: Upper limits on production cross section at 95% confidence level for Drell-Yan production of spin-1/2 monopoles as a function of monopole mass in various scenarios (dashed lines with markers). No cross-section limit is shown for mass/charge points with an acceptance lower than 1%. Overlaid on the plots are the leading-order theoretical cross sections (solid lines) [45].

7.3.2 Spin-0 pair production cross section

Table 7.3 presents the upper limits on the number of signal events and the corresponding upper limits on production cross section of spin-0 monopole–anti-monopole pairs assuming the Drell-Yan mechanism. Only results for mass/charge points with an acceptance greater than 1% are shown. Figure 7.2 summarizes the cross section limits as a function of monopole mass. Event selection efficiencies were obtained by extrapolating results from single particle samples using only generator-level four-vectors for spin-0 Drell-Yan monopoles, as described in Sec. 6.3.2. Upper limits were set using the systematic uncertainties from spin-1/2 Drell-Yan produced monopoles, as outlined in Sec. 6.5.8.

Spin-0	95% CL upper limit on number of signal events				95% CL upper limit on production cross section [fb]			
Mass [GeV]	$\|g\| = 0.5g_D$	$\|g\| = 1.0g_D$	$\|g\| = 1.5g_D$	$\|g\| = 2.0g_D$	$\|g\| = 0.5g_D$	$\|g\| = 1.0g_D$	$\|g\| = 1.5g_D$	$\|g\| = 2.0g_D$
200	2.95	3.06	—	—	0.99	4.37	—	—
500	3.01	2.97	3.04	—	0.8	1.22	10.58	—
1000	2.98	2.97	2.81	—	0.96	0.83	3.52	—
1500	3.07	3.07	2.91	—	1.2	0.88	3.01	—
2000	2.81	2.97	2.87	—	1.3	1.02	3.76	—
2500	2.87	3.08	2.91	—	1.79	1.43	6.03	—

Table 7.3: Upper limits on number of signal events and production cross section at 95% confidence level for spin-0 monopoles assuming Drell-Yan production. Only results for mass and charge combinations for which the event selection efficiency was greater than 1% are included in the search.

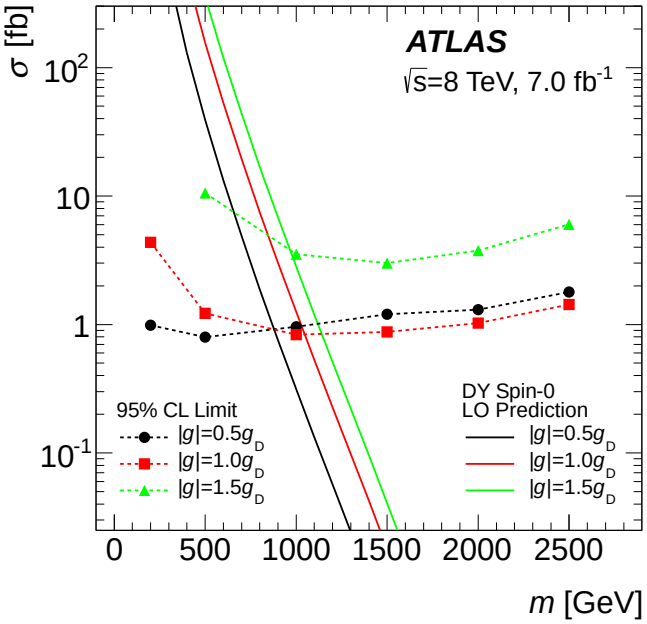

Figure 7.2: Upper limits on production cross section at 95% confidence level for Drell-Yan production of spin-0 monopoles as a function of monopole mass in various scenarios (dashed lines with markers). No cross-section limit is shown for mass/charge points with an acceptance lower than 1%. Overlaid on the plots are the leading-order theoretical cross sections (solid lines) [45].

7.3.3 Lower mass limits for pair-produced monopoles

Based on the cross section exclusion limits obtained for the monopole pair-production models, lower limits on the mass of the monopoles can be set. Lower mass limits were obtained

by finding the mass for which the theoretical cross section prediction drops below the upper cross section limit.

	Drell-Yan Lower Mass Limits [GeV]			
	$\|g\| = 0.5g_{\mathrm{D}}$	$\|g\| = 1.0g_{\mathrm{D}}$	$\|g\| = 1.5g_{\mathrm{D}}$	$\|g\| = 2.0g_{\mathrm{D}}$
Spin-1/2	1180	1340	1210	—
Spin-0	890	1050	970	—

Table 7.4: Lower mass limits (in GeV) at 95% confidence level in models of spin-1/2 (top) and spin-0 (bottom) Drell-Yan monopole pair production. These limits are based upon leading-order models, since the production mechanism is of a highly non-perturbative nature. No limits are given for monopoles of charge $|g| = 2.0g_{\mathrm{D}}$ as they were excluded from the search due to their low acceptance.

Table 7.4 shows the lower mass limits for spin-1/2 and spin-0 monopoles produced assuming the Drell-Yan mechanism. These limits are valid only for the production models considered, and therefore are limited by the accuracy of the theoretical cross section predictions. Nevertheless, these results can be directly compared with previous experimental searches at colliders that used the same production mechanism. This is the case of the search for spin-1/2 monopoles produced at the Tevatron by the CDF experiment, which obtained a lower mass limit of 476 GeV for monopoles of charge $|g| = 1.0g_{\mathrm{D}}$ [57], and the previous search at ATLAS for spin-1/2 monopoles produced at the LHC in 7 TeV pp collisions, which set a lower mass limit of 862 GeV for monopoles of charge $|g| = 1.0g_{\mathrm{D}}$ [77].

Chapter 8

Conclusion

Since their prediction by Dirac [9], magnetic monopoles have been a possible answer to one of the most fundamental open questions in physics: the quantization of charge. The prediction of monopoles by some electro-weak models [26] and grand unified theories [20,21], in which charge is quantized, reinforces the case for experimental searches. The search for magnetic monopoles has always been a field full of innovation, taking advantage of a number of instrumental and analysis methods in order to cover all possible scenarios, ranging from monopoles trapped in terrestrial or extraterrestrial rocks [37–39] to their direct production at high-energy particle colliders [45, 56, 77].

This search for magnetic monopoles produced at the LHC in high-energy pp collisions at a centre-of-mass energy of 8 TeV exploited their unique signature. Specific ATLAS subdetectors, such as the TRT and the EM calorimeter, were used to identify regions of high-ionization density, which constituted the main analysis objects. A dedicated trigger was deployed to select events with a high ionization density in the TRT. This trigger allowed for the search of monopoles with charge $|g| \geq 1.0 g_{\mathrm{D}}$. Analysis techniques to measure the ionization density in the TRT and in the EM calorimeter were developed to reconstruct monopole candidates in events that pass the dedicated trigger, achieving a very high reconstruction efficiency.

No events with a signature consistent with that of a monopole were observed in the 7.0 fb^{-1} of pp data analyzed. This observation is consistent with the background expec-

tation. In the absence of signal events in the collision data, upper limits on production cross sections were set in three different scenarios. A model-independent limit of 0.5 fb was obtained for monopoles with mass in the range 200 – 2500 GeV and charges $|g| = 0.5g_{\mathrm{D}}$, $|g| = 1.0g_{\mathrm{D}}$, $|g| = 1.5g_{\mathrm{D}}$ and $|g| = 2.0g_{\mathrm{D}}$ in fiducial regions of high and uniform event selection efficiency. Assuming pair production of spin-1/2 and spin-0 monopoles using the Drell-Yan mechanism limits were also set. Based on the theoretical cross section predictions, lower mass limits were set for pair-produced spin-1/2 and spin-0 monopoles of charge $|g| = 0.5g_{\mathrm{D}}$, $|g| = 1.0g_{\mathrm{D}}$ and $|g| = 1.5g_{\mathrm{D}}$. The limits obtained in this search represent the most competitive limits on magnetic monopoles produced at high-energy particle colliders to date.

This work contributes to the vast field of experimental searches for magnetic monopoles, in particular, monopoles produced at high-energy colliders. It provides improvements in the trigger and measurement of the energy deposition in the ATLAS EM calorimeter. Future searches for monopoles produced at the LHC using the ATLAS detector will be based upon these new developments and knowledge. The techniques developed for this work can also be applied in the search for any type of highly ionizing particles, such as objects with large electric charge, e.g., $|z| \geq 20$ [45].

Appendix A

HIP TRT trigger efficiency vs. monopole p_{T}

Figures A.4 to A.6 were used to determine the generator level minimum-p_{T} requirements for Drell-Yan produced spin-1/2 monopoles. This requirement is conservatively chosen as the point 50 to 100 GeV below the turn on of the trigger efficiency curve.

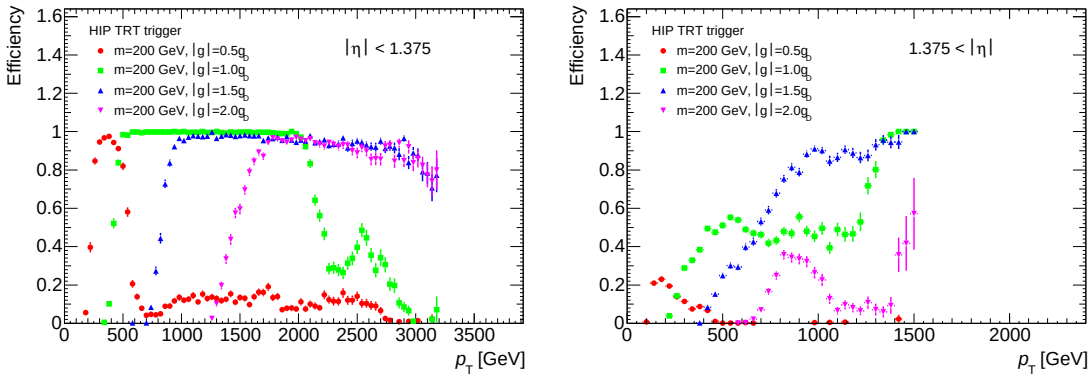

Figure A.1: HIP TRT trigger efficiency as a function of p_{T} for monopoles of mass 200 GeV in $|\eta| < 1.375$ (left) and $1.375 < |\eta|$ (right).

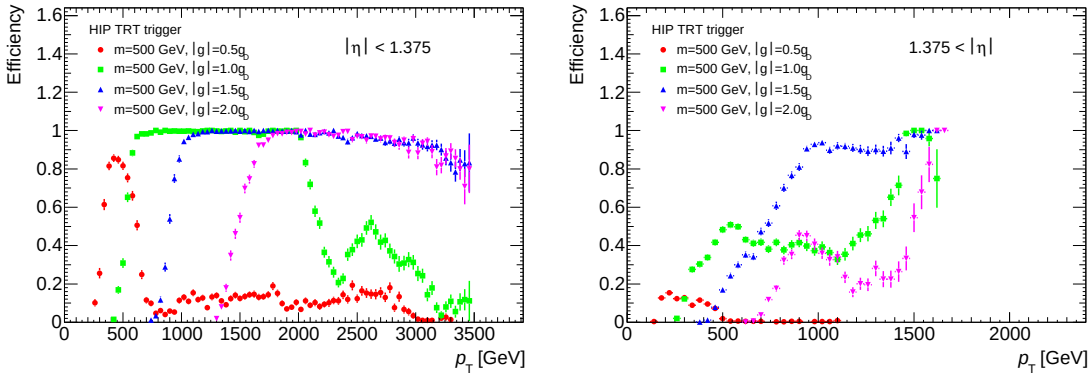

Figure A.2: HIP TRT trigger efficiency as a function of p_{T} for monopoles of mass 500 GeV in $|\eta| < 1.375$ (left) and $1.375 < |\eta|$ (right).

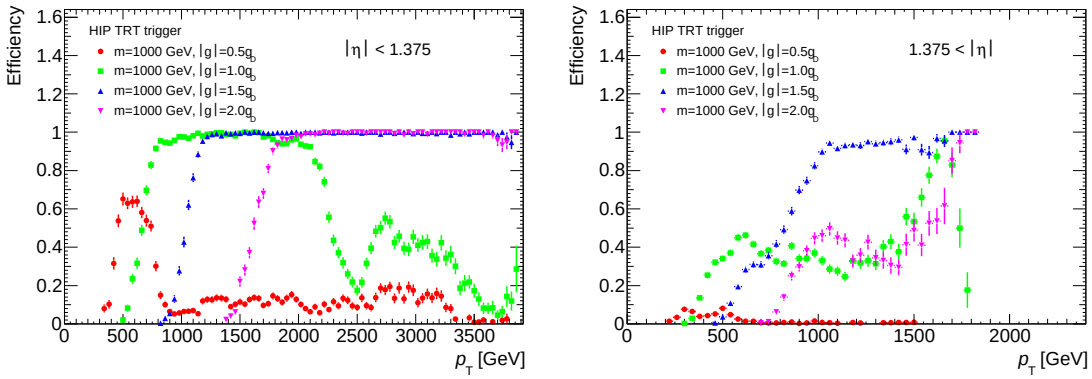

Figure A.3: HIP TRT trigger efficiency as a function of p_{T} for monopoles of mass 1000 GeV in $|\eta| < 1.375$ (left) and $1.375 < |\eta|$ (right).

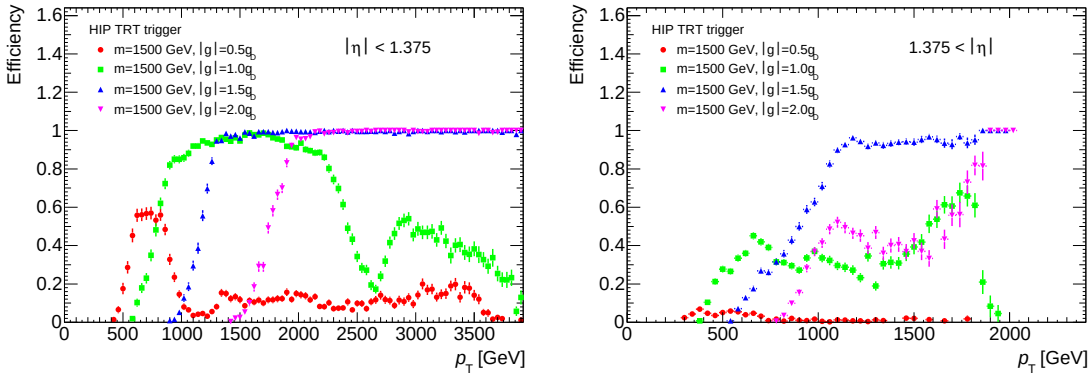

Figure A.4: HIP TRT trigger efficiency as a function of p_{T} for monopoles of mass 1500 GeV in $|\eta| < 1.375$ (left) and $1.375 < |\eta|$ (right).

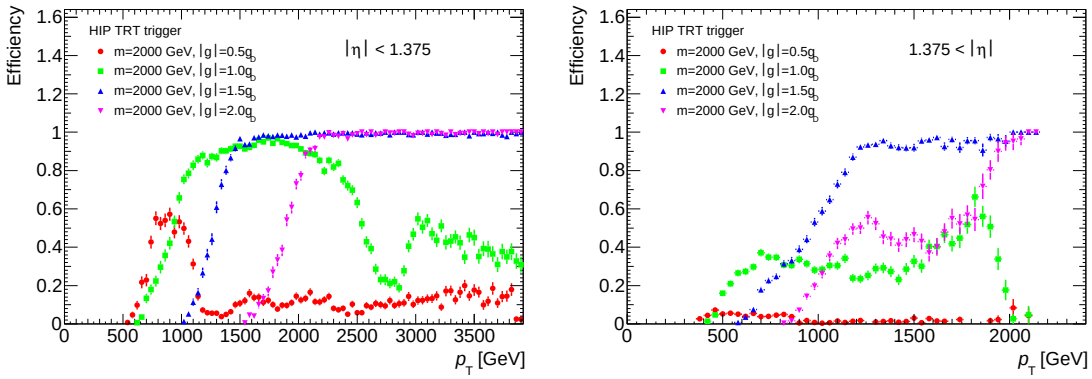

Figure A.5: HIP TRT trigger efficiency as a function of p_{T} for monopoles of mass 2000 GeV in $|\eta| < 1.375$ (left) and $1.375 < |\eta|$ (right).

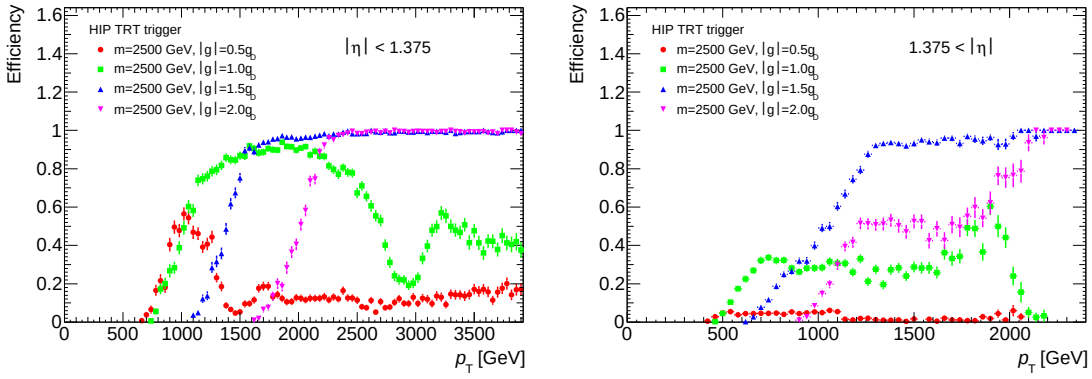

Figure A.6: HIP TRT trigger efficiency as a function of p_{T} for monopoles of mass 2500 GeV in $|\eta| < 1.375$ (left) and $1.375 < |\eta|$ (right).

Appendix B

Energy weighted cluster size σ_{R}

The search for magnetic monopoles by ATLAS with 7 TeV data [77] used an variable measuring the energy-weighted lateral size of the EM calorimeter clusters. It was required that monopoles reach the second layer of the EM calorimeter and thus the lateral size, σ_{R} was implemented for EM2 only. The energy-weighted lateral size is defined as

$$\sigma_{\mathrm{R}} = \sqrt{\sigma_{\eta}^2 + \sigma_{\phi}^2} \tag{B.1}$$

with

$$\sigma_{\phi} = \left(\sum_{i}^{n} \left(E_i \delta\phi_i^2 \right) / \sum_{i}^{n} E_i - \left[\sum_{i}^{n} (E_i \delta\phi_i) \right]^2 / \sum_{i}^{n} E_i \right)^{1/2} \tag{B.2}$$

where n is a predefined number of cells over which the calculation is performed and $\delta\phi$ the calorimeter cell size in ϕ. The formula for the size σ_{η} is equivalent to that of ϕ.

The current search uses a dedicated trigger that selects monopoles that stop in the presampler and EM1, before reaching EM2. Therefore, were the lateral cluster size, σ_{R}, to be used, it would have to be extended to the presampler and EM1. Such implementation would be slightly different for each calorimeter layer as the granularity changes from layer to layer. Additionally, the segmentation of the EM calorimeter is not constant in η forcing n to vary in order to keep the surface area over which the calculation is done approximately constant.

The lateral size, σ_{R}, was thus defined for the presampler, EM1 and EM2, and optimized

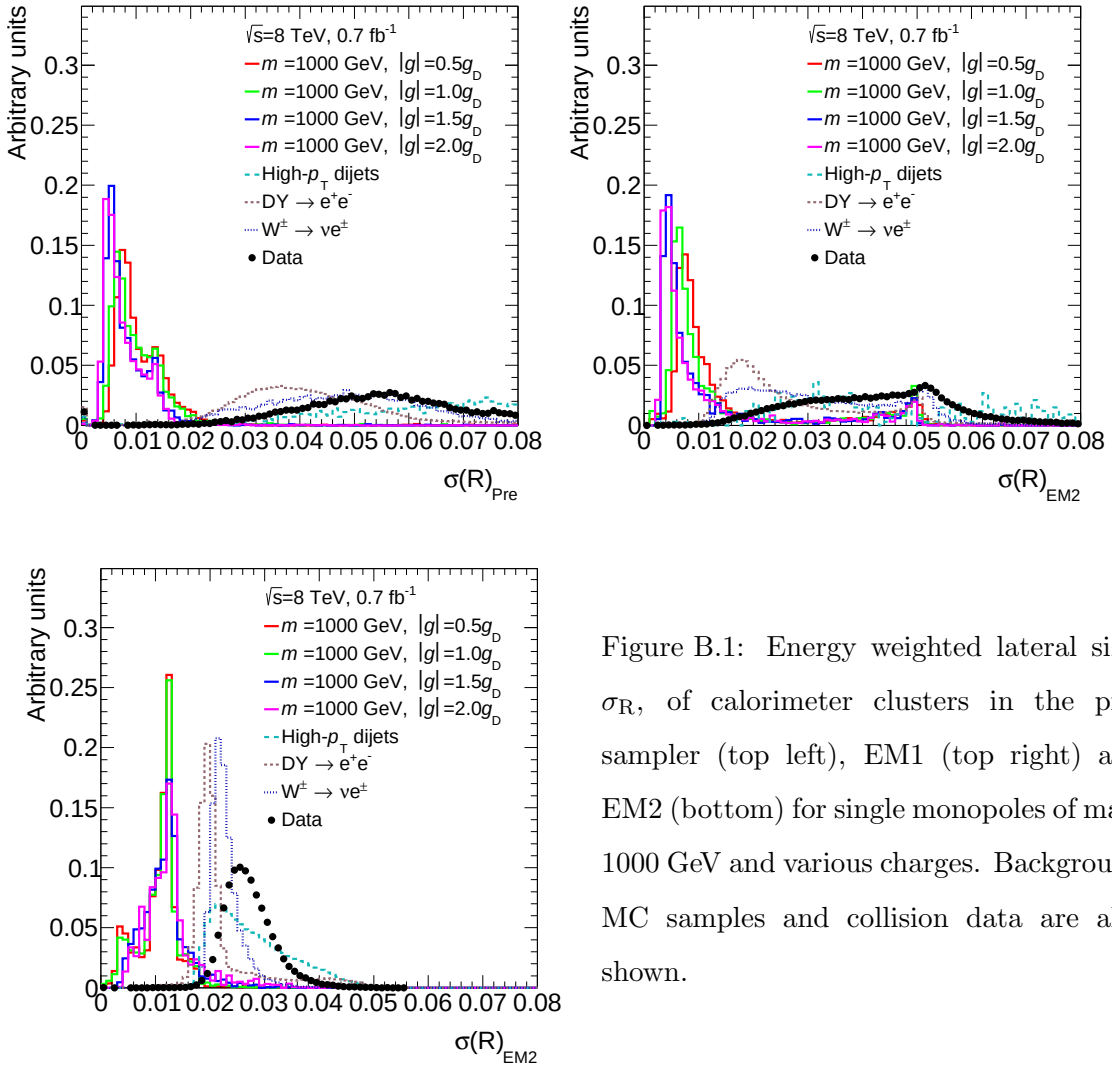

Figure B.1: Energy weighted lateral size, σ_{R}, of calorimeter clusters in the pre-sampler (top left), EM1 (top right) and EM2 (bottom) for single monopoles of mass 1000 GeV and various charges. Background MC samples and collision data are also shown.

to keep the surface area over which the size is calculated approximately constant. Figure B.1 shows the lateral size of the calorimeter clusters in signal, background MC and collision data.

The distributions of σ_{R} show that there are multiple spikes that cause the signal from monopole and background events to mix. The double peak structure observed is due to the coarse granularity of presampler and EM1. When a monopole deposits most of its energy in two calorimeter cells only, σ_{R} takes a value proportional to the cell size limiting the usability of this metric. Therefore, the use of the lateral size σ_{R} was dropped in favour of the more robust cluster dispersion variable w.

Appendix C

Run condition stability

It is important to ensure that the run conditions of the dataset used in the search are stable. Although the dataset used in the search includes events of high quality recorded with the ATLAS detector fully operational, runs with event rates that lie outside normal running conditions should be checked for possible detector performance anomalies not considered by the data acquisition quality group.

The total number of events that passed the HIP trigger is 876 895 for an integrated luminosity of 7.0 fb^{-1}, yielding an expected average of 125 270 events per fb^{-1}. Figure C.1 shows the number of recorded events per fb^{-1} as a function of the run number. The oscillations around 100 events/fb^{-1} reflect the beam conditions during the LHC fill. A fill corresponds to an arrangement of bunches of protons injected into the LHC. Data collected during a run at the beginning of a fill would have a lower event rate as the fraction of HT TRT hits would be diluted by additional minimum ionizing particles produced in additional collisions between protons in denser bunches. The event rate then increases as the density of the bunches decreases during the fill. A particular case can be spotted for run 213816, with a record number of events per fb^{-1} of about 490 000. The TRT log from the day points out that the "TRT turned yellow due to high threshold hits occupancy in end-cap having a spike." A sudden increase in TRT HT hit occupancy would undoubtedly cause an increase in the trigger event rate. Since this represents an instability of which the exact cause is unknown, this run is excluded from the search. The integrated luminosity of this run is

0.0472 fb^{-1}, the loss of which has a negligible impact in the full dataset.

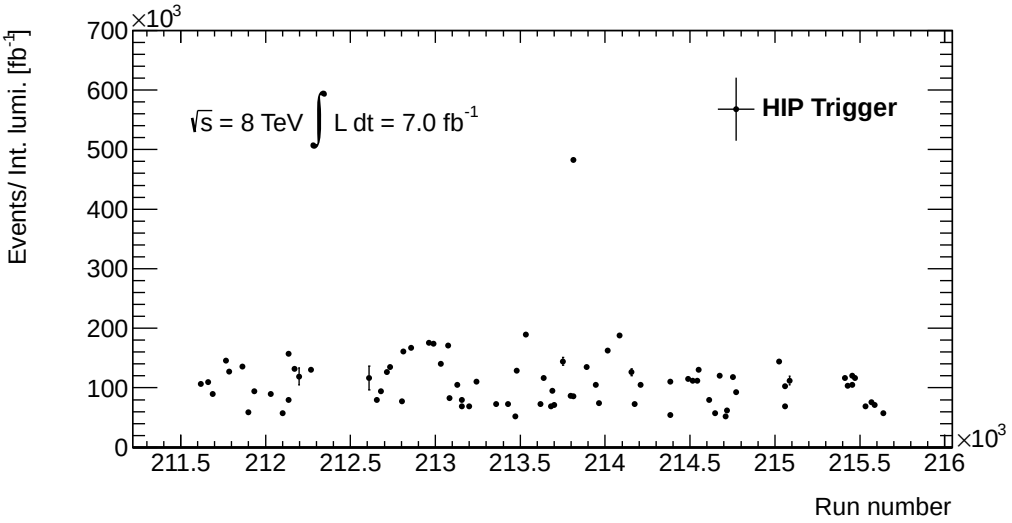

Figure C.1: Number of events per fb^{-1} as a function of run number for the dataset collected with the HIP trigger. The errors are statistical.

Appendix D

Event selection cut-flow tables

Selection	Candidates	Rel. eff.	Total eff.	Events	Rel. eff.	Total eff.
All	—	—	—	49997	—	—
HIP trigger	—	—	—	5649	11.30	11.30
Preselection	6639	—	—	5629	99.64	11.26
Overlap removal	5629	84.79	84.79	5629	100.00	11.26
$E_{\mathrm{T}}^{\mathrm{EM}} > 16$ GeV	5604	99.55	84.41	5604	99.55	11.21
$E_{\mathrm{Pre}} > 5$ GeV OR $E_{\mathrm{EM1}} > 5$ GeV	5596	99.86	84.29	5596	99.86	11.19
$\lvert\eta\rvert < 1.375$ OR $1.52 < \lvert\eta\rvert < 2.0$	5265	94.10	79.31	5265	94.10	10.53
Hadronic veto $E_{\mathrm{HCal}} \leq 1$ GeV	3694	70.16	55.65	3694	70.16	7.39
Max f_{HT} candidate	3694	100.00	55.65	3694	100.00	7.39
$w \geq 0.94$	3624	98.10	54.59	3624	98.10	7.25
$f_{\mathrm{HT}} \geq 0.7$	3542	97.72	53.35	3542	97.72	7.08

Table D.1: Event selection efficiency for single monopoles of mass 200 GeV and charge $|g| = 0.5g_{\mathrm{D}}$.

Selection	Candidates	Rel. eff.	Total eff.	Events	Rel. eff.	Total eff.
All	—	—	—	50000	—	—
HIP trigger	—	—	—	4696	9.39	9.39
Preselection	5511	—	—	4672	99.50	9.34
Overlap removal	4674	84.80	84.80	4672	100.00	9.34
$E_{\mathrm{T}}^{\mathrm{EM}} > 16$ GeV	4648	99.46	84.35	4648	99.49	9.30
$E_{\mathrm{Pre}} > 5$ GeV OR $E_{\mathrm{EM1}} > 5$ GeV	4626	99.52	83.94	4626	99.52	9.25
$\lvert\eta\rvert < 1.375$ OR $1.52 < \lvert\eta\rvert < 2.0$	4328	93.55	78.53	4328	93.55	8.66
Hadronic veto $E_{\mathrm{HCal}} \leq 1$ GeV	2745	63.43	49.81	2745	63.43	5.49
Max f_{HT} candidate	2745	100.00	49.81	2745	100.00	5.49
$w \geq 0.94$	2708	98.63	49.13	2708	98.63	5.42
$f_{\mathrm{HT}} \geq 0.7$	2594	95.80	47.07	2594	95.80	5.19

Table D.2: Event selection efficiency for single monopoles of mass 500 GeV and charge $|g| = 0.5g_{\mathrm{D}}$.

Selection	Candidates	Rel. eff.	Total eff.	Events	Rel. eff.	Total eff.
All	—	—	—	49074	—	—
HIP trigger	—	—	—	3628	7.39	7.39
Preselection	4128	—	—	3604	99.34	7.34
Overlap removal	3605	87.33	87.33	3604	100.00	7.34
$E_{\mathrm{T}}^{\mathrm{EM}} > 16$ GeV	3570	99.04	86.49	3570	99.06	7.27
$E_{\mathrm{Pre}} > 5$ GeV OR $E_{\mathrm{EM1}} > 5$ GeV	3554	99.56	86.11	3554	99.56	7.24
$\lvert\eta\rvert < 1.375$ OR $1.52 < \lvert\eta\rvert < 2.0$	3423	96.32	82.94	3423	96.32	6.98
Hadronic veto $E_{\mathrm{HCal}} \leq 1$ GeV	1900	55.50	46.03	1900	55.50	3.87
Max f_{HT} candidate	1900	100.00	46.03	1900	100.00	3.87
$w \geq 0.94$	1886	99.24	45.68	1886	99.24	3.84
$f_{\mathrm{HT}} \geq 0.7$	1569	83.22	38.02	1569	83.22	3.20

Table D.3: Event selection efficiency for single monopoles of mass 1000 GeV and charge $|g| = 0.5g_{\mathrm{D}}$.

Selection	Candidates	Rel. eff.	Total eff.	Events	Rel. eff.	Total eff.
All	—	—	—	50000	—	—
HIP trigger	—	—	—	3442	6.88	6.88
Preselection	4053	—	—	3423	99.45	6.85
Overlap removal	3425	84.49	84.49	3423	100.00	6.85
$E_{\mathrm{T}}^{\mathrm{EM}} > 16$ GeV	3396	99.16	83.78	3396	99.20	6.79
$E_{\mathrm{Pre}} > 5$ GeV OR $E_{\mathrm{EM1}} > 5$ GeV	3358	98.89	82.85	3358	98.89	6.72
$\lvert\eta\rvert < 1.375$ OR $1.52 < \lvert\eta\rvert < 2.0$	3224	96.01	79.54	3224	96.01	6.45
Hadronic veto $E_{\mathrm{HCal}} \leq 1$ GeV	1686	52.30	41.60	1686	52.30	3.37
Max f_{HT} candidate	1686	100.00	41.60	1686	100.00	3.37
$w \geq 0.94$	1683	99.79	41.52	1683	99.79	3.37
$f_{\mathrm{HT}} \geq 0.7$	1325	78.73	32.69	1325	78.73	2.65

Table D.4: Event selection efficiency for single monopoles of mass 1500 GeV and charge $|g| = 0.5g_{\mathrm{D}}$.

Selection	Candidates	Rel. eff.	Total eff.	Events	Rel. eff.	Total eff.
All	—	—	—	50000	—	—
HIP trigger	—	—	—	3345	6.69	6.69
Preselection	4130	—	—	3336	99.74	6.67
Overlap removal	3337	80.80	80.80	3336	100.00	6.67
$E_{\mathrm{T}}^{\mathrm{EM}} > 16$ GeV	3316	99.36	80.29	3316	99.39	6.63
$E_{\mathrm{Pre}} > 5$ GeV OR $E_{\mathrm{EM1}} > 5$ GeV	3281	98.96	79.45	3281	98.96	6.56
$\lvert\eta\rvert < 1.375$ OR $1.52 < \lvert\eta\rvert < 2.0$	3121	95.11	75.56	3121	95.11	6.24
Hadronic veto $E_{\mathrm{HCal}} \leq 1$ GeV	1503	48.17	36.39	1503	48.17	3.01
Max f_{HT} candidate	1503	100.00	36.39	1503	100.00	3.01
$w \geq 0.94$	1497	99.60	36.25	1497	99.60	2.99
$f_{\mathrm{HT}} \geq 0.7$	1133	75.68	27.43	1133	75.68	2.27

Table D.5: Event selection efficiency for single monopoles of mass 2000 GeV and charge $|g| = 0.5g_{\mathrm{D}}$.

Selection	Candidates	Rel. eff.	Total eff.	Events	Rel. eff.	Total eff.
All	—	—	—	49883	—	—
HIP trigger	—	—	—	3527	7.07	7.07
Preselection	4487	—	—	3517	99.72	7.05
Overlap removal	3517	78.39	78.39	3517	100.00	7.05
$E_{\mathrm{T}}^{\mathrm{EM}} > 16$ GeV	3478	98.89	77.52	3478	98.89	6.97
$E_{\mathrm{Pre}} > 5$ GeV OR $E_{\mathrm{EM1}} > 5$ GeV	3432	98.65	76.48	3432	98.65	6.88
$\lvert\eta\rvert < 1.375$ OR $1.52 < \lvert\eta\rvert < 2.0$	3237	94.32	72.13	3237	94.32	6.49
Hadronic veto $E_{\mathrm{HCal}} \leq 1$ GeV	1367	42.25	30.47	1367	42.25	2.74
Max f_{HT} candidate	1367	100.00	30.47	1367	100.00	2.74
$w \geq 0.94$	1354	99.06	30.19	1354	99.06	2.72
$f_{\mathrm{HT}} \geq 0.7$	1045	77.16	23.29	1045	77.16	2.10

Table D.6: Event selection efficiency for single monopoles of mass 2500 GeV and charge $|g| = 0.5g_{\mathrm{D}}$.

Selection	Candidates	Rel. eff.	Total eff.	Events	Rel. eff.	Total eff.
All	—	—	—	49601	—	—
HIP trigger	—	—	—	23035	46.44	46.44
Preselection	26389	—	—	22897	99.40	46.16
Overlap removal	22902	86.79	86.79	22897	100.00	46.16
$E_{\mathrm{T}}^{\mathrm{EM}} > 16$ GeV	22902	100.00	86.79	22897	100.00	46.16
$E_{\mathrm{Pre}} > 5$ GeV OR $E_{\mathrm{EM1}} > 5$ GeV	22902	100.00	86.79	22897	100.00	46.16
$\lvert\eta\rvert < 1.375$ OR $1.52 < \lvert\eta\rvert < 2.0$	20829	90.95	78.93	20824	90.95	41.98
Hadronic veto $E_{\mathrm{HCal}} \leq 1$ GeV	20364	97.77	77.17	20359	97.77	41.04
Max f_{HT} candidate	20359	99.98	77.15	20359	100.00	41.04
$w \geq 0.94$	18485	90.80	70.05	18485	90.80	37.27
$f_{\mathrm{HT}} \geq 0.7$	17878	96.71	67.75	17878	96.71	36.04

Table D.7: Event selection efficiency for single monopoles of mass 200 GeV and charge $|g| = 1.0 g_{\mathrm{D}}$.

Selection	Candidates	Rel. eff.	Total eff.	Events	Rel. eff.	Total eff.
All	—	—	—	50000	—	—
HIP trigger	—	—	—	21821	43.64	43.64
Preselection	25609	—	—	21742	99.64	43.48
Overlap removal	21745	84.91	84.91	21742	100.00	43.48
$E_{\mathrm{T}}^{\mathrm{EM}} > 16$ GeV	21744	100.00	84.91	21741	100.00	43.48
$E_{\mathrm{Pre}} > 5$ GeV OR $E_{\mathrm{EM1}} > 5$ GeV	21742	99.99	84.90	21739	99.99	43.48
$\lvert\eta\rvert < 1.375$ OR $1.52 < \lvert\eta\rvert < 2.0$	19613	90.21	76.59	19611	90.21	39.22
Hadronic veto $E_{\mathrm{HCal}} \leq 1$ GeV	18872	96.22	73.69	18871	96.22	37.74
Max f_{HT} candidate	18871	99.99	73.69	18871	100.00	37.74
$w \geq 0.94$	18722	99.21	73.11	18722	99.21	37.44
$f_{\mathrm{HT}} \geq 0.7$	18398	98.27	71.84	18398	98.27	36.80

Table D.8: Event selection efficiency for single monopoles of mass 500 GeV and charge $|g| = 1.0 g_{\mathrm{D}}$.

Selection	Candidates	Rel. eff.	Total eff.	Events	Rel. eff.	Total eff.
All	—	—	—	50000	—	—
HIP trigger	—	—	—	20326	40.65	40.65
Preselection	24263	—	—	20278	99.76	40.56
Overlap removal	20281	83.59	83.59	20278	100.00	40.56
$E_{\mathrm{T}}^{\mathrm{EM}} > 16$ GeV	20278	99.99	83.58	20276	99.99	40.55
$E_{\mathrm{Pre}} > 5$ GeV OR $E_{\mathrm{EM1}} > 5$ GeV	20276	99.99	83.57	20274	99.99	40.55
$\lvert\eta\rvert < 1.375$ OR $1.52 < \lvert\eta\rvert < 2.0$	18319	90.35	75.50	18318	90.35	36.64
Hadronic veto $E_{\mathrm{HCal}} \leq 1$ GeV	17276	94.30	71.20	17274	94.30	34.55
Max f_{HT} candidate	17274	99.99	71.19	17274	100.00	34.55
$w \geq 0.94$	17239	99.79	71.05	17239	99.79	34.48
$f_{\mathrm{HT}} \geq 0.7$	17082	99.09	70.40	17082	99.09	34.16

Table D.9: Event selection efficiency for single monopoles of mass 1000 GeV and charge $|g| = 1.0 g_{\mathrm{D}}$.

Selection	Candidates	Rel. eff.	Total eff.	Events	Rel. eff.	Total eff.
All	—	—	—	50000	—	—
HIP trigger	—	—	—	18746	37.49	37.49
Preselection	22435	—	—	18706	99.79	37.41
Overlap removal	18710	83.40	83.40	18706	100.00	37.41
$E_{\mathrm{T}}^{\mathrm{EM}} > 16$ GeV	18707	99.99	83.38	18705	99.99	37.41
$E_{\mathrm{Pre}} > 5$ GeV OR $E_{\mathrm{EM1}} > 5$ GeV	18705	99.99	83.37	18703	99.99	37.41
$\lvert\eta\rvert < 1.375$ OR $1.52 < \lvert\eta\rvert < 2.0$	16857	90.12	75.13	16855	90.12	33.71
Hadronic veto $E_{\mathrm{HCal}} \leq 1$ GeV	15605	92.58	69.56	15604	92.58	31.21
Max f_{HT} candidate	15604	99.99	69.55	15604	100.00	31.21
$w \geq 0.94$	15578	99.84	69.44	15578	99.84	31.16
$f_{\mathrm{HT}} \geq 0.7$	15420	98.99	68.73	15420	98.99	30.84

Table D.10: Event selection efficiency for single monopoles of mass 1500 GeV and charge $|g| = 1.0 g_{\mathrm{D}}$.

Selection	Candidates	Rel. eff.	Total eff.	Events	Rel. eff.	Total eff.
All	—	—	—	50000	—	—
HIP trigger	—	—	—	17189	34.38	34.38
Preselection	20779	—	—	17157	99.81	34.31
Overlap removal	17161	82.59	82.59	17157	100.00	34.31
$E_{\mathrm{T}}^{\mathrm{EM}} > 16$ GeV	17156	99.97	82.56	17155	99.99	34.31
$E_{\mathrm{Pre}} > 5$ GeV OR $E_{\mathrm{EM1}} > 5$ GeV	17151	99.97	82.54	17150	99.97	34.30
$\lvert\eta\rvert < 1.375$ OR $1.52 < \lvert\eta\rvert < 2.0$	15438	90.01	74.30	15438	90.02	30.88
Hadronic veto $E_{\mathrm{HCal}} \leq 1$ GeV	14085	91.24	67.79	14085	91.24	28.17
Max f_{HT} candidate	14085	100.00	67.79	14085	100.00	28.17
$w \geq 0.94$	14068	99.88	67.70	14068	99.88	28.14
$f_{\mathrm{HT}} \geq 0.7$	13850	98.45	66.65	13850	98.45	27.70

Table D.11: Event selection efficiency for single monopoles of mass 2000 GeV and charge $|g| = 1.0 g_{\mathrm{D}}$.

Selection	Candidates	Rel. eff.	Total eff.	Events	Rel. eff.	Total eff.
All	—	—	—	50000	—	—
HIP trigger	—	—	—	16114	32.23	32.23
Preselection	19611	—	—	16085	99.82	32.17
Overlap removal	16087	82.03	82.03	16085	100.00	32.17
$E_{\mathrm{T}}^{\mathrm{EM}} > 16$ GeV	16081	99.97	82.00	16080	99.97	32.16
$E_{\mathrm{Pre}} > 5$ GeV OR $E_{\mathrm{EM1}} > 5$ GeV	16070	99.93	81.94	16068	99.93	32.14
$\lvert\eta\rvert < 1.375$ OR $1.52 < \lvert\eta\rvert < 2.0$	14441	89.87	73.64	14440	89.87	28.88
Hadronic veto $E_{\mathrm{HCal}} \leq 1$ GeV	12956	89.72	66.07	12955	89.72	25.91
Max f_{HT} candidate	12955	99.99	66.06	12955	100.00	25.91
$w \geq 0.94$	12943	99.91	66.00	12943	99.91	25.89
$f_{\mathrm{HT}} \geq 0.7$	12669	97.88	64.60	12669	97.88	25.34

Table D.12: Event selection efficiency for single monopoles of mass 2500 GeV and charge $|g| = 1.0 g_{\mathrm{D}}$.

Selection	Candidates	Rel. eff.	Total eff.	Events	Rel. eff.	Total eff.
All	—	—	—	47054	—	—
HIP trigger	—	—	—	19403	41.24	41.24
Preselection	20784	—	—	19288	99.41	40.99
Overlap removal	19290	92.81	92.81	19288	100.00	40.99
$E_{\mathrm{T}}^{\mathrm{EM}} > 16$ GeV	19284	99.97	92.78	19282	99.97	40.98
$E_{\mathrm{Pre}} > 5$ GeV OR $E_{\mathrm{EM1}} > 5$ GeV	19284	100.00	92.78	19282	100.00	40.98
$\lvert\eta\rvert < 1.375$ OR $1.52 < \lvert\eta\rvert < 2.0$	17984	93.26	86.53	17982	93.26	38.22
Hadronic veto $E_{\mathrm{HCal}} \leq 1$ GeV	17961	99.88	86.42	17960	99.88	38.17
Max f_{HT} candidate	17960	99.99	86.41	17960	100.00	38.17
$w \geq 0.94$	16507	91.91	79.42	16507	91.91	35.08
$f_{\mathrm{HT}} \geq 0.7$	16071	97.36	77.33	16071	97.36	34.15

Table D.13: Event selection efficiency for single monopoles of mass 200 GeV and charge $|g| = 1.5g_{\mathrm{D}}$.

Selection	Candidates	Rel. eff.	Total eff.	Events	Rel. eff.	Total eff.
All	—	—	—	48443	—	—
HIP trigger	—	—	—	21437	44.25	44.25
Preselection	23048	—	—	21307	99.40	43.98
Overlap removal	21312	92.47	92.47	21307	100.00	43.98
$E_{\mathrm{T}}^{\mathrm{EM}} > 16$ GeV	21310	99.99	92.46	21307	100.00	43.98
$E_{\mathrm{Pre}} > 5$ GeV OR $E_{\mathrm{EM1}} > 5$ GeV	21309	100.00	92.46	21307	100.00	43.98
$\lvert\eta\rvert < 1.375$ OR $1.52 < \lvert\eta\rvert < 2.0$	19928	93.52	86.46	19928	93.53	41.14
Hadronic veto $E_{\mathrm{HCal}} \leq 1$ GeV	19912	99.92	86.39	19912	99.92	41.10
Max f_{HT} candidate	19912	100.00	86.39	19912	100.00	41.10
$w \geq 0.94$	19811	99.49	85.95	19811	99.49	40.89
$f_{\mathrm{HT}} \geq 0.7$	19487	98.37	84.55	19487	98.37	40.23

Table D.14: Event selection efficiency for single monopoles of mass 500 GeV and charge $|g| = 1.5g_{\mathrm{D}}$.

Selection	Candidates	Rel. eff.	Total eff.	Events	Rel. eff.	Total eff.
All	—	—	—	48527	—	—
HIP trigger	—	—	—	22901	47.19	47.19
Preselection	24748	—	—	22802	99.57	46.99
Overlap removal	22806	92.16	92.16	22802	100.00	46.99
$E_{\mathrm{T}}^{\mathrm{EM}} > 16$ GeV	22802	99.98	92.14	22801	99.99	46.99
$E_{\mathrm{Pre}} > 5$ GeV OR $E_{\mathrm{EM1}} > 5$ GeV	22802	100.00	92.14	22801	100.00	46.99
$\lvert\eta\rvert < 1.375$ OR $1.52 < \lvert\eta\rvert < 2.0$	21255	93.21	85.89	21254	93.21	43.80
Hadronic veto $E_{\mathrm{HCal}} \leq 1$ GeV	21234	99.90	85.80	21233	99.90	43.76
Max f_{HT} candidate	21233	99.99	85.80	21233	100.00	43.76
$w \geq 0.94$	21207	99.88	85.69	21207	99.88	43.70
$f_{\mathrm{HT}} \geq 0.7$	20993	98.99	84.83	20993	98.99	43.26

Table D.15: Event selection efficiency for single monopoles of mass 1000 GeV and charge $|g| = 1.5g_{\mathrm{D}}$.

Selection	Candidates	Rel. eff.	Total eff.	Events	Rel. eff.	Total eff.
All	—	—	—	48335	—	—
HIP trigger	—	—	—	23032	47.65	47.65
Preselection	25125	—	—	22934	99.57	47.45
Overlap removal	22941	91.31	91.31	22934	100.00	47.45
$E_{\mathrm{T}}^{\mathrm{EM}} > 16$ GeV	22937	99.98	91.29	22932	99.99	47.44
$E_{\mathrm{Pre}} > 5$ GeV OR $E_{\mathrm{EM1}} > 5$ GeV	22933	99.98	91.28	22928	99.98	47.44
$\lvert\eta\rvert < 1.375$ OR $1.52 < \lvert\eta\rvert < 2.0$	21291	92.84	84.74	21289	92.85	44.04
Hadronic veto $E_{\mathrm{HCal}} \leq 1$ GeV	21263	99.87	84.63	21260	99.87	43.99
Max f_{HT} candidate	21260	99.99	84.62	21260	100.00	43.99
$w \geq 0.94$	21232	99.87	84.51	21232	99.87	43.93
$f_{\mathrm{HT}} \geq 0.7$	21087	99.32	83.93	21087	99.32	43.63

Table D.16: Event selection efficiency for single monopoles of mass 1500 GeV and charge $|g| = 1.5g_{\mathrm{D}}$.

Selection	Candidates	Rel. eff.	Total eff.	Events	Rel. eff.	Total eff.
All	—	—	—	50000	—	—
HIP trigger	—	—	—	24284	48.57	48.57
Preselection	26440	—	—	24198	99.65	48.40
Overlap removal	24199	91.52	91.52	24198	100.00	48.40
$E_{\mathrm{T}}^{\mathrm{EM}} > 16$ GeV	24198	100.00	91.52	24197	100.00	48.39
$E_{\mathrm{Pre}} > 5$ GeV OR $E_{\mathrm{EM1}} > 5$ GeV	24195	99.99	91.51	24195	99.99	48.39
$\lvert\eta\rvert < 1.375$ OR $1.52 < \lvert\eta\rvert < 2.0$	22484	92.92	85.04	22483	92.92	44.97
Hadronic veto $E_{\mathrm{HCal}} \leq 1$ GeV	22469	99.93	84.98	22468	99.93	44.94
Max f_{HT} candidate	22468	100.00	84.98	22468	100.00	44.94
$w \geq 0.94$	22451	99.93	84.91	22451	99.93	44.90
$f_{\mathrm{HT}} \geq 0.7$	22261	99.15	84.19	22261	99.15	44.52

Table D.17: Event selection efficiency for single monopoles of mass 2000 GeV and charge $|g| = 1.5g_{\mathrm{D}}$.

Selection	Candidates	Rel. eff.	Total eff.	Events	Rel. eff.	Total eff.
All	—	—	—	50000	—	—
HIP trigger	—	—	—	24250	48.50	48.50
Preselection	26597	—	—	24176	99.70	48.35
Overlap removal	24180	90.91	90.91	24176	100.00	48.35
$E_{\mathrm{T}}^{\mathrm{EM}} > 16$ GeV	24179	100.00	90.91	24176	100.00	48.35
$E_{\mathrm{Pre}} > 5$ GeV OR $E_{\mathrm{EM1}} > 5$ GeV	24177	99.99	90.90	24174	99.99	48.35
$\lvert\eta\rvert < 1.375$ OR $1.52 < \lvert\eta\rvert < 2.0$	22358	92.48	84.06	22355	92.48	44.71
Hadronic veto $E_{\mathrm{HCal}} \leq 1$ GeV	22332	99.88	83.96	22329	99.88	44.66
Max f_{HT} candidate	22329	99.99	83.95	22329	100.00	44.66
$w \geq 0.94$	22309	99.91	83.88	22309	99.91	44.62
$f_{\mathrm{HT}} \geq 0.7$	22127	99.19	83.20	22127	99.19	44.25

Table D.18: Event selection efficiency for single monopoles of mass 2500 GeV and charge $|g| = 1.5g_{\mathrm{D}}$.

Selection	Candidates	Rel. eff.	Total eff.	Events	Rel. eff.	Total eff.
All	—	—	—	27197	—	—
HIP trigger	—	—	—	5321	19.56	19.56
Preselection	5419	—	—	5296	99.54	19.47
Overlap removal	5300	97.80	97.80	5296	100.00	19.47
$E_{\mathrm{T}}^{\mathrm{EM}} > 16$ GeV	5297	99.95	97.75	5296	100.00	19.47
$E_{\mathrm{Pre}} > 5$ GeV OR $E_{\mathrm{EM1}} > 5$ GeV	5297	100.00	97.75	5296	100.00	19.47
$\lvert\eta\rvert < 1.375$ OR $1.52 < \lvert\eta\rvert < 2.0$	5211	98.37	96.15	5210	98.37	19.16
Hadronic veto $E_{\mathrm{HCal}} \leq 1$ GeV	5208	99.94	96.10	5207	99.94	19.14
Max f_{HT} candidate	5207	99.98	96.08	5207	100.00	19.14
$w \geq 0.94$	4172	80.12	76.98	4172	80.12	15.34
$f_{\mathrm{HT}} \geq 0.7$	4115	98.63	75.93	4115	98.63	15.13

Table D.19: Event selection efficiency for single monopoles of mass 200 GeV and charge $|g| = 2.0 g_{\mathrm{D}}$.

Selection	Candidates	Rel. eff.	Total eff.	Events	Rel. eff.	Total eff.
All	—	—	—	27688	—	—
HIP trigger	—	—	—	6815	24.61	24.61
Preselection	6978	—	—	6775	99.42	24.47
Overlap removal	6775	97.08	97.08	6775	100.00	24.47
$E_{\mathrm{T}}^{\mathrm{EM}} > 16$ GeV	6774	99.99	97.07	6774	99.99	24.47
$E_{\mathrm{Pre}} > 5$ GeV OR $E_{\mathrm{EM1}} > 5$ GeV	6774	100.00	97.07	6774	100.00	24.47
$\lvert\eta\rvert < 1.375$ OR $1.52 < \lvert\eta\rvert < 2.0$	6609	97.55	94.70	6609	97.55	23.87
Hadronic veto $E_{\mathrm{HCal}} \leq 1$ GeV	6609	100.00	94.70	6609	100.00	23.87
Max f_{HT} candidate	6609	100.00	94.70	6609	100.00	23.87
$w \geq 0.94$	6579	99.55	94.27	6579	99.55	23.76
$f_{\mathrm{HT}} \geq 0.7$	6471	98.37	92.73	6471	98.37	23.37

Table D.20: Event selection efficiency for single monopoles of mass 500 GeV and charge $|g| = 2.0 g_{\mathrm{D}}$.

Selection	Candidates	Rel. eff.	Total eff.	Events	Rel. eff.	Total eff.
All	—	—	—	21045	—	—
HIP trigger	—	—	—	6090	28.94	28.94
Preselection	6270	—	—	6065	99.59	28.82
Overlap removal	6067	96.76	96.76	6065	100.00	28.82
$E_{\mathrm{T}}^{\mathrm{EM}} > 16$ GeV	6067	100.00	96.76	6065	100.00	28.82
$E_{\mathrm{Pre}} > 5$ GeV OR $E_{\mathrm{EM1}} > 5$ GeV	6067	100.00	96.76	6065	100.00	28.82
$\lvert\eta\rvert < 1.375$ OR $1.52 < \lvert\eta\rvert < 2.0$	5856	96.52	93.40	5854	96.52	27.82
Hadronic veto $E_{\mathrm{HCal}} \leq 1$ GeV	5851	99.92	93.32	5850	99.93	27.80
Max f_{HT} candidate	5850	99.98	93.31	5850	100.00	27.80
$w \geq 0.94$	5843	99.88	93.20	5843	99.88	27.76
$f_{\mathrm{HT}} \geq 0.7$	5808	99.40	92.64	5808	99.40	27.60

Table D.21: Event selection efficiency for single monopoles of mass 1000 GeV and charge $|g| = 2.0 g_{\mathrm{D}}$.

Selection	Candidates	Rel. eff.	Total eff.	Events	Rel. eff.	Total eff.
All	—	—	—	27625	—	—
HIP trigger	—	—	—	8641	31.28	31.28
Preselection	8950	—	—	8608	99.62	31.16
Overlap removal	8609	96.19	96.19	8608	100.00	31.16
$E_{\mathrm{T}}^{\mathrm{EM}} > 16$ GeV	8608	99.99	96.18	8608	100.00	31.16
$E_{\mathrm{Pre}} > 5$ GeV OR $E_{\mathrm{EM1}} > 5$ GeV	8608	100.00	96.18	8608	100.00	31.16
$\lvert\eta\rvert < 1.375$ OR $1.52 < \lvert\eta\rvert < 2.0$	8309	96.52	92.84	8308	96.52	30.07
Hadronic veto $E_{\mathrm{HCal}} \leq 1$ GeV	8305	99.96	92.80	8305	99.96	30.06
Max f_{HT} candidate	8305	99.99	92.79	8305	100.00	30.06
$w \geq 0.94$	8297	99.90	92.70	8297	99.90	30.03
$f_{\mathrm{HT}} \geq 0.7$	8267	99.64	92.37	8267	99.64	29.92

Table D.22: Event selection efficiency for single monopoles of mass 1500 GeV and charge $|g| = 2.0 g_{\mathrm{D}}$.

Selection	Candidates	Rel. eff.	Total eff.	Events	Rel. eff.	Total eff.
All	—	—	—	24332	—	—
HIP trigger	—	—	—	7931	32.59	32.59
Preselection	8257	—	—	7902	99.64	32.48
Overlap removal	7904	95.73	95.73	7902	100.00	32.48
$E_{\mathrm{T}}^{\mathrm{EM}} > 16$ GeV	7903	99.98	95.71	7902	100.00	32.48
$E_{\mathrm{Pre}} > 5$ GeV OR $E_{\mathrm{EM1}} > 5$ GeV	7903	100.00	95.71	7902	100.00	32.48
$\lvert\eta\rvert < 1.375$ OR $1.52 < \lvert\eta\rvert < 2.0$	7569	95.77	91.67	7568	95.77	31.10
Hadronic veto $E_{\mathrm{HCal}} \leq 1$ GeV	7566	99.97	91.64	7565	99.97	31.09
Max f_{HT} candidate	7565	99.99	91.63	7565	100.00	31.09
$w \geq 0.94$	7558	99.90	91.54	7558	99.90	31.06
$f_{\mathrm{HT}} \geq 0.7$	7525	99.56	91.14	7525	99.56	30.93

Table D.23: Event selection efficiency for single monopoles of mass 2000 GeV and charge $|g| = 2.0 g_{\mathrm{D}}$.

Selection	Candidates	Rel. eff.	Total eff.	Events	Rel. eff.	Total eff.
All	—	—	—	25003	—	—
HIP trigger	—	—	—	8509	34.03	34.03
Preselection	8877	—	—	8480	99.65	33.91
Overlap removal	8481	95.54	95.54	8480	100.00	33.91
$E_{\mathrm{T}}^{\mathrm{EM}} > 16$ GeV	8481	100.00	95.54	8480	100.00	33.91
$E_{\mathrm{Pre}} > 5$ GeV OR $E_{\mathrm{EM1}} > 5$ GeV	8478	99.97	95.51	8478	99.99	33.91
$\lvert\eta\rvert < 1.375$ OR $1.52 < \lvert\eta\rvert < 2.0$	8115	95.71	91.42	8115	95.71	32.46
Hadronic veto $E_{\mathrm{HCal}} \leq 1$ GeV	8112	99.96	91.39	8112	99.96	32.44
Max f_{HT} candidate	8112	100.00	91.39	8112	100.00	32.44
$w \geq 0.94$	8108	99.95	91.34	8108	99.95	32.43
$f_{\mathrm{HT}} \geq 0.7$	8067	99.49	90.87	8067	99.49	32.26

Table D.24: Event selection efficiency for single monopoles of mass 2500 GeV and charge $|g| = 2.0 g_{\mathrm{D}}$.

Selection	Candidates	Rel. eff.	Total eff.	Events	Rel. eff.	Total eff.
All	—	—	—	20000	—	—
HIP trigger	—	—	—	4780	23.90	23.90
Preselection	8761	—	—	4763	99.65	23.81
Overlap removal	7676	87.61	87.61	4763	100.00	23.81
$E_{\mathrm{T}}^{\mathrm{EM}} > 16$ GeV	7443	96.97	84.96	4753	99.80	23.77
$E_{\mathrm{Pre}} > 5$ GeV OR $E_{\mathrm{EM1}} > 5$ GeV	7406	99.50	84.53	4734	99.59	23.67
$\lvert\eta\rvert < 1.375$ OR $1.52 < \lvert\eta\rvert < 2.0$	6761	91.29	77.17	4509	95.24	22.54
Hadronic veto $E_{\mathrm{HCal}} \leq 1$ GeV	6691	98.97	76.38	4505	99.92	22.53
Max f_{HT} candidate	4505	67.33	51.42	4505	100.00	22.53
$w \geq 0.94$	4477	99.37	51.10	4477	99.37	22.39
$f_{\mathrm{HT}} \geq 0.7$	4459	99.60	50.90	4459	99.60	22.30

Table D.25: Event selection efficiency for pair-produced spin-1/2 monopoles of mass 200 GeV and charge $|g| = 0.5 g_{\mathrm{D}}$.

Selection	Candidates	Rel. eff.	Total eff.	Events	Rel. eff.	Total eff.
All	—	—	—	20619	—	—
HIP trigger	—	—	—	7462	36.19	36.19
Preselection	15735	—	—	7439	99.70	36.08
Overlap removal	13385	85.06	85.06	7439	100.00	36.08
$E_{\mathrm{T}}^{\mathrm{EM}} > 16$ GeV	13034	97.37	82.83	7410	99.60	35.94
$E_{\mathrm{Pre}} > 5$ GeV OR $E_{\mathrm{EM1}} > 5$ GeV	12969	99.51	82.42	7399	99.86	35.89
$\lvert\eta\rvert < 1.375$ OR $1.52 < \lvert\eta\rvert < 2.0$	12151	93.69	77.22	7217	97.55	35.00
Hadronic veto $E_{\mathrm{HCal}} \leq 1$ GeV	11819	97.26	75.11	7198	99.72	34.91
Max f_{HT} candidate	7198	60.90	45.74	7198	100.00	34.91
$w \geq 0.94$	7152	99.36	45.45	7152	99.36	34.68
$f_{\mathrm{HT}} \geq 0.7$	6908	96.59	43.90	6908	96.59	33.50

Table D.26: Event selection efficiency for pair-produced spin-1/2 monopoles of mass 500 GeV and charge $|g| = 0.5 g_{\mathrm{D}}$.

Selection	Candidates	Rel. eff.	Total eff.	Events	Rel. eff.	Total eff.
All	—	—	—	22072	—	—
HIP trigger	—	—	—	7499	33.97	33.97
Preselection	16533	—	—	7481	99.75	33.89
Overlap removal	14125	85.44	85.44	7481	100.00	33.89
$E_{\mathrm{T}}^{\mathrm{EM}} > 16$ GeV	13785	97.60	83.38	7461	99.74	33.80
$E_{\mathrm{Pre}} > 5$ GeV OR $E_{\mathrm{EM1}} > 5$ GeV	13624	98.83	82.41	7446	99.79	33.73
$\lvert\eta\rvert < 1.375$ OR $1.52 < \lvert\eta\rvert < 2.0$	13027	95.61	78.79	7348	98.69	33.29
Hadronic veto $E_{\mathrm{HCal}} \leq 1$ GeV	12203	93.68	73.81	7258	98.77	32.88
Max f_{HT} candidate	7258	59.47	43.90	7258	100.00	32.88
$w \geq 0.94$	7206	99.28	43.58	7206	99.28	32.65
$f_{\mathrm{HT}} \geq 0.7$	6140	85.21	37.14	6140	85.21	27.82

Table D.27: Event selection efficiency for pair-produced spin-1/2 monopoles of mass 1000 GeV and charge $|g| = 0.5g_{\mathrm{D}}$.

Selection	Candidates	Rel. eff.	Total eff.	Events	Rel. eff.	Total eff.
All	—	—	—	22353	—	—
HIP trigger	—	—	—	7277	32.55	32.55
Preselection	15967	—	—	7268	99.89	32.52
Overlap removal	13943	87.32	87.32	7268	100.00	32.52
$E_{\mathrm{T}}^{\mathrm{EM}} > 16$ GeV	13686	98.16	85.71	7251	99.76	32.44
$E_{\mathrm{Pre}} > 5$ GeV OR $E_{\mathrm{EM1}} > 5$ GeV	13262	96.90	83.06	7216	99.52	32.28
$\lvert\eta\rvert < 1.375$ OR $1.52 < \lvert\eta\rvert < 2.0$	12878	97.11	80.66	7163	99.26	32.04
Hadronic veto $E_{\mathrm{HCal}} \leq 1$ GeV	11545	89.65	72.31	6946	96.98	31.08
Max f_{HT} candidate	6946	60.17	43.51	6946	100.00	31.08
$w \geq 0.94$	6890	99.18	43.15	6890	99.18	30.82
$f_{\mathrm{HT}} \geq 0.7$	5287	76.74	33.11	5287	76.74	23.65

Table D.28: Event selection efficiency for pair-produced spin-1/2 monopoles of mass 1500 GeV and charge $|g| = 0.5g_{\mathrm{D}}$.

Selection	Candidates	Rel. eff.	Total eff.	Events	Rel. eff.	Total eff.
All	—	—	—	22974	—	—
HIP trigger	—	—	—	5843	25.43	25.43
Preselection	12943	—	—	5842	99.99	25.43
Overlap removal	11427	88.29	88.29	5842	100.00	25.43
$E_{\mathrm{T}}^{\mathrm{EM}} > 16$ GeV	11307	98.95	87.36	5834	99.86	25.39
$E_{\mathrm{Pre}} > 5$ GeV OR $E_{\mathrm{EM1}} > 5$ GeV	10728	94.88	82.89	5801	99.43	25.25
$\lvert\eta\rvert < 1.375$ OR $1.52 < \lvert\eta\rvert < 2.0$	10575	98.57	81.70	5777	99.59	25.14
Hadronic veto $E_{\mathrm{HCal}} \leq 1$ GeV	8796	83.18	67.96	5407	93.60	23.54
Max f_{HT} candidate	5407	61.47	41.78	5407	100.00	23.54
$w \geq 0.94$	5367	99.26	41.46	5367	99.26	23.36
$f_{\mathrm{HT}} \geq 0.7$	3832	71.40	29.60	3832	71.40	16.68

Table D.29: Event selection efficiency for pair-produced spin-1/2 monopoles of mass 2000 GeV and charge $|g| = 0.5g_{\mathrm{D}}$.

Selection	Candidates	Rel. eff.	Total eff.	Events	Rel. eff.	Total eff.
All	—	—	—	24321	—	—
HIP trigger	—	—	—	4029	16.57	16.57
Preselection	8976	—	—	4028	99.98	16.56
Overlap removal	7910	88.12	88.12	4028	100.00	16.56
$E_{\mathrm{T}}^{\mathrm{EM}} > 16$ GeV	7877	99.59	87.77	4028	100.00	16.56
$E_{\mathrm{Pre}} > 5$ GeV OR $E_{\mathrm{EM1}} > 5$ GeV	7422	94.21	82.69	4004	99.39	16.46
$\lvert\eta\rvert < 1.375$ OR $1.52 < \lvert\eta\rvert < 2.0$	7386	99.52	82.30	3998	99.85	16.44
Hadronic veto $E_{\mathrm{HCal}} \leq 1$ GeV	5311	71.91	59.17	3417	85.48	14.05
Max f_{HT} candidate	3417	64.34	38.07	3417	100.00	14.05
$w \geq 0.94$	3388	99.15	37.75	3388	99.15	13.93
$f_{\mathrm{HT}} \geq 0.7$	2380	70.26	26.52	2380	70.26	9.79

Table D.30: Event selection efficiency for pair-produced spin-1/2 monopoles of mass 2500 GeV and charge $|g| = 0.5g_{\mathrm{D}}$.

Selection	Candidates	Rel. eff.	Total eff.	Events	Rel. eff.	Total eff.
All	—	—	—	56075	—	—
HIP trigger	—	—	—	2152	3.84	3.84
Preselection	3106	—	—	2120	98.49	3.78
Overlap removal	3002	96.65	96.65	2120	100.00	3.78
$E_{\mathrm{T}}^{\mathrm{EM}} > 16$ GeV	2981	99.30	95.97	2119	99.96	3.78
$E_{\mathrm{Pre}} > 5$ GeV OR $E_{\mathrm{EM1}} > 5$ GeV	2976	99.83	95.81	2118	99.98	3.78
$\lvert\eta\rvert < 1.375$ OR $1.52 < \lvert\eta\rvert < 2.0$	2747	92.30	88.43	1987	93.77	3.54
Hadronic veto $E_{\mathrm{HCal}} \leq 1$ GeV	2741	99.78	88.24	1987	100.00	3.54
Max f_{HT} candidate	1987	72.48	63.96	1987	100.00	3.54
$w \geq 0.94$	1980	99.66	63.74	1980	99.66	3.53
$f_{\mathrm{HT}} \geq 0.7$	1968	99.38	63.35	1968	99.38	3.51

Table D.31: Event selection efficiency for pair-produced spin-1/2 monopoles of mass 200 GeV and charge $|g| = 1.0g_{\mathrm{D}}$.

Selection	Candidates	Rel. eff.	Total eff.	Events	Rel. eff.	Total eff.
All	—	—	—	31579	—	—
HIP trigger	—	—	—	5011	15.87	15.87
Preselection	8105	—	—	4992	99.64	15.81
Overlap removal	7791	96.13	96.13	4992	100.00	15.81
$E_{\mathrm{T}}^{\mathrm{EM}} > 16$ GeV	7719	99.07	95.23	4992	100.00	15.81
$E_{\mathrm{Pre}} > 5$ GeV OR $E_{\mathrm{EM1}} > 5$ GeV	7714	99.95	95.18	4992	100.00	15.81
$\lvert\eta\rvert < 1.375$ OR $1.52 < \lvert\eta\rvert < 2.0$	7230	93.72	89.21	4712	94.38	14.92
Hadronic veto $E_{\mathrm{HCal}} \leq 1$ GeV	7204	99.63	88.88	4712	100.00	14.92
Max f_{HT} candidate	4712	65.41	58.14	4712	100.00	14.92
$w \geq 0.94$	4699	99.73	57.98	4699	99.73	14.88
$f_{\mathrm{HT}} \geq 0.7$	4693	99.86	57.90	4693	99.86	14.86

Table D.32: Event selection efficiency for pair-produced spin-1/2 monopoles of mass 500 GeV and charge $|g| = 1.0g_{\mathrm{D}}$.

Selection	Candidates	Rel. eff.	Total eff.	Events	Rel. eff.	Total eff.
All	—	—	—	26502	—	—
HIP trigger	—	—	—	6526	24.62	24.62
Preselection	11253	—	—	6503	99.65	24.54
Overlap removal	10877	96.66	96.66	6503	100.00	24.54
$E_{\mathrm{T}}^{\mathrm{EM}} > 16$ GeV	10794	99.23	95.92	6503	100.00	24.54
$E_{\mathrm{Pre}} > 5$ GeV OR $E_{\mathrm{EM1}} > 5$ GeV	10787	99.94	95.86	6503	100.00	24.54
$\lvert\eta\rvert < 1.375$ OR $1.52 < \lvert\eta\rvert < 2.0$	10310	95.58	91.62	6242	95.97	23.55
Hadronic veto $E_{\mathrm{HCal}} \leq 1$ GeV	10286	99.77	91.41	6242	100.00	23.55
Max f_{HT} candidate	6242	60.68	55.46	6242	100.00	23.55
$w \geq 0.94$	6222	99.69	55.29	6222	99.69	23.48
$f_{\mathrm{HT}} \geq 0.7$	6193	99.53	55.04	6193	99.53	23.37

Table D.33: Event selection efficiency for pair-produced spin-1/2 monopoles of mass 1000 GeV and charge $|g| = 1.0 g_{\mathrm{D}}$.

Selection	Candidates	Rel. eff.	Total eff.	Events	Rel. eff.	Total eff.
All	—	—	—	25441	—	—
HIP trigger	—	—	—	6001	23.59	23.59
Preselection	10744	—	—	5972	99.52	23.47
Overlap removal	10426	97.04	97.04	5972	100.00	23.47
$E_{\mathrm{T}}^{\mathrm{EM}} > 16$ GeV	10331	99.09	96.15	5971	99.98	23.47
$E_{\mathrm{Pre}} > 5$ GeV OR $E_{\mathrm{EM1}} > 5$ GeV	10327	99.96	96.11	5971	100.00	23.47
$\lvert\eta\rvert < 1.375$ OR $1.52 < \lvert\eta\rvert < 2.0$	10000	96.84	93.07	5767	96.58	22.67
Hadronic veto $E_{\mathrm{HCal}} \leq 1$ GeV	9973	99.73	92.82	5762	99.92	22.65
Max f_{HT} candidate	5762	57.78	53.62	5762	100.00	22.65
$w \geq 0.94$	5737	99.57	53.40	5737	99.57	22.55
$f_{\mathrm{HT}} \geq 0.7$	5635	98.21	52.44	5635	98.21	22.15

Table D.34: Event selection efficiency for pair-produced spin-1/2 monopoles of mass 1500 GeV and charge $|g| = 1.0 g_{\mathrm{D}}$.

Selection	Candidates	Rel. eff.	Total eff.	Events	Rel. eff.	Total eff.
All	—	—	—	26285	—	—
HIP trigger	—	—	—	4761	18.11	18.11
Preselection	8653	—	—	4752	99.82	18.08
Overlap removal	8415	97.25	97.25	4752	100.00	18.08
$E_{\mathrm{T}}^{\mathrm{EM}} > 16$ GeV	8334	99.04	96.31	4752	99.98	18.08
$E_{\mathrm{Pre}} > 5$ GeV OR $E_{\mathrm{EM1}} > 5$ GeV	8330	99.96	96.27	4751	99.99	18.08
$\lvert\eta\rvert < 1.375$ OR $1.52 < \lvert\eta\rvert < 2.0$	8155	97.89	94.24	4617	97.17	17.57
Hadronic veto $E_{\mathrm{HCal}} \leq 1$ GeV	8140	99.82	94.07	4616	99.98	17.56
Max f_{HT} candidate	4616	56.71	53.35	4616	100.00	17.56
$w \geq 0.94$	4594	99.51	53.08	4594	99.51	17.48
$f_{\mathrm{HT}} \geq 0.7$	4342	94.53	50.18	4342	94.53	16.52

Table D.35: Event selection efficiency for pair-produced spin-1/2 monopoles of mass 2000 GeV and charge $|g| = 1.0 g_{\mathrm{D}}$.

Selection	Candidates	Rel. eff.	Total eff.	Events	Rel. eff.	Total eff.
All	—	—	—	26558	—	—
HIP trigger	—	—	—	3005	11.32	11.32
Preselection	5603	—	—	3001	99.87	11.30
Overlap removal	5513	98.40	98.40	3001	100.00	11.30
$E_{\mathrm{T}}^{\mathrm{EM}} > 16$ GeV	5463	99.10	97.51	3001	100.00	11.30
$E_{\mathrm{Pre}} > 5$ GeV OR $E_{\mathrm{EM1}} > 5$ GeV	5461	99.96	97.47	3001	100.00	11.30
$\lvert\eta\rvert < 1.375$ OR $1.52 < \lvert\eta\rvert < 2.0$	5405	98.98	96.47	2961	98.65	11.15
Hadronic veto $E_{\mathrm{HCal}} \leq 1$ GeV	5400	99.92	96.39	2961	100.00	11.15
Max f_{HT} candidate	2961	54.83	52.85	2961	100.00	11.15
$w \geq 0.94$	2954	99.78	52.73	2954	99.78	11.12
$f_{\mathrm{HT}} \geq 0.7$	2592	87.73	46.26	2592	87.73	9.76

Table D.36: Event selection efficiency for pair-produced spin-1/2 monopoles of mass 2500 GeV and charge $|g| = 1.0g_{\mathrm{D}}$.

Selection	Candidates	Rel. eff.	Total eff.	Events	Rel. eff.	Total eff.
All	—	—	—	155743	—	—
HIP trigger	—	—	—	254	0.16	0.16
Preselection	310	—	—	245	96.35	0.16
Overlap removal	305	98.48	98.48	245	100.00	0.16
$E_{\mathrm{T}}^{\mathrm{EM}} > 16$ GeV	304	99.54	98.02	245	100.00	0.16
$E_{\mathrm{Pre}} > 5$ GeV OR $E_{\mathrm{EM1}} > 5$ GeV	304	100.00	98.02	245	100.00	0.16
$\lvert\eta\rvert < 1.375$ OR $1.52 < \lvert\eta\rvert < 2.0$	287	94.48	92.61	232	94.77	0.15
Hadronic veto $E_{\mathrm{HCal}} \leq 1$ GeV	287	99.90	92.52	232	100.00	0.15
Max f_{HT} candidate	232	80.99	74.93	232	100.00	0.15
$w \geq 0.94$	228	98.00	73.43	228	98.00	0.15
$f_{\mathrm{HT}} \geq 0.7$	224	98.64	72.43	224	98.64	0.14

Table D.37: Event selection efficiency for pair-produced spin-1/2 monopoles of mass 200 GeV and charge $|g| = 1.5g_{\mathrm{D}}$.

Selection	Candidates	Rel. eff.	Total eff.	Events	Rel. eff.	Total eff.
All	—	—	—	39207	—	—
HIP trigger	—	—	—	483	1.23	1.23
Preselection	681	—	—	478	98.98	1.22
Overlap removal	667	98.01	98.01	478	100.00	1.22
$E_{\mathrm{T}}^{\mathrm{EM}} > 16$ GeV	662	99.11	97.13	478	100.00	1.22
$E_{\mathrm{Pre}} > 5$ GeV OR $E_{\mathrm{EM1}} > 5$ GeV	661	99.85	96.99	477	99.79	1.22
$\lvert\eta\rvert < 1.375$ OR $1.52 < \lvert\eta\rvert < 2.0$	637	96.38	93.47	456	95.53	1.16
Hadronic veto $E_{\mathrm{HCal}} \leq 1$ GeV	631	99.18	92.71	455	99.91	1.16
Max f_{HT} candidate	455	72.08	66.83	455	100.00	1.16
$w \geq 0.94$	454	99.84	66.72	454	99.84	1.16
$f_{\mathrm{HT}} \geq 0.7$	454	100.00	66.72	454	100.00	1.16

Table D.38: Event selection efficiency for pair-produced spin-1/2 monopoles of mass 500 GeV and charge $|g| = 1.5g_{\mathrm{D}}$.

Selection	Candidates	Rel. eff.	Total eff.	Events	Rel. eff.	Total eff.
All	—	—	—	33757	—	—
HIP trigger	—	—	—	1263	3.74	3.74
Preselection	1967	—	—	1251	99.09	3.71
Overlap removal	1947	99.02	99.02	1251	100.00	3.71
$E_{\mathrm{T}}^{\mathrm{EM}} > 16$ GeV	1923	98.75	97.79	1251	100.00	3.71
$E_{\mathrm{Pre}} > 5$ GeV OR $E_{\mathrm{EM1}} > 5$ GeV	1923	100.00	97.79	1251	100.00	3.71
$\lvert\eta\rvert < 1.375$ OR $1.52 < \lvert\eta\rvert < 2.0$	1903	98.95	96.76	1236	98.81	3.66
Hadronic veto $E_{\mathrm{HCal}} \leq 1$ GeV	1902	99.96	96.72	1236	100.00	3.66
Max f_{HT} candidate	1236	65.01	62.88	1236	100.00	3.66
$w \geq 0.94$	1234	99.76	62.73	1234	99.76	3.65
$f_{\mathrm{HT}} \geq 0.7$	1230	99.74	62.57	1230	99.74	3.64

Table D.39: Event selection efficiency for pair-produced spin-1/2 monopoles of mass 1000 GeV and charge $|g| = 1.5g_{\mathrm{D}}$.

Selection	Candidates	Rel. eff.	Total eff.	Events	Rel. eff.	Total eff.
All	—	—	—	31048	—	—
HIP trigger	—	—	—	1117	3.60	3.60
Preselection	1780	—	—	1117	100.00	3.60
Overlap removal	1768	99.32	99.32	1117	100.00	3.60
$E_{\mathrm{T}}^{\mathrm{EM}} > 16$ GeV	1757	99.38	98.71	1117	100.00	3.60
$E_{\mathrm{Pre}} > 5$ GeV OR $E_{\mathrm{EM1}} > 5$ GeV	1757	99.98	98.69	1117	99.97	3.60
$\lvert\eta\rvert < 1.375$ OR $1.52 < \lvert\eta\rvert < 2.0$	1746	99.35	98.05	1106	99.00	3.56
Hadronic veto $E_{\mathrm{HCal}} \leq 1$ GeV	1743	99.86	97.91	1106	100.00	3.56
Max f_{HT} candidate	1106	63.42	62.10	1106	100.00	3.56
$w \geq 0.94$	1102	99.63	61.87	1102	99.63	3.55
$f_{\mathrm{HT}} \geq 0.7$	1097	99.60	61.62	1097	99.60	3.53

Table D.40: Event selection efficiency for pair-produced spin-1/2 monopoles of mass 1500 GeV and charge $|g| = 1.5g_{\mathrm{D}}$.

Selection	Candidates	Rel. eff.	Total eff.	Events	Rel. eff.	Total eff.
All	—	—	—	29828	—	—
HIP trigger	—	—	—	844	2.83	2.83
Preselection	1367	—	—	844	99.97	2.83
Overlap removal	1362	99.61	99.61	844	100.00	2.83
$E_{\mathrm{T}}^{\mathrm{EM}} > 16$ GeV	1347	98.90	98.52	844	100.00	2.83
$E_{\mathrm{Pre}} > 5$ GeV OR $E_{\mathrm{EM1}} > 5$ GeV	1347	100.00	98.52	844	100.00	2.83
$\lvert\eta\rvert < 1.375$ OR $1.52 < \lvert\eta\rvert < 2.0$	1343	99.76	98.28	840	99.62	2.82
Hadronic veto $E_{\mathrm{HCal}} \leq 1$ GeV	1343	99.94	98.22	840	100.00	2.82
Max f_{HT} candidate	840	62.61	61.49	840	100.00	2.82
$w \geq 0.94$	838	99.69	61.30	838	99.69	2.81
$f_{\mathrm{HT}} \geq 0.7$	832	99.32	60.89	832	99.32	2.79

Table D.41: Event selection efficiency for pair-produced spin-1/2 monopoles of mass 2000 GeV and charge $|g| = 1.5g_{\mathrm{D}}$.

Selection	Candidates	Rel. eff.	Total eff.	Events	Rel. eff.	Total eff.
All	—	—	—	38147	—	—
HIP trigger	—	—	—	652	1.71	1.71
Preselection	1069	—	—	647	99.24	1.70
Overlap removal	1065	99.64	99.64	647	100.00	1.70
$E_{\mathrm{T}}^{\mathrm{EM}} > 16$ GeV	1053	98.93	98.57	647	100.00	1.70
$E_{\mathrm{Pre}} > 5$ GeV OR $E_{\mathrm{EM1}} > 5$ GeV	1053	100.00	98.57	647	100.00	1.70
$\lvert\eta\rvert < 1.375$ OR $1.52 < \lvert\eta\rvert < 2.0$	1052	99.85	98.42	646	99.87	1.69
Hadronic veto $E_{\mathrm{HCal}} \leq 1$ GeV	1049	99.76	98.19	646	100.00	1.69
Max f_{HT} candidate	646	61.61	60.49	646	100.00	1.69
$w \geq 0.94$	645	99.75	60.34	645	99.75	1.69
$f_{\mathrm{HT}} \geq 0.7$	615	95.31	57.51	615	95.31	1.61

Table D.42: Event selection efficiency for pair-produced spin-1/2 monopoles of mass 2500 GeV and charge $|g| = 1.5g_{\mathrm{D}}$.

Appendix E

Event selection efficiency maps for single monopoles

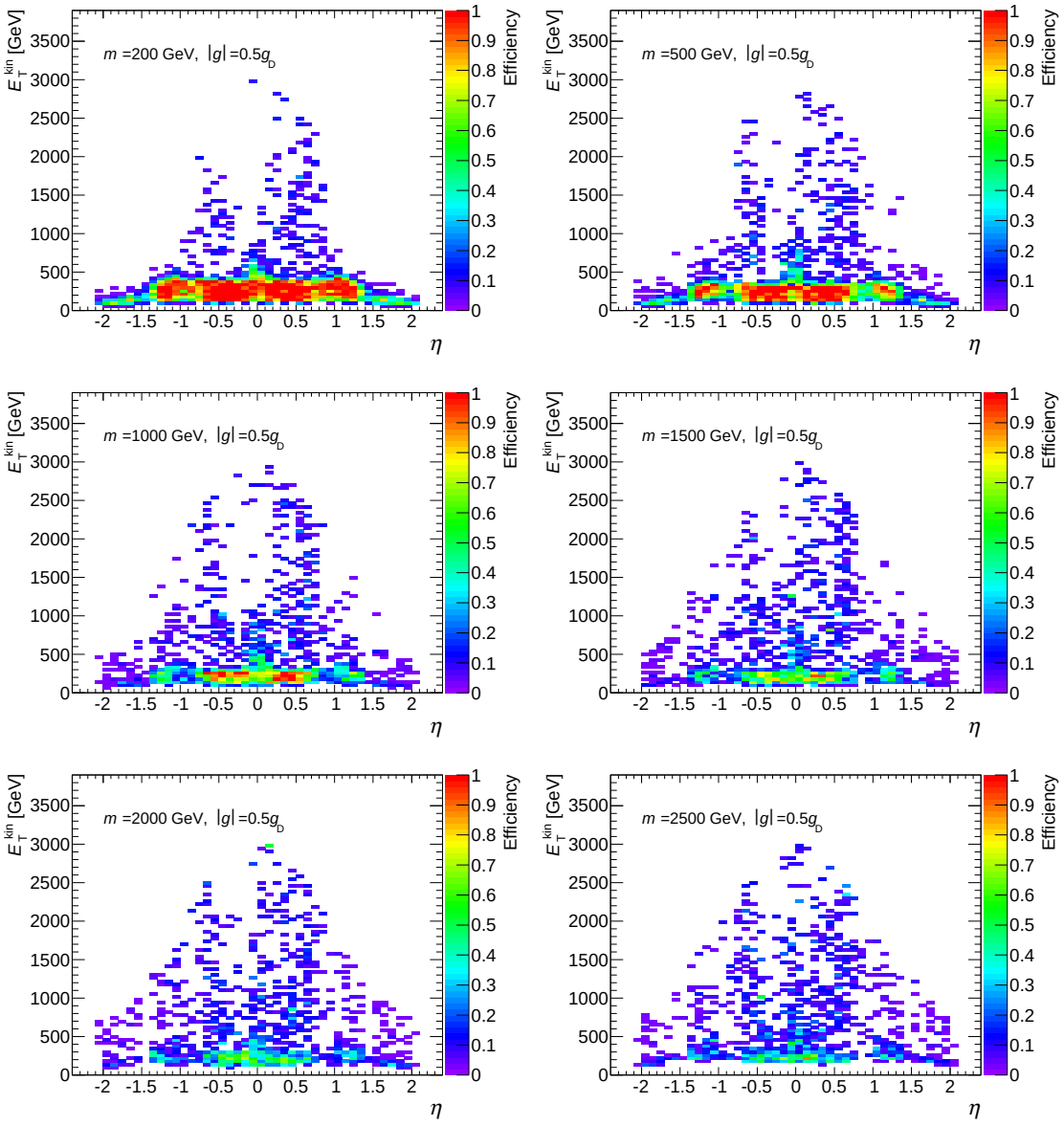

Figure E.1: Event selection efficiency as a function of the transverse kinetic energy, $E_{\mathrm{T}}^{\mathrm{kin}}$, and pseudorapidity, η, for single monopoles of charge $|g| = 0.5g_{\mathrm{D}}$.

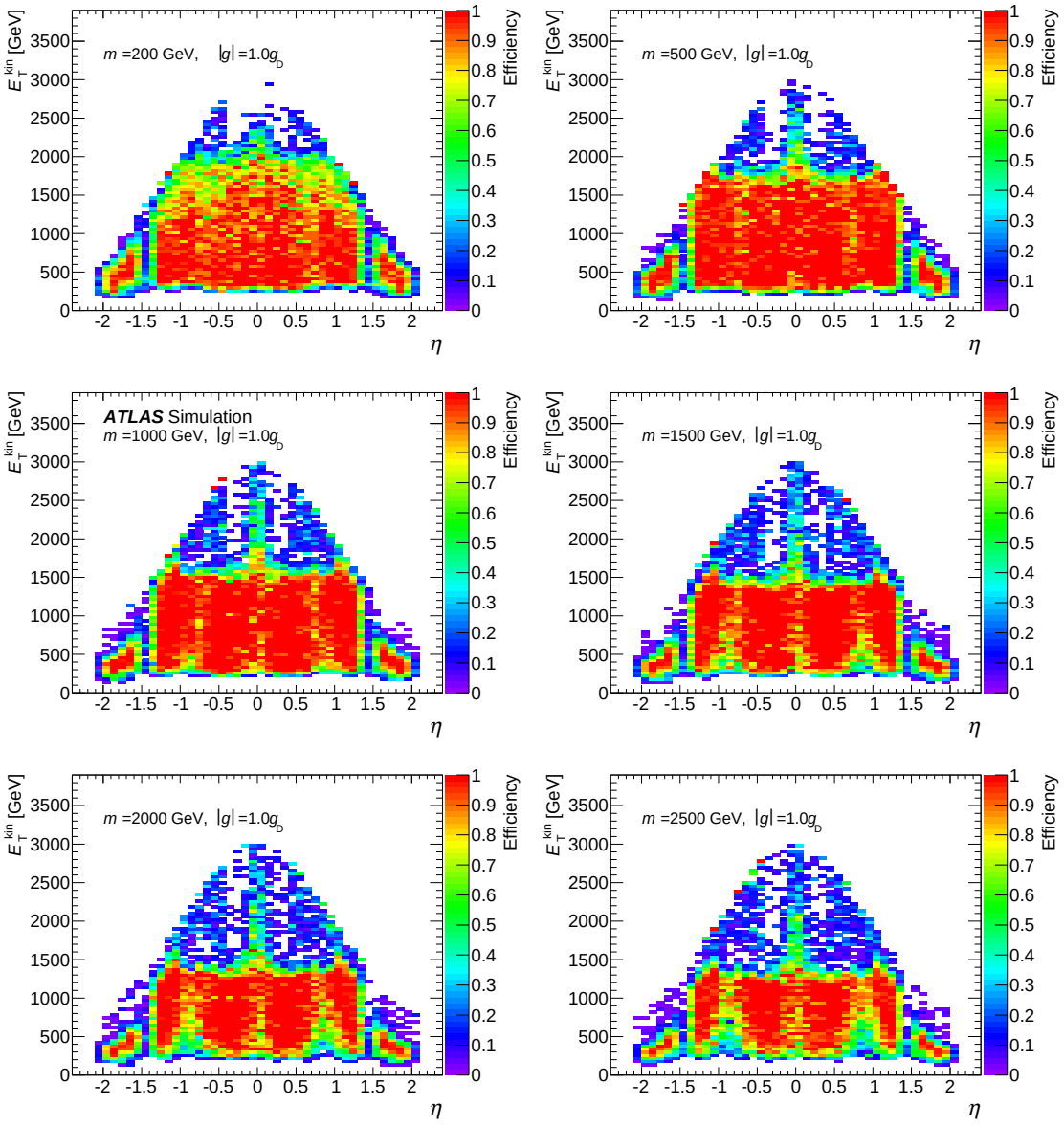

Figure E.2: Event selection efficiency as a function of the transverse kinetic energy, $E_{\mathrm{T}}^{\mathrm{kin}}$, and pseudorapidity, η, for single monopoles of charge $|g| = 1.0g_{\mathrm{D}}$.

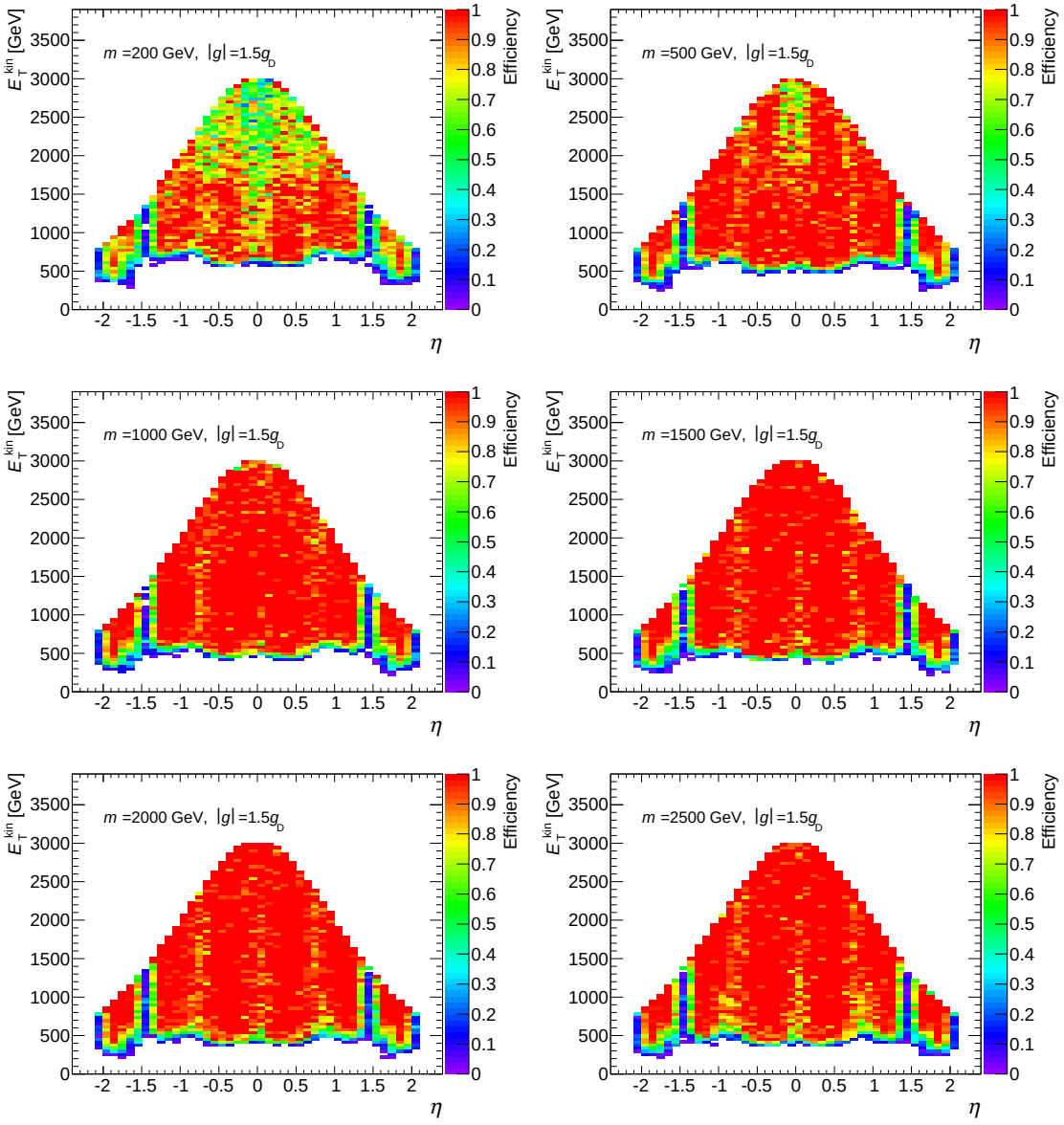

Figure E.3: Event selection efficiency as a function of the transverse kinetic energy, $E_{\mathrm{T}}^{\mathrm{kin}}$, and pseudorapidity, η, for single monopoles of charge $|g| = 1.5g_{\mathrm{D}}$.

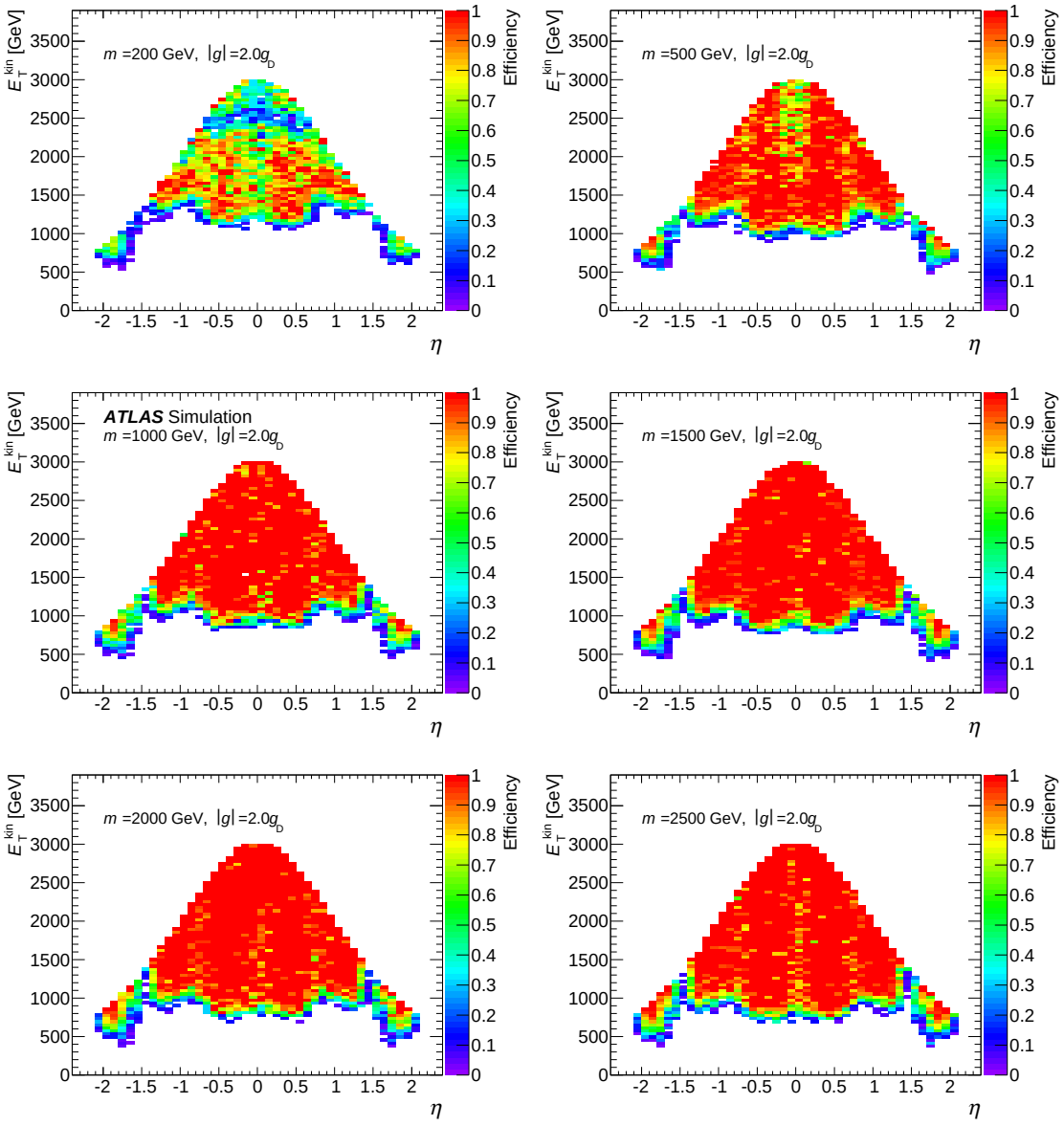

Figure E.4: Event selection efficiency as a function of the transverse kinetic energy, $E_{\mathrm{T}}^{\mathrm{kin}}$, and pseudorapidity, η, for single monopoles of charge $|g| = 2.0g_{\mathrm{D}}$.

Appendix F

Pseudorapidity asymmetry in selected monopole candidates

An asymmetry in pseudorapidity was observed in the selected candidates for some samples. This asymmetry was also observed in the collision data. Figure F.1 shows that there is a greater number of candidates from collision data selected at positive pseudorapidity values. The left plot shows preselected candidates after overlap removal while the right plot shows candidates after tight selection. Therefore, the asymmetry is not introduced by any of the requirements of the event selection. It is important to note that this asymmetry occurs at $|\eta| > 1.7$, beyond the coverage of the Tile calorimeter responsible for the hadronic veto at Level-1 and tight selection.

The asymmetry in the signal samples is shown in Fig. F.2 and it is quantified as

$$A = \frac{N_F - N_B}{N_F + N_B}, \tag{F.1}$$

where N_F (N_B) is the number of candidates in the forward (backward) region $\eta > 0$ ($\eta < 0$) after full event selection. It is interesting to see that there is no asymmetry for candidates that have transverse kinetic energies below the HIP trigger efficiency drop-off energy. On the other hand, the asymmetry becomes more significant for candidates with energies above the HIP trigger efficiency drop-off energy. It should be noted that the asymmetry reaches the highest values of about 10% for monopoles of charge $|g| = 0.5g_{\mathrm{D}}$, which are more likely to

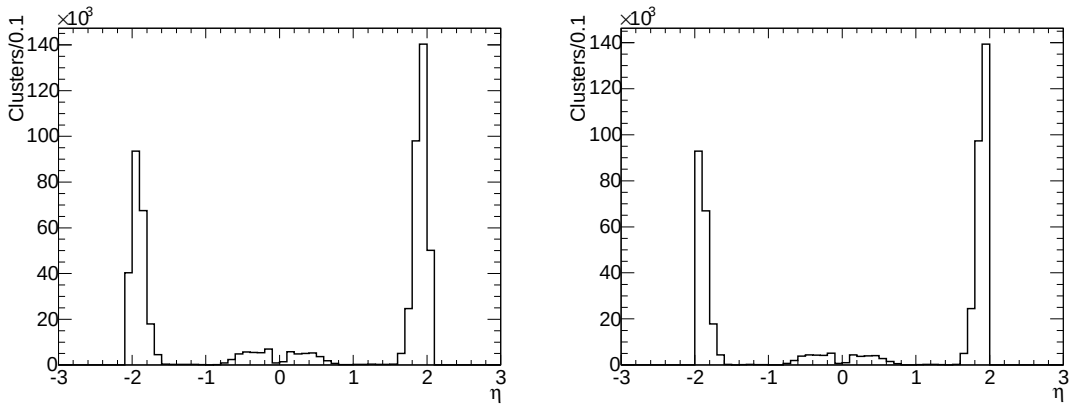

Figure F.1: Pseudorapidity distribution of preselected candidates from collision data after overlap removal (left) and after tight selection (right).

penetrate to the hadronic calorimeter, while it is negligible for monopoles of higher charge.

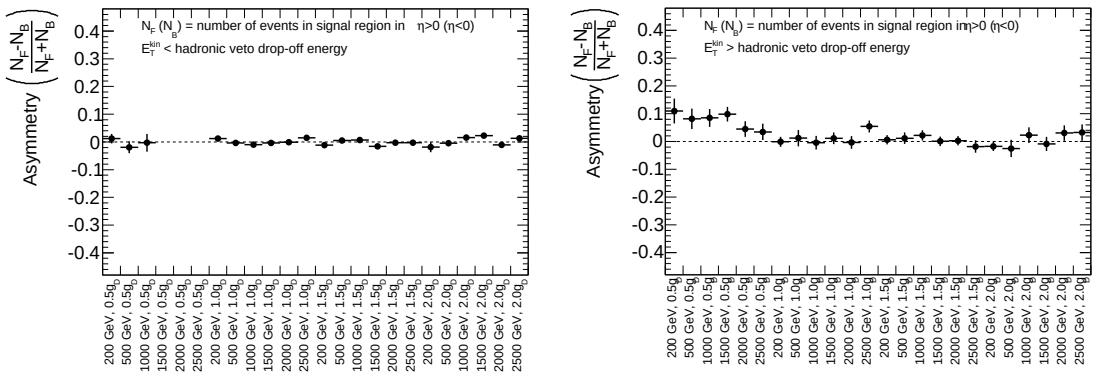

Figure F.2: Asymmetry in signal monopole samples for monopoles with transverse kinetic energy below (left) and above (right) the HIP trigger efficiency drop-off energy.

An additional test was performed on a simulated MC sample of electrons from W boson decays (the sample used for background studies). Figure F.3 shows the pseudorapidity distribution of the generated electrons. No selection criteria has been applied to this sample. However, the sample has been processed by the DESD HIP filter, which requires the HIP trigger. Therefore, the asymmetry must be related to the trigger performance. Thus, the source of the asymmetry is partially understood. Since the asymmetry is present in the

collision data and in the simulated data, it does not require a special treatment, e.g., the introduction of an associated systematic uncertainty.

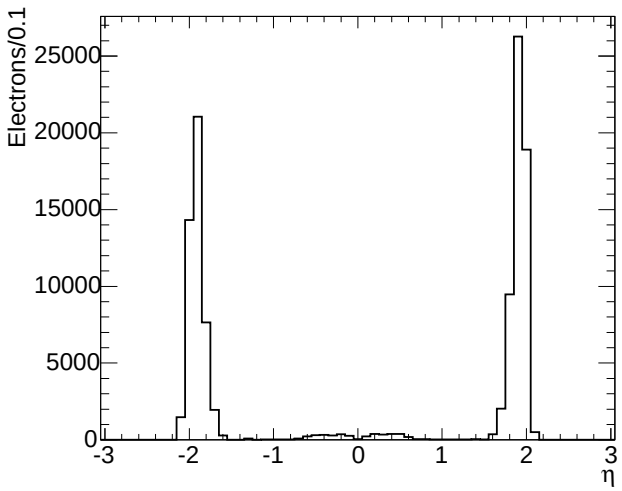

Figure F.3: Pseudorapidity distribution of generated electrons from simulated MC sample of electrons from W boson decays.

Appendix G

Tables of systematic uncertainties on the event selection efficiency for signal samples

Spin-1/2 $\lvert g\rvert = 0.5$	MC Stat.	Det. material	G4 range cut	Birks' high	Birks' low	$\delta-$ray	TRT Occ.	LAr xTalk	Total (UP)	Total (DOWN)
m =200 GeV	$\pm$1.62	$\pm(1 \pm 5)$	$+(1 \pm 5)$	$+(1 \pm 5)$	0 ± 5	$\pm(3 \pm 5)$	$-(1 \pm 2)$	$-(6 \pm 2)$	+5	−8
m =500 GeV	$\pm$1.91	$\pm(4 \pm 6)$	$-(4 \pm 6)$	$-(2 \pm 6)$	$-(7 \pm 6)$	$\pm(6 \pm 6)$	(0 ± 3)	$-(6 \pm 3)$	+8	−13
m =1000 GeV	$\pm$2.48	$\pm(9 \pm 8)$	$+(5 \pm 8)$	$+(4 \pm 8)$	$+(4 \pm 8)$	$\pm(1 \pm 8)$	$+(11 \pm 4)$	$-(4 \pm 3)$	+16	−10
m =1500 GeV	$\pm$2.71	$\pm(9 \pm 8)$	$-(12 \pm 8)$	$-(8 \pm 9)$	$-(9 \pm 8)$	$\pm(10 \pm 8)$	$+(10 \pm 4)$	$-(8 \pm 4)$	+17	−23
m =2000 GeV	$\pm$2.94	$\pm(28 \pm 11)$	$+(27 \pm 11)$	$+(33 \pm 11)$	$+(24 \pm 11)$	$\pm(27 \pm 11)$	$+(13 \pm 4)$	$-(7 \pm 4)$	+64	−40
m =2500 GeV	$\pm$3.06	$\pm(14 \pm 9)$	$-(12 \pm 10)$	$-(11 \pm 10)$	$-(18 \pm 9)$	$\pm(6 \pm 10)$	$+(10 \pm 5)$	$-(7 \pm 4)$	+18	−29

Spin-1/2 $\lvert g\rvert = 1.0$	MC Stat.	Det. material	G4 range cut	Birks' high	Birks' low	$\delta-$ray	TRT Occ.	LAr xTalk	Total (UP)	Total (DOWN)
m =200 GeV	$\pm$3.71	$\pm(2 \pm 3)$	$+(6 \pm 3)$	$+(12 \pm 3)$	$+(3 \pm 3)$	$\pm(7 \pm 3)$	$+(1 \pm 2)$	0 ± 2	+16	−9
m =500 GeV	$\pm$1.69	$\pm(3 \pm 2)$	0 ± 2	$+(3 \pm 2)$	$-(7 \pm 2)$	$\pm(0 \pm 2)$	0 ± 2	$-(1 \pm 2)$	+6	−8
m =1000 GeV	$\pm$1.28	$\pm(4 \pm 2)$	$-(3 \pm 2)$	$+(10 \pm 2)$	$-(10 \pm 2)$	$\pm(2 \pm 2)$	$-(1 \pm 1)$	$-(3 \pm 1)$	+12	−12
m =1500 GeV	$\pm$1.33	$\pm(8 \pm 2)$	$-(2 \pm 2)$	$+(13 \pm 2)$	$-(9 \pm 2)$	$\pm(1 \pm 2)$	$+(1 \pm 2)$	$-(1 \pm 2)$	+15	−13
m =2000 GeV	$\pm$1.59	$\pm(3 \pm 3)$	$-(1 \pm 3)$	$+(15 \pm 3)$	$-(9 \pm 3)$	$\pm(3 \pm 3)$	$+(2 \pm 2)$	$-(3 \pm 2)$	+16	−11
m =2500 GeV	$\pm$2.21	$\pm(9 \pm 3)$	$-(10 \pm 3)$	$+(9 \pm 4)$	$-(17 \pm 3)$	$\pm(6 \pm 3)$	$+(6 \pm 2)$	$-(3 \pm 2)$	+16	−24

Spin-1/2 $\lvert g\rvert = 1.5$	MC Stat.	Det. material	G4 range cut	Birks' high	Birks' low	$\delta-$ray	TRT Occ.	LAr xTalk	Total (UP)	Total (DOWN)
m =500 GeV	$\pm$7.52	$\pm(19 \pm 5)$	$-(7 \pm 6)$	$-(3 \pm 6)$	$-(12 \pm 5)$	$\pm(13 \pm 5)$	0 ± 4	$-(1 \pm 4)$	+24	−28
m =1000 GeV	$\pm$3.65	$\pm(8 \pm 5)$	$-(4 \pm 5)$	$+(1 \pm 5)$	$-(9 \pm 4)$	$\pm(5 \pm 5)$	$+(3 \pm 3)$	$+(2 \pm 3)$	+11	−14
m =1500 GeV	$\pm$3.69	$\pm(8 \pm 5)$	$-(5 \pm 5)$	$+(1 \pm 5)$	$-(8 \pm 5)$	$\pm(4 \pm 5)$	0 ± 3	$-(1 \pm 3)$	+10	−14
m =2000 GeV	$\pm$4.28	$\pm(14 \pm 6)$	$-(10 \pm 6)$	$-(7 \pm 6)$	$-(12 \pm 6)$	$\pm(12 \pm 6)$	$+(3 \pm 4)$	$+(3 \pm 4)$	+19	−26
m =2500 GeV	$\pm$5.53	$\pm(8 \pm 6)$	$-(6 \pm 6)$	$-(6 \pm 6)$	$-(15 \pm 6)$	$\pm(4 \pm 6)$	0 ± 4	$-(4 \pm 4)$	+11	−21

Table G.1: Systematic uncertainties on the signal efficiencies in percentages for Drell-Yan produced spin-1/2 monopoles of charge $|g| = 0.5g_{\mathrm{D}}$ (top), $|g| = 1.0g_{\mathrm{D}}$ (centre) and $|g| = 1.5g_{\mathrm{D}}$ (bottom).

Spin-0 $\lvert g\rvert = 0.5$	MC Stat.	Det. material	G4 range cut	Birks' high	Birks' low	$\delta-$ray	TRT Occ.	LAr xTalk	Extrapolation	Total (UP)	Total (DOWN)
m =200 GeV	$\pm$0.78	$\pm(2 \pm 3)$	$+(3 \pm 3)$	$+(9 \pm 3)$	$-(5 \pm 3)$	$\pm(3 \pm 3)$	0 ± 2	$-(2 \pm 2)$	-11	$+11$	-13
m =500 GeV	$\pm$0.62	$\pm(2 \pm 2)$	$-(3 \pm 2)$	$+(2 \pm 2)$	$-(11 \pm 2)$	$\pm(4 \pm 2)$	$+(1 \pm 1)$	$-(4 \pm 1)$	-9.8	$+6$	-17
m =1000 GeV	$\pm$0.76	$\pm(2 \pm 2)$	$-(1 \pm 2)$	$+(3 \pm 2)$	$-(7 \pm 2)$	$\pm(1 \pm 2)$	$+(9 \pm 2)$	$-(5 \pm 1)$	-8.8	$+10$	-13
m =1500 GeV	$\pm$0.89	$\pm(6 \pm 2)$	$-(4 \pm 2)$	$-(1 \pm 2)$	$-(12 \pm 2)$	$\pm(8 \pm 2)$	$+(14 \pm 2)$	$-(6 \pm 2)$	-7.8	$+18$	-19
m =2000 GeV	$\pm$1.01	$\pm(4 \pm 3)$	$-(8 \pm 3)$	$-(1 \pm 3)$	$-(12 \pm 3)$	$\pm(5 \pm 3)$	$+(18 \pm 2)$	$-(7 \pm 2)$	-6.8	$+19$	-19
m =2500 GeV	$\pm$1.24	$\pm(5 \pm 4)$	$-(9 \pm 4)$	$-(2 \pm 4)$	$-(14 \pm 4)$	$\pm(10 \pm 4)$	$+(16 \pm 3)$	$-(7 \pm 2)$	-5.8	$+20$	-23

Spin-0 $\lvert g\rvert = 1.0$	MC Stat.	Det. material	G4 range cut	Birks' high	Birks' low	$\delta-$ray	TRT Occ.	LAr xTalk	Extrapolation	Total (UP)	Total (DOWN)
m =200 GeV	$\pm$2.02	$\pm(2 \pm 3)$	$+(6 \pm 3)$	$+(12 \pm 3)$	$+(3 \pm 3)$	$\pm(7 \pm 3)$	0 ± 2	0 ± 2	-10	$+16$	-13
m =500 GeV	$\pm$0.92	$\pm(3 \pm 2)$	0 ± 2	$+(3 \pm 2)$	$-(7 \pm 2)$	$\pm(0 \pm 2)$	0 ± 2	$-(1 \pm 2)$	-9.5	$+6$	-12
m =1000 GeV	$\pm$0.66	$\pm(4 \pm 2)$	$-(3 \pm 2)$	$+(10 \pm 2)$	$-(10 \pm 2)$	$\pm(2 \pm 2)$	$-(1 \pm 1)$	$-(3 \pm 1)$	-8.5	$+12$	-14
m =1500 GeV	$\pm$0.68	$\pm(8 \pm 2)$	$-(2 \pm 2)$	$+(13 \pm 2)$	$-(10 \pm 2)$	$\pm(1 \pm 2)$	$+(1 \pm 2)$	$-(1 \pm 2)$	-7.5	$+15$	-15
m =2000 GeV	$\pm$0.80	$\pm(3 \pm 3)$	$-(1 \pm 3)$	$+(15 \pm 3)$	$-(9 \pm 3)$	$\pm(3 \pm 3)$	$+(2 \pm 2)$	$-(3 \pm 2)$	-6.5	$+16$	-13
m =2500 GeV	$\pm$1.01	$\pm(9 \pm 3)$	$-(10 \pm 3)$	$+(9 \pm 4)$	$-(17 \pm 3)$	$\pm(6 \pm 3)$	$+(6 \pm 2)$	$-(3 \pm 2)$	-5.5	$+15$	-24

Spin-0 $\lvert g\rvert = 1.5$	MC Stat.	Det. material	G4 range cut	Birks' high	Birks' low	$\delta-$ray	TRT Occ.	LAr xTalk	Extrapolation	Total (UP)	Total (DOWN)
m =500 GeV	$\pm$3.25	$\pm(19 \pm 5)$	$-(7 \pm 6)$	$-(3 \pm 6)$	$-(12 \pm 5)$	$\pm(13 \pm 5)$	0 ± 4	$-(1 \pm 4)$	-20	$+23$	-33
m =1000 GeV	$\pm$1.88	$\pm(8 \pm 5)$	$-(4 \pm 5)$	$+(1 \pm 5)$	$-(9 \pm 4)$	$\pm(5 \pm 5)$	$+(3 \pm 3)$	$+(2 \pm 3)$	-19	$+11$	-24
m =1500 GeV	$\pm$1.68	$\pm(8 \pm 5)$	$-(5 \pm 5)$	$+(1 \pm 5)$	$-(8 \pm 5)$	$\pm(4 \pm 5)$	0 ± 3	$-(1 \pm 3)$	-18	$+9.4$	-22
m =2000 GeV	$\pm$1.93	$\pm(14 \pm 6)$	$-(10 \pm 6)$	$-(6 \pm 6)$	$-(12 \pm 6)$	$\pm(12 \pm 6)$	$+(3 \pm 4)$	$+(3 \pm 4)$	-17	$+19$	-30
m =2500 GeV	$\pm$2.48	$\pm(8 \pm 6)$	$-(6 \pm 6)$	$-(6 \pm 6)$	$-(15 \pm 6)$	$\pm(4 \pm 6)$	0 ± 4	$-(4 \pm 4)$	-16	$+10$	-26

Table G.2: Systematic uncertainties on the signal efficiencies for Drell-Yan produced spin-0 monopoles of charge $|g| = 0.5g_{\mathrm{D}}$ (top), $|g| = 1.0g_{\mathrm{D}}$ (centre) and $|g| = 1.5g_{\mathrm{D}}$ (bottom).

Bibliography

[1] S. Galshow, *Partial-symmetries of weak interactions*, Nucl. Phys. **22** (1961) 579.

[2] S. Weinberg, *A model of leptons*, Phys. Rev. Lett. **19** (1967) 1264.

[3] A. Salam, *Elementary Particle Physics: Relativistic Groups and Analyticity*, in *8th Nobel Symposium*, N. Svartholm, ed., p. 367. Almqvist and Wikell, Stockholm, 1968.

[4] MissMJ, *Standard model of elementary particles*, `http://upload.wikimedia.org/wikipedia/commons/0/00/Standard_Model_of_Elementary_Particles.svg`. Wikimedia Commons. CC BY 3.0.

[5] ATLAS Collaboration, G. Aad *et al.*, *Measurements of underlying-event properties using neutral and charged particles in pp collisions at* $\sqrt{s}$ *=900 GeV and* $\sqrt{s}$ *=7 TeV with the ATLAS detector at the LHC*, Eur. Phys. J. **C 71** (2011) 1636.

[6] ATLAS Collaboration, G. Aad *et al.*, *Measurement of the underlying event in jet events from 7 TeV protonproton collisions with the ATLAS detector*, Eur. Phys. J. **C 74** (2014) 2965.

[7] ATLAS Collaboration, G. Aad *et al.*, *Rapidity gap cross sections measured with the ATLAS detector in pp collisions at* $\sqrt{s}$ *=7 TeV*, Eur. Phys. J. **C 76** (2012) 1926.

[8] L. Vant-Hull, *Experimenal upper limit on the magnetic monopole moment of electrons, protons, and neutrons, utilizing a superconducting quantum interferometer*, Phys. Rev. **173** (1968) 1412.

[9] P. Dirac, *Quantised Singularities in the Electromagnetic Field*, Proc. Roy. Soc. **A 133** (1931) 60.

[10] P. Dirac, *The Theory of Magnetic Poles*, Phys. Rev. **74** (1948) 817.

[11] T. Wu and C. Yang, *Concept of nonintegrable phase factors and global formulation of gauge fields*, Phys. Rev. **D 12** (1975) 3845.

[12] Y. Aharonov and D. Bohm, *Significance of electromagnetic potentials in the quantum theory*, Phys. Rev. **115** (1959) 485.

[13] D. Griffiths, *Introduction to Electrodynamics*. Prentice Hall, second ed., 1999.

[14] R. Millikan, *The electron : its isolation and measurement and the determination of some of its properties*. The University of Chicago Press: Science Series, 1917.

[15] J. Schwinger, *Magnetic charge and quantum field theory*, Phys. Rev. **144** (1966) 1087.

[16] J. Schwinger, *Sources and magnetic charge*, Phys. Rev. **173** (1968) 1536.

[17] S. Drell and T. Yan, *Massive lepton-pair production in hadron-hadron collisions at high energies*, Phys. Rev. Lett. **25** (1970) 316.

[18] T. Dougall and S. Wick, *Dirac magnetic monopole production from photon fusion in proton collisions*, Eur. Phys. J. **A 39** (2009) 213.

[19] Y. Kurochkin *et al.*, *On production of magnetic monopoles via $\gamma\gamma$ fusion at high-energy pp collisions*, Mod. Phys. Lett. **A 21** (2006) 2873.

[20] G. 't Hooft, *Magnetic monopoles in unified gauge theories*, Nucl. Phys. **B 79** (1974) 276.

[21] A. Polyakov, *Particle spectrum in quantum field theory*, JETP Lett. **20** (1974) 194.

[22] M. Barriola, T. Vachaspati, and M. Bucher, *A new class of defects*, Phys. Rev. Lett. **69** (1992) 1867.

[23] M. Barriola, T. Vachaspati, and M. Bucher, *Embedded defects*, Phys. Rev. **D 50** (1994) 2819.

[24] Y. Shnir, *Magnetic monopoles*. Springer-Verlag, first ed., 2005.

[25] U. Amaldi, W. Boer, and H. Fürstenau, *Comparison of grand unified theories with electroweak and strong coupling constants measured at LEP*, Phys. Lett. **B 260** (1991) 447.

[26] Y. Cho and D. Maison, *Monopole configuration in Weinberg-Salam model*, Phys. Lett. **B 391** (1997) 360.

[27] Y. Cho *et al.*, *Mass of the electroweak monopole*, `arXiv:1212.3885 [hep-ph]`.

[28] Y. Kazama, C. Yang, and S. Goldhaber, *Scattering of a Dirac particle with charge Ze by a fixed magnetic monopole*, Phys. Rev. **B 15** (1977) 2287.

[29] S. Ahlen, *Stopping-power formula for magnetic monopoles*, Phys. Rev. **D 17** (1978) 229.

[30] S. Ahlen and K. Kinoshita, *Calculation of the stopping power of very-low-velocity magnetic monopoles*, Phys. Rev. **D 26** (1982) 2347.

[31] A. De Roek *et al.*, *Sensitivity of LHC experiments to exotic highly ionising particles*, Eur. Phys. J. **C 72** (2012) 1985.

[32] J. Jackson, *Classical electrodynamics*. John Wiley and sons, Inc., third ed., 1999.

[33] E. Papageorgiu and L. Stodolsky, *Identification of magnetic monopoles via electron-positron pair production*, Phys. Lett. **B 197** (1987) 277.

[34] S. Wick *et al.*, *Signatures for a cosmic flux of magnetic monopoles*, Astro. Phys. **18** (2003) 663.

[35] S. Burdin, A. Firan, and W. Tayor, *A search for magnetic monopoles at ATLAS*, ATLAS internal note ATL-COM-PHYS-2012-367, 2013.

[36] K. A. Milton, *Theoretical and experimental status of magnetic monopoles*, Rep. Prog. Phys. **69** (2006) 1637.

[37] H. Jeon and M. Longo, *Search for magnetic monopoles trapped in matter*, Phys. Rev. Lett. **75** (1995) 1443.

[38] R. Ross *et al.*, *Search for magnetic monopoles in lunar material using an electromagnetic detector*, Phys. Rev. **D 8** (1973) 698.

[39] K. Bendtz *et al.*, *Search for magnetic monopoles in polar volcanic rocks*, Phys. Rev. Lett. **110** (2013) 121803.

[40] H1 Collaboration, A. Aktas *et al.*, *A direct search for stable magnetic monopoles produced in positron-proton collisions at HERA*, Eur. Phys. J **C 41** (2005) 133.

[41] G. Kalbfleisch *et al.*, *Limits on production of magnetic monopoles utilizing samples from the D0 and CDF detectors at the Fermilab Tevatron*, Phys. Rev. **D 69** (2004) 052002.

[42] B. Cabrera, *First results from a superconductive detector for moving magnetic monopoles*, Phys. Rev. **D 48** (1982) 1378.

[43] E. Amaldi *et al.*, *Search for Dirac magnetic poles*, Nuovo Cimento **28** (1963) 773.

[44] J. Preskill, *Magnetic monopoles*, Annu. Rev. Nucl. Part. Sci. **34** (1984) 461.

[45] ATLAS Collaboration, G. Aad *et al.*, *Search for magnetic monopoles and stable particles with high electric charges in 8 TeV pp collisions with the ATLAS detector*, `arXiv:1509.08059 [hep-ex]`.

[46] SLIM Collaboration, S. Balestra *et al.*, *Magnetic monopole search at high altitude with the SLIM experiment*, Eur. Phys. J. **C 55** (2008) 57.

[47] S. Orito *et al.*, *Search for supermassive relics with a 2000 m^2 array of plastic track detectors*, Phys. Rev. Lett. **66** (1991) 1951.

[48] J. Pinfold *et al.*, *A search for highly ionizing particles produced at the OPAL intersection point at LEP*, Phys. Lett. **B 316** (1993) 407.

[49] K. Kinoshita *et al.*, *Search for highly ionizing particles in e^+e^- annihilations at $\sqrt{s} = 91.1$ GeV*, Phys. Rev. **D 46** (1992) R881.

[50] MoEDAL Collaboration, B. Acharya *et al.*, *The physics programme of the MoEDAL experiment at the LHC*, Int. J. Mod. Phys. **A 29** (2014) 1430050.

[51] M. Fairbairn *et al.*, *Stable massive particles at colliders*, Phys. Rep. **438** (2007) 1.

[52] P. Price *et al.*, *Evidence for detection of a moving magnetic monopole*, Phys. Rev. Lett. **35** (1975) 487.

[53] P. Price *et al.*, *Further measurements and reassessment of the magnetic-monopole candidate*, Phys. Rev. **D 18** (1978) 1382.

[54] TASSO Collaboration, W. Braunschweig *et al.*, *A search for particles with magnetic charge produced in e^+e^- annihilations at $\sqrt{s} = 35$ GeV*, Z. Phys. **C 38** (1988) 543.

[55] CLEO Collaboration, T. Gentile *et al.*, *Search for magnetically charged particles produced in e^+e^- annihilations at $\sqrt{s} = 10.6$ GeV*, Phys. Rev. **D 35** (1987) 1081.

[56] CDF Collaboration, A. Abulencia *et al.*, *Direct Search for Dirac Magnetic Monopoles in $p\bar{p}$ Collisions at $\sqrt{s} = 1.96$ TeV*, Phys. Rev. Lett. **96** (2006) 201801.

[57] CDF Collaboration, N. Cothard *et al.*, *Search for Dirac monopoles with the CDF II detector*, CDF Note 11102, 2014.

[58] RICE Collaboration, D. Hogan *et al.*, *Relativistic magnetic monopole flux constraints from RICE*, Phys. Rev. **D 78** (2008) 075031.

[59] ANTARES Collaboration, S. Adrián-Martínez *et al.*, *Search for relativistic magnetic monopoles with the ANTARES neutrino telescope*, Astropart. Phys. **35** (2012) 634.

[60] S. Anderson *et al.*, *Possible evidence for magnetic-monopole interactions: Anomalous long-range α-particle tracks deep underground*, Phys. Rev. **D 28** (1983) 2308.

[61] K. Olive *et al.* (Particle Data Group), *The review of particle physics*, Chin. Phys. **C 38** (2014) 090001.

[62] A. Caplin *et al.*, *Observation of an unexplained event from a magnetic monopole detector*, Nature **321** (1986) 402.

[63] J. Preskill, *Cosmological production of superheavy magnetic monopoles*, Phys. Rev. Lett. **43** (1979) 1365.

[64] E. Parker *et al.*, *The origin of magnetic fields*, Astrop. J. **160** (1970) 383.

[65] M. Turner, E. Parker, and T. Bogdan, *Magnetic monopoles and the survival of galactic magnetic fields*, Phys. Rev. **D 26** (1982) 1296.

[66] MACRO Collaboration, E. Ambrosio *et al.*, *Final results of magnetic monopole searches with the MACRO experiment*, Eur. Phys. J. **C 25** (2002) 511.

[67] ANITA Collaboration, M. Detrixhe *et al.*, *Ultrarelativistic magnetic monopole search with the ANITA-II balloon-borne radio interferometer*, Phys. Rev. **D 83** (2011) 023513.

[68] IceCube Collaboration, R. Abbasi *et al.*, *Search for relativistic magnetic monopoles with IceCube*, Phys. Rev. **D 87** (2013) 022001.

[69] IceCube Collaboration, M. G. Aartsen *et al.*, *Search for relativistic magnetic monopoles in IceCube*, `arXiv:1511.01350 [astro-ph]`.

[70] Super-Kamiokande Collaboration, K. Ueno *et al.*, *Search for GUT monopoles at SuperKamiokande*, Astropart. Phys. **36** (2012) 131.

[71] V. Rubakov, *Superheavy Magnetic Monopoles and Proton Decay*, JETP Lett. **33** (1981) 644.

[72] C. Callan, *Monopole catalysis of baryon decay*, Nucl. Phys. **B 212** (1983) 391.

[73] T. Ebisu and T. Watanabe, *Search for magnetic monopoles trapped in old iron ores using a superconducting detector*, Phys. Rev. **D 36** (1987) 3359.

[74] L3 Collaboration, M. Acciarri *et al.*, *Search for anomalous $Z \to \gamma\gamma\gamma$ events at LEP*, Phys. Lett. **B 345** (1995) 609.

[75] D0 Collaboration, B. Abbott *et al.*, *Search for heavy pointlike Dirac monopoles*, Phys. Rev. Lett. **81** (1998) 524.

[76] OPAL Collaboration, G. Abbiendi *et al.*, *Search for Dirac magnetic monopoles in collisions with the OPAL detector at LEP2*, Phys. Lett. **B 663** (2008) 37.

[77] ATLAS Collaboration, G. Aad *et al.*, *Search for Magnetic Monopoles in $\sqrt{s} = 7$ TeV pp Collisions with the ATLAS Detector*, Phys. Rev. Lett. **109** (2012) 261803.

[78] L. Evans and P. Bryant (eds.), *LHC machine*, JINST **3** (2008) S08001.

[79] F. Marcastel, *CERN's Accelerator Complex*, OPEN-PHO-CHART-2013-001, General Photo, 2013.

[80] M. Lamont, *Status of the LHC*, J. Phys.: Conf. Ser. **455** (2013) 012001.

[81] ATLAS Collaboration, G. Aad *et al.*, *The ATLAS Experiment at the CERN Large Hadron Collider*, JINST **3** (2008) S08003.

[82] G. Aad *et al.*, *ATLAS pixel detector electronics and sensors*, JINST **3** (2008) P07007.

[83] ATLAS Collaboration, G. Aad *et al.*, *dE/dx measurement in the ATLAS Pixel Detector and its use for particle identification*, ATLAS note ATLAS-CONF-2011-016, 2011.

[84] M. Juengst, M. Schultens, and S. Zimmermann, *A time-over-threshold based approach for particle identification with the ATLAS TRT detector*, ATLAS internal note ATL-INDET-INT-2012-001, 2012.

[85] S. Fratina and E. Klinkby, *The Geometry of the ATLAS Transition Radiation Tracker*, ATLAS internal note ATL-COM-INDET-2010-002, 2010.

[86] F. Luehring, *Description of the TRT Readout Scheme*, ATLAS internal note ATL-INDET-2002-026, 2002.

[87] ATLAS Collaboration, *Calibration of the ATLAS Transition Radiation Tracker*, ATLAS note ATLAS-CONF-2011-006, 2011.

[88] ATLAS Collaboration, *Liquid argon calorimeter technical design report*, Tech. Rep. CERN-LHCC-96-041, CERN, Geneva, Apr, 2013.

[89] H. Ma, *Upgraded Trigger Readout Electronics for the ATLAS LAr Calorimeters for Future LHC Running*, J. Phys. Conf. Ser. **587** (2015) 012019.

[90] *Performance of the Electronic Readout of the ATLAS Liquid Argon Calorimeters*, JINST **5** (2010) P09003.

[91] ATLAS Collaboration, *Tile calorimeter technical design report*, Tech. Rep. CERN-LHCC-96-042, CERN, Geneva, 1996.

[92] R. Achenbach *et al.*, *The ATLAS Level-1 calorimeter trigger*, JINST **3** (2008) P03001.

[93] WLCG, *Worldwide LHC Computing Grid*, `http://wlcg.web.cern.ch`, 2015.

[94] K. Cranmer, *Athena analysis tutorial*, USATLAS Analysis Jamboree, May, 2007.

[95] R. Brun and F. Rademakers, *ROOT: An object oriented data analysis framework*, Nucl. Instrum. Meth. A **389** (1997) 81.

[96] A. Farbin, *ATLAS Analysis Model*, J. Phys. Conf. Ser. **119** (2008) 042012.

[97] ATLAS Collaboration, G. Aad *et al.*, *Electron and photon energy calibration with the ATLAS detector using LHC Run 1 data*, Eur. Phys. J. **C 74** (2014) 3071.

[98] M. Mangano *et al.*, ALPGEN, *a generator for hard multiparton processes in hadronic collisions*, JHEP **0307** (2003) 001.

[99] T. Sjöstrand *et al.*, PYTHIA *6.4 physics and manual*, JHEP **05** (2006) 026.

[100] ATLAS Collaboration, G. Aad *et al.*, *Basic ATLAS TRT performance studies of Run 1*, ATLAS note ATL-INDET-PUB-2014-001, 2014.

[101] M. Cherry *et al.*, *Transition radiation from relativistic electrons in periodic radiators*, Phys. Rev. **D 10** (1974) 3595.

[102] ATLAS Collaboration, G. Aad *et al.*, *Electron reconstruction and identification efficiency measurements with the ATLAS detector using the 2011 LHC protonproton collision data*, Eur. Phys. J. **C 74** (2014) 2941.

[103] W. Leo, *Techniques for nuclear and particle physics experiments: a how-to approach*. Springer-Verlag, second revised ed., 1994.

[104] ATLAS-GEO-21-02-02, *ATLAS geometry database tags*, `https://twiki.cern.ch/twiki/bin/view/AtlasComputing/AtlasGeomDBTags`, 2013.

[105] OFLCOND-MC12-SIM-00, *ATLAS COOL database tags*, `https://twiki.cern.ch/twiki/bin/view/AtlasComputing/CoolProdTags`, 2012.

[106] GEANT4 Collaboration, GEANT*4 physics lists*, `http://geant4.cern.ch/support/proc_mod_catalog/physics_lists/useCases.shtml`, 2014.

[107] OFLCOND-MC12b-SDR-01, *ATLAS COOL database tags*, `https://twiki.cern.ch/twiki/bin/view/AtlasComputing/CoolProdTags`, 2012.

[108] J. Alwall *et al.*, *The automated computation of tree-level and next-to-leading order differential cross sections, and their matching to parton shower simulations*, JHEP **07** (2014) 79.

[109] J. Pumplin *et al.*, *New Generation of Parton Distributions with Uncertainties from Global QCD Analysis*, JHEP **07** (2002) 012.

[110] ATLAS Collaboration, G. Aad *et al.*, *Summary of ATLAS* PYTHIA *8 tunes*, ATLAS note ATL-PHYS-PUB-2012-003, 2012.

[111] T. Sjöstrand *et al.*, *A brief introduction to* PYTHIA *8.1*, Comput. Phys. Commun. **178** (2008) 852.

[112] A. D. Martin *et al.*, *Parton distributions for the LHC*, Eur. Phys. J. **C 63** (2009) 189.

[113] G. Watta and R. S. Thorne, *Study of Monte Carlo approach to experimental uncertainty propagation with MSTW 2008 PDFs*, JHEP **08** (2012) 052.

[114] GEANT4 Collaboration, S. Agostinelli *et al.*, GEANT*4—a simulation toolkit*, Nucl. Instrum. Methods Phys. Res. Sect. A **506** (2003) 250.

[115] S. P. Ahlen, *Theoretical and experimiental aspects of the energy loss of relativistic heavily ionizing particles*, Rev. Mod. Phys. **52** (1980) 121.

[116] J. B. Birks, *Scintillations from Organic Crystals: Specific Fluorescence and Relative Response to Different Radiations*, Proc. Phys. Soc. A **64** (1951) 874.

[117] J. B. Birks, *The theory and practice of scintillation counting*. Pergamon Press, first ed., 1967.

[118] ICARUS Collaboration, S. Amoruso *et al.*, *Study of electron recombination in liquid argon with the ICARUS TPC*, Nucl. Instrum. Meth. **A523** (2004) 275.

[119] S. Burdin *et al.*, *A correction to Birks Law in liquid argon ionization chamber simulations for highly ionizing particles*, Nucl. Instrum. Meth. **A664** (2012) 111.

[120] W. Lampl *et al.*, *Calorimeter clustering algorithms: description and performance*, ATLAS note ATL-LARG-PUB-2008-002, 2008.

[121] MC_pp_v4_tight_prescales, *ATLAS trigger configuration*, `https://atlas-trigconf.cern.ch/mc1/smkey/333/l1key/144/hltkey/271`, 2014.

[122] S. Klein, *Suppression of bremsstrahlung and pair production due to environmental factors*, Rev. Mod. Phys. **71** (1999) 1501.

[123] R. Alon et al., *Measurements of the characteristics of boosted, massive jets in pp collisions at 7 TeV with the ATLAS detector.*, ATLAS internal note ATL-PHYS-INT-2013-010, 2013.

[124] ATLAS Collaboration, G. Aad *et al.*, *Performance of the ATLAS Electron and Photon Trigger in pp Collisions at* $\sqrt{s} = 7$ *TeV in 2011*, ATLAS note ATLAS-CONF-2012-048, 2012.

[125] G. Punzi, *Sensitivity of searches for new signals and its optimization*, in *Proceedings of the conference on statistical problems in particle physics, astrophysics and cosmology*, L. Lyons and R. Mount, eds. 2003.

[126] PHYS_StandardGRL_All_Good, *Good run lists for analysis*, `https://twiki.cern.ch/twiki/bin/view/AtlasProtected/GoodRunListsForAnalysis`, 2015.

[127] ATLAS Collaboration, G. Add *et al.*, *Improved luminosity determination in pp collisions at* $\sqrt{s}$ *= 7 TeV using the ATLAS detector at the LHC*, Eur. Phys. J. **C 73** (2013) 2518.

[128] E. Noordeh and W. Taylor, *Extension of the Magnetic Monopole Search to Include Scalar Monopoles*, ATLAS internal note ATL-COM-PHYS-2014-1417, 2014.

[129] M. Hance, *Photon physics at the LHC: A Measurement of Inclusive Isolated Prompt Photon Production at* $\sqrt{s} = 7$ TeV *with the ATLAS Detector*. Springer Theses, first ed., 2003.

[130] ROOT Collaboration, K. Cranmer et al., *HistFactory: A tool for creating statistical models for use with RooFit and RooStats*, Tech. Rep. CERN-OPEN-2012-016, CERN, Geneva, Jan, 2012.

[131] GEANT4 Collaboration, *GEANT4 developments and applications*, IEEE Trans. Nucl. Sci. **53** (2006) 270.

[132] S. Burdin, M. Horbatsch, and W. Taylor, *A correction to Birks' Law in liquid argon ionization chamber simulations for highly ionizing particles*, Nucl. Instrum. Meth. A **664** (2012) 111.

[133] J. Labbé and R. Ishmukhametov, *Crosstalk measurements in the electromagnetic calorimeter during ATLAS final installation*, ATLAS internal note ATL-LARG-INT-2009-004, 2009.

[134] A. Read, *Presentation of search results: the CL_s technique*, J. Phys. G **28** (2002) 2693.

[135] G. Cowan *et al.*, *Asymptotic formulae for likelihood-based tests of new physics*, Eur. Phys. J. **C 73** (2013) 2501.